A STUDY OF NOVEL MAGNESIUM ISOTOPE TRACERS IN GEOLOGICAL, PALEOCEANOGRAPHIC AND BIOGEOCHEMICAL SYSTEMS

A Thesis Submitted to the

College of Graduate and Postdoctoral Studies

In Partial Fulfillment of the Requirements

For the Degree of Doctor of Philosophy

In the Department of Geological Sciences

University of Saskatchewan

Saskatoon

By

SARA ROSE KIMMIG

PERMISSION TO USE

In presenting this thesis in partial fulfillment of the requirements for a Postgraduate degree from the University of Saskatchewan, I agree that the Libraries of this University may make it freely available for inspection. I further agree that permission for the copying of this thesis in any manner, in whole or in part, for scholarly purposes may be granted by the professor who supervised my thesis work (Dr. C. Holmden) or, in his absence, by the Head of the Department of Geological Sciences, or the Dean of the College of Graduate and Postdoctoral Studies. It is understood that any copying or publication or use of this thesis or parts thereof for financial gain shall not be allowed without my written permission. It is also understood that due recognition shall be given to me and to the University of Saskatchewan in any use which may be made of any material in my thesis titled "*A Study of Novel Magnesium Isotope Tracers in Geological, Paleoceanographic and Biogeochemical Systems*."

DISCLAIMER

Reference in this thesis/dissertation to any specific commercial products, process, or service by trade name, trademark, manufacturer, or otherwise, does not constitute or imply its endorsement, recommendation, or favoring by the University of Saskatchewan. The views and opinions of the author expressed herein do not state or reflect those of the University of Saskatchewan, and shall not be used for advertising or product endorsement purposes.

Requests for permission to copy or make use of materials in this thesis, in whole or in part, should be addressed to:

Department Head
Department of Geological Sciences
University of Saskatchewan
114 Science Place
Saskatoon, Saskatchewan, S7H 5E2, Canada

--OR--

Dean
College of Graduate and Postdoctoral Studies
University of Saskatchewan
Room 116 Thorvaldson Building
110 Science Place
Saskatoon, Saskatchewan, S7N 5C9, Canada

DEDICATION

I dedicate this work to Rose Smith and Caroline Worsham, two extraordinary women who taught me to never shy away from a challenge. You are both deeply missed.

ABSTRACT

This thesis explores Mg isotopes as tracers in geological and biological systems. Chapters 2 and 3 investigate Mg isotopes as tracers of fluid flow during dolomitization. The studied carbonate is the variably dolomitized Late Ordovician Red River Formation in the Williston Basin. Three types of dolomite are described (burrow, matrix, saddle) with all three yielding identical δ^{26}Mg values at the hand-sample scale, indicating that the dolomite formed from the same fluid, or was overprinted by successive dolomitizing events. A broader study was undertaken to determine whether large dolomite bodies might preserve gradients in δ^{26}Mg values at the basin-scale. Because dolomite preferentially sequesters light isotopes of Mg during its formation, the dolomitizing fluid (and product dolomite) should become progressively enriched in heavy isotopes in the direction of fluid flow. The studied dolomite body is the interconnected network of *Thalassinoides* burrows in the 'C' member carbonate of the Red River, where it is found that δ^{26}Mg values increase radially away from the center of the Williston Basin. As such, dolomitizing fluids must have originated in the deep center of the basin, using the burrows to flow up toward the basin margins. This interpretation is strengthened by decreasingly radiogenic $^{87}Sr/^{86}Sr$ ratios in the direction of fluid flow. While the timing of dolomitization is unknown, the formation of overpressurized fluids in the deep center of the basin could have been triggered by a late Paleozoic thermal event, and/or the far-field tectonic effects of the Antler Orogeny, which caused crustal fluids to ascend upwards into the bottom of the Williston Basin through a system of down-to-the-basement vertical faults, which still exist in the basin center today.

Chapter 4 presents a technique for determining original limestone δ^{26}Mg values in marine carbonates with trace dolomite. The study section is a carbonate platform in Nevada recording the Late Ordovician (Hirnantian) glaciation event. The δ^{26}Mg value for limestone deposited during the sea-level lowstand, and bracketing highstands, is calculated from a graphical mixing technique using chemostratigraphic data. Carbonate deposited during the lowstand has the highest δ^{26}Mg value, consistent with precipitation of primary aragonite during the Hirnantian glaciation in a tropical-shelf setting, while limestone deposited before and after the glaciation yields lower δ^{26}Mg values, consistent with precipitation of calcite. While diagenetic effects on δ^{26}Mg values in carbonate sediment are difficult to predict, a negative shift in $\delta^{44/40}$Ca, a positive shift in δ^{13}C, and the highest Sr/Ca ratios in the study section, strengthen the case for aragonite deposition during

the sea-level lowstand. This result is significant in that the studied carbonates formed in the midst of a 'calcite sea', which identifies a period of seawater composition favoring abiotic precipitation of calcite, rather than aragonite, in shallow marine settings. This study emphasizes the problem of misinterpreting stratigraphic trends in Mg, Ca, and C isotope profiles as genuine reflections of global-scale changes in the geochemical cycling of these elements.

Chapter 5 examines Mg-cycling in the 'critical zone' with the aim of deciphering whether or not first-order streams exhibit plant-fractionated Mg isotope signatures. This has implications for the δ^{26}Mg value of the weathering flux to the oceans, which is a component of the ocean Mg-cycle. There is no evidence in a studied sugar maple stand for Mg isotope fractionation associated with uptake from soil solutions into mature trees and seedlings. There is, however, large within-tree fractionation between tissues. While sugar maple in the field exhibit no uptake related fractionation effects, seedlings grown in the laboratory yield contrasting results, exhibiting higher δ^{26}Mg values than the nutrient source. The difference is attributed to the absence of arbuscular mycorrhizal fungi in the artificial soils in which the seedlings were grown in the laboratory. It is speculated that these fungi are important vectors in the uptake of Mg into tree fine roots in natural settings, and that the fungi do not fractionate Mg isotopes. It is also found that δ^{26}Mg values and Mg/Ca ratios of soil solutions and stream water, and acid leaches of the C horizon mineral soil are identical to each other, and to the aboveground vegetation as well, indicating that plant-recycled fluxes of Mg and Ca, filtering down through the soil profile from the surface, appear to completely overwhelm the much smaller annualized input fluxes of these elements from atmospheric deposition and soil mineral weathering.

ACKNOWLEDGEMENTS

I would like to express my gratitude to my supervisor, Dr. C. Holmden, for providing me the opportunity to study under his direction and full use of his research facilities, as well as for his valuable advice, support, and patience throughout my studies. I am also very much appreciative to Dr. N. Bélanger for providing me necessary guidance and training in the field, as well as for his numerous other contributions in both the field and the laboratory including collecting samples and information about the study location, data analysis that was crucial for this thesis, and overseeing a laboratory plant growth experiment. This project would not have been possible without his support and expertise, and I am grateful for his mentorship. I would like to extend my thanks to Drs. M. Amini and S. Timsic, as well as D. Besic and M. Nasreen for their assistance in the lab and for their friendship. A special thank you to J. Rosen for his technical expertise and mentorship in the lab. Thanks to Drs. T. Huston, J. Gleason, B. Eglington, and B. Pratt, as well as M. Johnson and R. Millar, B. Novakovski, and T. Bonli for their analytical expertise. Also, thanks to B. Brenna, F. Bélanger, E. Valiquette, A. Collin, as well as Drs. K. Scheiderich and J. Kimmig for their assistance in the field. To the Saskatchewan Ministry of the Economy Subsurface Geological Laboratory, the Manitoba Mineral Resources Midland Sample and Core Library, the Wilson M. Laird Core and Sample Library in Grand Forks, ND, and the Station de biologie des Laurentides of the Université de Montréal, thank you for granting me sampling privileges and the use of your facilities. Thank you to Dr. A. Galy for providing me with the isotope standards used for sample analyses. Thanks to T. Hudson and W.D. Plastics for help constructing lab equipment used in this study. I would also like to thank the rest of my committee for their advice and support. This thesis was funded by University of Saskatchewan Dean's and Devolved Scholarships, the Geological Society of America Graduate Student Research Grant, as well as NSERC Discovery Grants and Saskatchewan Ministry of the Economy Grants. Finally, I would like to give a special thank you to my loving husband, Julien, and to my parents Mona and Joseph Worsham, for their thoughtful support and understanding throughout my studies.

TABLE OF CONTENTS

LIST OF FIGURES

LIST OF TABLES

CHAPTER 1 – Introduction

1.1. Geochemistry – History and keywords

The term *Geochemie* was coined in 1838 by Christian Friedrich Schöbein, however it wasn't until the publication of *'Elements of Chemical and Physical Geology'* (1854–1859) that the field of chemistry was truly introduced to the field of geology, the author Gustav Bischof was largely to thank for the introduction (Wedepohl, 1969). An abridged definition by V. M. Goldschmidt (1888–1947), the labelled 'father of modern geochemistry,' in 1933 serves as a foundation for the field, "Geochemistry is concerned with the laws governing the distribution of the chemical elements and their isotopes throughout the Earth." (Wedepohl, 1969; Mason, 1992). Geochemistry is essentially the study of the chemical constitution of the Earth and its chemical changes, having occurred recently or in the past (Fairbridge, 1972).

Chemical elements are cycled through the Earth by various processes and are contained in various exchangeable reservoirs. These reservoirs are interconnected by processes in a complex fashion in what is referred to as 'the Geochemical Cycle' (Fig. 1.1). Every element follows its own path through the various reservoirs of the geochemical cycle, based on their chemical properties and characteristics, and are cycled based on the element's 'residence time' (τ) in each system (Eq. 1.1). The residence time is the average time a tracer spends in a reservoir, where M_{SS} is the total mass of the reservoir at steady state and $F_{in,SS}$ is the total input or $F_{out,SS}$ output flux to the system, at steady state.

$$\tau = \frac{\mathrm{M_{SS}}}{\mathrm{F_{in,SS}}} = \frac{\mathrm{M_{SS}}}{\mathrm{F_{out,SS}}} \tag{1.1}$$

When there is a perturbation in a steady state system, elements with a long residence time take longer to react to the perturbation, as well as longer to return to steady state once the perturbation ends. Magnesium (Mg) is an element with a long residence time in the ocean ~ 13 Myr (Broecker and Peng, 1982), compared to elements such as carbon (C) (0.1 Myr) (Berner and Berner, 1996) and calcium (Ca) (0.5–1 Myr) (Milliman, 1993; Holmden et al., 2012b). Thus, perturbations in the Mg oceanic system will take far longer to respond and return to steady state than for C or Ca. In some cases, an element may accumulate and reside for an extended period of time in one reservoir or another, what is collectively referred to as a 'sink.' Not only may

chemical elements flux through the various Earth reservoirs, but the geochemical cycle can be broken down even further to the variants of the elements, or isotopes. Isotopes of an element contain the same number of protons, however, the number of neutrons for each varies thus creating different isotopic masses. Isotopes are denoted as such, ^{n}Element, *n* being the mass of the isotope. The atomic weight of an element reflects the isotopic abundances and masses of its isotopes. Magnesium, the subject of this study, has three stable isotopes, ^{24}Mg, ^{25}Mg, and ^{26}Mg, and is discussed in more detail in the following section.

1.2. Magnesium – The element, isotopes, and geochemical analyses

Magnesium was discovered in 1755 by Joseph Black (Leicester and Klickstein, 1952), and later isolated by Sir Humphry Davy in 1808 (Davy, 1840), the term '*magnium'* was originally applied to the new element because, at the time, metallic manganese was named magnesium. However, in 1812 Sir Davy, with the help of some of his 'philosophical friends' changed the name of the new metal to magnesium (Davy, 1812), derived from *Magnesia*, a district of Thessaly, Greece and the location from where the magnesium carbonate Sir Davy used in his experiments was sourced. It wasn't until 1830, when Antoine Bussy produced a viable quantity of Mg, that the pure metal could be studied in detail. Magnesium is the 8th most abundant element of the continental crust (Taylor and McLennan, 1985) and the 4th most abundant species in seawater (Millero, 1974), as well as a vital macronutrient for plants, a common aqueous cation in natural waters, and a significant component in carbonate, silicate, and sulfate rocks and minerals. Magnesium ions are soluble and highly mobile in the environment, and are lost from the continents and transported by rivers to the ocean mainly as a consequence of mineral weathering, and especially of carbonate (dolomite) weathering (e.g., Tipper et al., 2006a, b). Magnesium is removed during hydrothermal circulation of seawater through the oceanic crust beneath mid-ocean ridges, and to lesser amounts via ion-exchange reactions with clays (Drever, 1974; Elderfield and Schultz, 1996; Holland, 2005). It is also removed by co-precipitation with Ca in various marine carbonates, and during the formation of dolomite during diagenesis (Wilkinson and Algeo, 1989). Most of the removal processes fractionate Mg isotopes, with the exception of Mg that is removed by hydrothermal weathering of the oceanic crust (Tipper et al., 2006b), as none is returned to seawater at hydrothermal vents (Edmond et al., 1979; Elderfield and Schultz, 1996). The continental weathering flux of Mg

isotopes may be fractionated by rock and mineral weathering processes and biogeochemical cycling in soils and vegetation (e.g., Tipper et al., 2006a, b, 2010; 2012a, b; Brenot et al., 2008; Black et al., 2008; Pogge von Strandmann et al., 2008; Bolou-Bi et al., 2010, 2012, 2016; Wimpenny 2010, 2011, 2014a, b; Opfergelt 2012, 2014; Mavromatis et al., 2014; 2016). Changes in the input and output fluxes of Mg to and from the oceans, and the isotopic composition of the fluxes, has the potential to drive long-term secular variation in the Mg concentration of seawater and its isotopic composition.

The study of Mg isotopes has been underway since the late 1960s, mostly aimed at discerning isotopic anomalies in meteorites (e.g., Catanzaro et al., 1966; Lee and Papanastassiou 1974) or in artificially spiked systems in which the abundance of one isotope is artificially enriched (Cary et al., 1990). The very small mass dependently fractionated variations of Mg isotopes in terrestrial samples did not receive much attention before advances in commercially available mass spectrometers made accurate measurements possible in the late 1990s and early 2000s with the introduction of multiple collector inductively coupled plasma mass spectrometry (MC-ICP-MS) (e.g., Galy et al., 2001).

The three naturally occurring stable isotopes denoted with their respective natural abundances and atomic weights in parentheses are: ^{24}Mg (78.99%, 23.985 u), ^{25}Mg (10.00%, 24.986 u), and ^{26}Mg (11.01%, 25.983 u) (Catanzaro et al., 1966). The relative mass difference is 4% between ^{25}Mg and ^{24}Mg, and 8% between ^{26}Mg and ^{24}Mg, which predicts significant isotopic variation of Mg isotopes in nature. Both the ^{26}Mg/^{24}Mg and ^{25}Mg/^{24}Mg ratios are measured, and the data reported in the conventional delta notation as permil (‰) deviations from the mass dependent fractionation of the sample isotope ratio relative to a standard (Eq. 1.2, where x = 25 or 26). A second notation, denoted as alpha (α), is defined as the 'fractionation factor' between two δ^{x}Mg values, relative to the same reference material (Eq. 1.3). A capital delta (Δ_{A-B} or Δ^{A}_{B}) is used to denote mass dependent differences (fractionation) in δ-values between samples A and B (Eq. 1.4).

$$\delta\,{}^{x}\mathrm{Mg}_{\mathrm{smp}}(‰) = \left(\frac{\left({}^{x}\mathrm{Mg}/{}^{24}\mathrm{Mg}\right)_{\mathrm{smp}}}{\left({}^{x}\mathrm{Mg}/{}^{24}\mathrm{Mg}\right)_{\mathrm{DSM3}}} - 1\right)\times 1000 \qquad (1.2)$$

$$\alpha_{A-B} = \frac{1000+\delta\,{}^{x}\mathrm{Mg}_{A}}{1000+\delta\,{}^{x}\mathrm{Mg}_{B}} \qquad (1.3)$$

$$\Delta\,^{x}Mg_{A-B} = \delta\,^{x}Mg_{A} - \delta\,^{x}Mg_{B} \quad (1.4)$$

The total range of variation in Mg isotopes in terrestrial materials to date is ~ 7–8‰ (Fig. 1.2) (Teng, 2017), and the fractionation of Mg isotopes, as with other stable isotopes, is larger when associated with low temperature processes. A common interlaboratory standard reference material used for Mg isotope analyses, and used throughout this study, is **D**ead **S**ea **M**etal **3** (DSM3) (Galy et al., 2003), when referenced against itself it yields a δ^{26}Mg value of 0‰ (using Eq. 1.2). Analytical uncertainty within the Saskatchewan Isotope Laboratory (SIL) is ± 0.08‰ (2σ) for δ^{26}Mg, and ± 0.04‰ (2σ) for δ^{25}Mg. These estimates of uncertainty are based on repeated analyses of the external mono-elemental Mg standard, **Cam**bridge-**1** (CAM1) (Fig. 1.3a, b). The standard CAM1 is commonly used to monitor the interlaboratory quality of Mg isotopic analyses with an expected δ^{26}Mg value of –2.58 ± 0.14‰ and a δ^{25}Mg value of –1.33 ± 0.07‰ (Galy et al., 2003). Measurements in the Saskatchewan Isotope Laboratory give a δ^{26}Mg value of –2.62 ± 0.08‰ (2σ, N=123) and a δ^{25}Mg value of –1.35 ± 0.04‰ (2σ, N=123) for this standard (Fig. 1.3b).

In the mid-1960s, the National Institute of Standards and Technology (NIST), formerly known as the National Bureau of Standards (NBS), developed a standard reference material for Mg isotope analysis as a pure Mg metal, dubbed SRM980 (Catanzaro et al., 1966). SRM980 was sold as chips of Mg metal, dissolved in nitric acid (HNO_3) in each individual laboratory. Galy et al. (2003) reported that SRM980 is too isotopically variable and is therefore inappropriate to use as a reference material for reporting data at the sub-permil level, with up to 8‰ variation in measured δ^{26}Mg values. Isotopic heterogeneity is resolved by keeping standards in solution. Galy et al. (2003) prepared a new isotopically homogeneous standard solution, DSM3, by dissolving approximately 10 g of pure magnesium metal into 1 L of ~ 0.3N HNO_3. An aliquot of this standard solution is available from the senior author of the paper upon request.

Instrumentation associated with measuring Mg isotopes has evolved through time. Early measurements of Mg isotopes by thermal ionization mass spectrometry (TIMS) and secondary ion mass spectrometry (SIMS) could be precise, but inaccurate because it was not possible to correct for isotopic fractionation in the instruments during measurement. It was therefore necessary to precisely replicate the instrumental fractionation from sample to sample to obtain

useful results. The introduction of MC-ICP-MS solved this issue because the Mg is introduced into the plasma source from a weak acid solution, making it possible to bracket the measurement of samples with standards of a known isotopic composition repeatedly (i.e. $std_n - smp_n - std_{n+1} - smp_{n+1} - std_{n+2}$, etc.), without fractionating the Mg in the sample and standard solutions (Galy et al., 2001; Young and Galy, 2004). Cross-contamination of samples is avoided by flushing the sample introduction system of the instrument with a weak acid for several minutes between each measurement. The isotopic fractionation occurring in the ion source of the instrument is corrected for when the delta-value is constructed from the measurement of the sample normalized to the average of the bracketed-standard measurements (Albarède and Beard, 2004).

Magnesium isotope measurements by MC-ICP-MS are not without their own set of difficulties. The plasma ion source creates numerous molecular interferences from the acid used to introduce the sample to the plasma. Magnesium is introduced in a weak nitric acid solution (0.3N HNO_3) which creates metal hydride and metal nitride species and dissolved organic matter creates metal carbide interferences that may directly impact Mg isotopic measurements (C_2^+, C_2H^+, $C_2H_2^+$, CN^+, and NaH^+) (Galy et al., 2001). There are also elemental interferences from doubly charged ions ($^{48}Ca^{2+}$, $^{48}Ti^{2+}$, $^{50}Ti^{2+}$, $^{50}V^{2+}$, $^{50}Cr^{2+}$, $^{52}Mn^{2+}$ and $^{52}Cr^{2+}$ (Galy et al., 2001), creating unwanted isobars (isotopes of different elements with the same atomic weight) with masses 24, 25, and 26 (Albarède and Beard, 2004). Matrix effects can also create isotopic bias between measurements of samples and standards. It is essential to obtain very pure aliquots of Mg in samples using cation exchange resin to match the (low matrix concentration) in the high purity Mg standard (Appendix A). If the matrices of the sample and standard are very similar, isotopic fractionation of the sample and standard in the ion source will be the same, and the effect will cancel when the data are expressed as delta-values. The use of a desolvating nebulizer (Aridus, Apex), which creates a 'dry-plasma' has been deemed essential in many laboratories to reduce the amount of C, H, O, and N to insignificant levels. However, testing using the Thermo Scientific NEPTUNE MC-ICP-MS housed in the SIL has shown that 'wet plasma' conditions (sample introduction using a glass cyclonic spray chamber) give precise and accurate Mg isotope data as well, and is easier to use. In addition, wet plasma conditions are less sensitive to concentration mismatches between samples and bracketing standards than dry plasma conditions (Teng and Yang, 2014). Another important consideration is that recovery of nearly 100% of the Mg passed through the cation exchange columns is necessary to avoid isotopically fractionating

the sample during its purification (Appendix A). Heavy Mg isotopes elute from the column slightly ahead of the lighter ones (Chang et al., 2003; Teng et al., 2007).

1.2.1. Magnesium isotope tracer potential

Under the misconception of negligible terrestrial variation in Mg isotopes in the early years of study based on inferior measurement techniques, the primary focus of Mg isotope research was aimed at searching for isotopic anomalies in meteorites based on the presence of short-lived ^{26}Al in the solar nebula just prior to planetary formation, which decays to ^{26}Mg (e.g., Young et al., 2002, Young and Galy, 2004). Since the advent of MC-ICP-MS, evidence for mass dependent fractionation of Mg isotopes in terrestrial samples is ubiquitous (e.g., Galy et al., 2002; Chang et al., 2003, 2004; Wombacher et al., 2006, 2011; Bolou-Bi et al., 2009; Hippler et al., 2009; Jacobson et al., 2010; Immenhauser et al., 2010; Higgins and Schrag, 2010, 2012, 2015; Yoshimura et al., 2011; Riechelmann et al., 2012, 2016; Fantle and Higgins, 2014; Geske et al., 2012, 2015a, 2015b; Blättler et al., 2015; Huang et al., 2012, 2015; Husson et al., 2015; Peng et al., 2016; Farkaš et al., 2016).

Carbonates are important minerals within the biosphere, hydrosphere, and lithosphere and are integral to the cycling of Mg, Ca, and C. They also exhibit the lowest δ^{26}Mg values and the widest range of values of any geological or organic material measured to date (Fig. 1.2). Sedimentary successions of marine carbonate are important geochemical archives of biosphere evolution (Saenger and Wang, 2014) and seawater chemical evolution over geological time (Wilkinson and Given, 1986). However, carbonates are also highly susceptible to post-depositional alteration during diagenesis that may negatively impact their record-keeping integrity (Swart, 2015). Dolomitization, or the diagenetic process of replacing half of the calcium (Ca) in limestone ($CaCO_3$) with magnesium (Mg) to form dolomite (Eq. 1.5), is believed to be an important mechanism for driving secular change in the Mg concentration and Mg/Ca ratio of seawater through time (Wilkinson and Algeo, 1989; Holland, 2005).

$$2CaCO_3 + Mg^{2+} = CaMg(CO_3)_2 + Ca^{2+} \quad (1.5)$$

The origin of dolomite is still poorly understood, as stated by Zenger and Mazzullo (1982), “No other sedimentary rock has been more enigmatic and perplexing to geologists than

dolomites." Dolomite is named for Déodat de Dolomieu (1750–1801), a French geologist who described the calcareous rocks of the southern Italian Alps, observing that despite their similarities to limestones, the exposed rocks did not effervesce freely when exposed to weak acid (de Dolomieu, 1791). A common sedimentary rock and rock-forming mineral, dolomite is found extensively in the geologic record, but is relatively absent in modern environments. Despite 225 years of research on the origins of dolomite, especially of massive deposits, the mechanisms for dolomite formation remain enigmatic due to the poorly understood chemical, biological, and hydrological conditions under which dolomite can form and is even further convoluted by petrographic and geochemical data permitting multiple interpretations (Warren, 2000; Machel, 2004). In addition, formation of well-ordered stoichiometric dolomite ($Ca_{0.5}Mg_{0.5}(CO_3)_2$) at ambient temperatures and pressures is notoriously difficult (Land, 1998). The enigmatic aspects of the origin of dolomite are commonly referred to as the '*dolomite problem*.'

Uptake of Mg during the formation of dolomite is accompanied by a fractionation of the isotopes of Mg, with light isotopes preferentially incorporated into dolomite and heavy isotopes remaining in solution (e.g., Higgins and Schrag, 2010, 2012; Fantle and Higgins, 2014; Li et al., 2015; Geske et al., 2015a; Kimmig and Holmden, 2017). Models of replacement dolomitization require large supplies of Mg to be transported to the sites of dolomitization by subsurface fluid-flow (Land, 1985). Thusly, subsurface dolomitization is essentially a hydrogeological phenomenon (Machel, 2004). As a result of isotopic fractionation associated with dolomite precipitation (Eq. 1.5), it is predicted that the reactant Mg in the dolomitizing fluid and the product dolomite will become progressively enriched in heavy Mg isotopes in the direction of fluid flow. Thus, information on the direction of fluid flow during dolomitization may be preserved as Mg isotope gradients in dolomite bodies. Establishing that these gradients exist would represent a major step forward in the evaluation of dolomite formation models, as the flow direction of the dolomitizing fluids is basic information that may be used to reject some models of dolomitization, while favoring others.

Dolomite is not the only carbonate mineral in marine sedimentary successions whose diagenetic origins can be studied with Mg isotopes. There is also the potential for Mg isotope studies to reveal changes in the primary mineralogy of carbonate sediment over geological time, namely aragonite and calcite, thus complementing information gleaned from C, O, and Ca isotope tracers used for the same purpose, as well as trace element (Te) to Ca ratios (e.g., Brand

and Veizer, 1980; Mazzullo, 1980; Given and Lohmann, 1985). Aragonite and calcite are minerals with the same chemical formula ($CaCO_3$) but exist as polymorphs with different crystal structures (i.e., orthorhombic aragonite and rhombohedral calcite). As a consequence, aragonite is a more unstable mineral than calcite and is thus more susceptible to diagenetic alteration. Although aragonite is a common primary marine precipitate of seawater, its preservation potential declines with the geological age of the sediment due to its inversion to calcite during diagenesis. The presence of aragonite must therefore be inferred from the texture of the secondary calcite produced (aragonite has a more acicular crystal habit than calcite in the marine environment) (e.g., Bathurst, 1975; Lasemi and Sandberg, 1984; Sandberg, 1985), or the elemental and isotopic geochemistry of the calcite, which may retain certain geochemical signatures diagnostic of aragonite that has inverted to calcite. For example, aragonite is higher in Sr concentration, and may be higher and lower in Mg and Ca isotope composition, respectively (Gussone et al., 2005; Saenger and Wang, 2014). However, there are also problems to consider. Aragonite is very low in Mg concentration, lower than co-precipitated low magnesium calcite (LMC), and much lower than the compositional variant known as high magnesium calcite (HMC), which is even more soluble than aragonite. The HMC also dissolves during diagenesis, and as a result any aragonite inverting to LMC will take on the isotopic composition of the HMC (offset by a fractionation factor), rather than retaining the Mg isotopic signature of the original aragonite. A related problem is small quantities of dolomite that may exist in marine limestone. Even the smallest amounts of dolomite (e.g., < 10%) in whole-rock carbonates can significantly shift the average $\delta^{26}Mg$ of the sediment (Kimmig and Holmden, 2017).

The 'critical zone' (zone in which rock, soil, water, air, and living organisms interact) is another promising area of Mg isotope research (e.g., de Villiers et al., 2005; Tipper et al., 2006a, b, 2008, 2010, 2012a, b; Brenot et al., 2008; Teng et al., 2010; Wimpenny et al., 2010, 2011, 2014a, b; Huang et al., 2012; Pogge von Strandmann et al., 2008a, b, 2012). Chemical weathering of Mg and Ca bearing silicate rocks is known to influence global climate through the drawdown of atmospheric CO_2 (Eq. 1.6). Investigations into the processes responsible for Mg exchange within and the transfer of Mg out of the 'critical zone,' are important for determining continentally derived weathering signatures of Mg isotopes to the oceans, and ultimately the mediation of the atmospheric carbon budget (Berner et al., 1983), according to Eq. 1.6.

$$(Mg, Ca)SiO_3 + 2CO_2 + 3H_2O \rightarrow (Mg, Ca)^{2+} + 2HCO_3^- + Si(OH)_4 \quad (1.6)$$

Understanding how biogeochemical tracers such as Mg isotopes behave during vegetation uptake and associated weathering processes contributes to our broad understanding of how processes in the 'critical zone' may ultimately affect the chemistry of the ocean and climate of the Earth. Magnesium is an essential macronutrient for plants. It is used for the synthesis of the chlorophyll molecule, as an enzyme activator for energy metabolism, and aids phosphate metabolism (ATP) and plant respiration (Wilkinson et al., 1990; Marschner, 1995; Epstein and Bloom, 2005; Barker and Pilbeam, 2007). Magnesium is absorbed by the roots of a plant as an aqueous complex ($Mg(H_2O)_6)^{2+}{}_{(aq)}$). It is readily translocated from older plant tissues to younger growing leaves and seeds (Black et al. 2008), and exists within plants in both the free ion and chelated forms. In forested ecosystems, biogeochemical cycling of Mg by vegetation may release light isotopes of Mg to rivers (Black et al., 2008), as heavy isotopes have been shown to be retained in vegetation (Black et al., 2008; Tipper et al., 2010, 2012b; Bolou-Bi et al., 2010, 2012; Opfergelt et al., 2014; Mavromatis et al., 2014), thereby contributing to an isotopically fractionated flux of Mg isotopes to nearby rivers, and consequently the ocean. A return flux of Mg to the soil pool also occurs via litterfall and subsequent decomposition, thus contributing another biologically fractionated source of Mg to soil pools and rivers. It is necessary to understand the biogeochemical cycling of Mg isotopes in forested ecosystems to characterize the net effect of this cycling on Mg isotope compositions in rivers, and ultimately the effect of vegetation on the δ^{26}Mg value of the continental weathering flux of Mg to the oceans.

1.3. Outline of thesis

This thesis is organized into six chapters, Chapter 1 (Introduction), provides background information and keywords on the topics covered by the thesis. It is followed by four chapters that describe original work, forming the main body of the thesis: (Chapter 2) Magnesium isotope compositions of three types of dolomite in the Late Ordovician Red River Formation in a single core from southeastern Saskatchewan, (Chapter 3) Magnesium isotope tracing of paleo-fluid flow preserved in dolomite from the 'C' member carbonate of the Red River Formation in 17 cores sampled across the Williston Basin, (Chapter 4) Magnesium isotope tracing of local-scale oscillations of aragonite and calcite during the Hirnantian glaciation event in Nevada, (Chapter

5) Magnesium isotope tracing of biogeochemical cycling of Mg in a forested ecosystem in Québec. Chapter 6 is the Conclusion.

Chapters 2 and 4 have been published in peer-reviewed journals. Chapter 5 has been submitted to a peer-reviewed journal. Chapter 3 is written in manuscript-style with the aim of submitting it to a peer-reviewed journal for consideration of publication. Each chapter contains an abstract, an introduction that identifies background and objectives, information on field site, sampling and analytical methods, results, discussion, and conclusions. Transitions are provided between each chapter, linking each chapter to one another. Chapter 6 (Conclusion) includes a final summary of the thesis including the relationship between each of the previous chapters to the central objectives of the thesis, as described in section *1.4*. Supplementary methods, data, figures, tables and abstracts presented at meetings and seminars attended over the course of the thesis work, are included in three Appendices (A–C).

1.4. Objectives of thesis

Chapter 2 documents Mg isotope variation in the three types of dolomite from the Red River Formation in a core in southeastern Saskatchewan, identified by petrography, texture, and geochemistry. The objective is to identify whether these three types of dolomite record similar or different Mg isotope signatures. These three types of dolomite could reflect different dolomitization events, or different phases of a single event.

Chapter 3 expands on Chapter 2, with the objective of evaluating whether gradients in δ^{26}Mg values exist in dolomite bodies, and if they reflect the direction of fluid flow during dolomitization. The studied dolomite body is an anastomosing network of burrows in the 'C' member carbonate of the Red River Formation. Information gleaned from the paleo-fluid flow is crucial to the development of a dolomitization model, as it helps to identify the hydrogeological drivers of fluid flow. This, in turn, helps to constrain the conditions of dolomite formation, the relative timing of dolomite formation, and the source of Mg ions.

Chapter 4 is a whole-rock study of Mg isotope variation in a succession of marine limestone spanning the Late Ordovician Hirnantian glaciation and mass extinction event. The objective is two-fold: (1) to determine the effect of small quantities of dolomite on the stratigraphic record of sedimentary δ^{26}Mg values in a study section from the Monitor Range, Nevada and to 'correct' for the effect of the dolomite, and (2) to use the corrected (limestone)

δ^{26}Mg values to look for stratigraphic changes in carbonate polymorph mineralogy that may have occurred in the study section during the glaciation.

Chapter 5 uses Mg isotopes to study Mg-cycling in a forested ecosystem in Québec, Canada. The objective is three-fold: (1) to determine the range of δ^{26}Mg variation in the 'critical zone' at the study site, (2) to resolve the processes that control Mg isotope fractionation in the 'critical zone,' and (3) to determine the net effect of the various Mg isotope fractionations occurring in the 'critical zone' on the isotopic composition of Mg exported to a first-order stream, which has bearing on whether or not the continental Mg-flux to the oceans is fractionated from igneous inventory values.

1.5. Figures

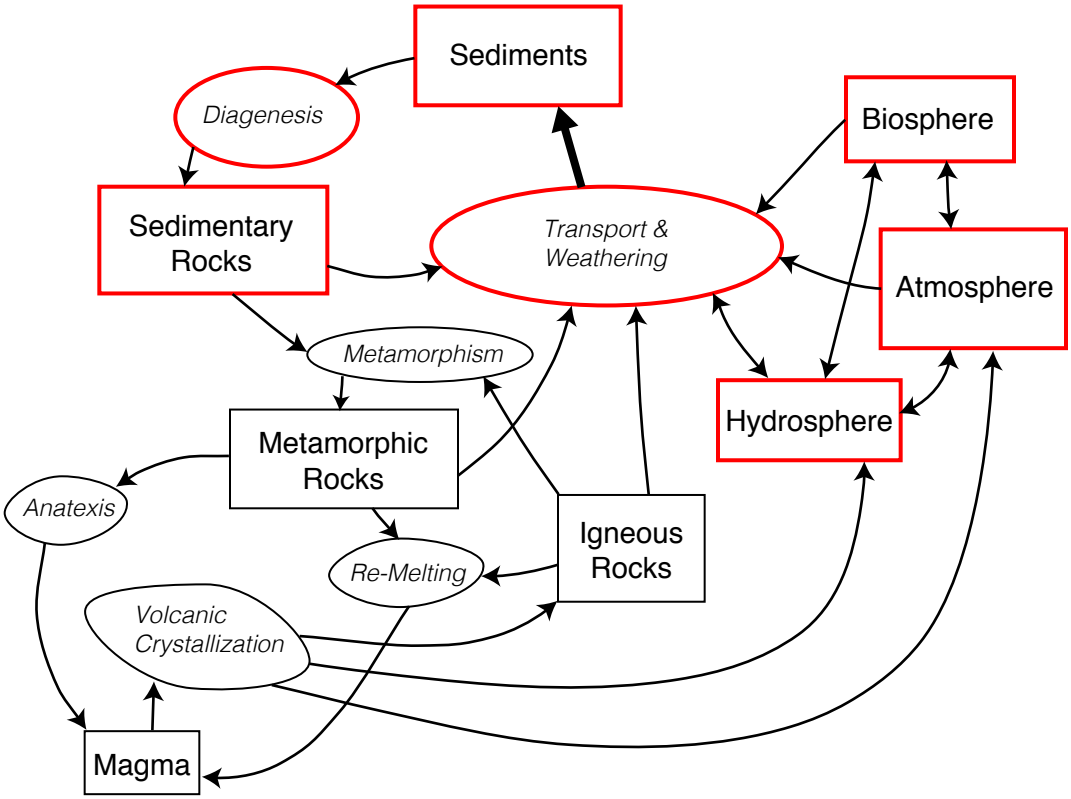

Figure 1.1 Geochemical cycle on Earth's crust and surface. Processes are denoted by circles, reservoirs by boxes. Reservoirs and processes that occur in the low temperature field, and are the main focus of this thesis, are highlighted in red. These low temperature processes exhibit the largest variation of Mg isotopes on the planet. Figure modified from Fairbridge (1972) and Mason (1992).

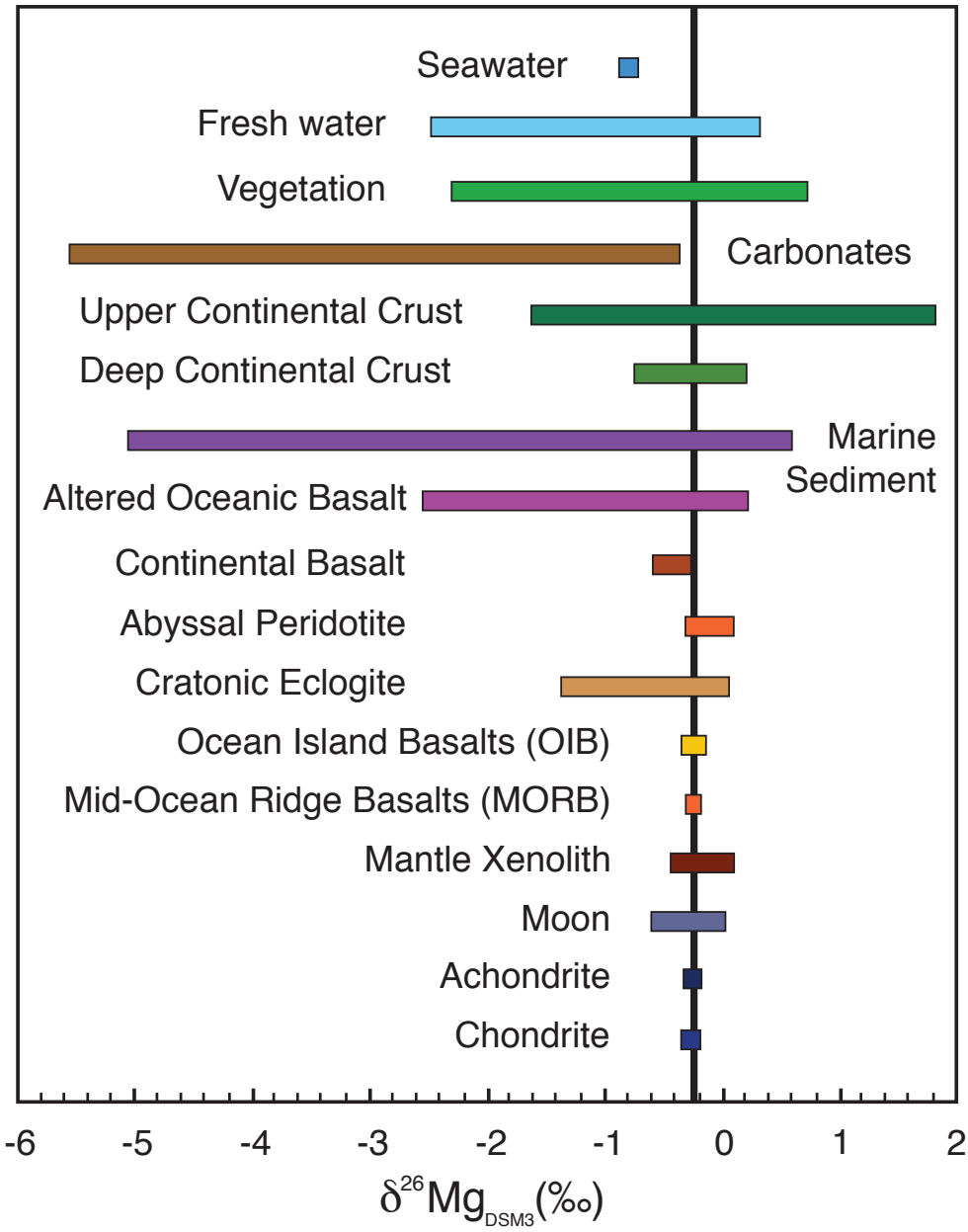

Figure 1.2 Magnesium isotope distribution across terrestrial and extraterrestrial reservoirs. The vertical black line represents the Mg isotopic composition of bulk silicate Earth. Figure reproduced from Teng (2017).

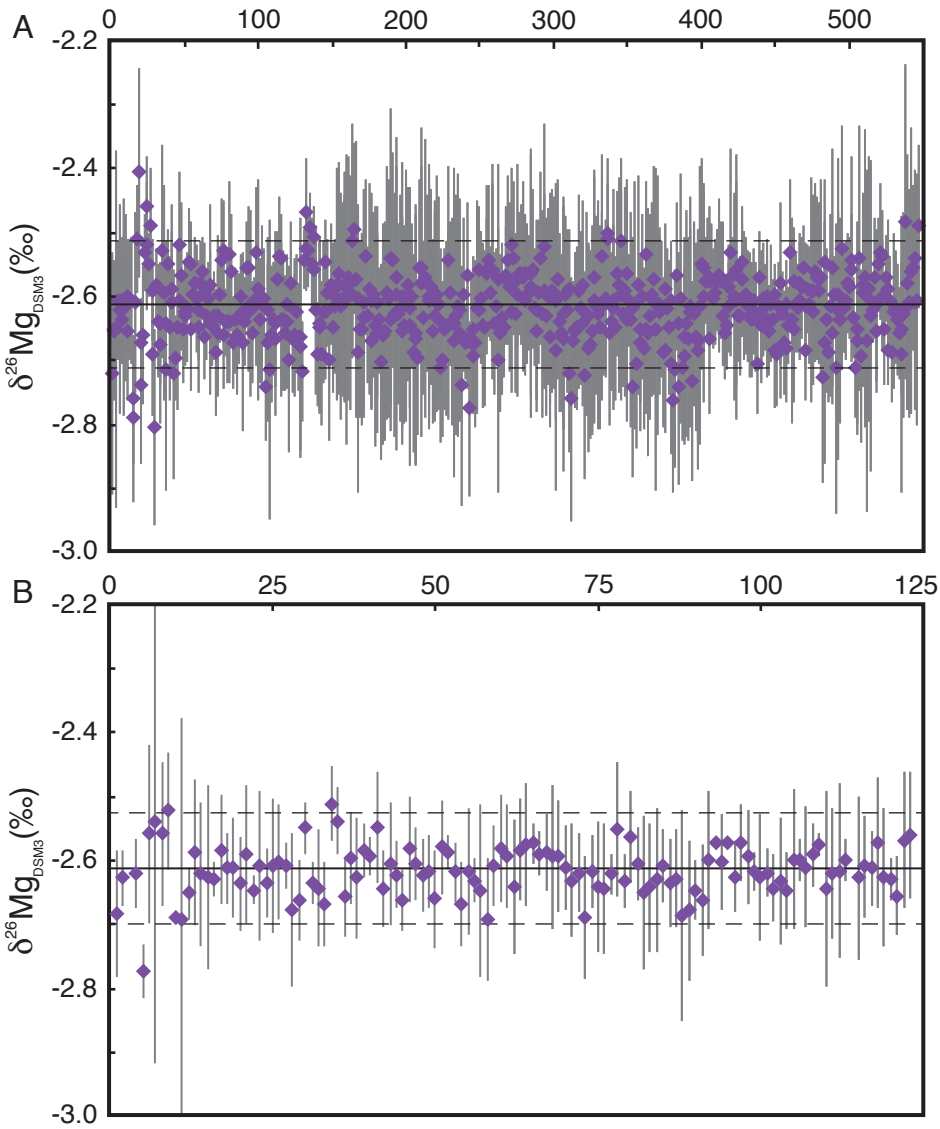

Figure 1.3 Long-term monitoring of CAM1 standard in the Saskatchewan Isotope Laboratory over the course of thesis study. (A) Plot depicting every individual analysis during each instrument run, including outliers, of CAM1. Error bars are ± 2σ for each individual analysis, with a long-term mean value of –2.62 ± 0.10‰, 2σ n = 547. The solid horizontal black line shows the mean value and dashed lines indicate the 2σ error envelope from the mean. (B) Plot depicting the mean value of CAM1 from each separately tuned analytical session. Error bars are ± 2σ of the mean CAM1 value from each individual analytical session, with a long-term mean value of –2.62 ± 0.08‰, 2σ n = 123. Solid horizontal black line shows the mean value and dashed lines indicate the 2σ error envelope from the mean.

CHAPTER 2 – Magnesium isotope compositions of three types of dolomite in the Late Ordovician Red River Formation in a single core from southeastern Saskatchewan

Published as:

Worsham S. R., Holmden C. and Qing H. (2013) Preliminary results of a magnesium isotope study of dolomite in Upper Ordovician strata, southeastern Saskatchewan, northern Williston Basin. In *Summary of Investigations 2013*, Sask. Geol. Survey, **1**, 1–8.

First author surname changed from Worsham to Kimmig since the publication of this manuscript. Modifications made for thesis consistency include changing 'Upper Ordovician' to 'Late Ordovician' in the main text and figures. Updated data is provided in Table 2.1 and Figures 2.2, 2.3 and the main text from samples that were analyzed after the chapter was originally published.

2.1. Abstract

In this chapter, preliminary findings are reported for a magnesium (Mg) isotope study of Late Ordovician dolomite in the Yeoman and Herald formations in the subsurface of southeastern Saskatchewan (northern portion of the Williston Basin). Three types of dolomite have been previously described: 1) burrows, 2) matrix, and 3) saddle dolomite, representing multiple stages of dolomitization. Samples from each type were collected from four depths in the core selected for this study, but only two distinct groupings of δ^{26}Mg values were found: –1.34 ± 0.12‰ ($2\sigma_{mean}$) and –1.55 ± 0.11‰ ($2\sigma_{mean}$). These groupings are unrelated to the type of dolomite sampled, indicating that: 1) the three types of dolomite were formed from a single dolomitizing fluid with a uniform δ^{26}Mg value, or 2) the dolomitizing fluid from each successive stage of dolomitization overprinted the δ^{26}Mg value of the earlier-formed dolomite. Small differences in δ^{26}Mg values of dolomite at different depths in the core may be attributed to local-scale conditions of dolomitization, such as changes in precipitation rate, temperature, and the δ^{26}Mg value of the migrating subsurface dolomitizing fluid.

2.2. Introduction

The Late Ordovician Red River Formation (Herald and Yeoman formations in southeastern Saskatchewan) is an economically important unit of the Williston Basin, producing oil from reservoirs located in Saskatchewan, North Dakota, and Montana. To the end of 2012, Red River

reservoirs in Saskatchewan had produced 4.2 million m^3 of oil (Haidl et al., 2013).

Complex and discontinuous dolomitization patterns in the Yeoman and lower Herald formations are responsible for the reservoir-quality porosity and permeability of the Red River strata (e.g., Kendall, 1976, 1977; Longman and Haidl, 1996; Kreis and Kent, 2000). The Herald Formation consists of interbedded limestone, dolomite, and anhydrite strata of the Lake Alma and Coronach members, and the upper Redvers unit. The Yeoman Formation consists of variably dolomitized packstone, wackestones, and mudstone, and contains abundant macrofossils such as brachiopods, corals, stromatoporoids, and a characteristic burrow-mottled fabric reminiscent of *Thalassinoides* (e.g. Kendall, 1976), but more recently interpreted as smaller diameter burrows of *Palaeophycus* and *Chondrites* that have been broadened in appearance by diagenetic halos of dolomite (Gingras et al., 2004). In a portion of southeastern Saskatchewan and in North Dakota, Montana and into South Dakota, kukersitic beds and laminae are present in Yeoman strata and, where they are thermally mature, the kukersites are the source rock for most of the Red River oil (Fowler et al., 1998).

Striking characteristics of the Yeoman, and its stratigraphic equivalents in the Williston Basin succession, involve several types and patterns of dolomitization, including: 1) preferential dolomitization of the burrow network, 2) complete dolomitization of burrows and matrix carbonate, and 3) carbonate sediment that has evaded dolomitization entirely. Deposits where the carbonate sediment associated with the burrows is the only dolomitized fabric in the rock led researchers to propose that seawater flowed preferentially through the burrow network, thus resulting in the early dolomitization of the burrows (Kendall, 1977; Longman et al., 1983). Gingras et al. (2004) offered an alternative hypothesis. These authors presented evidence that the centimeter-scale burrows are actually diagenetic halos of dolomite formed around millimeter-scale worm burrows. Recognizing that smaller burrows would be less likely to channelize fluid flow through the sediment, these authors suggested that the dolomite halos formed as a by-product of the metabolic activity of sulphate-reducing bacteria. The bacteria colonized the burrows, rather than the matrix sediment, due to the organic matter accumulated by the feeding activities of the burrowing organisms.

In cases where the matrix carbonate was also dolomitized, a second episode of dolomitization must have occurred, driven by a different mechanism. Indeed, matrix dolomite is theorized to have formed later than the burrow dolomite, by the downward flux of seawater into

the sediment (concentrated through evaporation) (Longman et al., 1983; Qing et al., 2004). The 'brining upward' conditions of deposition recorded in the Yeoman/Herald succession supports this interpretation. However, the brine reflux hypothesis does not explain why completely dolomitized strata (burrows and matrix) are interbedded with limestone units or strata with dolomitized burrows and limestone matrix. Kendall (1977) and Longman and Haidl (1996) discuss the possibility that the distribution of dolomite reflects patterns in the deposition of high-magnesium calcite in the original limestone deposits. These authors hypothesized that the units that were dolomitized contained higher concentrations of magnesium than the surrounding carbonate lithologies, which aided the formation of dolomite when this magnesium was released during diagenesis. Recent work by Nash et al. (2011) supports this idea by demonstrating that high concentrations of magnesium can be achieved through biologically mediated activity in the formation of protodolomite from magnesite in modern calcifying algae.

The last stage of dolomitization of the Yeoman carbonates is represented by saddle dolomite, which is interpreted to reflect the passage of a hydrothermal fluid through the succession sometime after the matrix dolomite had formed (Qing et al., 2001).

The seawater hypothesis for the source of the dolomitizing fluid, whether it was seawater of normal salinity in sedimentary pore fluids (e.g., burrows), or evaporated seawater with potentially elevated Mg/Ca ratios (e.g., matrix dolomite), was tested for each type of dolomite using $^{87}Sr/^{86}Sr$ as a tracer (Qing et al., 2001). Due to the long residence time of strontium in the modern ocean (~ 2.5 million years), the $^{87}Sr/^{86}Sr$ ratio of seawater is effectively constant on million-year time scales. Accordingly, if seawater was the source of the magnesium that dolomitized the Herald and Yeoman formations, then the $^{87}Sr/^{86}Sr$ ratio of the dolomites should be nearly uniform, in the likelihood that the diagenetic time frame for dolomitization was no more than a few million years. The $^{87}Sr/^{86}Sr$ ratio of seawater at the time of Yeoman and Herald deposition is 0.7080, as measured by Holmden (2009). By contrast, the $^{87}Sr/^{86}Sr$ ratios of Yeoman and Herald dolomite are higher than this (Qing et al., 2001; Holmden, 2009), ranging between 0.7084 and 0.7091, suggesting that contemporaneous seawater was not the dolomitizing fluid. Qing et al. (2001) offered three hypotheses for sources of dolomitizing fluid that could potentially explain the results, 1) late Silurian seawater that filtered downward into the succession when seawater $^{87}Sr/^{86}Sr$ ratios were higher; 2) formation waters expelled from Cambro-Ordovician formations located lower in the succession, also with high $^{87}Sr/^{86}Sr$ ratios (0.7085 to 0.7090); and

3) connate waters whose $^{87}Sr/^{86}Sr$ ratios were modified by strontium exchange reactions with Precambrian basement rocks. Note that for the second and third hypotheses the dolomitizing fluids would have flowed upward through the succession.

In this study, magnesium isotopes are used to study the process of dolomitization. In contrast to $^{87}Sr/^{86}Sr$, which is an indirect tracer of dolomitization, the isotopes of magnesium ($^{26}Mg/^{24}Mg$ and $^{25}Mg/^{24}Mg$) have the potential to trace the dolomitizing fluids directly. By obtaining magnesium isotope data ($\delta^{26}Mg$ values) from samples within dolomitized burrows, matrix, and saddle dolomite, the aim is to improve the understanding of the sources of the dolomitizing fluids, the paleo-flow paths taken by the dolomitizing fluids, and the general process of dolomitization.

2.3. Sampling and analytical procedures

Small powdered samples of Yeoman carbonate were collected from core of the Home Dome Torquay S 41/03-08-001-11W2M; 85B212 well in southeastern Saskatchewan (Figures 2.1 and 2.2) using a power drill and carbide cutter bit. All three types of dolomite (burrow, matrix, and saddle) are present in this core. The sampling of the burrows and matrix dolomite was performed on hand-sample–scale slabs of core. One sample of saddle dolomite was collected (precipitated as infill vug cement) (Figure 2.3). Analyses of elemental concentrations were carried out at the Saskatchewan Research Council's (SRC) Geoanalytical Laboratories. Magnesium isotopic analyses were conducted at the Saskatchewan Isotope Laboratory in the Department of Geological Sciences, University of Saskatchewan.

Rock powders were dissolved drop-wise with ultrapure 6N HCl and brought up to 50 ml total solution volume with deionized water (18.2 MΩ·cm). Elemental concentrations of the solutions were measured by inductively coupled plasma mass spectrometry (ICP-MS) at SRC's Geoanalytical Lab. The magnesium was purified prior to mass spectrometry using traditional gravity flow cation exchange columns filled with 2 ml of Bio-Rad® AG® MP-50 resin. Aliquots were taken before and after the magnesium elution from the column to ensure that more than 98% of the magnesium was collected, in order to avoid isotopic fractionation during the purification procedure (Chang et al., 2003). The purified magnesium solutions were dried down and treated with ultrapure H_2O_2 and concentrated HNO_3 to destroy residual organics. Magnesium isotope ratios were measured with a Thermo Fisher Scientific NEPTUNE multi-collector ICP-MS using a

cyclonic glass spray chamber sample introduction system. Samples of approximately 1 ppm Mg dissolved in 0.3N HNO_3 were measured using the low-resolution slit with an uptake rate of 100 µl/min, yielding 8-10V signals on mass 24. Magnesium isotope ratios were measured using a standard-sample bracketing technique. Sample intensities were matched to within 5% of the intensity of the bracketing standard (DSM3). The quality of the measurements was monitored using an interlaboratory standard (CAM1) and an internal magnesium standard (Mg Specpure), which is isotopically distinct from CAM1.

Magnesium has three naturally occurring stable isotopes: ^{24}Mg (78.99%), ^{25}Mg (10.00%), and ^{26}Mg (11.01%). ^{26}Mg/^{24}Mg and ^{25}Mg/^{24}Mg ratios are reported as δ^{26}Mg and δ^{25}Mg values, respectively, in the conventional delta notation as per mil (‰) deviations of the sample isotope ratio relative to the standard DSM3 (Galy et al., 2003), as shown in Equation (2.1) for δ^{26}Mg.

$$\delta^{26}\mathrm{Mg} = \left(\frac{\left(^{26}\mathrm{Mg}/^{24}\mathrm{Mg}\right)_{\mathrm{sample}}}{\left(^{26}\mathrm{Mg}/^{24}\mathrm{Mg}\right)_{\mathrm{DSM3}}} - 1\right) \times 1000 \qquad (2.1)$$

The analytical uncertainty for δ^{26}Mg is ± 0.10‰ (2σ), and for δ^{25}Mg it is ± 0.05‰ (2σ), which is determined on the basis of repeated analyses of CAM1 (n = 48) from different mass spectrometry sessions. Uncertainties associated with measurements of samples within the same mass spectrometry session are reported as two standard errors of the mean (2se). In cases where sample measurements are repeated between different mass spectrometry sessions, the average value is reported, along with the 2σ uncertainty.

2.4. Results

The δ^{26}Mg and ^{87}Sr/^{86}Sr data are listed in Table 2.1. Dolomite from the Home Dome Torquay S 41/03 08-001-11W2M; 85B212 well core yielded δ^{26}Mg values ranging from –1.27‰ to –1.62‰, showing significant variability considering the uncertainty of the measurements (± 0.10‰, 2σ). The results are broadly consistent with previously reported δ^{26}Mg values for dolomite ranging from Mississippian to Jurassic in age (–1.63‰ to –1.40‰) (Young and Galy, 2004; Brenot et al., 2008; Jacobson et al., 2010). A modern Atlantic seawater standard measured in our laboratory yielded –0.84‰ ± 0.08‰ ($2\sigma_{mean}$), which is within the uncertainty of the values reported for modern seawater measured in other laboratories (–0.82‰) (e.g., Chang et al., 2003; Carder et al., 2004; Young and Galy, 2004; de Villiers et al., 2005; Tipper et al., 2006a). The

average $^{87}Sr/^{86}Sr$ ratio for SRM987 measured over the course of this work is 0.710288 ± 0.000014 ($2\sigma_{mean}$). There is no correlation between $\delta^{26}Mg$ and $^{87}Sr/^{86}Sr$ in the dolomite samples ($R^2 = 0.11$). The $\delta^{26}Mg$ values for the burrow dolomite and matrix dolomite are nearly identical when sampled from the same slab of core, but differ significantly between slabs sampled at different depths. The first four samples (HDT4 to 6 and HDT7 and 8), which were collected at depths of 3209.1 m (HDT4 to 6) and 3198.7 m (HDT7 and 8) (Figure 2.2, Table 2.1), yielded an average $\delta^{26}Mg$ value of –1.33 ± 0.12‰ ($2\sigma_{mean}$) for the combined burrow and matrix dolomite, whereas the last slab of samples (HDT9 to 13), which were collected higher in the core at ~ 3193.3 m, yielded an average value of –1.55 ± 0.11‰ ($2\sigma_{mean}$). Saddle dolomite (HDT1) collected at ~ 3195.6 m yielded an average value of –1.37 ± 0.14‰ ($2\sigma_{mean}$).

2.5. Discussion

The burrow and matrix dolomite in this study yielded nearly identical $\delta^{26}Mg$ values when sampled from the same slab of core (centimeter-scale distances between burrow and matrix dolomite). Taken at face value, this finding suggests that a single dolomitizing fluid is responsible for both types of dolomite, which seems at odds with the petrographic evidence for separate episodes of dolomitization (e.g., Kendall, 1976). Equally puzzling are the high $^{87}Sr/^{86}Sr$ ratios, which suggest that the dolomitizing fluid cannot be Late Ordovician seawater (Qing et al., 2001; Holmden, 2009). If the earlier-formed burrow and matrix dolomite were susceptible to overprinting by later-stage dolomitizing fluids, then it is possible to reconcile the geochemical and petrographic constraints. In this scenario, the last major stage of dolomitization of the Yeoman and Herald formations caused both the homogenization of $\delta^{26}Mg$ values between burrow and matrix dolomite in the same slab of core, and the increase in $^{87}Sr/^{86}Sr$ ratios. In support of this hypothesis, Malone et al. (1996) reported that dolomite is very susceptible to magnesium exchange with fluids at high temperature, based on laboratory experiments. Field support for the overprinting hypothesis comes from a recent study of a thick succession of Triassic dolomites by Geske et al. (2012), who reported a decrease in $\delta^{26}Mg$ variability between four phases of dolomite with an increase in stratigraphic depth correlating with increased burial temperature.

If the overprinting hypothesis is correct, it remains to be explained why pervasively dolomitized strata are interbedded with limestone beds or units in which the burrows are

dolomitized and the matrix is not. Could late-stage dolomitizing fluids have travelled through the succession without passing through the limestones? One promising explanation is that earlier formed burrow and bedded dolomite resulted in channelization of later-stage dolomitizing fluids, which protected the limestone units from being dolomitized. The variability in δ^{26}Mg values between slabs sampled at different depths may be evidence for differences in local-scale conditions of dolomitization, such as temperature, precipitation rate, and fluid migration rate. Although the magnitude of the fractionation factor ($\Delta^{26}Mg_{fluid}^{dolomite}$) is not well established (–2.0‰ to –2.7‰, as stated by Higgins and Schrag, 2010), the sign of the fractionation factor indicates that dolomite is preferentially enriched in the light isotopes of magnesium compared to the dolomitizing fluid. Accordingly, if the precipitation rate is high and fluid migration rate is low, such that a significant fraction of the aqueous magnesium is used up before it can be replenished, the dolomite will record progressively higher δ^{26}Mg values, i.e., the δ^{26}Mg value of the dolomite will be closer to the δ^{26}Mg value of the fluid. The opposite is the case where precipitation rate is low and fluid migration rate is high; these dolomites will record the maximum fractionation between dolomite and fluid. This local reservoir effect may explain the differences in δ^{26}Mg values between different slabs of core measured in this study.

If the dolomitizing fluids experience changes in δ^{26}Mg values along fluid migration flow paths due to the process of dolomitization, then δ^{26}Mg gradients may be recorded in large dolomite bodies. These hypothetical gradients could reveal the direction of fluid flow during dolomitization—the flow direction being recorded by increasing δ^{26}Mg values in the dolomite. The fluid migration hypothesis is testable with additional work aimed at documenting whether spatial gradients in δ^{26}Mg values exist within the Yeoman and Herald dolomite. The presence of gradients could help to resolve whether seawater percolating downward through the sedimentary succession, or connate water flowing upward through the succession, is the source of the dolomitizing fluid, bearing in mind the possibility that magnesium isotope signatures of early-stage fluid migration events might be overprinted by later-stage events.

2.6. Conclusion

Preliminary results of a magnesium isotope study of dolomite within core of the Home Dome Torquay S 41/03-08-001-11W2M; 85B212 well exhibit small but significant variability in δ^{26}Mg values, ranging from –1.27‰ to –1.62‰. Three types of dolomite have been described in

the studied core, including burrow, matrix, and saddle dolomite (Qing et al., 2001). Nevertheless, only two distinct groupings of δ^{26}Mg values emerge from the dolomite samples analyzed in this study, regardless of which type is measured: –1.34 ± 0.12‰ ($2\sigma_{mean}$) and –1.55 ± 0.11‰ ($2\sigma_{mean}$). It was also found that burrow and matrix dolomite from the same slab of core gave identical results, and that the two groupings of δ^{26}Mg values correlate to slabs sampled at different depths in the core. It is possible that the uniformity in δ^{26}Mg values reflects one source of dolomitizing fluid for both the burrow and matrix dolomite. On the other hand, magnesium exchange with a late-stage dolomitizing fluid might overprint the isotopic signatures of the earlier formed dolomite. If this hypothesis is correct, then the high $^{87}Sr/^{86}Sr$ ratios recorded in these dolomites might also be the product of overprinting by late-stage fluids, and the high $^{87}Sr/^{86}Sr$ ratios do not necessarily preclude Late Ordovician seawater as the source of the fluid that dolomitized the Yeoman Formation burrow and matrix carbonate.

By contrast, the difference in δ^{26}Mg values between slabs from different depths in the core may reflect differences in local-scale processes of dolomitization, in particular, differences in dolomite formation rate vs. fluid migration rate. These data also suggest the possibility that large dolomite bodies might record subsurface gradients in dolomite δ^{26}Mg values. If gradients exist, then it may be possible to use them to determine paleo-flow directions of dolomitizing fluids. Petroleum industry workers could use magnesium isotope gradients in dolomite bodies to target new exploration wells, as migrating petroleum systems might be expected to follow the same subsurface pathways in the Williston Basin as the dolomitizing fluids. The gradient hypothesis is testable with further work aimed at sampling many more core slabs from spatially distributed wells.

2.7. Figures

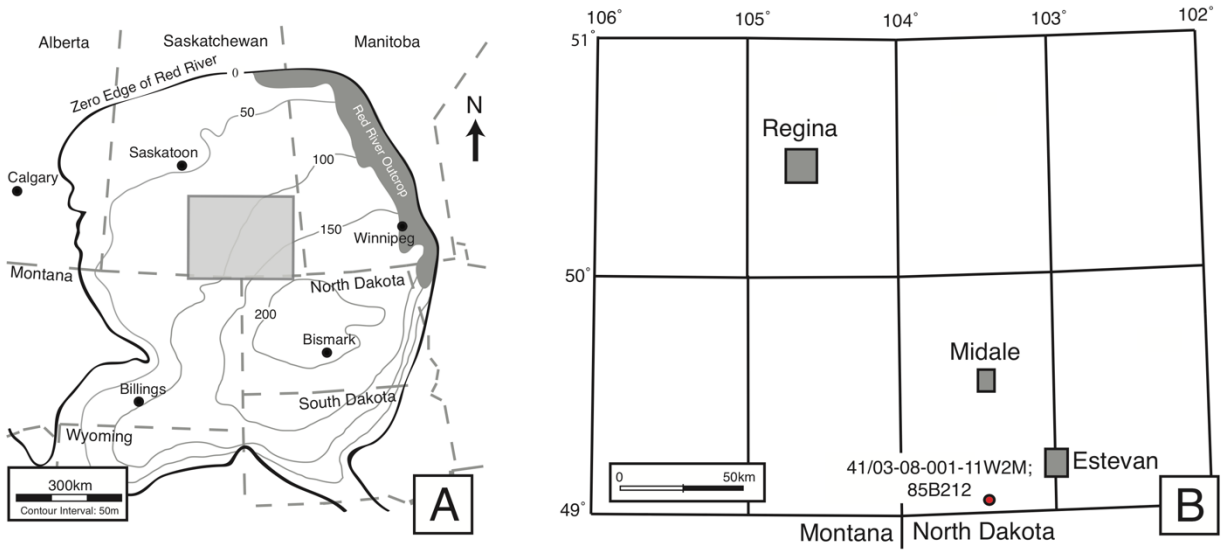

Figure 2.1 Maps showing the location of the sampling site. (A) Map showing the distribution of Red River strata in central North America. Isopachs of the Red River strata in the Williston Basin, indicating the center of the basin located in North Dakota. The grey shaded box represents the study area in Fig. 2.1b. Modified from Pratt and Haidl (2008) and Norford et al. (1994). (B) Detailed view of southeastern Saskatchewan and location of the Home Dome Torquay S 41/03-08-001-11W2M; 85B212 well.

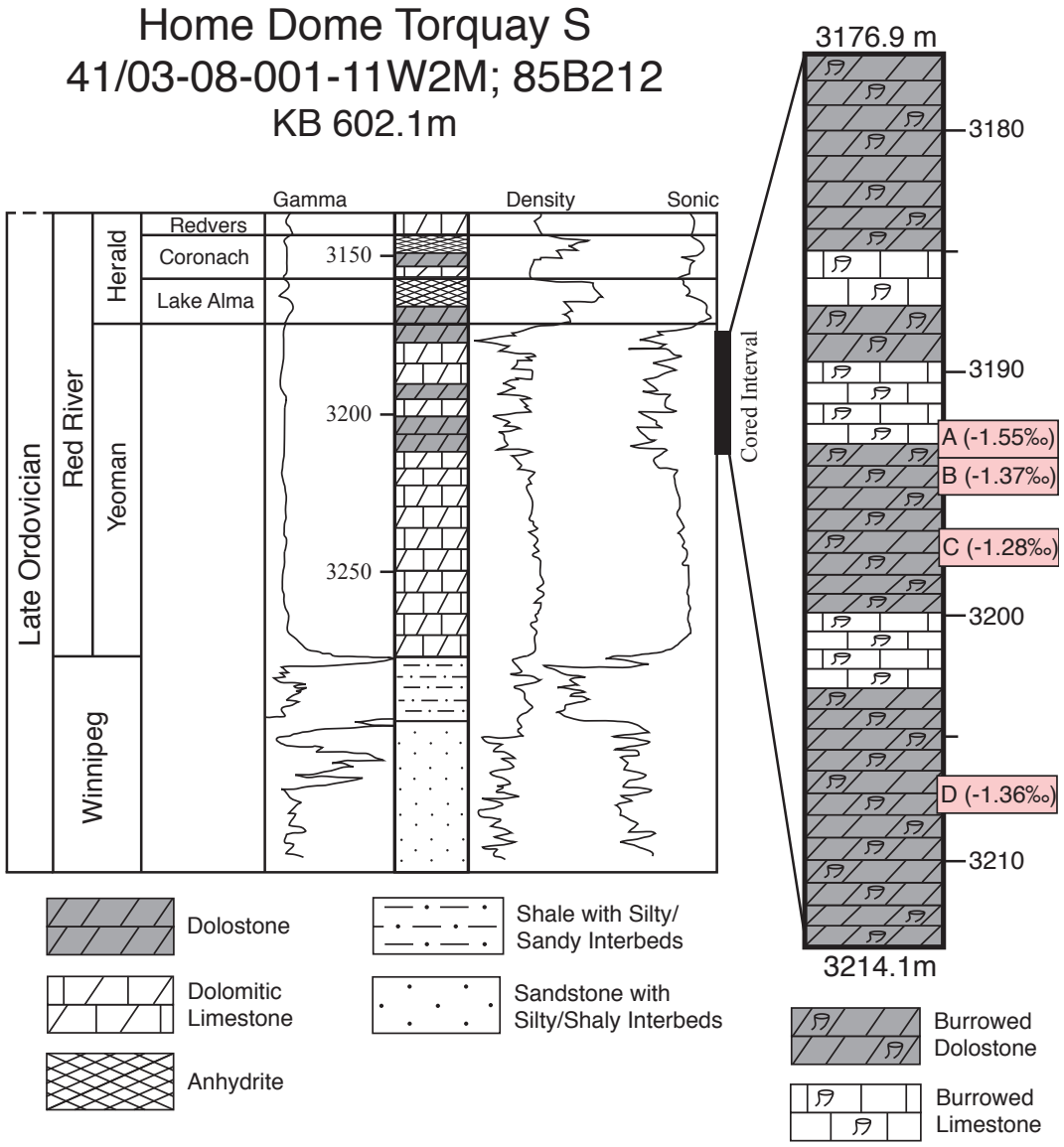

Figure 2.2 General stratigraphy of Late Ordovician Red River strata in southeastern Saskatchewan, and the lithologies identified in core of the Home Dome Torquay S 41/03-08-001-11W2M; 85B212 well (KB = kelly bushing). Sampling locations of rock powders for magnesium isotope analyses are indicated on the close-up of the cored interval. Modified from Qing et al. (2001). Note: Burrow features indicated on the close-up cored interval have been dolomitized. Refer to Fig. 2.3 for additional sample details.

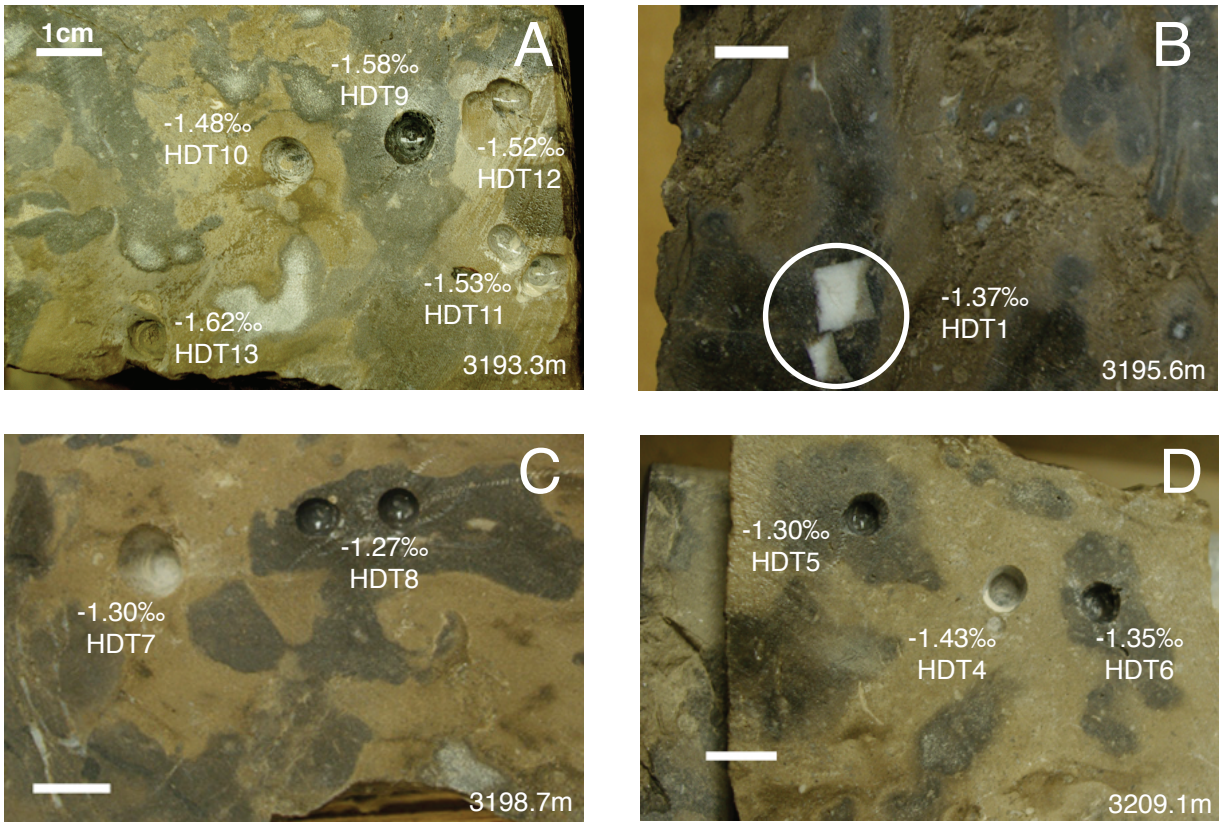

Figure 2.3 Photographs showing sampling locations of burrow, matrix, and saddle dolomite within the core taken from the Home Dome Torquay (HDT) S 41/03-08-001-11W2M; 85B212 well. Magnesium isotope (δ^{26}Mg ‰DSM3) values are reported with sample IDs. Scale bars are all 1 cm length. (A) Burrow HDT9 and matrix dolomite samples HDT10–13 at 3193.3 m depth. (B) Saddle dolomite (circled) precipitated within a rectangular-shaped vug, occurring within a burrow at 3195.6 m depth. Saddle dolomite HDT1 was sampled from the other side of the slab in order to preserve this pristine example. (C) Matrix HDT7 and burrow HDT8 dolomite at 3198.7 m depth. (D) Matrix HDT4, burrows HDT5 and HDT6 dolomite at 3209.1 m depth.

2.9. Tables

Table 2.1

Sample	Depth (m)	Type	N	δ^{26}Mg DSM3 (‰)	Uncertainties *int* 2se	*ext* 2σ	δ^{25}Mg DSM3 (‰)	Uncertainties *int* 2se	*ext* 2σ	$^{87}Sr/^{86}Sr$	Mg/Ca (mol/mol)
CAM1		Cambridge 1 Standard	48	-2.62		0.10	-1.35		0.05		
DSM3		Dead Sea Metal 3 Standard	39	-0.03		0.06	-0.02		0.05		
Mg Specpure		Alfa Aesar Single Element Standard	47	-3.79		0.10	-1.95		0.06		
OSIL		Modern Atlantic Seawater	2	-0.84		0.08	-0.42		0.04	0.7092	5.136
9830-B		Yeoman Formation Water (31/03-14-006-11W2; 98B196)	4	-0.43	0.08		-0.22	0.02			0.174
Slab A											
HDT9	3193.3	Burrow	2	-1.58		0.25	-0.82		0.11		0.923
HDT10	3193.3	Matrix	2	-1.48		0.12	-0.78		0.07		0.843
HDT11	3193.3	Matrix	4	-1.53	0.03		-0.79	0.02		0.7085	0.885
HDT12	3193.3	Matrix	4	-1.52	0.03		-0.79	0.01		0.7086	0.867
HDT13	3193.3	Matrix	2	-1.62		0.13	-0.85		0.08	0.7085	0.822
Slab B											
HDT1	3195.6	Saddle Dolomite	2	-1.37		0.14	-0.72		0.08	0.7082	0.764
Slab C											
HDT7	3198.7	Matrix	2	-1.30		0.11	-0.67		0.05	0.7088	0.852
HDT8	3198.7	Burrow	2	-1.27		0.00	-0.67		0.01	0.7089	0.869
Slab D											
HDT4	3209.1	Matrix	2	-1.43		0.08	-0.75		0.06	0.7091	0.933
HDT5	3209.1	Burrow	2	-1.30		0.04	-0.68		0.00	0.7090	0.935
HDT6	3209.1	Burrow	2	-1.35		0.08	-0.70		0.03	0.7091	0.840

Magnesium isotope data for single element magnesium standards (CAM1, DSM3, Mg Specpure), as well as magnesium isotope and Mg/Ca molar ratios for a modern Atlantic seawater standard (OSIL) and Late Ordovician dolomite samples collected for this study (HDT1, 4 to 13). $^{87}Sr/^{86}Sr$ ratios are also reported for the modern Atlantic seawater standard, strontium isotope standard SRM987, and the Late Ordovician dolomite samples. All dolomite samples were collected from core taken from the Home Dome Torquay S 41/03-08-001-11W2M; 85B212 well. N is the number of analyses. 2σ (two standard deviations) is the external (Ext) analytical uncertainty based on replicates of standards and samples measured in more than one instrument session. 2se (two standard deviations divided by the square root of the number of runs) is the internal (Int) uncertainty based on multiple runs of each sample during one instrument session.

TRANSITION BETWEEN CHAPTERS 2 AND 3

Chapter 2 serves as an investigation into the formation of dolomite and processes of subsurface dolomitization in the Williston Basin, using Mg isotopes as a tracer of dolomitizing fluids in the Red River Formation. One fully dolomitized well core was the focus of Chapter 2, with results showing that three types of dolomitized carbonate within the core record the same δ^{26}Mg values, pointing to the possibility that each type of dolomite overprinted the δ^{26}Mg values of the earlier formed dolomite during later dolomitization events. Evidence also exists for variation in average δ^{26}Mg values between hand-samples at different depths, a finding that appears to be significant, albeit difficult to interpret and could relate to the changing isotopic composition of the dolomitizing fluid, the rate of precipitation of dolomite, or both. It is also possible that the three types of dolomite may reflect dolomitization at increasing burial temperatures. These questions led to the consideration of a new study, described in Chapter 3, aimed at addressing spatial variation in δ^{26}Mg values in Red River dolomite on the basin-scale under the presumption that dolomitizing fluids would be expected to flow laterally, following the strike of the beds. The sampling of 16 additional cores and one outcrop sample, regionally distributed across the Williston Basin was conducted in order to better assess the diagenetic fluid-flow event(s) that led to the reservoir-quality porosity and permeability of the Red River Formation. The results of the expanded application of Mg isotopes as a tracer of the dolomitizing paleo-fluid flow regime in the Red River Formation throughout the Williston Basin are presented in the following chapter.

CHAPTER 3 – Magnesium isotope tracing of paleo-fluid flow preserved in dolomite from the 'C' member carbonate of the Red River Formation in 17 cores sampled across the Williston Basin

3.1. Abstract

Since its discovery in the late 18th century, dolomite ($CaMg(CO_3)_2$) has been shrouded with controversy. Vast deposits occur in the geologic past but relatively few occur in modern environments (Warren, 2000; Machel, 2004). Dolomite is also notoriously difficult to create in the laboratory at ambient temperatures and pressures (Land, 1998). Due to these constraints, examples provided in nature must be studied. Conversion of calcite to dolomite during sedimentation (early diagenesis) or later following the solidification of the sediment (late diagenesis) results in a volume reduction (Moore, 1989), creating porous and permeable rock through which fluids (including large petroleum reservoirs) may migrate (Warren, 2000), making the understanding of the process of dolomitization important for the petroleum industry. Magnesium (Mg) and strontium (Sr) isotopes serve as useful tools to trace subsurface migration of dolomitizing fluids in the Red River Formation (Late Ordovician) of the Williston Basin. It is proposed in this chapter that the dolomitization recorded in the Red River carbonate today is tied to the thermal history of the basin, in contrast to previous investigations attributing dolomitization to the evaporative reflux of seawater (Longman et al., 1983; Longman and Haidl, 1996). Instead, it is suggested that dolomitization occurred as a result of a thermal event during either the late Paleozoic or Late Cretaceous–Paleogene (Osadetz et al., 2002; Feinstein et al., 2009), mobilizing Mg-rich basinal fluids from the deep center of the basin upwards and outwards into the overlying strata. These results hold promise for the interpretation and understanding of other similar large-scale dolomitization events in the geologic record. Furthermore, these results demonstrate that Mg and Sr isotope gradients in dolomite bodies may hold the potential to be used for future petroleum exploration, as migrating petroleum systems would be expected to follow the same subsurface pathways as dolomitizing fluids.

3.2. Introduction

A common sedimentary rock and rock-forming mineral, dolomite ($CaMg(CO_3)_2$) is found extensively in the geologic record, but is rare in modern environments. The formation of well-ordered, stoichiometric dolomite ($Ca_{0.5}Mg_{0.5}(CO_3)_2$) at Earth surface temperature and pressure is

rare (Land, 1998), despite the present day ocean being super-saturated with respect to it. The majority of dolomite occurrences are post-depositional, formed by replacement of calcium (Ca) in limestone ($CaCO_3$) by magnesium (Mg) (Eq. 3.1).

$$2CaCO_3 + Mg^{2+} = CaMg(CO_3)_2 + Ca^{2+} \quad (3.1)$$

Despite many years of extensive research, exactly how and when this transformation occurs remains the subject of heated debate among dolomite researchers, fueled in part by the range of hypothesized chemical, biological, and hydrological conditions under which dolomite can form, and petrographic and geochemical data in the field permitting multiple interpretations (Machel, 2004; Warren, 2000). Dolomite may have only garnered academic interest over the past several decades if it were not for the fact that approximately 80% of the oil and gas reserves in North America are hosted within dolomitized carbonate rocks (Zenger et al., 1980; Warren, 2000). The carbonates of the Red River Formation, deposited in the Williston Basin in the Late Ordovician (Figs. 3.1, 3.2) and the subject of this study, contain large hydrocarbon reserves in Saskatchewan, North Dakota, Manitoba, and Montana with porosity and permeability introduced through the process of dolomitization (Kohm and Louden, 1978).

Replacement dolomitization is essentially a hydrogeological phenomenon (Machel, 2004). Subsurface fluid flow delivers Mg to the sites of dolomitization, subsequently removing Ca from the host rock (Eq. 3.1). Because flow is confined to pore spaces that comprise only a small fraction of the rock, hundreds to thousands of pore-volumes of fluid (depending on the Mg concentration) must pass through the host limestone for the rock to become completely dolomitized (Morrow, 1982; Land, 1985; Shields and Brady, 1995; Machel, 2004). Knowledge of the flow direction of the Mg-bearing fluids can help narrow the choice among the numerous various models of dolomitization for a dolomite body (Fig. 3.3), aiding in the identification of the Mg source. In the brine reflux model, Mg is supplied by evaporite basins (Fig. 3.3a). Brines sink vertically into the underlying carbonate rock until it is deflected down-dip towards the low point in the basin by a low permeability stratum, such as shale. The sediment compaction model describes salty formation waters (also referred to as connate water) flowing up-dip from the deep-basin towards the shallow edges of the basin (Fig. 3.3b). Many models of dolomitization describe fluid flow that changes direction with time along the flow-path. Forced thermal convection describes upwards, circular

flow (Fig. 3.3c), while changes in topography generate descending flows beneath regions of high surface elevation, and ascending flows beneath regions of low surface elevation (Fig. 3.3d, e).

Geochemical proxies have been applied as tracers of field-based dolomitization studies in the past, and a number of influential studies have been published over the years (e.g., Adams and Rhodes, 1960; Deffeyes et al., 1964; Land, 1973, 1980; Swart et al., 1987; Moore et al., 1988; Machel and Anderson, 1989; Wilson et al., 1990; Qing and Mountjoy, 1992; 1994) as well as notable, detailed reviews summarizing such efforts (Warren, 2000; Machel, 2004). Nevertheless, the approach is not widely practiced in large-scale, regional dolomitization research today, despite greater access to and precision of analytical techniques. Reasons for the apparent downward trend in regional studies remain unknown. For one, dolomitization patterns only reveal themselves when a dolomite body is studied over sufficiently broad spatial scales. Today, there is a penchant for probing dolomite's origins through detailed petrographic examination of thin sections to identify dolomite 'types', followed by microsampling for geochemical analysis. Reasons for the paucity of large-scale tracer studies may be ambiguities that arise when attempting to employ indirect tracers of Mg to trace fluid flow during dolomitization (*i.e.* Sr/Ca, or $^{87}Sr/^{86}Sr$, $\delta^{18}O$ and $\delta^{13}C$).

Herein, it is demonstrated that Mg isotopes ($^{26}Mg/^{24}Mg$) may be used to directly trace the flow path of the dolomitizing fluids. Light isotopes of Mg are preferentially taken up into dolomite, leaving heavy isotopes enriched in the fluid (Higgins and Schrag, 2010; 2012; Schauble, 2011; Geske et al., 2012; 2015a, b; Wang et al., 2013; Fantle and Higgins, 2014; Li et al., 2015; Husson et al., 2015; Peng et al., 2016; Kimmig and Holmden, 2017). As a result, the dolomitizing fluid will become progressively enriched in ^{26}Mg in the direction of fluid flow, and subsequently the replacement dolomite formed in the flow system will have a progressively higher $\delta^{26}Mg$ value (Peng et al., 2016). This interpretive framework is utilized in a Mg isotope study of dolomitization of the 'C' member carbonate of the Red River Formation, which is characterized by an extensive, anastomosing network of *Thalassinoides* burrows (Kendall, 1976).

Selective dolomitization of the burrows (which make up ~ 45% of the studied limestone) has previously been attributed to Mg-rich brines that filtered downward into the sediment during periods of basin restriction that resulted in three distinct deposits of anhydrite—the largest of which is directly overlying the studied carbonate (Longman et al., 1983; Longman and Haidl, 1996). If the brines seeping into the Red River carbonate resulted in burrow dolomitization, $\delta^{26}Mg$ values are expected to increase from the top to the bottom of the Red River 'C' member carbonate,

in all locations. The 'C' burrowed member carbonate, however, is only ~ 100 to 150 m thick (Kohm and Louden, 1978), and toward the bottom there exists a relatively impermeable layer of shale belonging to the Winnipeg Formation that would have deflected the flow of brine (through the burrows) in the down-dip direction, which is roughly representative of the present day structural center of the Williston Basin in NW North Dakota (Fig. 3.1b). Furthermore, when it is considered that brine infiltration will eventually be hampered or even blocked by the accumulation of anhydrite salts in the bottom of the evaporite basin, and that the salt deposits are the thickest in the basin center, the likelihood of the brine entering the burrows would be greatest near the edges of the basin where the anhydrite bed is thin or absent altogether. Accordingly, the predominant regional-scale flow direction of brine through the burrows would be down-dip from the edge of the basin towards the center.

To test this hypothesis, δ^{26}Mg values were measured in 'C' member burrow-dolomite across a large geographical area in North Dakota, Saskatchewan, and Manitoba (Fig. 3.4). Carbonates in which the burrows are dolomitized and the matrix carbonate remains undolomitized were selected for this study in an effort to circumvent sampling of an overprinted Mg isotope signature from a subsequent dolomitization event (e.g., Malone et al., 1996; Warren, 2000; Geske et al., 2012; Kaczmarek and Sibley, 2014; Hu et al., 2017). Because it is difficult to sample only the dolomitized part of the burrow, multiple dolomitized burrows and limestone matrix were sub-sampled over cm distance-scales in each core, and mixing diagrams (δ^{26}Mg *vs*. Ca/Mg (mol/mol)) were used to determine the stoichiometric dolomite (Ca/Mg = 1) end-member δ^{26}Mg values of the burrows (Fig. 3.5; Tables 3.1 and 3.2).

3.3. Sampling and analytical methods

3.3.1. Carbonate rock sampling and preparation

Samples of Red River carbonate underlying the central and east-central part of the Williston Basin were collected from 16 drill cores in Saskatchewan, Manitoba, and North Dakota, as well as one outcropping sample collected from Manitoba (Fig. 3.4). Small powdered samples from each well core were extracted with a power drill and carbide cutter drill bit, with the burrow and matrix carbonate sampling performed at hand-sample scale slabs of each core. Approximately 150 mg of carbonate powder was dissolved drop-wise with ultrapure 1N HCl, until effervescence ceased, then diluted to a 30 ml total solution volume with 1N HCl. Sample solutions were

centrifuged and the supernatant collected as the final sample solution. Elemental concentrations of the final solutions were measured by ICP-MS at the University of Michigan Department of Earth and Environmental Science Keck Elemental Geochemistry Laboratory (KEGL). Aliquots of the final solution were taken for Mg and Sr cation exchange chemistry.

3.3.2. Magnesium and strontium isotope analyses

Magnesium was chemically purified from other matrix elements prior to analysis with a two-stage cation exchange column procedure using 2 ml of Bio-Rad® AG® MP-50 resin (100–200 mesh, H-form) packed in a polypropylene column (Eichrom® Technologies, 8 mm inner diameter, 25 ml reservoir connector). The Mg was eluted using a two-column separation procedure. The first column used 1N HCl with 30 μg of Mg loaded in 0.5 ml of 0.5N HCl, allowed to enter the resin completely and then rinsed with 1.5 ml of 0.5N HCl. The Mg fraction was eluted with 1N HCl between 10 ml and 32 ml. An additional clean-up column elution using 1N HNO_3 was for the second separation. The eluted Mg from the HCl separation was loaded in 0.5 ml of 0.5N HNO_3, allowed to enter the resin and rinsed with 1.5 ml 0.5N HNO_3. The Mg fraction was collected with 1N HNO_3 between 15 ml and 39 ml. Strontium was chemically purified with a one-stage cation exchange column (Bio-Rad® AG® 50-X12). Magnesium and strontium procedural blanks were negligible. Yields were checked in purified solutions by sampling 2 ml before and after Mg was eluted from the calibrated cation exchange columns to ensure > 98% of Mg was collected to minimize fractionation associated with column chemistry (Chang et al., 2003). Final sample solutions were dried down at 80°C, the residue was treated with one drop of high purity 30% H_2O_2 and 15N HNO_3 to destroy residual organics from the column, then the sample was diluted in 0.3N HNO_3 to a 30 ppm stock solution to await isotopic analysis. Aliquots of sample stock solutions were taken and diluted to approximately 1 ppm concentrations with 0.3N HNO_3 for analysis. Matrix interfering elements in purified solutions were also checked prior to isotopic analysis to minimize the effects of molecular interferences during analysis (Galy et al., 2001). Sample solutions of approximately 1 ppm Mg were analyzed using low resolution multiple-collector inductively coupled plasma mass spectrometer (Thermo Scientific NEPTUNE MC-ICP-MS), equipped with 9 faraday collectors and 10^{11} Ω resistors, in the Saskatchewan Isotope Laboratory. Samples were introduced to the plasma at 100 μl/min into a glass cyclonic spray chamber. The 1 ppm solutions yielded signal intensities > 8V on mass 24. DSM3 standard solutions with a

magnesium concentration ± 5% to that of the samples were used as the bracketing standard (Galy et al., 2003). A long-term record of an external mono-elemental magnesium standard (CAM1), measured in individually tuned mass spectrometer sessions was noted as an indicator of analytical uncertainty (–2.62 ± 0.08‰, 2σ n = 123). The quality of chemical separation was monitored through the processing of several North Atlantic seawater standards (OSIL), serving as a more complex multi-element standard, yielding a value of –0.79 ± 0.08‰, 2σ n = 18, consistent with values reported in the literature of –0.83‰ ± 0.09‰, 2σ n = 90 (Ling et al., 2011). Strontium isotopes were measured on a thermal ionization mass spectrometer (Thermo Scientific TRITON TIMS) in the Saskatchewan Isotope Laboratory with samples renormalized to 0.710262 for SRM987.

The $^{26}Mg/^{24}Mg$ ratios are reported as $\delta^{26}Mg$ in the conventional delta notation as permil (‰) deviations of the sample isotope ratio relative to the bracketing standard (DSM3), $\delta^{26}Mg = (((^{26}Mg/^{24}Mg)_{sample} \div (^{26}Mg/^{24}Mg)_{DSM3} - 1) * 1000$. Uncertainties associated with measurements of samples within the same analytical session are reported as two standard errors of the mean (2se). Samples analyzed between multiple mass spectrometry sessions, are reported with 2σ uncertainty. Replicate samples (Nrep) are sample solutions that have been analyzed in separately tuned instrument sessions, these are indicated in Table 3.2.

3.3.3. Magnesium stoichiometric dolomite end-member calculations and contour mapping

Magnesium isotope values ($\delta^{26}Mg_{DSM3}$) were plotted against Ca/Mg molar ratios, yielding a well-constrained linear relationship consistent with two component mixing between limestone and dolomite end-members for each sampled rock core (Fig. 3.5; Table 3.2). $\delta^{26}Mg$ values were calculated from the line-of best fit for each rock core for when Ca/Mg molar ratio was equal to 1, thus representative of a 50/50 mix of Ca and Mg expected from stoichiometric dolomite. Burrow samples exhibiting Ca/Mg molar ratios closest to stoichiometric dolomite were selected for Sr mapping.

Stoichiometric dolomite end-member $\delta^{26}Mg$ and Sr isotope values for each sampled rock core were plotted with their associated drill well coordinates. Contour shading was applied to the mapped area using the Kriging algorithm in Surfer® 10 mapping software package (Fig. 3.4). Estimated trajectories of dolomitizing fluid flow were added with arrows situated approximately perpendicular to the isotopic contouring.

3.4. Results and discussion

3.4.1. Magnesium and strontium isotope patterns in the Red River Formation

δ^{26}Mg values of the burrow dolomite are plotted on a map and contoured to show the regional trends (Fig. 3.4a, Table 3.1). Values increase from the center of the basin towards the edges, in all directions. Applying the interpretive framework, dolomitizing fluids must have migrated up-dip through the permeable network of burrows, not down-dip as previously predicted by the brine reflux model. The spatial pattern of $^{87}Sr/^{86}Sr$ ratios in the burrow-dolomite also supports the up-dip migration of Mg-bearing fluids through the burrows (Fig. 3.4b). Higher $^{87}Sr/^{86}Sr$ in burrow-dolomite in the center of the basin is consistent with subsurface, high salinity formation waters (brines) being the source of Mg. There are two likely origins for these brines: (1) evaporatively concentrated seawater that filtered downward into the center of the basin during periods of evaporite deposition, and (2) topographically driven recharge of meteoric waters whose high salinities reflect dissolution of bedded salt deposits encountered during their descent. Only formation waters derived from the former have sufficiently high Mg concentrations to dolomitize the burrows.

Upon reaching the deep center of the basin, evaporatively concentrated seawater will begin to accumulate ^{87}Sr released from Rb-containing minerals (e.g. muscovite, biotite) through rock-water interaction (radioactive ^{87}Rb slowly decays over geological timescales to produce ^{87}Sr) with Rb-bearing minerals in the crystalline Precambrian basement rocks and the siliciclastic rocks of the Deadwood and Winnipeg Formations underlying the Red River. This interpretation is supported by the similarly high $^{87}Sr/^{86}Sr$ ratios in formation waters pumped from the Deadwood and Winnipeg Formation in the center of the Williston Basin today, ranging from 0.7148 to 0.7218 (Table 3.3). The main difference is that these modern deep formation waters have low Mg and high Ca concentrations, which is the geochemical signature of a fluid that has been modified by previous episode(s) of dolomitization. By contrast, the brine that flowed up and out of the Williston Basin at the time of dolomitization of the 'C' member carbonate of the Red River would have been high in Mg (and low in Ca); in other words, a deep formation water that had not yet lost its capacity for dolomitization. The geochemical behavior of Ca is similar to Sr, and therefore both were released to pore fluids during the replacement dolomitization. Moreover, the distribution coefficient for Sr ($D_{Sr} = Sr/Ca_{carb} \div Sr/Ca_{fluid}$) partitioning into dolomite ($D_{Sr} \approx 0.01$; Vahrenkamp and Swart, 1990) is smaller than for calcite ($D_{Sr} \approx 0.1$; Baker et al., 1982), this means that both the

Sr concentration and Sr/Ca ratio of the dolomitizing fluid will increase along the flow-path. Because the Late Ordovician marine carbonate that is being replaced has a constant, and low $^{87}Sr/^{86}Sr$ ratio of 0.7080 (Holmden, 2009) (compared to ~ 0.710 for the dolomitizing fluid at its source) burrow-dolomite $^{87}Sr/^{86}Sr$ should *decrease* along the flow path in the direction of *increasing* $\delta^{26}Mg$ values, which is exactly what is observed (Fig. 3.4a, b).

3.4.2. Hydrostatic models of dolomitization of the Red River Formation

The $^{87}Sr/^{86}Sr$ results rule out one other hypothesis for the origin of the burrow-dolomite that does not involve regional-scale fluid flow. Gingras et al. (2004) suggested that burrow dolomite precipitated with the assistance of a consortium of microbiota dwelling in the burrows. If this interpretation is correct, the dolomite would have formed as a primary precipitate very early in the diagenetic history of the deposit, and the Mg for dolomitization would logically have been derived from seawater, evaporated seawater, or directly the carbonate itself. In all three scenarios, the burrow-dolomite would therefore record an $^{87}Sr/^{86}Sr$ ratio of Late Ordovician seawater (0.7080), which is discordant with the observations presented in this study. From the center to the edge of the basin, $^{87}Sr/^{86}Sr$ ratios of burrow-dolomite are always higher than the limestone matrix (Fig. 3.4b; Tables 3.1 and 3.2), which rules out contemporaneous seawater and carbonate sediment as significant sources of Sr (and Mg) to the dolomite.

Most dolomitization models conceptualize fluid flow in sedimentary basins as occurring in response to hydrostatically controlled pressure gradients in persistently permeable sediment. Three of these models picture deep-seated components of upward fluid flow along a *basal* aquifer: (1) sediment compaction (Fig. 3.3b), (2) tectonic compaction (Fig. 3.3e), and (3) topographically controlled meteoric water recharge (Fig. 3.3d), and assume that the crystalline basement is impenetrable to fluids. The 'C' member carbonate is not located within the lowermost aquifer in the Williston Basin, rather, this distinction belongs to the conglomerate and sandstone of the Cambrian Deadwood Formation. The Deadwood and Red River Formations, however, are crosscut by numerous vertical faults that extend upwards from the Precambrian basement, and these may have acted as conduits for fluid flow, allowing waters moving up-dip along the Deadwood to cross into the Red River (Figs. 3.6, 3.7). Moreover, the stratigraphic continuity of the Deadwood Formation is interrupted by blocks of basement rock thrust upwards along vertical faults which were present at the time of deposition (Fig. 3.7; Gerhard et al., 1987; Kreis and Kent, 2000). It is

therefore feasible that formation waters flowing upwards from the Deadwood could use these faults to cut across the Winnipeg Formation aquitard into the 'C' member carbonate of the Red River. Although there are faults that continue further into the overlying successions, the capping 'C' anhydrite unit would deflect some of the flow up-dip along the length of the 'C' member carbonate, being channelized by the burrow network (Fig. 3.7). The youngest known fault reaches Paleogene age strata, which provides a minimum age for dolomitization of the Red River carbonate, if all of the faults are considered to be roughly similar in age. This, naturally, cannot be proven, but it serves to illustrate the point that dolomitization of the 'C' member carbonate may have occurred up to 390 million-years after the depositional age of the Red River Formation. It also opens up the possibility that the event that mobilized formation waters to flow upward from the center of the basin may also be responsible for the dolomitization of the overlying 'B' and 'A' member carbonates of the Red River, which are also confined by capping anhydrite layers (although not as massive or regionally extensive as the capping 'C' member anhydrite). The age of dolomitization will be further discussed in section *3.4.4*.

Despite the aforementioned argument that the basal aquifer in the Williston Basin may have included the 'C' member carbonate of the Red River, none of the commonly considered hydrostatic models of dolomitization satisfactorily explain the radial pattern of up-dip directed fluid flow originating from the deep center of the Williston Basin, with the exception of the sediment compaction model (Fig. 3.3b). Sediment compaction creates fluid overpressures in the deep basin through the reduction of pore volume in shale. Applied to the Williston Basin, the underlying Winnipeg Formation shale is a prime candidate for dewatering during compaction, and it directly underlies the Red River. Numerical models of sediment compaction, however, yield fluid velocities along the basal aquifer that are exceptionally low (e.g., Bethke, 1985; Whitaker et al., 2004). In the Williston Basin, it would take ~ 400 Myr for fluid to travel 600 km from the center to the edge of the basin, and carbonate deposits near the edge of the basin would not receive the hundreds to thousands of pore-volumes of fluid required to completely dolomitize the burrows. The tectonic compaction and topographic recharge models fail because they predict upward fluid flow along only one side of the basin (Fig. 3.3d, e).

The *intracratonic* Williston Basin was unaffected by crustal shortening during the Cretaceous–Paleogene Laramide Orogeny. However, there are a number of magmatic intrusions of nearly the same age (Paleogene) that lifted the crust, locally, along the SW margin of the

Williston Basin, creating the Black Hills and the Little Rocky Mountains. Sedimentary rocks drape the flanks of the central core of uplifted crust, which is typically composed of crystalline Precambrian basement or Paleogene-aged magmatic intrusions. A high elevation-head drives meteoric water into the Williston Basin along each permeable outcropping unit (Bachu and Hitchon, 1996), as evidenced by the very low δD and $\delta^{18}O$ values in formation waters found in many locations throughout the Williston Basin (Rostron and Holmden, 2000, 2003; Jensen et al., 2006). The recharge in the Black Hills is believed to drive salt water discharge from springs in the outcrop belt along the Manitoba escarpment 1200 km away, indicating a southwest-northeast direction of flow (Bachu and Hitchon, 1996). However, there is no clear stable isotope evidence that these Tertiary age (or younger) meteoric waters mixed with the densest brines in the deepest center of the Williston Basin. These brines may be classified as Ca-Cl brines (Iampen and Rostron, 2000), based on their major cation and anion chemistry. By contrast, formation waters in Manitoba sampled northeast and up-dip from the center of the Williston Basin, are Na-Cl type (including the springs) with relatively low δD and $\delta^{18}O$ values (Palombi, 2008), indicating that they are meteoric waters that have dissolved halite at some point during their flow across the basin, most likely from the dissolution of the Devonian Prairie Evaporite Formation. From this evidence, this study concludes that the topographic uplifts along the southwestern margin of the Williston Basin are not high enough to drive the densest brines out of the deep center of the basin in the present day.

3.4.3. Dynamic (supra-hydrostatic) models of dolomitization

The failure of the hydrostatic models to account for the observed pattern of fluid flow deduced from the Mg and Sr isotopes in the 'C' member dolomite of the Red River Formation leads us to consider dynamic models of fluid flow driven by anomalous (supra-hydrostatic) pressurization in the basin. It is therefore useful at this juncture to discuss the problematical origin of Mississippi Valley Type (MVT) lead–zinc deposits. Most MVT deposits, containing economic quantities of Pb and Zn are hosted within dolomite bodies (Warren, 1999). These sediment-hosted ores are emplaced at relatively shallow burial depths (600–1500 m), near the edges of sedimentary basins, from fluids that migrated hundreds of kilometers from deep basin centers (Sverjensky, 1986). This interpretation is supported by fluid inclusion analyses showing temperatures and salinities of the ore forming fluids that are higher than the thermal environment at the stratigraphic level of their emplacement (Qing and Mountjoy, 1992; Davies and Smith Jr., 2006) with the high

temperatures indicative of relatively rapid fluid flow (Cathles and Smith, 1983). Some MVT ore deposits are associated with the fluid migration along vertical faults connected to basement highs. Numerous dolomite bodies have also been described that are associated with vertical faults, indicating that the ascent of hot basement-derived fluids can serve as a source of metals for MVT ores as well as a source of Mg for dolomitization (Davies and Smith Jr., 2006, and references therein). Conventional hydrostatic models of fluid flow in constant permeability strata have been constructed to explain MVT ores in *foreland* basins: specifically, tectonic compaction (Fig. 3.3e) and topography-driven fluid flow (Fig. 3.3d) (Leach et al., 2001, 2010). These models cannot be generalized for MVT ores found in *intracratonic* sedimentary basins because these settings lack the style of tectonism that produces crustal thickening (through thrusting) to drive sediment compaction flow, as well as the elevation-head to drive meteoric waters deeply into the sedimentary basin, analogous to the formation of dolomite in the 'C' member carbonate of the Red River Formation.

Over-pressurized fluids play a critical role in faulting in the seismogenic crust, which covers approximately the top 10 km of the brittle crust. Fracture networks around large-scale faults create lithostatically pressurized fluid reservoirs. Slippage on the main faults de-pressurizes these reservoirs, driving fluid into the faults, which then channelizes the flow upwards in the crust (Davies and Smith Jr., 2006). Release of fluid pressure in one fracture-network during a seismic event can pressurize another fluid compartment, or hydro-fracture the crust to create new fluid reservoirs (Hunt, 1990). The underlying crystalline basement exhibits numerous vertical to sub-vertical faults and structures that bear witness to the tectonic forces that initiated subsidence in this region, many of which propagate upwards into, and even extending above, the Red River Formation (Figs. 3.6, 3.7; Gerhard et al., 1987; Anna, 2013; Anderson, 2011). Patterns of faulting in the basement can even be observed on the surface, in the form of NE and NW trending lineaments, reflecting slippage on faults between lithospheric blocks, with vertical and horizontal subsurface fluid migration enhanced along these boundaries (Thomas, 1974; Gerhard, et al., 1987; Shurr et al., 1994; Anderson, 2011). Detailed mapping of the north-south trending Nesson anticline, the largest known anticlinal structure beneath the center of the Williston Basin in North Dakota (Figs. 3.1, 3.4, 3.6, 3.7), is associated with major normal faults and lineament zones that are part of a 'master fault' system, active since late Precambrian time and located on the west side of the main anticline (Gerhard et al., 1982, 1987). It seems likely that seismic activity along some

of these faults drove crustal fluids upwards into the deep center of the Williston Basin, where most of the faults are concentrated (Fig. 3.6) (Anna, 2013). Fluid in the seismogenic crust may originate from multiple sources, including surface meteoric water, connate water leaking into the basement from the sedimentary basin above, mineral dehydration waters released during metamorphism, and magmatic waters liberated during igneous crystallization. 'Fault-valve action' could serve to pump these hot, saline waters into the bottom of the Williston Basin, where they could then spread radially outwards and upwards along the most permeable sedimentary units (Sibson, 1994). If these upwardly migrating fluids caused dolomitization, then they must have contained very high Mg concentrations.

Anomalous pressurizations in the form of 'pressure compartmentation' may also occur within intracratonic sedimentary basins, typically below 3 km depth based on empirical measurements, as a result of planar barriers referred to as (pressure) 'seals' (e.g., Hunt, 1990; Powley, 1990; Bradley and Powley, 1994; Cathles, 2001). This led to the recognition of capillary blockage (seals), as a mechanism for creating pressure compartments in sedimentary basins in areas with significant organic matter burial and hydrocarbon generation. Capillary seals form in sediment characterized by spatial gradients in grain-size and, at minimum, two pore filling fluids (typically natural gas and connate water) (Iverson et al., 1994; Cathles, 2007). Connate water is drawn into the smaller pore volumes of the finer grained sediment by the capillary force, which pushes gas into adjacent sedimentary layers with larger pore volumes, thus blocking the channels in the sediment through which water might flow (Deming et al., 2002). Capillary seals have been formed and tested using quartz sediment (45 μm) in a pressure cell in the laboratory, interlayered with fine-quartz sediment (2 μm) of centimeter-scale thickness (Cathles, 2001; Shosa and Cathles, 2001). Flow of water through the cell effectively ceases when gas added to the cell reaches a concentration of ~ 50% in the coarse-grained layers. This amount of gas is enough to block the pore throats of the smaller grains, resulting in a fluid flow seal. In addition, the seal is relatively strong, as twelve pore volumes of additional pressure was inadequate for rupture. Graded deposits are common in sedimentary successions, and subsequently, pressure seals should also be common in places where natural gas mixes with water. Moreover, the pressure drop across multiple seals is additive, thus increasing the effectiveness of the seal. Capillary seals can be exceeded when the internal pressure of a compartment increases enough to deform the gas bubbles, resulting in a dynamic drive through the fine pores.

When capillary seals rupture, the backing pressure of the compartment will send hot, saline water and gas up and out of the deep center of the basin, where many compartments are located due to the pervasiveness of basin-centered gas. This led Cathles (2007) to propose that capillary-sealed pressure compartments may periodically rupture, forcing gas and connate water to migrate up and out of the basin along the most permeable paths to the surface. Pressure compartments are self-sealing (Hunt,1990; Bradley and Powley, 1994; Sibson, 1994; Cathles, 2001; Deming et al., 2002; Cathles, 2007), and can presumably recover from *in situ* production of thermogenic gas, resulting in the high probability of future rupture. With these considerations, Cathles (2007) constructed a 'gas pulsar' model for the origin of MVT ores. This model explains a number of puzzling features of MVT deposits that conventional hydrogeological models have had difficulty addressing. For example, tracer data in ore minerals shows that they form in layers representing discrete pulses of fluid numbering multiple individual events (Cathles and Smith, 1983). The 'gas pulsar' explains the multi-episodic nature of ore formation, albeit this model can only be applied under a rather restrictive set of conditions. Dating of the ore minerals limits their formation to time frames of only a few million years, whereas tectonic compaction and topographically driven meteoric recharge produce steady flow systems that operate over tens of millions of years. Moreover, these models encounter some difficulties transporting hot, highly saline waters hundreds of kilometers up-dip to the sites of ore formation in the required time-frame. Topographically driven meteoric water recharge permits faster flows than tectonic compaction, but it is difficult to escape the conclusion that some evidence for meteoric waters should be found in fluid inclusions within the ore minerals, such as low salinities correlating with low δD and $\delta^{18}O$ values. By contrast, the salinities most often resemble those of connate waters (10–30 wt% NaCl), with heavy hydrogen and oxygen isotope compositions (Leach et al., 2010, and references therein).

3.4.4. Anomalous thermal events in the Williston Basin

Two heat flow anomalies punctuate the thermal history of the Williston Basin, one in the Late Devonian to Mississippian time and the other in the Late Cretaceous–Paleogene (e.g., Chipley and Kyser, 1992; Koehler et al., 1997; Osadetz et al., 2002; Cioppa, 2003; Szabo and Cioppa, 2006; Feinstein et al., 2009) (Fig. 3.8). These heating events are associated with thermal remnant magnetizations and fluid inclusions preserved in potash deposits of the middle Devonian Prairie Evaporite, and dolomite of the Red River Formation (Chipley and Kyser, 1992; Koehler et al.,

1997; Szabo and Cioppa, 2006). The magnetizations are also consistent with the widespread circulation of fluids in the basin during these times, as fluid flow is required to mobilize the ferrous iron that records the magnetic signatures in the rocks. Fluid flow during the Cretaceous thermal event is undoubtedly linked to the creation of a high elevation-head in the ancestral Rocky Mountains during the Laramide Orogeny, and in the Williston Basin during the emplacement of Paleogene-age intrusions that resulted in the formation of the Black Hills and the Little Rocky Mountains. However, as discussed above, topographically-driven fluids migrate from southwest to the northeast in the Williston Basin and, thus, cannot explain the radial pattern of fluid flow rising up and out of the center of the Williston Basin inferred from the Mg and Sr isotope signatures of 'C' member dolomite in the Red River Formation (Fig. 3.4a, b). Therefore, if dolomitization occurred during one of these two heating events, it would have to be the late Paleozoic event (Fig. 3.8). Interestingly, many of the early Paleozoic source rocks became mature during this time (Osadetz et al., 2002), and as noted by Cathles (2007), the development of pressure compartments should coincide with organic maturation and production of oil and gas, as pressure seals require connate waters to be mixed with a gas. In fact, the Red River Formation and the underlying Winnipeg and Deadwood are recognized not only for their petroleum production, but also for gas production (Fig. 3.2). No doubt, the higher geothermal gradient in the late Paleozoic accelerated these processes, in particular the production of thermogenic gas. The late Paleozoic heating event has been related to far-field tectonic effects of the Antler Orogeny, occurring on the west coast of North America between the Late Devonian and Mississippian (Speed and Sleep, 1982).

3.4.5. A novel model of dolomitization of the Red River Formation in the Williston Basin

The following model is offered for the origin of the dolomite in the 'C' member carbonate of the Red River, which is tentatively attributed to events surrounding the basinal heating during the late Paleozoic. The heating anomaly, which caused thermal expansion (and subsequent contraction) of the crust will logically increase earthquake activity during the event. This will increase the likelihood of 'fault-valve action' occurring in the seismogenic crust (Sibson, 1994). Vertical faults will transmit hot pressurized fluids into the bottom of the Williston Basin, pressurizing some capillary-sealed compartments, while triggering others to rupture, thus sending Mg-rich connate waters upwards into the basin flowing along the paths of least resistance. This study suggests that the 'C' member carbonate of the Red River Formation, with its anastomosing,

permeable network of burrows and overlying impermeable anhydrite cap, behaved as one of the conduits for the flow of these waters to the surface, and that the burrows were dolomitized in stages by these upwardly migrating fluids (Fig. 3.7).

The model generates three predictions. The first is that MVT ores should have been deposited in the Williston Basin. To date, only one small showing of MVT ore minerals has been located near the present day erosional edge of the Williston Basin in Manitoba (Bamburak and Klyne, 2004). There exists the possibility that more will be discovered, or that larger deposits have since been eroded, due to their emplacement near the basin-edge. The second is that saddle dolomite should be found in the Red River carbonate. Saddle dolomite is one of the most often cited hallmarks of dolomitization by high temperature fluids (Spötl and Pitman, 1998) and has been reported in the burrows in a few locations. The third prediction is that stylolites should be common in Red River carbonates. The origin of stylolites is controversial however, as one model suggests that they are formed from hydro-fracturing of carbonate rocks due to fluid over-pressurization, serving as open fluid conduits and subsequently collapsing following fluid flow as formation water pressures subsided (Braithwaite, 1989; Heap et al., 2014). Stylolites are, in fact, common in the 'C' member laminated carbonate of the Red River Formation (Zenger, 1996), however the relative proportion of stylolites located within the basin-center and away from basin-center is at this time unconstrained.

The exact timing and duration of the heating event, which provides an important constraint on the window for dolomitization of the Red River according to the model, is also not well constrained. Figure 3.8 summarizes data from five sources: (1) apatite fission track (AFT) data, (2) thermal remnant magnetizations, (3) K/Ar dating of the Devonian Prairie Evaporite Formation, (4) fluid inclusion geochemistry in the Devonian Prairie Evaporite Formation and (5) radiometric dating of MVT ores (in the Alberta Basin at Pine Point), pointing to two distinct clusters of data in the late Paleozoic and Cretaceous–Paleogene for the potential timing of dolomitization. Dolomitization is apparently younger than the depositional age of the Prairie Evaporite Formation, which is interesting because most of the dolomite in the Williston Basin occurs below this stratigraphic level. This could be taken as evidence supporting the brine reflux model of dolomitization of the underlying strata, but as is the case in the 'C' member carbonate of the Red River, which also directly underlies an aerially extensive evaporite deposit, the proximity argument is not supported by Mg and Sr isotope evidence for fluid flow direction during the

formation of the dolomite. On the other hand, fluids migrating upwards in the Williston Basin would be blocked by the Prairie Evaporite, and this too might explain why dolomite is less common above the evaporite than below. It is possible that most of the dolomite in the Williston Basin formed in a way that is similar to the model presented in this study for the dolomitization of the 'C' member carbonate of the Red River Formation. Late Paleozoic re-magnetizations are recorded in both the Red River and Prairie Evaporite Formations as well as the Lower Pennsylvanian/Jurassic Watrous Formation (Chipley and Kyser, 1992; Koehler et al., 1997; Cioppa, 2003; Szabo and Cioppa, 2006), lending some support to this hypothesis. However, the true test is to look at reconstructed patterns of fluid flow using $\delta^{26}Mg$ and $^{87}Sr/^{86}Sr$ recorded in dolomite bodies.

The most significant challenge facing the upward-directed flow model for dolomitization of the 'C' member carbonate of the Red River Formation, is the apparently limited supply of Mg in formation waters. However, this problem is not exclusive for the supra-hydrostatic model of pressure-induced flows in sedimentary basins. Traditional hydrogeological models, such as topographically driven meteoric recharge (Fig. 3.3d) and tectonic compaction (Fig. 3.3e), face the same shortcoming. In fact, only the brine reflux model (Fig. 3.3a) and thermal convection model (Fig. 3.3c) of dolomitization (as well as other models not discussed herein involving normal marine seawater not described in this study) resolve this issue by tapping into the nearly limitless supply of Mg in the oceans.

The Mg inventory in formation waters is limited to the pore spaces and fractures in sediment. However, if the fluid trapped in crust beneath the sedimentary basin is also a sizeable repository of Mg, and this Mg is accessible through 'fault-valve action' (Sibson, 1994), then the view of formation waters as being Mg-limited needs to be reconsidered. In addition, some of the Mg sequestered for dolomitization is sourced from the rocks themselves, particularly those that were composed of high magnesium calcite (HMC) (Kendall, 1977; Longman and Haidl, 1996; Zenger, 1996). However, the Late Ordovician falls in a 'calcite sea' period, where the Mg concentration in HMC is not expected to reach the high levels found in modern marine carbonates precipitated in the 'aragonite sea' of the present day. An alternative Mg source from within the rocks is the presence of 'proto-dolomite' that may have existed within the burrows themselves, having been formed during early burial and later overprinted by burial dolomitization (Gingras et al., 2004).

3.5. Conclusion

Burrow dolomite of the Red River Formation in the Williston Basin, originally hypothesized to be the result of a brine reflux model of dolomitization, is now perceived to be related to the thermal history of the basin, based on Mg and Sr isotope evidence provided in the burrowed 'C' member carbonate beds. Burrow-dolomite $\delta^{26}Mg$ values increase from the center to the edges of the basin (Fig. 3.4a), indicating that Mg-bearing fluids ascended through the burrows. This, coupled with burrow-dolomite $^{87}Sr/^{86}Sr$ ratios decreasing away from the basin-center (Fig. 3.4b), is evidence that the dolomitizing fluids were likely formation waters originating in the deep center of the basin. The hypothesized mechanism triggering the mobilization of the deep basinal fluids involved a dynamic (supra-hydrostatic) model wherein a release of over-pressurized, capillary-sealed compartments by the activation of vertical faults resulted in the upward flow of fluids into the porous and permeable conduit of the Red River 'C' member burrow network.

There are great implications attached to the ability to trace such a large-scale event. First, the use of Mg and Sr isotopes to elucidate paleo-fluid flow paths of dolomitizing events offers opportunities for re-exploration of other similarly dolomitized carbonate successions and sheds new light on the complicated dolomite system of the long-studied and extensively explored Williston Basin. Second, these results demonstrate that $\delta^{26}Mg$ and $^{87}Sr/^{86}Sr$ subsurface gradients in large-scale dolomite bodies hold the potential to be used for future petroleum exploration, as they are well-known to play host to petroleum reservoirs (Warren, 2000) and migrating petroleum systems would be expected to follow the same subsurface pathways as dolomitizing fluids. Finally, applying novel stable isotope systems (such as Mg) as tracers to dolomitization events may yield new insights into the origins of massive dolomites and allow future researchers to gain a firm grip on the elusive '*dolomite problem*' as they pull the field forward using state-of-the-art, multi-proxy isotope approaches.

3.6. Figures

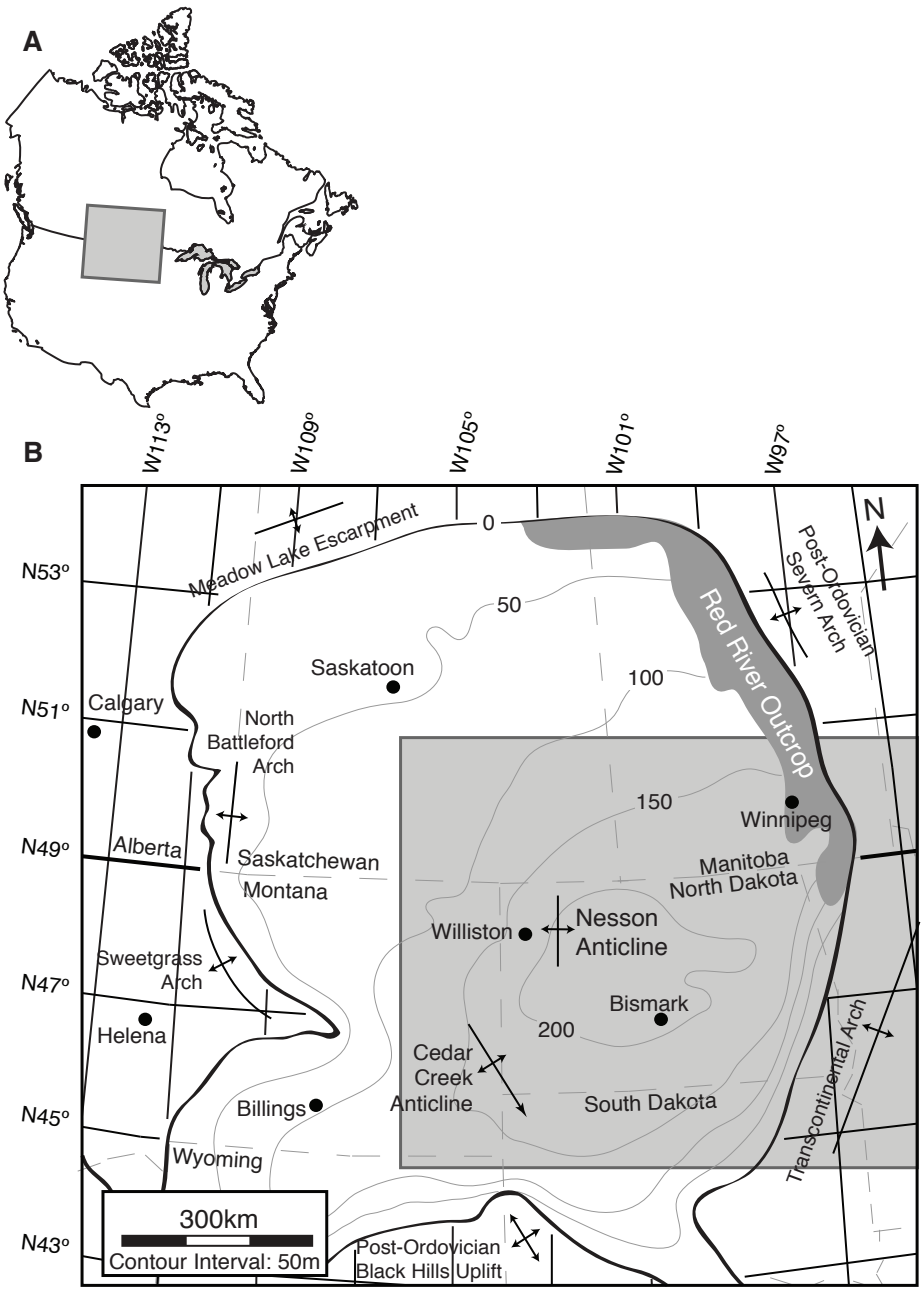

Figure 3.1 Maps showing the location of sampling sites within the Williston Basin, North America. (A) Location of the study site in Canada and the US. (B) Isopach map portraying the extent of the Red River Formation within and beyond the margins of the Williston Basin proper. The center of the Red River is indicated by the thickest part of the formation, shown above in the northwest of North Dakota. Modified from Longman and Haidl, 1996 and Pratt and Haidl, 2008. See Fig. 3.4 for additional details included in the large shaded box.

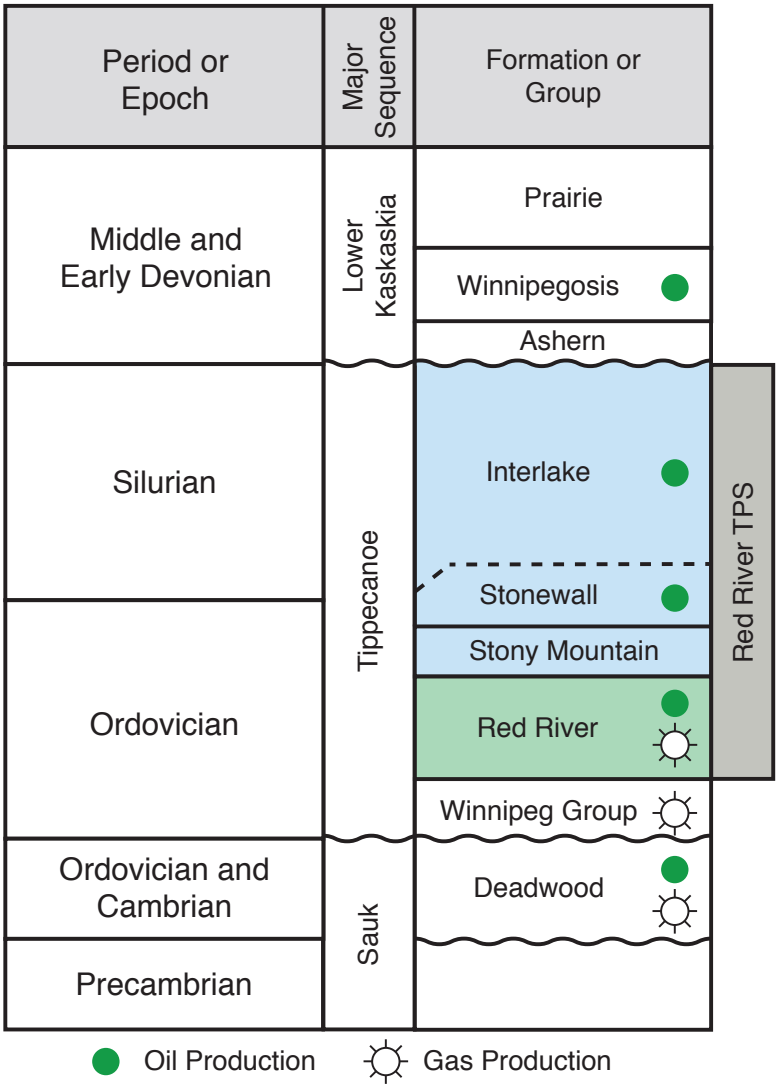

Figure 3.2 Stratigraphic chart depicting the position of the Red River Formation and the units associated with the Red River Formation Total Petroleum System (TPS). Solid green circles denote petroleum production and the sun shapes denote gas production within the marked units. Wavy lines indicate the presence of unconformities. The blue shaded units indicated intrusion of petroleum having migrated up from the Red River (shaded in green) into the overlying formations, likely through complex faults and fracture networks, subsequently horizontally through carrier beds. Modified from Anna (2013).

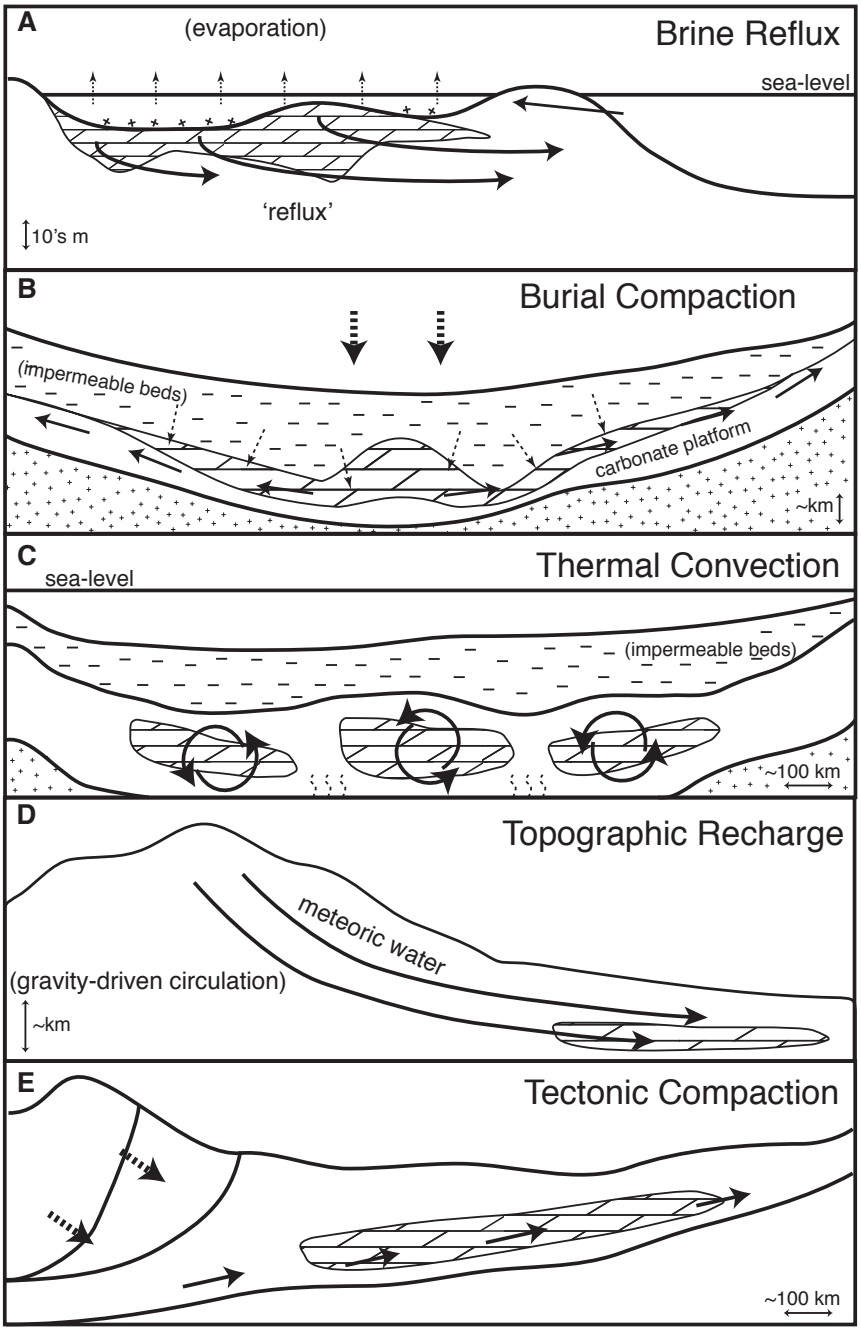

Figure 3.3 Conceptual hydrogeological dolomitization models and associated patterns of dolomitization (modified after Land, 1985; Morrow, 1982; Warren, 2000; Machel, 2004). (A) Brine reflux model of dolomitization. The dashed arrows denote evaporation from the isolated hyper-saline lagoon. Small 'x' shapes represent formation of evaporite minerals as a result of extreme evaporation in the restricted basin. Dense, Mg-rich, highly evaporative waters are shown to sink down-dip into the underlying strata with the solid arrows. Recharge of water into the lagoon

from the ocean provides the Mg source. Vertical scale is ~ 10's m. (B) Burial (sediment) compaction model of dolomitization. Dashed arrows denote pressures exerted on the rock formations resulting from sediment-load compaction from above. Solid arrows denote subsurface fluid migration up-dip, toward the basin edge as a result of downward pressures associated with compaction and the inability for those fluids to move upward into overlying impermeable strata or downward into impermeable basement rock. Vertical scale is ~ 1 km. (C) Thermal convection model of dolomitization. Solid arrows show circular subsurface fluid flow resulting from heating of the underlying strata (denoted as dashed wavy lines). Fluids are confined to the small circular cells as a result of overlying impermeable rock units. Horizontal scale is ~ 100 km. (D) Topographic recharge model of dolomitization. Meteoric waters are introduced from topographically high areas resulting from orogenic uplift. As a result of gravity-driven circulation, meteoric waters act as a hydraulic head, pushing subsurface connate waters along a topographically lower formation, resulting in dolomitization. Vertical scale is ~ 1 km. (E) Tectonic compaction model of dolomitization. This model, as with the topographic recharge model, results from orogenic uplift. High pressures associated with tectonic loading of overlying strata cause migration of subsurface fluids up-dip and unidirectional. Horizontal scale is ~ 100 km, vertical scale is exaggerated.

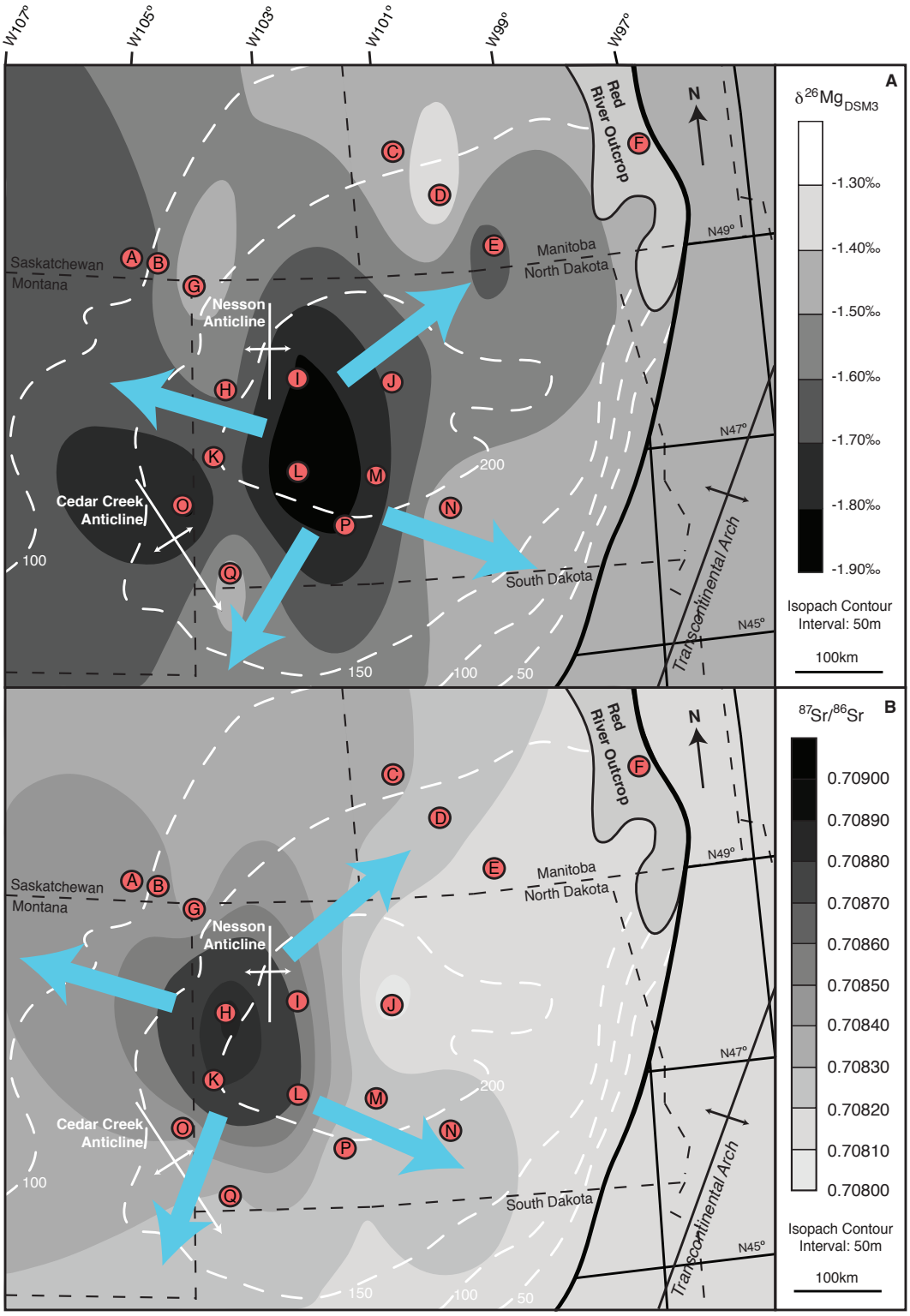

Figure 3.4 Shaded contour maps of $\delta^{26}Mg$ and $^{87}Sr/^{86}Sr$ values of well cores sampled within the Williston Basin. (A) Stoichiometric dolomite end-member $\delta^{26}Mg$ values and (B) burrow $^{87}Sr/^{86}Sr$

ratio shaded contour map within the Red River Formation in the Williston Basin. Red River Formation isopach overlay (white, dashed) is also shown. Note the location of the sampled well cores with letter designations (Table 3.1) and the regional structural features (Fig. 3.1b). Large blue arrows pointing outward from the center of the basin illustrate interpreted dolomitizing fluid flow directions.

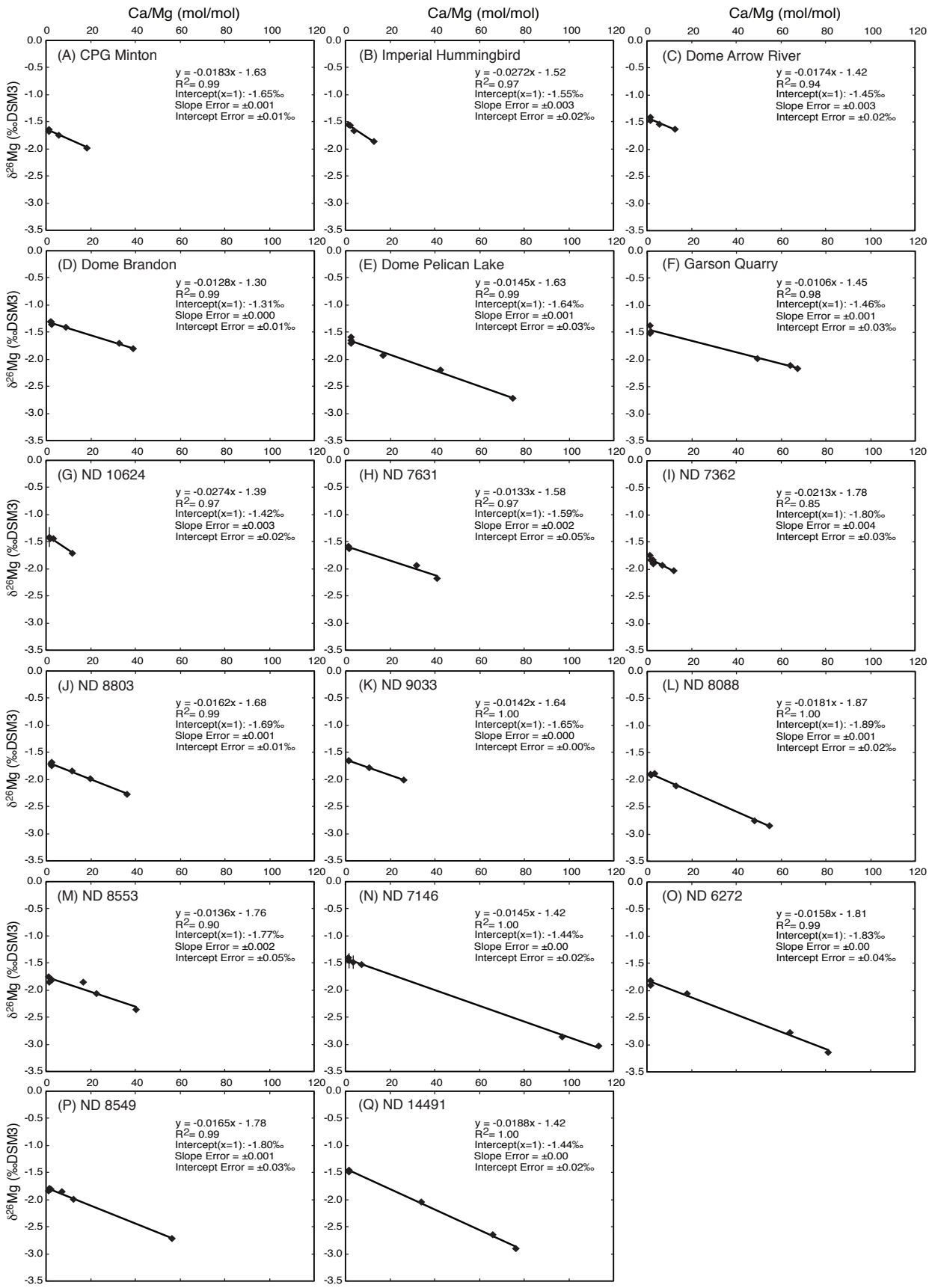
Ca/Mg (mol/mol)
δ26Mg (‰DSM3)
(A) CPG Minton
y = -0.0183x - 1.63
R2= 0.99
Intercept(x=1): -1.65‰
Slope Error = ±0.001
Intercept Error = ±0.01‰
(B) Imperial Hummingbird
y = -0.0272x - 1.52
R2= 0.97
Intercept(x=1): -1.55‰
Slope Error = ±0.003
Intercept Error = ±0.02‰
(C) Dome Arrow River
y = -0.0174x - 1.42
R2= 0.94
Intercept(x=1): -1.45‰
Slope Error = ±0.003
Intercept Error = ±0.02‰
(D) Dome Brandon
y = -0.0128x - 1.30
R2= 0.99
Intercept(x=1): -1.31‰
Slope Error = ±0.000
Intercept Error = ±0.01‰
(E) Dome Pelican Lake
y = -0.0145x - 1.63
R2= 0.99
Intercept(x=1): -1.64‰
Slope Error = ±0.001
Intercept Error = ±0.03‰
(F) Garson Quarry
y = -0.0106x - 1.45
R2= 0.98
Intercept(x=1): -1.46‰
Slope Error = ±0.001
Intercept Error = ±0.03‰
(G) ND 10624
y = -0.0274x - 1.39
R2= 0.97
Intercept(x=1): -1.42‰
Slope Error = ±0.003
Intercept Error = ±0.02‰
(H) ND 7631
y = -0.0133x - 1.58
R2= 0.97
Intercept(x=1): -1.59‰
Slope Error = ±0.002
Intercept Error = ±0.05‰
(I) ND 7362
y = -0.0213x - 1.78
R2= 0.85
Intercept(x=1): -1.80‰
Slope Error = ±0.004
Intercept Error = ±0.03‰
(J) ND 8803
y = -0.0162x - 1.68
R2= 0.99
Intercept(x=1): -1.69‰
Slope Error = ±0.001
Intercept Error = ±0.01‰
(K) ND 9033
y = -0.0142x - 1.64
R2= 1.00
Intercept(x=1): -1.65‰
Slope Error = ±0.000
Intercept Error = ±0.00‰
(L) ND 8088
y = -0.0181x - 1.87
R2= 1.00
Intercept(x=1): -1.89‰
Slope Error = ±0.001
Intercept Error = ±0.02‰
(M) ND 8553
y = -0.0136x - 1.76
R2= 0.90
Intercept(x=1): -1.77‰
Slope Error = ±0.002
Intercept Error = ±0.05‰
(N) ND 7146
y = -0.0145x - 1.42
R2= 1.00
Intercept(x=1): -1.44‰
Slope Error = ±0.00
Intercept Error = ±0.02‰
(O) ND 6272
y = -0.0158x - 1.81
R2= 0.99
Intercept(x=1): -1.83‰
Slope Error = ±0.00
Intercept Error = ±0.04‰
(P) ND 8549
y = -0.0165x - 1.78
R2= 0.99
Intercept(x=1): -1.80‰
Slope Error = ±0.001
Intercept Error = ±0.03‰
(Q) ND 14491
y = -0.0188x - 1.42
R2= 1.00
Intercept(x=1): -1.44‰
Slope Error = ±0.00
Intercept Error = ±0.02‰

Figure 3.5 The $\delta^{26}Mg$ (‰) *vs*. Ca/Mg (mol/mol) cross-plots for each sampled well core. The $\delta^{26}Mg$ errors indicated with ± 2 standard errors of the mean (2se). Line of best-fit equations are shown as well as the R^2 values for each line, dolomite end-member values (x = 1), slope error (± 1se), and y-intercept error (± 1se).

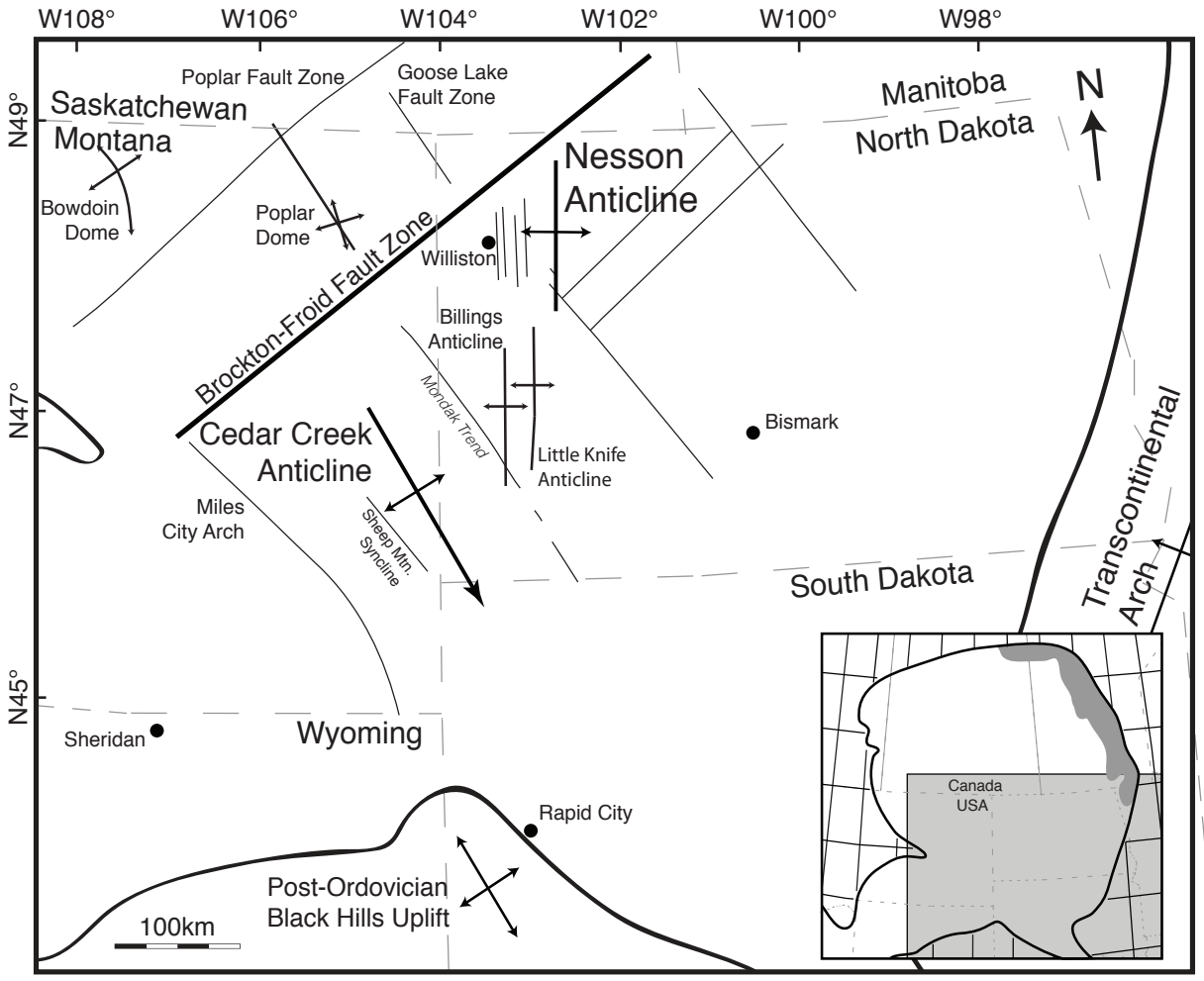

Figure 3.6 Detailed map of the Williston Basin center showing major structural features that have been identified and mapped. Thin, unlabeled black lines indicate mapped faults. Note the cluster of identified faults around the basin center. The inset map shows the outline of the extent of the Red River Formation, shown in more detail in Fig. 3.1b. Modified from Anna (2013).

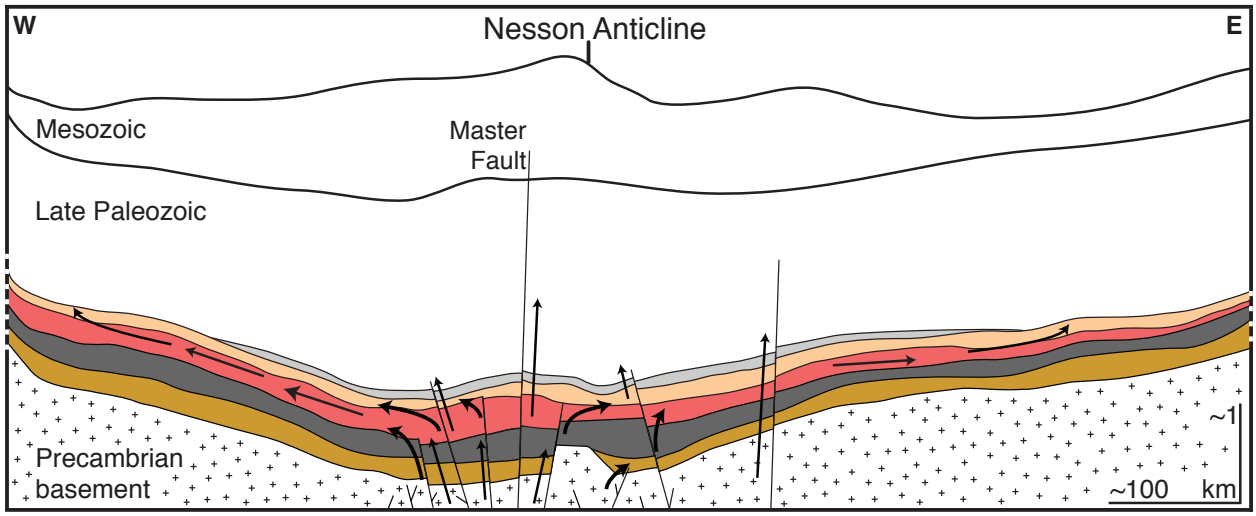

Figure 3.7 Conceptual model of the fluid flow up and out of the center of the Williston Basin along faults and fractures. The brown bottommost layer denotes the Cambrian Deadwood Formation, dark gray denotes the Ordovician Winnipeg Formation, red denotes the burrowed 'C' member of the Red River Formation, yellow denotes the 'C' member laminated dolomite of the Red River Formation, and light gray denotes the 'C' member anhydrite of the Red River Formation. Note that the anhydrite unit diminishes toward the basin edge. The large fault depicts the structural 'Master fault' located west of the Nesson Anticline. Arrows denote hypothetical subsurface fluid migration up and out from the conceptual faults, shown breaking through the rock formations.

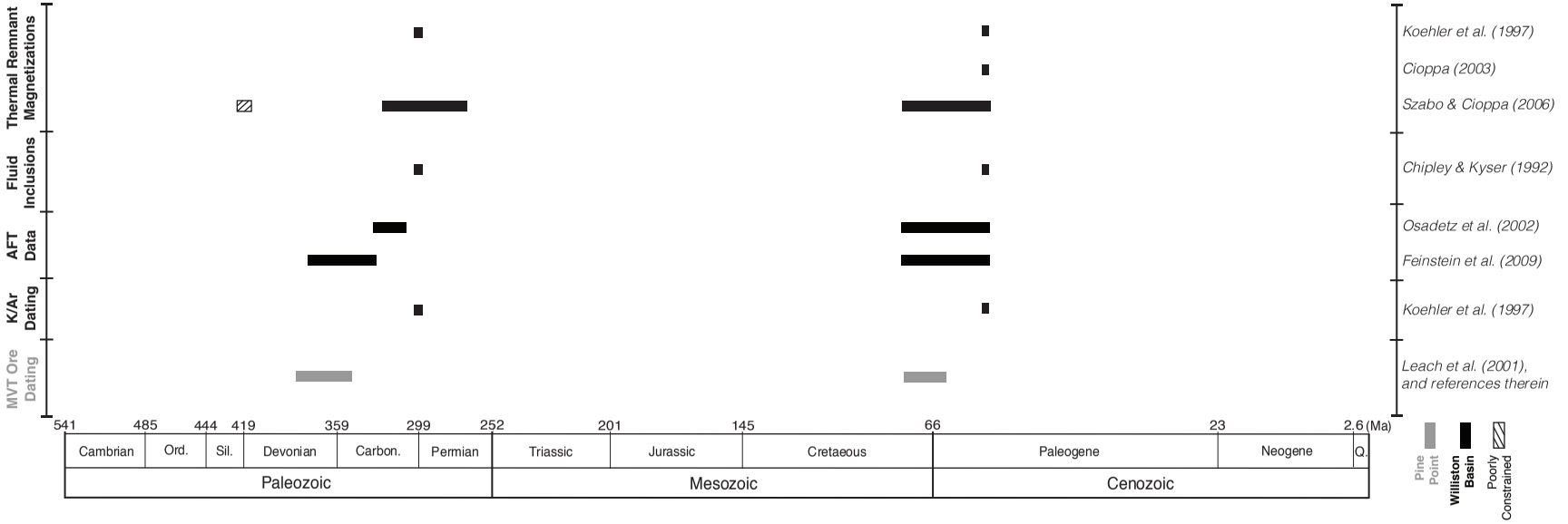

Figure 3.8 Geological time-scale depicting timing of anomalous heating events in the Williston Basin and surrounding areas recorded as thermal remnant magnetizations, fluid inclusions, apatite fission track (AFT) data, K/Ar dating of evaporite minerals, and Mississippi Valley-Type (MVT) ore paleo-magnetic and radiogenic isotope dates (Pine Point, Alberta). Associated references are provided. Solid black bars show timings for each event within the Williston Basin that is well-constrained. Dashed bars show timings for events that are poorly constrained. Gray bars denote the dating of MVT ore located within the Alberta basin at Pine Point.

3.7. Tables

Table 3.1

Core Letter	Core Name	Core Location	Northing	Westing	Depth (m)	$^{87}Sr/^{86}Sr$	δ^{26}Mg Dolomite (‰) DSM3
A	CPG Minton	03-17-03-21W-2M	49.205	-104.801	2811	0.708445	-1.65
B	Imperial Hummingbird	06-13-02-19W2	49.122	-104.424	3031	0.708463	-1.55
C	Dome Arrow River	12-10-14-25WPM	50.175	-100.801	1223	0.708326	-1.45
D	Dome Brandon	03-05-09-19WPM	49.711	-100.003	1020	0.708270	-1.31
E	Dome Pelican Lake	07-34-04-15WPM	49.346	-99.396	1002	0.708177	-1.64
F	Tyndall Stone	Garson Quarry	50.103	-96.609	Outcrop	0.708144	-1.46
G	ND 10624	NESE 9-163-102	48.958	-103.928	3223	0.708319	-1.42
H	ND 7631	NENE 33-151-99	47.861	-103.350	4289	0.708945	-1.59
I	ND 7362	NESW 13-155-91	48.246	-102.323	3948	0.708535	-1.80
J	ND 8803	NENE 22-151-80	47.890	-100.888	2399	0.708057	-1.69
K	ND 9033	NESW 4-142-102	47.142	-103.619	3832	0.708832	-1.65
L	ND 8088	NWNE 28-141-93	47.008	-102.470	3587	0.708675	-1.89
M	ND 8553	SENW 17-140-82	46.944	-101.063	2421	0.708260	-1.77
N	ND 7146	NWNE 15-136-75	46.602	-100.092	1421	0.708278	-1.44
O	ND 6272	LT2 22-137-106	46.670	-104.041	3245	0.708426	-1.83
P	ND 8549	SESE 16-134-87	46.417	-101.614	2530	0.708200	-1.80
Q	ND 14491	NWNE 27-130-102	46.061	-103.419	2902	0.708295	-1.44

Strontium isotope data for dolomitized burrow samples, and calculated dolomite Mg isotope end-member data for each sampled core.

Table 3.2 (part 1 of 2)

Core Letter	Core Name	Sample	Sample Type	N	δ^{26}Mg (‰ DSM3)	2se	δ^{25}Mg (‰ DSM3)	2se	$^{87}Sr/^{86}Sr$	2se	Ca/Mg (mol/mol)	Mg/Ca (mol/mol)	Sr/Ca (mmol/mol)	Sr/Mg (mmol/mol)
A	CPG Minton	1	Matrix	3	-1.97	0.02	-1.02	0.01	0.708017	0.000003	18.4	0.054	0.225	4.14
		2	Matrix	3	-1.74	0.03	-0.89	0.01			5.92	0.169	0.186	1.10
		3	Burrow	3	-1.67	0.02	-0.88	0.01	0.708445	0.000015	1.33	0.752	0.106	0.141
		4	Burrow	3	-1.64	0.02	-0.87	0.01			1.32	0.758	0.104	0.137
B	Imperial Hummingbird	1	Burrow	3	-1.55	0.02	-0.79	0.01	0.708463	0.000007	1.40	0.717	0.102	0.142
		2	Burrow	4	-1.56	0.03	-0.81	0.02			2.12	0.471	0.154	0.327
		3	Matrix	4	-1.86	0.04	-0.97	0.02	0.707967	0.000004	12.8	0.078	0.224	2.85
		4	Matrix	4	-1.66	0.02	-0.86	0.01			3.87	0.258	0.161	0.624
C	Dome Arrow River	1	Matrix	4	-1.64	0.06	-0.86	0.04	0.707963	0.000003	12.4	0.081	0.291	3.61
		2	Matrix	2	-1.54	0.14	-0.79	0.09			5.30	0.189	0.205	1.09
		2rep	Matrix	4	-1.54	0.04	-0.80	0.03						
		3	Burrow	4	-1.42	0.04	-0.74	0.04	0.708326	0.000005	1.25	0.798	0.098	0.122
		4	Burrow	3	-1.47	0.04	-0.78	0.03			1.36	0.733	0.162	0.220
D	Dome Brandon	1	Matrix	4	-1.71	0.04	-0.89	0.02			32.4	0.031	0.122	3.95
		1fullrep	Matrix	3	-1.74	0.06	-0.91	0.03						
		2	Matrix	3	-1.40	0.03	-0.74	0.02			8.56	0.117	0.106	0.904
		3	Matrix	3	-1.80	0.06	-0.94	0.05	0.708116	0.000012	38.9	0.026	0.114	4.42
		4	Burrow	4	-1.30	0.05	-0.68	0.02	0.708270	0.000009	1.98	0.504	0.093	0.185
		5	Burrow	3	-1.34	0.04	-0.66	0.01			1.98	0.506	0.083	0.164
		6	Burrow	4	-1.35	0.03	-0.71	0.02			2.40	0.417	0.095	0.228
E	Dome Pelican Lake	1	Matrix	3	-2.20	0.06	-1.17	0.05			42.2	0.024	0.334	14.1
		2	Matrix	3	-2.73	0.06	-1.42	0.02	0.707959	0.000009	74.7	0.013	0.266	19.9
		2rep	Matrix	3	-2.72	0.04	-1.41	0.01						
		3	Matrix	3	-1.92	0.12	-1.00	0.05			16.6	0.060	0.294	4.87
		3rep	Matrix	3	-1.94	0.06	-1.01	0.02						
		4	Burrow	3	-1.59	0.06	-0.85	0.05	0.708176	0.000007	2.30	0.435	0.170	0.390
		4rep	Burrow						0.708178	0.000009				
		5	Burrow	4	-1.65	0.03	-0.88	0.02			2.16	0.463	0.161	0.349
		6	Burrow	4	-1.71	0.04	-0.89	0.03			2.24	0.446	0.166	0.372
F	Tyndall Stone	1	Burrow	4	-1.52	0.03	-0.81	0.02	0.708184	0.000010	1.21	0.824	0.079	0.096
	(Garson Quarry)	2	Matrix	4	-2.16	0.03	-1.13	0.01	0.707974	0.000007	67.3	0.015	0.133	8.92
		3	Burrow	4	-1.48	0.04	-0.76	0.04	0.708127	0.000008	1.27	0.789	0.097	0.123
		4	Matrix	4	-2.10	0.05	-1.09	0.03	0.707975	0.000010	63.9	0.016	0.147	9.41
		5	Burrow	4	-1.37	0.03	-0.74	0.02	0.708144	0.000010	1.12	0.892	0.092	0.103
		6	Matrix	4	-1.98	0.06	-1.05	0.04	0.707971	0.000006	49.3	0.020	0.138	6.79
G	ND 10624	3	Matrix	4	-1.44	0.05	-0.76	0.03			2.93	0.342	0.148	0.433
		4	Matrix	4	-1.71	0.06	-0.90	0.04	0.708087	0.000005	11.6	0.086	0.184	2.14
		5	Burrow	4	-1.45	0.03	-0.75	0.02			1.36	0.737	0.093	0.127
		6	Burrow	3	-1.35	0.04	-0.70	0.04	0.708319	0.000010	1.20	0.837	0.087	0.104
H	ND 7631	1	Burrow	4	-1.63	0.03	-0.83	0.03	0.708945	0.000004	1.42	0.703	0.087	0.124
		2	Matrix	4	-2.18	0.03	-1.14	0.03	0.708198	0.000008	41.0	0.024	0.209	8.57
		3	Matrix	3	-1.94	0.03	-1.02	0.02	0.708137	0.000016	31.8	0.031	0.215	6.85
		4	Burrow	3	-1.58	0.01	-0.82	0.04	0.708612	0.000008	1.17	0.857	0.068	0.080
I	ND 7362	1	Matrix	3	-1.91	0.11	-0.99	0.06			7.01	0.143	0.249	1.74
		1rep	Matrix	3	-1.95	0.05	-1.02	0.03						
		2	Matrix	3	-1.83	0.04	-0.95	0.01			2.77	0.361	0.201	0.557
		3	Matrix	3	-2.02	0.07	-1.03	0.05	0.707942	0.000004	12.1	0.083	0.303	3.67
		4	Burrow	3	-1.80	0.05	-0.93	0.03			1.77	0.566	0.159	0.281
		4rep	Burrow	3	-1.86	0.03	-0.97	0.01						
		5	Burrow	3	-1.75	0.04	-0.90	0.02	0.708535	0.000005	1.35	0.743	0.109	0.146
		6	Burrow	3	-1.90	0.05	-0.97	0.03			3.08	0.324	0.219	0.675

Table 3.2 (part 2 of 2)

Core Letter	Core Name	Sample	Sample Type	N	δ^{26}Mg (‰ DSM3)	2se	δ^{25}Mg (‰ DSM3)	2se	$^{87}Sr/^{86}Sr$	2se	Ca/Mg (mol/mol)	Mg/Ca (mol/mol)	Sr/Ca (mmol/mol)	Sr/Mg (mmol/mol)
J	ND 8803	1	Matrix	4	-1.85	0.01	-0.95	0.02			11.3	0.088	0.276	3.13
		2	Matrix	4	-2.27	0.06	-1.19	0.03	0.707947	0.000006	36.1	0.028	0.328	11.8
		3	Matrix	3	-1.98	0.04	-1.03	0.02			19.4	0.051	0.356	6.91
		4	Burrow	3	-1.71	0.07	-0.89	0.04	0.708057	0.000003	1.80	0.556	0.180	0.324
		5	Burrow	4	-1.74	0.03	-0.92	0.02			2.12	0.472	0.210	0.445
		6	Burrow	3	-1.69	0.09	-0.89	0.03			2.16	0.462	0.179	0.388
		6rep	Burrow	3	-1.68	0.01	-0.88	0.02						
K	ND 9033	1	Matrix	4	-1.78	0.01	-0.92	0.01		0.000015	10.4	0.096	0.527	5.48
		2	Matrix	4	-2.01	0.04	-1.04	0.02			26.1	0.038	0.402	10.47
		3	Burrow	4	-1.66	0.02	-0.89	0.01	0.708832	0.000010	1.19	0.839	0.096	0.115
		4	Burrow	4	-1.65	0.04	-0.88	0.02			1.21	0.824	0.100	0.121
L	ND 8088	1	Matrix	3	-2.12	0.01	-1.11	0.00			12.8	0.078	0.371	4.73
		2	Matrix	3	-2.76	0.06	-1.45	0.05			47.9	0.021	0.464	22.20
		3	Matrix	4	-2.84	0.06	-1.47	0.05	0.708093	0.000005	54.5	0.018	0.495	26.98
		4	Burrow	4	-1.90	0.06	-0.98	0.03			1.47	0.682	0.111	0.162
		4rep	Burrow	4	-1.94	0.05	-1.01	0.02						
		5	Burrow	4	-1.88	0.04	-0.98	0.01			2.99	0.335	0.242	0.724
		6	Burrow	4	-1.90	0.05	-0.99	0.04	0.708675	0.000005	1.33	0.752	0.101	0.135
M	ND 8553	1	Matrix	3	-1.86	0.06	-0.96	0.01			16.6	0.060	0.221	3.67
		2	Matrix	3	-2.06	0.07	-1.09	0.03			22.8	0.044	0.270	6.14
		3	Matrix	4	-2.35	0.06	-1.22	0.04	0.707979	0.000005	40.4	0.025	0.251	10.1
		4	Burrow	4	-1.86	0.05	-0.96	0.03			1.47	0.680	0.141	0.207
		5	Burrow	4	-1.81	0.04	-0.92	0.02			2.67	0.375	0.200	0.533
		6	Burrow	4	-1.75	0.04	-0.89	0.02	0.708260	0.000007	1.33	0.753	0.114	0.151
N	ND 7146	1	Matrix	3	-2.84	0.08	-1.48	0.02			97.0	0.010	0.186	18.0
		1rep	Matrix	3	-2.88	0.05	-1.50	0.03						
		2	Matrix	4	-3.03	0.02	-1.58	0.02	0.708013	0.000010	113.3	0.009	0.244	27.6
		3	Matrix	4	-1.53	0.06	-0.79	0.04			7.19	0.139	0.166	1.19
		4	Burrow	3	-1.41	0.11	-0.73	0.03			1.49	0.671	0.132	0.196
		4rep	Burrow	3	-1.51	0.01	-0.79	0.02						
		5	Burrow	3	-1.44	0.09	-0.75	0.04			3.35	0.298	0.151	0.507
		5rep	Burrow	3	-1.53	0.01	-0.80	0.02						
		6	Burrow	3	-1.40	0.06	-0.74	0.03	0.708278	0.000015	1.21	0.827	0.141	0.170
O	ND 6272	1	Matrix Burrow Mix	4	-2.06	0.03	-1.08	0.02			18.0	0.055	0.279	5.04
		2	Matrix	4	-3.14	0.03	-1.62	0.03	0.708109	0.000026	81.1	0.012	0.263	21.3
		3	Matrix	4	-2.77	0.02	-1.46	0.02			64.1	0.016	0.284	18.2
		4	Burrow	4	-1.82	0.04	-0.94	0.02			1.74	0.574	0.102	0.179
		5	Burrow	4	-1.90	0.02	-0.98	0.01	0.708426	0.000014	1.63	0.615	0.113	0.184
P	ND 8549	1	Matrix	4	-1.85	0.06	-0.94	0.02			6.94	0.144	0.220	1.53
		2	Matrix	4	-2.00	0.02	-1.05	0.02			12.2	0.082	0.260	3.17
		3	Matrix	4	-2.71	0.02	-1.42	0.03	0.708035	0.000007	56.5	0.018	0.252	14.24
		4	Burrow	3	-1.81	0.05	-0.94	0.05			2.14	0.467	0.185	0.396
		5	Burrow	3	-1.78	0.11	-0.91	0.08			1.63	0.613	0.148	0.241
		5rep	Burrow	4	-1.80	0.05	-0.93	0.02						
		6	Burrow	4	-1.84	0.04	-0.95	0.03	0.708200	0.000006	1.37	0.732	0.144	0.197
Q	ND 14491	2	Matrix Burrow Mix	4	-2.90	0.05	-1.51	0.01			76.1	0.013	0.286	21.8
		3	Matrix	3	-2.63	0.00	-1.36	0.02	0.707977	0.000006	65.7	0.015	0.226	14.8
		4	Matrix	3	-2.04	0.03	-1.06	0.01			33.9	0.029	0.229	7.77
		5	Burrow	4	-1.48	0.03	-0.76	0.01			1.74	0.575	0.131	0.229
		6	Burrow	4	-1.43	0.04	-0.76	0.03	0.708295	0.000007	1.71	0.585	0.143	0.244
		6rep	Burrow	4	-1.48	0.07	-0.77	0.05						

Core and outcrop data including sample ID, type, number of Mg isotope analyses, Mg isotope values and errors, Sr isotope values and errors, Ca/Mg, Mg/Ca, Sr/Ca, and Sr/Mg molar ratios. Replicate samples (Nrep) are sample solutions that have been analyzed in a separately tuned instrument session, these are indicated above for both Mg and Sr. Core D - Dome Brandon (1fullrep) was a full procedural replicate sample.

Table 3.3

Sample ID	Well Name	Field	Formation	Northing	Westing	$^{87}Sr/^{86}Sr$	se	$\delta^{26}Mg$ (‰) DSM3	2se	Ca (ppm)	Mg (ppm)
UofA-9822	Mott #32X-3	Newporte	Deadwood	48.977	-101.939	0.721181	0.000008	-0.24	0.02	31400	2140
UofA-9823	Larson #23X-9	Newporte	Deadwood	48.957	-101.969	0.721835	0.000010	-0.44	0.05	35300	2160
UofA-9810	Berkley et al.	Midale	Winnipeg			0.714804	0.000008	0.03	0.06	8450	908
UofA-9824	Berkley et al.	Midale	Winnipeg	49.490	-103.443	0.715240	0.000007	-0.04	0.04	10900	1030
UofA-9965B	Drawbond 9 #3	Skjermo	Red River C	48.958	-103.928	0.708688	0.000012	-0.50	0.03	34200	3510
UofA-01-111A	EIDE #35-11R	Juniper	Red River C	47.680	-103.318	0.708998	0.000010	-0.60	0.05	36100	2200

Strontium and Mg isotope data and Ca and Mg concentrations for Deadwood, Winnipeg, and Red River Formation waters.

TRANSITION BETWEEN CHAPTERS 3 AND 4

As Chapters 2 and 3 have demonstrated, Mg isotopes can serve as powerful tracers of geological processes, particularly with dolomitization associated with subsurface fluid-flow. As Mg isotopes have the ability to trace subsurface fluid migration in the Williston Basin, so do they have the potential to serve as a useful tracer of paleo-ocean chemistry and ecology. Whole-rock carbonate successions may record changes in the δ^{26}Mg value of seawater and overall seawater chemistry, as well as serve as recorders for fluctuations in the primary carbonate producers of the geological past. There are certain pitfalls, however, that must and will be evaluated. Foremost among these is the role of carbonate diagenesis impacting the ability of Mg isotopes to serve as a reliable tracer of ocean Mg secular variation in whole-rock carbonates. Chapter 4 will explore the feasibility and address the preservation potential of whole-rock carbonates as archives for recording secular variation in seawater δ^{26}Mg values through a geologically interesting interval of Earth history, the Late Ordovician (Hirnantian) glaciation and mass extinction event.

CHAPTER 4 – Magnesium isotope tracing of local-scale oscillations of aragonite and calcite precipitation during the Hirnantian glaciation event in Nevada

Published as:

Kimmig S. R. and Holmden C. (2017) Multi-proxy geochemical evidence for primary aragonite precipitation in tropical-shelf 'calcite sea' during the Hirnantian glaciation. *Geochim. Cosmochim. Acta.* **206**, 254–272.

4.1. Abstract

A positive excursion in sedimentary δ^{26}Mg values (2–3‰) is recorded in a mud dominated carbonate succession spanning the Hirnantian glaciation event in a tropical-shelf sea in Nevada. The increase is coincident with lithofacies and biofacies indicators of sea-level change, and previously reported changes in sedimentary δ^{13}C and $\delta^{44/40}$Ca values in the same section. The synchronousness of the isotopic changes is inconsistent with differences in the oceanic residence times of Mg (13 Myr), Ca (0.5–1 Myr), and C (0.1 Myr), indicating that the isotopic trends cannot be attributed to perturbations in the oceanic cycling of these elements. Instead, a mixing analysis (δ^{26}Mg *vs.* Ca/Mg) reveals that the stratigraphic shift in sedimentary δ^{26}Mg values is an artifact of changing dolomite abundance in the carbonate succession, which increases by an average of ~ 12 mol% during the glaciation. The mixing analysis also uncovers stratigraphic changes in end-member limestone δ^{26}Mg values that are tentatively attributed to variations in aragonite abundance. The aragonite, which inverted to calcite during diagenesis, accumulated during the glacio-eustatically controlled sea-level lowstand in the study setting. Although this interpretation is vulnerable to diagenetic effects that are difficult to evaluate, it is strengthened by shifts to lower $\delta^{44/40}$Ca values and higher δ^{13}C values in the same section. Experiments show that aragonite can precipitate in seawater with the chemistry of a 'calcite sea' at temperatures above 20–23ºC. Considering the warm climates of the early Paleozoic, temperatures above this range were likely common in low latitudes. This study shows that the isotopes of Mg, Ca, and C have the potential to fingerprint aragonite that has inverted to calcite in the rock record. It is important recognize carbonate successions where this has occurred so as to avoid misinterpreting facies-dependent changes in carbonate polymorph mineralogy as genuine records of secular changes in the elemental and isotopic geochemistry of seawater.

4.2. Introduction

Two periods of 'aragonite seas' and two periods of 'calcite seas' occurred during Phanerozoic time (Sandberg, 1983). These oscillations in the mineralogy of inorganically precipitated carbonate are attributed to secular changes in the Mg/Ca ratio of seawater, with a high Mg/Ca ratio favoring precipitation of aragonite and a low Mg/Ca ratio favoring calcite (Hardie, 1996; Stanley and Hardie, 1998). The present-day 'aragonite sea' is characterized by a seawater Mg/Ca ratio of 5.2 (mol/mol), whereas 'calcite seas' formed when seawater Mg/Ca ratios decreased below 2.0 (Hardie, 1996) or 1.0 (Wilkinson and Algeo, 1989). Controls over aragonite/calcite precipitation are complex and exclusive 'calcite sea' scenarios may be rare in the geological past, even when the seawater Mg/Ca ratio was low. Variations in temperature (Burton and Walter, 1987; Morse et al., 1997), dissolved SO_4^{2-} concentration (Bots et al., 2011), alkalinity, and *p*CO2 (Lee and Morse, 2010; Wilkinson and Given, 1986) may, in addition to the Mg/Ca ratio, also influence whether calcite, aragonite, or a mixture of the two will precipitate (Wilkinson et al., 1984). True 'calcite seas' appear to require temperatures below 15–21ºC (Balthasar and Cusack, 2015), which is lower than sea surface temperatures in the tropics today, and likely in the warmer climates of the geological past as well. Considering temperature alone, aragonite should have precipitated in the early Paleozoic 'calcite sea', and yet it is rarely reported in marine carbonates older than the Mesozoic. The reason is that aragonite is metastable, and has a strong tendency to invert to calcite over geological time. Therefore, incidences of primary aragonite must be interpreted from petrographic and geochemical evidence preserved in secondary calcite (e.g., Bathurst, 1975; Brand and Veizer, 1980; Mazzullo, 1980; Given and Lohmann, 1985; Sandberg, 1985).

In this chapter, a mixing analysis is employed using δ^{26}Mg values and Ca/Mg ratios that has the potential to uncover deposits of aragonite that have inverted to calcite during diagenesis. It is based on the assumption that aragonite will record higher δ^{26}Mg values than either high magnesium calcite (HMC) or low magnesium calcite (LMC) (Chang et al., 2004; Wombacher et al., 2006, 2011; Pogge von Strandmann, 2008; Hippler et al., 2009; Yoshimura et al., 2011; Saenger and Wang, 2014). The technique is applied to a succession of Late Ordovician carbonate mud spanning the Hirnantian glaciation and mass extinction event in the Monitor Range section of Nevada (Finney et al., 1999). A stratigraphic change in limestone δ^{26}Mg values is revealed

through the mixing analysis that cannot be attributed to the very small quantity of dolomite scattered throughout the deposit. With help from previously published data on sedimentary carbonate $\delta^{44/40}Ca$ and $\delta^{13}C$ values in the study section (Finney et al., 1999; LaPorte et al., 2009; Holmden et al., 2012a), and a re-evaluation of Sr/Ca ratios, a case is made for aragonite having precipitated in this tropical-shelf setting during the glacio-eustatically controlled sea-level lowstand.

4.3. Stratigraphy, lithofacies, and depositional setting of the study section

The Monitor Range section (Finney et al., 1997; 1999) is a composite section assembled from outcrops of the Hanson Creek Formation in two locations along the Martin Ridge in Nevada (Fig. 4.1). The topmost 120 m of the Copenhagen Canyon section is the subject of the present study, which covers the stratigraphic interval containing the Hirnantian glaciation and mass extinction event (Fig. 4.2). Here, the carbonates are predominantly composed of carbonate mud deposited in the quiet waters of the Martin Ridge Basin, which Dunham (1977) described as a bathymetric low that was ~ 100 m deeper than the surrounding carbonate platform. The absence of bioturbation indicates that oxygen levels were low in the bottom waters of the basin, and that carbonate mud was likely transported into the basin from surrounding shallow water carbonate factories (LaPorte et al., 2009). Stratigraphically equivalent carbonates of the Lone Mountain section are coarser-grained, indicating deposition in a wave-agitated setting, and have been pervasively dolomitized (Finney et al., 1997). By contrast, the Monitor Range section is predominantly limestone.

The sea-level curve for the Monitor Range section (Fig. 4.2) is based on the occurrence of graptolites and other fossils in the section, as well as the stratigraphic succession of lithofacies. A deepening event occurs at approximately 148 m, immediately prior to the sea-level fall that marks the beginning of the Hirnantian glaciation (Finney et al., 1997; 1999; 2007). The drop in sea-level is nearly synchronous with an increase in sedimentary carbonate $\delta^{13}C$ values (Finney et al., 1999) and a decrease in $\delta^{44/40}Ca$ values (Holmden et al., 2012a). The maximum sea-level lowering is marked by an exposure surface at ~ 187 m, which is overlain by wave-rippled fine quartz sand (Finney et al., 1997; 1999). The post-glacial sea-level rise is marked by a fining upward sequence of packstones, wackestones, and lime mudstones (Finney et al., 1997). The sea-level fall occurs near the base of the *Normalograptus extraordinarius* Biozone, and the post-glacial sea-level rise

in the mid-Upper *N. persculptus* Biozone (Fig. 4.2) (LaPorte et al., 2009). The duration of the glaciation is estimated to be 1.03 ± 0.2 Myr based on the most recent time scale of Cooper and Sadler (2012), which is constrained by two graptolite zones as described in Holmden et al. (2012a).

4.4. Sampling and analytical methods

The Mg isotope measurements were performed on aliquots of the same powders prepared from whole-rock carbonates collected and analyzed for sedimentary inorganic C isotopes by Finney et al. (1999), organic C and N isotopes by LaPorte et al. (2009), and Ca isotopes by Holmden et al. (2012a). Approximately 5 mg of carbonate powder was dissolved by the addition of 0.5N HCl until effervescence ceased. The supernate was decanted and the residue tested with a few drops of 6N HCl to ensure that any dolomite in the sample was fully digested by the acid attack. The supernate was dried on a hot plate and then resolubilized in 0.3N HNO_3 to create a stock solution. Sample solutions were analyzed for Ca, Mg, and Sr concentrations by ICP-AES at the Saskatchewan Research Council with an external precision of better than 10% (2σ). The Sr/Ca ratios are reported in units of mmol/mol, Ca/Mg and Mg/Ca ratios in units of mol/mol (Table 4.1).

Aliquots of digested carbonate solutions were purified prior to mass spectrometry using gravity-flow cation exchange columns packed with 2 ml of Bio-Rad® AG® MP-50 resin. The Mg samples were eluted through two sets of cation exchange columns, the first elution performed with 1N HCl and a second stage elution for further purification of Mg with 1N HNO_3. Column cuts were taken before and after each Mg elution to ensure that > 98% of the Mg was collected in order to avoid imparting isotopic fractionation effects to the samples from the purification procedure (Chang et al., 2003).

A Thermo Scientific Neptune MC-ICP-MS instrument, housed in the Saskatchewan Isotope Laboratory, was used to perform the Mg isotope analyses using a cyclonic glass spray chamber for sample introduction. Samples of approximately 1 ppm Mg (dissolved in 0.3N HNO_3) were measured with an uptake rate of 100 μl/min using the low-resolution source-slit, yielding 8–10V signals on mass 24. Measurements utilized a standard-sample bracketing technique with sample intensities matched to within ± 5% of the intensity of the bracketing standard DSM3 (Galy et al., 2003) to correct for instrumental mass fractionation (Galy et al., 2001). The quality of the measurements was monitored using an interlaboratory standard (CAM1) and an in-house mono-elemental standard solution (Mg Alfa Aesar Specpure), which is isotopically distinct from CAM1

(Table 1). Full procedural blanks, with measured Mg concentrations < 16 ppb (n = 4), and additional aliquots of CAM1 were also passed through the same ion exchange columns.

The $^{26}Mg/^{24}Mg$ and $^{25}Mg/^{24}Mg$ ratios are reported in the conventional delta notation as permil (‰) deviations of the sample isotope ratios relative to the measured standard (DSM3) using Eq. (4.1), where x = 25 or 26. The external reproducibility of measurements is ± 0.08‰ (2σ) for $\delta^{26}Mg$ and ± 0.04‰ (2σ) for $\delta^{25}Mg$, determined from analyses of the CAM1 standard representing 123 separately tuned mass spectrometry sessions. Uncertainties associated with the measurements of samples within the same mass spectrometry session are reported as two standard errors of the mean (2se).

$$\delta\ ^{x}Mg_{smp} = \left(\frac{\left(\ ^{x}Mg/^{24}Mg\right)_{smp}}{\left(\ ^{x}Mg/^{24}Mg\right)_{DSM3}} - 1\right) \times 1000 \qquad (4.1)$$

Seawater purchased from OSIL (North Atlantic Seawater) was processed using the same procedure as the samples, yielding a $\delta^{26}Mg$ value of –0.79‰ ± 0.08 (2σ n = 18). This value falls within the uncertainty of the average seawater $\delta^{26}Mg$ value measured in other laboratories of –0.83 ± 0.09‰ (e.g., Chang et al., 2003; Young and Galy, 2004; de Villiers et al., 2005; Tipper et al., 2006a; Foster et al., 2010; Ling et al., 2011).

X-ray diffraction analyses were performed using a PANalytical Empyrean XRD housed in the Department of Geological Sciences, University of Saskatchewan, using a cobalt radiation source (40kV and 45 mA). The sample stage was rotated at a rate of 2 rpm with a step size of 0.0167º and a dwell time of 135 ms.

4.5. Results

The Monitor Range section exhibits a 2–3‰ positive excursion in whole-rock carbonate $\delta^{26}Mg$ values. The stratigraphic timing of the excursion occurs nearly synchronously with the previously described positive $\delta^{13}C$ and the negative $\delta^{44/40}Ca$ excursions in the section.

The $\delta^{26}Mg$ values in the peak interval of the excursion correlate strongly with Ca/Mg ratios (Fig. 4.3a). The observed linear trend is a characteristic of two-component mixing. Petrographic analysis reveals small amounts of dolomite in the limestone (Fig. 4.4), including a more pervasively dolomitized interval at ~ 151 m seen in Figure 4.2. This serves as evidence that the correlation between $\delta^{26}Mg$ and Ca/Mg (Fig. 4.3a) is due to mixing between dolomite and calcite.

Substituting Ca/Mg (mol/mol) of 1.0 into the best-fit equation of the line yields a δ^{26}Mg value of –1.66‰ for the stoichiometric dolomite end-member. There is no theoretically fixed ratio of Mg/Ca to assign to the calcite end-member. The predicted δ^{26}Mg value of the limestone is therefore sensitive to the Mg/Ca ratio used in the calculation, which is dependent on many factors, including: (1) original carbonate mineralogy; (2) pH, salinity, and temperature of seawater; (3) vital effects influencing the Mg distribution coefficient; (4) secular variation of the seawater Mg/Ca ratio; and (5) carbonate diagenesis (Folk, 1965; Veizer, 1983; Oomori et al., 1987; Stanley and Hardie, 1998; Lea et al., 1999; Ferguson et al., 2008; Yoshimura et al., 2011). Re-plotting δ^{26}Mg against Mg/Ca (rather than Ca/Mg) yields the hyperbolic form of the mixing relationship. From this plot, the Mg/Ca ratio of the limestone end-member (LMC) may be asymptotically constrained to ~ 0.015 (Fig. 4.3b), determined by visual inspection with the help of a model curve fitted to the data using Equation 4.2 (Langmuir et al., 1978; Capo et al., 1998; Stewart et al., 1998). The subscripts *m* in Equation 4.2 represent the mixed composition of the whole-rock carbonate, *A* is the dolomite, *B* is the limestone, and superscript *c* identifies concentrations of Mg and Ca (μmol/g).

$$\delta^{26}\mathrm{Mg_m} = \frac{\mathrm{Mg_A^c Mg_B^c}\left(\delta^{26}\mathrm{Mg_B} - \delta^{26}\mathrm{Mg_A}\right)}{\left(\frac{\mathrm{Mg}}{\mathrm{Ca}}\right)_\mathrm{m}\left(\mathrm{Mg_A^c Ca_B^c} - \mathrm{Mg_B^c Ca_A^c}\right)} + \frac{\mathrm{Mg_A^c Ca_B^c}\,\delta^{26}\mathrm{Mg_A} - \mathrm{Mg_B^c Ca_A^c}\,\delta^{26}\mathrm{Mg_B}}{\left(\mathrm{Mg_A^c Ca_B^c} - \mathrm{Mg_B^c Ca_A^c}\right)} \qquad (4.2)$$

Substituting Mg/Ca of 0.015 (equivalent to Ca/Mg of 66.7) into the best-fit equation for the line on the δ^{26}Mg *vs*. Ca/Mg diagram (Fig. 4.3a) yields a calcite (limestone) end-member δ^{26}Mg value of –2.54 ± 0.23‰ (2σ) for the sea-level lowstand deposit (Table 4.2).

Two additional dolomite-calcite mixtures are plotted in Figure 4.3a. One is for carbonate deposited before the Hirnantian glaciation, and the other for carbonate deposited after the glaciation. These mixing lines are anchored by the same composition of dolomite (δ^{26}Mg = –1.66‰) as determined for the sea-level lowstand carbonates, but the slope is slightly steeper for carbonates deposited after the Hirnantian glaciation, and much steeper for carbonates deposited before the glaciation. This difference in slope implies a variation in the δ^{26}Mg value for the limestone end-members in the study section. The slope-uncertainties are higher for the sea-level highstand mixing lines, which prohibits using the asymptotic approach for determining end-member Ca/Mg ratios for these units. Therefore, Ca/Mg ratios were assigned that are 10% higher than the highest measured Ca/Mg ratio along each mixing line. Substituting Ca/Mg ratios of 69.9 and 67.8 into their respective equations for the best-fit lines yields δ^{26}Mg values of –4.45 ± 0.82‰

(2σ) for pre-glacial limestone, and –3.05 ± 0.27‰ (2σ) for post-glacial limestone (Table 4.2). The uncertainty estimates are based on the error envelopes for the regressions (Fig. 4.3a) determined using GEODATE software (Eglington and Harmer, 1999).

The mixing lines can also be used to determine the amount of dolomite in each sample. First, the individual data points are orthogonally projected onto their respective average mixing lines (Moore et al., 2013) using Equations 4.3 and 4.4 (Fig. 4.3c; Table 4.3), where *m* and *b* are the slopes and the *y*-intercepts of the original linear regressions, respectively, while X_i and Y_i denote the coordinates of the initial measured data points and X_p and Y_p denote the projected coordinates.

$$X_p = (X_i + m * Y_i - m * b)/(m^2 + 1) \tag{4.3}$$

$$Y_p = m * X_p + b \tag{4.4}$$

Second, the amount of dolomite is determined using Equation 4.5 (Langmuir et al., 1978; Capo et al., 1998; Stewart et al., 1998) where X_A is the mole fraction of dolomite in the whole-rock carbonate, M_A is the moles of dolomite, M_m is the moles of whole-rock carbonate, the subscripts *m* used in Equation 4.5 represents the mixed composition of the whole-rock carbonate, *A* is the dolomite, *B* is the limestone, and superscript *c* identifies concentrations of Mg and Ca (μmol/g).

$$X_A = \frac{M_A}{M_m} = \frac{Mg_B^c \delta^{26}Mg_B - \left(\frac{Mg}{Ca}\right)_m \delta^{26}Mg_m Ca_B^c}{\left(\frac{Mg}{Ca}\right)_m \delta^{26}Mg_m (Ca_A^c - Ca_B^c) + Mg_B^c \delta^{26}Mg_B - Mg_A^c \delta^{26}Mg_A} \tag{4.5}$$

The mole fraction of dolomite in the study section varies between 0.27 mol% and 83.0 mol% with most of the carbonates containing < 10 mol% (Table 4.1, Fig. 4.2).

X-ray diffraction (XRD) analyses were performed to test for aragonite in six samples (K11, K20, K31, K35, K38.5, and K49). The most prominent aragonite peaks are expected at 111 and 221, which are found at 30.56º and 53.78° 2θ respectively. No aragonite was detected in any of the samples.

4.6. Discussion

The stratigraphic timing of the Mg isotope changes occurs nearly synchronously with previously described positive and negative excursions in the respective $\delta^{13}C$ and $\delta^{44/40}Ca$ profiles in the study section. All three geochemical proxies track lithofacies indicators of sea-level change (attributed to continental ice-volume change) during the Hirnantian glaciation. The ~ 1.03 Myr

duration of the glaciation is short compared to the residence time of Mg in the modern ocean of ~ 13 Myr (Broecker and Peng, 1982), thus ruling out a glacial-age perturbation of the ocean Mg-cycle as an explanation for the change in (dolomite-corrected) limestone δ^{26}Mg values. Holmden et al. (2012a) reached the same conclusion for the origin of the negative $\delta^{44/40}$Ca excursion, based on an oceanic residence time for Ca of 0.5–1.0 Myr (Milliman, 1993; Holmden et al., 2012b). The magnitude of the 7‰ δ^{13}C excursion is likewise too large to reflect a perturbation of ocean C-cycling during the glaciation (Melchin and Holmden, 2006; LaPorte et al., 2009). Therefore, other phenomena must be explored to be able to explain these findings. Generally, they fall into three categories: (1) local element-cycling effects in circulation restricted settings, (2) mineralogical effects, and (3) diagenetic effects, while bearing in mind that local-scale changes in one or more of these effects can be replicated in shallow marine settings across the globe if a eustatic sea-level change is driving the local changes (Holmden et al., 1998; Immenhauser et al., 2003; 2008; Swart, 2008).

4.6.1. Multi-proxy evidence for secular-change in carbonate polymorph mineralogy or stratigraphic-change in diagenetic outcomes

4.6.1.1. Mg isotopes

The apportionment calculations reveal that a ~ 12 mol% increase in the average dolomite content of the limestone is enough to cause the observed 2–3‰ positive excursion in whole-rock carbonate δ^{26}Mg values in the Monitor Range section during the Hirnantian glaciation (Fig. 4.2). Less than 0.2 mol% dolomite is needed to shift the δ^{26}Mg value of the limestone by an amount that is slightly greater than the analytical uncertainty of the Mg isotope analyses (± 0.08‰). These findings reveal that small amounts of dolomite can effectively overprint δ^{26}Mg values of whole-rock limestone.

The dolomite problem was solved by dividing the studied carbonate succession into three contiguous stratigraphic units (or bins) using the δ^{26}Mg *vs.* Ca/Mg diagram (Fig. 4.3a), where linear trends reveal evidence for mixing between dolomite and limestone. Three mixing lines with different slopes converge on a single composition of dolomite (Ca/Mg = 1.0), yielding a high δ^{26}Mg value of –1.66‰; and three compositions of limestone, yielding –4.45‰ before the glaciation, –2.54‰ during the glaciation, and –3.05‰ after the glaciation (Table 4.2).

The ~ 2‰ range in δ^{26}Mg values is large enough to reflect changes in the mineralogy of the carbonate sediment deposited over the time frame of the glaciation. The general pattern of ^{26}Mg-enrichment is aragonite > HMC > LMC in modern marine carbonates (Fig. 4.5a). There are notable exceptions, particularly among the biological producers of LMC. Consider the fractionation between inorganically precipitated aragonite and calcite ($\Delta_{\mathrm{LMC}}^{\mathrm{aragonite}}$) of ~ 1.4‰ (at 25ºC) (Fig. 4.5b) (Wang et al., 2013; Li et al., 2012). This increases to 3.0–4.0‰ when substituting LMC precipitated by foraminifera, which exhibit some of the lowest δ^{26}Mg values of any marine carbonate formed in the present day. Although the difference is large, the heavy-isotope enrichment pattern remains the same as in the abiotic precipitation experiments (aragonite > calcite). Coccolithophorids are counterexamples to the rule, producing LMC with δ^{26}Mg values that overlap abiotically produced aragonite (Fig. 4.5a) (Ra et al., 2010; Wombacher et al., 2011; Saenger and Wang, 2014). Fortunately, these calcifying plankton did not evolve until the Mesozoic and can be disregarded as carbonate producers in the Late Ordovician time frame of this study. However, the lesson to be learned is that vital effects may be more important than mineralogy in controlling δ^{26}Mg values in some biologically produced carbonates. This is especially true for biologically produced LMC, but perhaps less so for the major biological producers of aragonite. For example, literature values for δ^{26}Mg in aragonite (with the minor exception of sponges and bivalves) exhibit a narrow range of fractionation ($\Delta_{\mathrm{Mg_{(aq)}}}^{\mathrm{arag}}$) between –0.8‰ and –1.2‰ (Fig. 4.5b), which compares favorably with the fractionation factor of –1.09‰ for inorganically precipitated aragonite at 25ºC (Wang et al., 2013).

The carbonate measured in this study is mostly mud, the origins of which are difficult to decipher. It could be formed by calcareous algae, as in many shallow marine environments today, as a by-product of microbial activity, or by direct inorganic precipitation from seawater (Gischler et al., 2013; and references therein). One of the aims of Mg isotope research is to develop tools that can be used to probe the origin of carbonate mud and its range of encoded vital effects, mineralogical effects, and diagenetic alterations (section *4.6.1.3*). In the studied carbonates, the *slopes* of the mixing lines in Fig. 3a are the best evidence for secular change in the mineralogy of carbonate mud in the Monitor Range study section, because the limestone end-member δ^{26}Mg values are dependent on assumed ratios of Mg/Ca. The primary mineralogy of the carbonate deposit with the lowest slope (the sea-level lowstand carbonate) could have been aragonite, and

the deposits with higher slopes (the sea-level highstand carbonates) could have been LMC. The underpinning assumptions are that mineralogical effects outweigh vital effects in controlling the δ^{26}Mg values of the originally produced carbonate sediment, and that diagenesis did not alone produce these slope-differences in the mixing lines (see section *4.6.1.3*).

4.6.1.2. Sr/Ca ratios

The Sr/Ca ratio of Late Ordovician seawater is estimated to be ~ 11.0 (mmol/mol). This is based on Sr/Ca ratios in carbonaceous fossils, and assumed values of Sr distribution coefficients (Steuber and Veizer, 2002). Aragonitic sediment should have precipitated with a similarly high Sr/Ca, but the highest ratio measured in the study section is only 2.84, located in the lower part of the sea-level lowstand interval (K32; Table 4.1). If aragonite was the main carbonate polymorph deposited during this time, then most of its Sr was removed during open-system diagenesis.

Aragonite incorporates Sr with very little discrimination relative to Ca (D_{Sr} ≈ 1.1) (Kinsman, 1969). By contrast, LMC discriminates strongly against Sr (D_{Sr} ≈ 0.1) (Baker et al., 1982). When secondary calcite is formed by inversion of primary aragonite, it will almost always record lower Sr concentrations. Released to pore-fluids, the excess Sr is removed by fluid advection in cases where the diagenetic system is open (high volumes of fluid relative to rock) (Swart, 2015). However, there are some reported instances of calcite with very high Sr concentrations in the sedimentary rock record, and these findings are nearly always interpreted as evidence for inversion of primary aragonite to calcite in a rock-dominated or fluid restricted (closed) system (Land, 1967; Bathurst, 1975; Veizer, 1977; Brand and Veizer, 1980; Mazzullo, 1980; Waite and Swart, 2015).

The stratigraphic variability in Sr/Ca ratios (0.42–2.84) indicates that the loss of Sr was uneven, possibly reflecting variations in fluid flow through the deposit during the inversion of aragonite to calcite. Information on the initial permeability of the carbonate sediment may be gleaned from the pattern of dolomite abundance in the study section. Dolomite requires Mg to form, which is delivered by fluids passing through the deposit. Higher dolomite abundance translates to higher fluid/rock ratios, assuming that the dolomite was not detrital or eolian in origin, and that there was insufficient Mg in the carbonate at the time it was deposited to form the volume of dolomite observed. As for the origin of the dolomite, thin-section analysis reveals perfectly formed rhombohedral crystals (Fig. 4.4) indicating that the dolomite formed after sedimentation.

Moreover, stratigraphically equivalent carbonates deposited in the nearby Lone Mountain section of Nevada are pervasively dolomitized, revealing that dolomitizing fluids moved through the Nevada carbonate platform, regionally.

The most dolomitized interval in the study section occurs at 151 m (which reaches ~ 83 mol% dolomite), indicating that the pre-dolomitized carbonate sediment at this level was highly permeable, and that the flow was parallel to the paleo-slope of the beds. By contrast, the overlying carbonate at 158 m contains a low abundance of dolomite and the highest Sr/Ca ratio. Here, the sediment permeability was lower, and less Sr was lost to diagenetic fluids. On the whole, dolomite is more common in the sea-level lowstand carbonate than in the overlying and underlying sea-level highstand carbonates (Fig. 4.2). This indicates that the lowstand sediment was more permeable, which is supported by the appearance of intermixed wackestones and packstones (Finney et al., 1997). If the carbonate was originally composed of aragonite, then the metastable mineralogy coupled with the higher sediment permeability would have combined to make the sea-level lowstand deposit particularly susceptible to diagenetic alteration. The diagenetic fluids could have been seawater, meteoric water, mixed seawater/meteoric waters, or connate waters at different stages in the diagenetic history of the deposit.

4.6.1.3. Diagenetic effects influencing Mg isotopes

From the above discussion, it might be wondered whether the different slopes of the three mixing lines on the δ^{26}Mg *vs*. Ca/Mg ratio diagram (Fig. 3a) stem from stratigraphic differences in diagenetic outcomes rather than secular changes in carbonate mineralogy. To address this question, diagenetic studies of Cenozoic marine sediment cores collected from the modern ocean basins were turned to, where δ^{26}Mg values of both sediment and pore-fluids have been measured (Higgins and Schrag, 2012; Fantle and Higgins, 2014). Down-core changes in pore-fluid geochemistry monitors diagenetic reactions such as the dissolution and re-precipitation of metastable carbonates. The most important findings relate to the magnitude of the equilibrium Mg isotope fractionation factor between LMC and pore-fluids ($\Delta^{LMC}_{Mg(aq)} \equiv 1000\ln\alpha$) and the Mg distribution coefficient (D_{Mg} = $Mg/Ca_{carb} \div Mg/Ca_{aq}$). The Mg isotope fractionation factors, depicted in Fig. 4.5b, are likely affected by varying degrees of kinetic isotope fractionation as a result of high carbonate precipitation rates and vital effects imposed by organisms that produced the carbonate. For this reason, empirically determined fractionation factors may not accurately

reflect fractionation processes occurring in diagenetic systems where reaction rates are very slow, and likely to occur under conditions approximating chemical and isotopic equilibrium. *Ab initio* modeling suggests a large equilibrium fractionation factor of –5.3‰ ($\Delta^{LMC}_{Mg(aq)}$) at 25ºC (Rustad et al., 2010), indicating a preference for light Mg isotopes in diagenetic calcite. Model-determined fractionation factors from pore-fluid studies of carbonate recrystallization in deep-sea sediment are smaller, yielding –4.5‰ (Fantle and Higgins, 2014) and –3.7‰ (Higgins and Schrag, 2012).

The modeled D_{Mg} (~ 0.001–0.0024) (Fantle and Higgins, 2014; Higgins and Schrag, 2012) is ~ 30 times smaller than distribution coefficients measured in laboratory precipitation experiments (e.g., 0.057 at 25°C; Katz, 1973). The low D_{Mg} decreases the uptake of pore-fluid derived Mg into the recrystallized carbonates, which would be important in cases where the δ^{26}Mg value of the pore-fluid differed significantly from the dissolving carbonate phases. For example, if pore-fluid was seawater, which is ~ 1–4‰ enriched in ^{26}Mg compared to modern carbonates (Fig. 4.5a), then recrystallization of aragonite to diagenetically stable LMC will tend to shift whole-rock carbonate δ^{26}Mg towards higher values, due to the uptake of seawater derived Mg into the recrystallized carbonates. When isotopic fractionation is also considered, the drive for change reverses, and lower δ^{26}Mg values are favored in the recrystallized carbonate due to the large size of the fractionation factor. It would appear that diagenetic effects will be minimized where the magnitude of the isotopic fractionation effect is curbed by the mixing effects, in cases where seawater is the source of Mg in sedimentary pore-fluids. Two additional factors to consider are: (1) the fractionation factor is temperature dependent and smaller fractionations may be expected at higher temperatures in the later stages of diagenesis, and (2) the degree to which the diagenetic system is open or closed. For example, Rayleigh effects in a closed system can minimize the fractionation of Mg isotopes in the diagenetic calcite.

Although there is plenty of scope for altering original Mg isotope compositions of marine carbonate sediment, the size of the diagenetic fractionation effect is difficult to predict. Another approach is to study these effects through direct experimentation. Riechelmann et al. (2016) subjected punctate brachiopod shells composed of LMC to alteration in the laboratory under conditions simulating meteoric, marine, and burial diagenesis at hydrothermal temperatures (100ºC and 175ºC). In most cases, the lighter isotopes of Mg were incorporated into the altered brachiopod calcite, indicating a dominance of fractionation effects over mixing effects. The net

fractionations ($\Delta^{\text{brachiopod}}_{\text{Mg (aq)}}$) show a striking degree of uniformity despite the different diagenetic scenarios investigated, yielding (1) –1.1 ± 0.8‰, 2σ n = 5 for alteration in the presence of meteoric waters (outlier removed), where the Mg source was the carbonate itself, (2) –1.1 ± 0.5‰, 2σ n = 6 for alteration in the present of seawater with higher δ^{26}Mg value, and (3) –0.9 ± 1.2‰, 2σ n = 6 for experiments simulating burial in sedimentary basins involving 'connate water.' The direction and magnitude of the diagenetic change is similar to those documented in a field-based study of δ^{26}Mg values in altered whole-rock carbonate from the Southern Marion Platform near the Great Barrier Reef, Australia (Fantle and Higgins, 2014). In that study, the most altered carbonates were ~ 0.6‰ lower than the least altered carbonates.

It is concluded that the δ^{26}Mg values for the three limestone end-members deduced from the mixing analysis in this study must be altered, most likely to lower δ^{26}Mg values than the originally deposited carbonate sediment. This means that the limestone δ^{26}Mg values cannot be used to provide estimates of the δ^{26}Mg value of Late Ordovician seawater, even if certainty exists about the original mineralogy of the sediment and the fractionation factors. However, the possibility remains that the alteration effects were not so severe, or stratigraphically variable, as to conceal facies-dependent changes in the mineralogy of the original carbonate sediment.

4.6.1.4. Ca and C isotopes

The relative resistance of isotopic tracers to diagenetic resetting in carbonates is δ^{13}C > $\delta^{44/40}$Ca > δ^{26}Mg > δ^{18}O (Husson et al., 2015), determined using a water-rock interaction model simulating progressive degrees of isotopic exchange. If dolomite-corrected δ^{26}Mg values provide information on the aragonite *vs.* calcite composition of marine carbonate sediment in the study section at the time of deposition, then further evidence for aragonite should also be found in the more diagenetically resistant δ^{13}C and $\delta^{44/40}$Ca tracers. Indeed, the peak minimum in the $\delta^{44/40}$Ca profile, and peak maximum in the δ^{13}C profile both occur in the interval of the highest Sr/Ca ratio at ~ 158 m in the study section, which is also consistent with Mg isotope evidence for aragonite deposition during the Hirnantian sea-level lowstand. In fact, the –0.5‰ shift in sedimentary $\delta^{44/40}$Ca values is nearly in perfect agreement with the –0.6‰ fractionation between inorganically precipitated aragonite and calcite ($\Delta^{aragonite}_{calcite}$) (Gussone et al., 2005). By contrast, aragonite can account for only ~ 1.8‰ (Rubinson and Clayton, 1969) of the 7‰ change in δ^{13}C values.

Sedimentary Ca and C isotopes co-vary strongly through the study section (Fig. 4.2; Fig. 4.6a) (Holmden et al., 2012a). This is best seen on a plot of $\delta^{13}C$ *vs.* $\delta^{44/40}Ca$ values (Fig. 4.6b; Table 4.4). Here, the data exhibit two trends that are parallel to one another. The lower trend represents the beginning of glaciation (marked by sea-level regression) and the early part of the glacial interval. The upper trend represents the latter part of the glacial interval and the end of the glaciation (marked by sea-level transgression). These trends may be interpreted to reflect mixing between calcite and aragonite (the latter having inverted to calcite during diagenesis). The $\delta^{44/40}Ca$ value of the original aragonite is –1.63‰ for the lower mixing line and –1.49‰ for the upper mixing line. The LMC end-members are –1.11‰ and –0.97‰, respectively, taken from the *y*-intercept of each mixing line, which roughly corresponds to a $\delta^{13}C$ value of ~ 0.0‰. The $\delta^{13}C$ value for aragonite end-members is +7.57‰.

The possibility that the data define two mixing lines, rather than a single less-well-correlated mixing line may be explained by a change in carbonate-producers (and their associated vital effects) midway through the glacial cycle. Alternatively, a local-scale change in environmental conditions may have occurred that resulted in a change in carbonate precipitation rate, which also affects Ca isotope fractionation (Tang et al., 2008). The two mixing lines in Fig. 6b are offset by ~ 0.14‰ in $\delta^{44/40}Ca$ or ~ 2.0‰ in $\delta^{13}C$. If the origin of the offset is mostly attributed to the smaller 0.14‰ increase in $\delta^{44/40}Ca$ values in the latter stages of glaciation, this could be explained by a decrease in carbonate precipitation rate affecting both aragonite and LMC. In addition, changing vital effects or photosynthesis rates can influence on $\delta^{13}C$ values in carbonates (Smith and Kroopnick, 1981; Patterson and Walter, 1994; LaPorte et al., 2009).

The apportioning of aragonite and calcite in the lowstand carbonate may be determined from a mixing analysis using Equation 4.6, after orthogonally projecting the $\delta^{44/40}Ca$ data onto their average respective mixing lines (using Eqns. 4.3 and 4.4). The fraction of aragonite in the mixture is f_{arag}. Combining the results (listed in Table 4.4) yields an average of 78 mol% aragonite in the sea-level lowstand interval between 153 m and 187 m (Fig. 4.7). If this interpretation is correct, all of this aragonite inverted to calcite at some point in its diagenetic history.

$$f_{\mathrm{arag}} = \frac{\left(\delta^{44/40}\mathrm{Ca_{mix}} - \delta^{44/40}\mathrm{Ca_{LMC}}\right)}{\left(\delta^{44/40}\mathrm{Ca_{arag}} - \delta^{44/40}\mathrm{Ca_{LMC}}\right)} \tag{4.6}$$

4.6.1.5. Diagenetic effects influencing Ca isotopes

Only mixing processes can alter sedimentary $\delta^{44/40}$Ca values during diagenesis because fractionation effects are negligible at the low carbonate precipitation rates that typify diagenetic reactions (Fantle and DePaolo, 2007; Jacobson and Holmden, 2008). If diagenetic pore-fluids are meteoric waters, then diagenetic calcite will inherit the $\delta^{44/40}$Ca value of the primary carbonate mineral (aragonite and/or calcite). This is because meteoric waters have very low initial Ca concentrations. On the other hand, if the pore-fluids contain seawater, which is higher in Ca concentration than meteoric waters, and ~ 0.8–1.5‰ higher in $\delta^{44/40}$Ca than most marine carbonates, then diagenetic calcite will precipitate with higher $\delta^{44/40}$Ca values than the original carbonate minerals (Fantle and Higgins, 2014). How much higher will depend on the degree to which the diagenetic system was open or closed to fluid flow. Slow reaction rates and high fluid flow rates will generate the largest effects. This combination is most likely to occur in the early stages of diagenesis when the path-length of the flow system is relatively short (i.e., sediment in close proximity to seawater). With longer path-lengths, the Ca in pore-fluids will begin to equilibrate with the Ca in the carbonate sediment, thus diminishing the isotopic leverage for shifting the $\delta^{44/40}$Ca value of diagenetic calcite towards the heavy Ca isotopic composition of seawater.

Calcium isotopes would appear to be simpler to interpret than Mg isotopes, but it is still difficult to separate mineralogical effects from diagenetic effects, and vital effects as well. The only diagenetic effect of real significance occurs when a metastable mineral (e.g., aragonite) inverts to LMC in the presence of seawater-derived Ca in sedimentary pore-fluids. Accordingly, to create the negative excursion, the alteration effects would need to be concentrated mainly in the highstand carbonates. This would imply that high volumes of seawater passed through these units in the early stages of diagenesis, a prediction that is not in accord with the stratigraphic distribution of dolomite in the study section, which was interpreted as a proxy for original sediment permeability. Further complications arise when considering the metastable mineralogy of the highstand carbonates. If they were composed of aragonite, their original $\delta^{44/40}$Ca values were likely lower than the measured values, possibly even approaching the –1.5‰ value of the lowstand carbonate. But in this diagenetic scenario, the lowstand carbonate would have been originally composed of a polymorph resistant to diagenetic alteration (e.g., LMC). In order for LMC and aragonite to have similar $\delta^{44/40}$Ca values, vital effects and/or precipitation rate effects must be more

important than mineralogical effects. There is a precedent for this in the modern marine environment. Scleractinian corals are composed of aragonite and yet have $\delta^{44/40}$Ca values that are indistinguishable from LMC (Böhm et al., 2006; Holmden et al., 2012b). Strong vital effects and selective diagenesis are not the simplest explanations of the $\delta^{44/40}$Ca profile in the study section, but neither can they be ruled out with confidence at this early stage in Ca isotope studies of early Paleozoic carbonates.

4.6.2. Dolomitization

The δ^{26}Mg value of the dolomitizing fluid may be determined by substituting the δ^{26}Mg value of dolomite (–1.66‰) (see Fig. 4.3) into the temperature dependent equilibrium isotope fractionation equation of Li et al. (2015), which is based on the results of laboratory experiments forming dolomite under hydrothermal conditions. Extrapolation from higher temperatures down to 25ºC yields a fractionation factor of –1.75‰ ($\Delta^{\text{dolomite}}_{\text{Mg(aq)}}$). Applying this fractionation factor to the –1.66‰ value of dolomite yields +0.09‰ for the composition of the dolomitizing fluid. This is much higher than the –0.83‰ value for seawater today, indicating that if the dolomitizing fluid were of seawater origin, then there has been a shift in the composition of seawater over geological time, or that the temperature of dolomitization was higher. At higher temperatures the fractionation factor is smaller. For example, the fractionation factor at 70ºC is –1.32‰ further decreasing to –1.01‰ at 100ºC, yielding an estimated δ^{26}Mg value for the dolomitizing fluids of –0.34‰ and –0.65‰, respectively. Conodonts from the Monitor Range section yield color alteration index (CAI) values (Epstein et al., 1977) of ~ 3.0, described as being thermally mature (Harris et al., 1980), indicating that dolomitization at 70ºC or higher is feasible in this setting.

4.6.3. Implications for the origin of shelf-gradients in sedimentary $\delta^{13}C$ values during the Hirnantian sea-level lowstand

The origin of the Hirnantian δ^{13}C excursion has received much attention in the literature (Brenchley et al., 1994, 1995; Finney et al., 1999; Kump et al., 1999; Melchin and Holmden, 2006; LaPorte et al., 2009; Holmden et al., 2012a; Jones et al., 2016). Originally, it was presumed to be the result of increased organic carbon burial in the oceans (Brenchley et al., 1995). This interpretation was challenged by Kump et al. (1999) on the basis that it would be difficult to sustain the ~ 50–75% increase in organic carbon burial rate required to change the ocean-atmosphere C-

reservoir by 7‰, the size of the $\delta^{13}C$ excursion in the Monitor Range section. Moreover, as pointed out by Melchin and Holmden (2006), sedimentary organic carbon concentrations decrease rather than increase during the glaciation.

Kump et al. (1999) introduced a carbonate weathering hypothesis to explain ~ 2‰ of the 7‰ positive $\delta^{13}C$ excursion in the Monitor Range section during the Hirnantian event. The rest of the excursion was attributed to a global-scale change in the photosynthetic fractionation factor. However, the $\Delta^{13}C$ profile (= $\delta^{13}C_{carb} - \delta^{13}C_{org}$) in the Monitor Range section (the basis of the interpretation) could not be reproduced in a later study (LaPorte et al., 2009). Alternatively, if the largest $\delta^{13}C$ excursions are anomalous, i.e. not truly representative of the perturbation of the ocean-atmosphere C-reservoir during the Hirnantian event (Melchin and Holmden, 2006; LaPorte et al., 2009), then a large change in the fractionation factor is unnecessary. LaPorte et al. (2009) identified shelf-gradients in sedimentary $\delta^{13}C$ values in several locations during the Hirnantian sea-level lowstand, and used these patterns to predict a 2.7 ± 0.4‰ change in the ocean-atmosphere C-reservoir during the glaciation. A glacial-age shift in carbonate mineralogy (LMC to aragonite) would add 1.8‰ to this estimate, allowing the excursion to reach 4.5 ± 0.4‰ in some settings. Further amplification of the $\delta^{13}C$ signal requires local C-cycling effects in circulation-restricted nearshore settings, such as carbonate weathering and intense photosynthesis (Melchin and Holmden, 2006; LaPorte et al., 2009). Gradients in $\delta^{13}C$ values have also been found in deep water sediments draping the edge of the Bahamas carbonate platform. In this environment, mixing occurs between ^{13}C-enriched sedimentary aragonite transported from the shelf and ^{13}C-depleted sedimentary calcite (coccoliths and forams) settling through the water column from the photic zone (Swart and Eberli, 2005; Swart et al., 2009). These findings indicate that stratigraphic changes in sedimentary $\delta^{13}C$ values of the order of 2‰ may be due to local-scale carbonate polymorph mixing effects rather than global-scale C-cycling effects (Swart, 2008).

There is a large C isotope excursion in the Silurian that reaches 11‰ in some sections (Andrew et al., 1994; Wigforss-Lange, 1999). This mid-Ludfordian event shares many similarities with the older Hirnantian one, including: (1) global variability in the magnitude of the positive $\delta^{13}C$ excursion, (2) larger excursions in nearshore environments than offshore ones, (3) elevated rates of biological extinction, (4) climate cooling, and (5) global sea-level regression. This has prompted numerous authors to link the mid-Ludfordian event with an episode of glaciation in

Gondwana (Lehnert et al., 2007; Loydell, 2007; Calner, 2008; Trotter et al., 2016), even though tillites of this age have not yet been reported.

The mid-Ludfordian $\delta^{13}C$ excursion in the Prague Basin reaches peak-magnitude values of +8.9‰ above baseline, and a recently published Ca isotope study shows synchronous changes in $\delta^{44/40}Ca$ values occur only near the top of the section where $\delta^{13}C$ values decrease from 8.9‰ to ~ 0.0‰. In the same stratigraphic interval, $\delta^{44/40}Ca$ values change from –1.6‰ to –1.1‰ (Farkaš et al., 2016). In the lower part of the study section $\delta^{44/40}Ca$ values are steady and low (–1.6‰) and unrelated to changes in $\delta^{13}C$ values. If the low $\delta^{44/40}Ca$ values signal aragonite, then the sediment in the Prague Basin was aragonitic before and during the Ludfordian event, switching only to LMC in the stratigraphic interval of rising sea-level at the end of the event. This shows that whatever may have caused the $\delta^{44/40}Ca$ changes in the Prague Basin (e.g., mineralogy, vital effects, or precipitation rate effects), the $\delta^{13}C$ changes are decoupled from the $\delta^{44/40}Ca$ changes. The implications are equally valid for the Hirnantian event in the Monitor Range, even though in this setting the inferred mineralogical changes coordinate perfectly with the $\delta^{13}C$ changes. In other words, the synchronousness of the Ca and C isotope changes in the Monitor Range section reflect associated but not dependent processes.

Tang et al. (2008) showed in a series of calcite precipitation experiments that $\delta^{44/40}Ca$ values and Sr concentrations are strongly negatively correlated—higher carbonate precipitation rates yielding lower $\delta^{44/40}Ca$ values and higher Sr concentrations. Farkaš et al. (2016) showed that carbonate $\delta^{44/40}Ca$ values and Sr concentrations vary in a similar way in the Ludfordian study section in the Prague Basin, prompting consideration of a decrease in precipitation rate as an alternative to the mineralogical explanation for the increase in $\delta^{44/40}Ca$ values near the top of the study section (i.e., a change from aragonite to calcite). Holmden et al. (2012a) looked for but could not find similar evidence for precipitation rate effects in carbonates deposited in the Monitor Range section during the Hirnantian event, but made them a centerpiece of their interpretation of the Ca isotope changes nonetheless. They justified this decision on the basis of the lack of evidence for the very high Sr concentrations necessary to support precipitation of aragonite during the sea-level lowstand, as suggested by the low $\delta^{44/40}Ca$ values. However, the Mg isotope evidence presented in this chapter encourages reconsideration of the mineralogical interpretation of the $\delta^{44/40}Ca$ profile in the Monitor Rage section, despite the low Sr concentrations. And while it is admitted that none

of these lines of evidence strongly stand on their own to uniquely identify aragonite deposition during the sea-level lowstand, the combined evidence is more persuasive, including a portion of the ^{13}C-enrichment in the carbonates.

4.6.4. Implications of facies-dependent changes in carbonate polymorph mineralogy

It has been proposed that the dominant reef-building and sediment-producing taxa for a given age would create skeletons composed of aragonite or calcite, depending on which polymorph of $CaCO_3$ was favored by the chemistry of seawater at the time. Calcifying biota whose preferred carbonate mineralogy was out of step with the oscillating pattern of calcite and aragonite seas produced less carbonate and, thus, faced greater habitat restriction and predation pressures, factors that could contribute to species decline and extinction (Stanley and Hardie, 1998; Knoll, 2003). This has been studied in experiments growing modern aragonite-producing taxa in artificial seawater with the chemistry of a 'calcite sea' (Ries, 2010). While the organisms did produce minor amounts of calcite, they mostly retained their preference for precipitation of aragonite, and their growth was inhibited. These and other experiments show that the chemistry of seawater influences the abiotic mineralogy of marine precipitates, but is less likely to control the mineralogy of the taxa that have already evolved mineralized skeletons (Porter, 2010).

Trimerellid brachiopods thrived in low latitude 'calcite seas' of the Late Ordovician and early Silurian, and secreted aragonitic shells (Jaanusson, 1966; Balthasar et al., 2011). Not only is this the oldest evidence for aragonite in brachiopods, but it would appear to reflect a primary mineralogical change from a calcitic ancestor during a time when the chemistry of seawater favored inorganic precipitation of calcite (Balthasar et al., 2011). The appearance of the trimerellid brachiopods in the Late Ordovician is therefore out of sync with selection pressures favoring evolution of calcite secreting organisms in the 'calcite sea'. Alternatively, this may be interpreted as evidence that the physical and chemical attributes of seawater in the reef environments of the shallow seas and seaways where the trimerellids thrived were favorable to the inorganic precipitation of aragonite. These seas may have provided a refuge for aragonite secreting organisms that evolved in earlier times, such as calcareous algae (Ries, 2006), and perhaps stromatoporoid sponges (Kershaw, 2013), and conditions where aragonitic muds could precipitate and accumulate. Mud is one of the most often targeted carbonate lithologies for geochemical and isotopic investigations of environmental change. It is also susceptible to alteration during early

diagenesis (Lasemi and Sandberg, 1984; Walter and Burton, 1990; Hover et al., 2001), particularly where the mud was composed of aragonite.

The Monitor Range section was near the equator in the Late Ordovician (Fig. 4.1). Tropical sea surface temperatures ranged between 28ºC and 32ºC based on $\delta^{18}O$ studies of conodonts, decreasing only slightly to 24–28ºC during the Hirnantian glaciation (Trotter et al., 2008). Clumped isotopes yield even higher sea surface temperatures between 32ºC and 37ºC, dropping to 28ºC during the glaciation (Finnegan et al., 2011). All of these temperatures are high enough to permit the formation of aragonite in a 'calcite sea' (Balthasar and Cusack, 2015) independently of the timing of the glaciation. If atmospheric CO_2 concentration was lower during the Hirnantian glaciation, analogous to the Pleistocene glaciations, then aragonite may have precipitated more easily during the glacial period (Wilkinson and Given, 1986; Lee and Morse, 2010). Changing oceanic sulfate concentrations can affect aragonite precipitation as well (Bots et al., 2011), but the duration of the glaciation is short compared to the modern oceanic residence time of sulfate (10 Myr). Therefore, the sulfate concentration was likely unchanged during the glaciation.

Of all the factors that may have controlled the distribution of aragonite during the Hirnantian event, local temperature was likely the most important. On this basis, aragonite would have formed more easily at low latitudes than high latitudes, and in shallow-water nearshore settings rather than deeper offshore ones. The stratigraphic distribution of aragonite will respond to sea-level change because water temperature and bathymetry are correlated. The global sea-level regression that occurred in response to the Hirnantian glaciation initiated a cool- to warm-water transition in carbonate facies in tropical-shelf seas, ushering in the hypothesized appearance of aragonite during the glacial period in the Monitor Range section in Nevada. The appearance of aragonite at this time has the potential to be a global-change signal, but one that is driven by local-scale processes. Because aragonite may record significantly different Mg, Ca, and C isotopic compositions compared to calcite, I therefore agree with Ries (2010) who cautioned that some isotopic excursions in the sedimentary rock record may reflect stratigraphic changes in primary carbonate mineralogy rather than perturbations of global biogeochemical cycles.

4.7. Conclusion

The Monitor Range section in the Martin Ridge Basin, Nevada, records a (2–3‰) excursion in $\delta^{26}Mg$ values during the Late Ordovician Hirnantian glaciation event. The changes

are nearly synchronous with lithofacies and biofacies indicators of sea-level change, as well as previously reported excursions in sedimentary $\delta^{13}C$ and $\delta^{44/40}Ca$ values in the same section. A mixing model was presented on the basis of trends in $\delta^{26}Mg$ values and Ca/Mg ratios in three contiguous carbonate units in the study section yielding evidence that the varying dolomite abundance in the host limestone accounts for the positive $\delta^{26}Mg$ excursion. However, the mixing analysis also reveals significant sea-level related stratigraphic changes in the (dolomite-corrected) composition of the limestone in the study section, yielding $\delta^{26}Mg$ values of –4.45 ± 0.82‰ (2σ) before the glaciation, –2.54 ± 0.23‰ (2σ) during the glaciation, and –3.05 ± 0.27‰ (2σ) after the glaciation. Shifts of this magnitude are consistent with changes in carbonate mineralogy, more specifically, aragonite during the glaciation and calcite before and after the glaciation. This interpretation is supported by shifts to lower $\delta^{44/40}Ca$ and higher $\delta^{13}C$ values, and intermittently higher Sr/Ca ratios in the carbonates deposited during the glacial interval.

The Late Ordovician lies in the midst of a long period of 'calcite seas', and although Sr concentration is a key indicator of primary aragonite that has inverted to secondary calcite in carbonate rocks, the loss of Sr may be too severe to make this a generally reliable proxy. The Mg isotope proxy also shows promise for fingerprinting primary aragonite, but only if the effects of small amounts of dolomite in the whole-rock carbonate samples can be corrected for, and carbonate diagenesis is not severe enough to obliterate the anticipated enrichment of ^{26}Mg in aragonite compared to calcite. The Ca isotope proxy is even better suited to the task because it is more resistant to alteration during diagenesis, but it is still difficult to distinguish among the three factors that can cause changes in carbonate $\delta^{44/40}Ca$ values: (1) carbonate precipitation rate, (1) carbonate mineralogy, and (3) vital effects of carbonate producing organisms.

Approximately 1.8‰ of the 7‰ change in sedimentary $\delta^{13}C$ values in the Monitor Range section can be explained by the hypothesized shift to aragonite deposition during the Hirnantian sea-level lowstand. This brings the C isotope excursion in the Monitor Range section closer to the the smaller excursions (2.7 ± 0.4‰) recorded in carbonates and sedimentary organic matter deposited in deeper water settings, which LaPorte et al. (2009) considered to be better estimates of the true shift in the $\delta^{13}C$ values of the ocean-atmosphere C-reservoir during the Hirnantian event. Numerous suggestions have been offered to explain how carbonate $\delta^{13}C$ values could be elevated in the nearshore regions of low-latitude epeiric seas during the glaciation. Most hypothesize

circulation-restriction with the open ocean, paired with changes in environmental conditions, such as local-scale increases in nutrient fluxes, intensified photosynthesis, and/or methanogenesis in small C-reservoirs (Panchuk et al., 2006; LaPorte et al., 2009; Holmden et al., 2012a; Kozłowski and Sobién, 2012; Jones et al., 2016). This study finds that a change in carbonate polymorph mineralogy may have occurred during the Hirnantian glaciation as well. A mineralogical change implies a change in the carbonate factory, a point that underscores the importance of searching for local-scale environmental effects as possible explanations for anomalously large positive $\delta^{13}C$ excursions in the sedimentary rock record, even though the mineralogical effect may explain only a small fraction of the observed change.

4.8. Figures

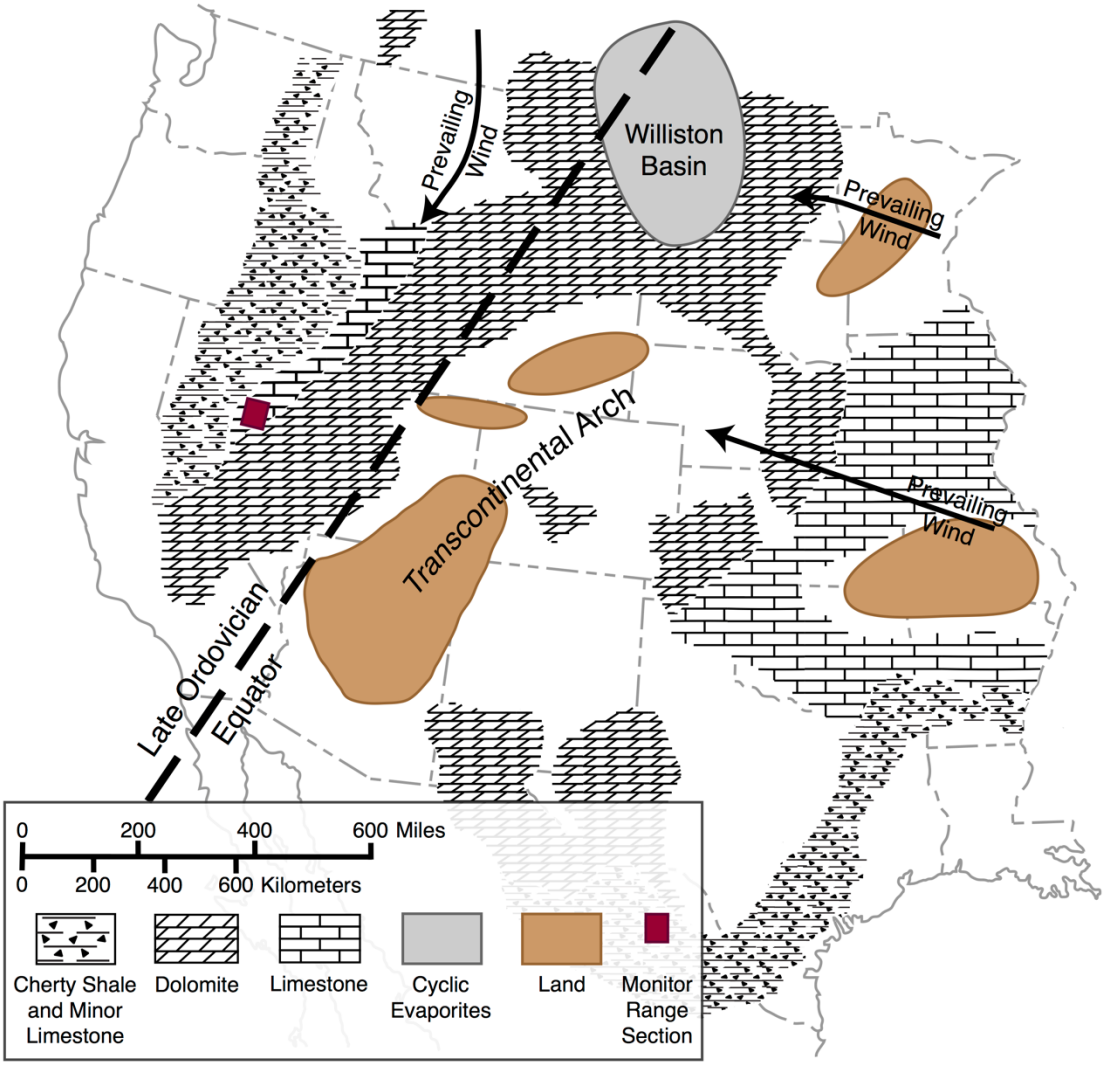

Figure 4.1 Paleogeographic map showing the approximate position of Laurentia along the paleo-equator at the time of the Hirnantian glaciation (adapted from Ross, 1976) and the approximate location of the Monitor Range section. Position of the Late Ordovician equator is based on Cocks and Torsvik (2011). Prevailing trade winds are denoted with arrows. Declining Hirnantian sea-level caused carbonate sediment to be exposed across Laurentia, possibly resulting in increased weathering inputs of nutrients (runoff and carbonate dust) to the shallow seas along the western margin (Kump et al., 1999; LaPorte et al., 2009; Kozłowski, 2015).

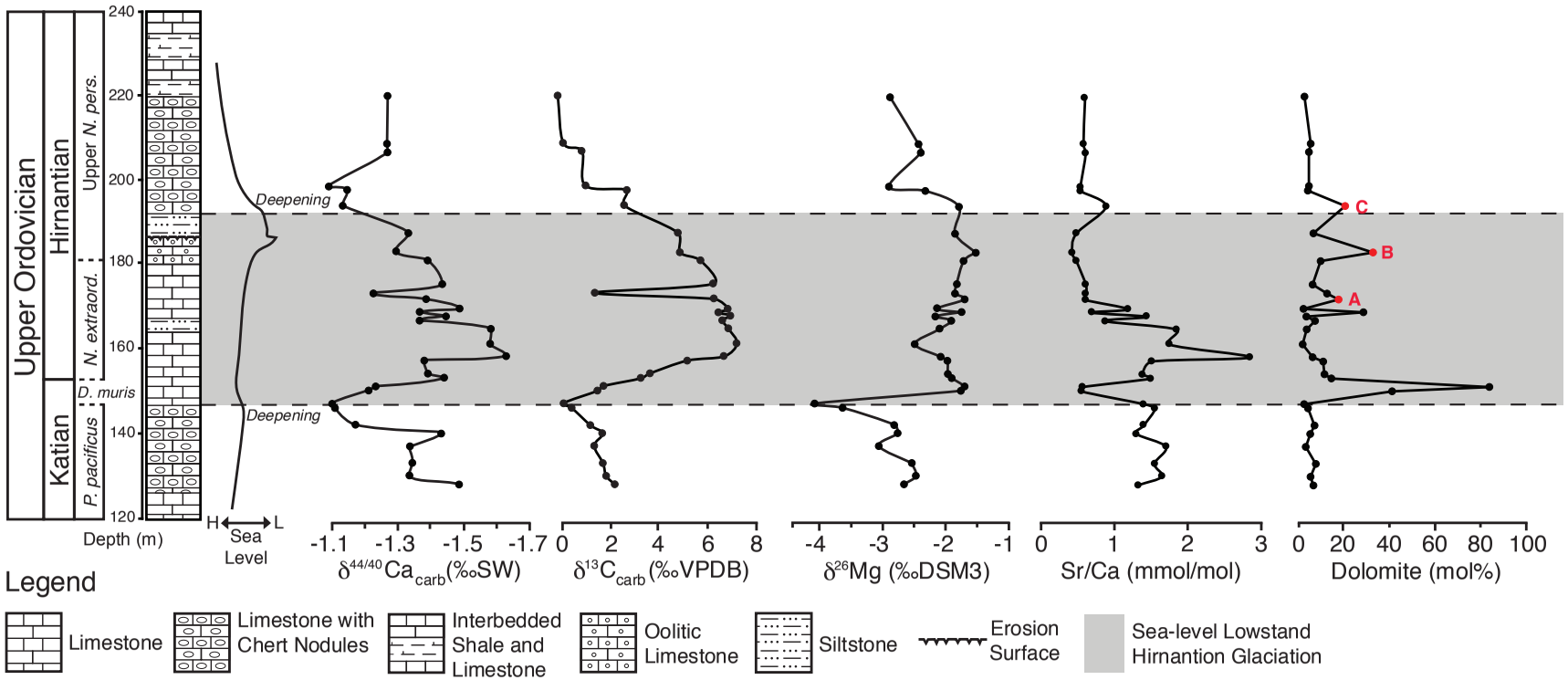

Figure 4.2 The δ^{26}Mg, Sr/Ca (mmol/mol), and mol% dolomite profiles through the Monitor Range section in Nevada. The $\delta^{44/40}$Ca and δ^{13}C profiles are reproduced from Holmden at al. (2012a) and LaPorte et al. (2009), respectively. Graptolite zones, lithologies, stratigraphic ages, and sea-level curve are modified from Finney et al. (1999) and Finney et al. (1997). The interval of low sea-level marking the duration of the glaciation is shaded gray. The δ^{26}Mg values were determined from the same samples as those analyzed for $\delta^{44/40}$Ca and δ^{13}C. Note that the scale for the $\delta^{44/40}$Ca profile is inverted. Thin-sections shown in Fig. 4.4 are from samples identified as A, B, and C in the mol% dolomite profile.

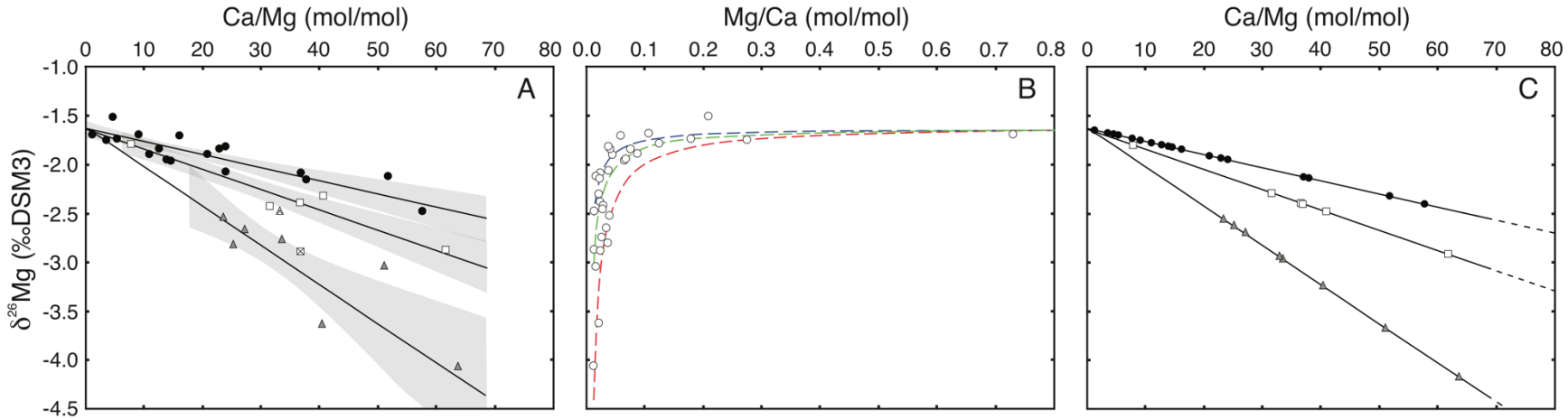

Figure 4.3 (A) Cross-plot of δ^{26}Mg vs. Ca/Mg (mol/mol): (1) black circles are samples from carbonates deposited during the Hirnantian sea-level lowstand (y = –0.0134x–1.64, slope error = ± 0.002 1σ, intercept error = ± 0.04‰ 1σ), (2) white squares are samples from carbonates deposited during the post-glacial sea-level highstand (y = –0.0209x–1.63, slope error = ± 0.003 1σ, intercept error = ± 0.08‰ 1σ), and (3) gray triangles are samples from carbonates deposited during the pre-glacial sea-level highstand (y = –0.0406x–1.61, slope error = ± 0.011 1σ, intercept error = ± 0.34‰ 1σ). The best-fit lines and error envelopes were determined using GEODATE software (Eglington and Harmer, 1999) with 1σ uncertainties of 0.04‰ for δ^{26}Mg and 10% for Ca/Mg. Unconstrained regression of the Hirnantian sea-level lowstand data resulted in a line with MSWD of 5.46. Two outliers (samples K4 and K72) were removed from the regressions of the pre-glacial and post-glacial sea-level highstand carbonates (symbols depicted with an X), which yielded MSWDs of 3.83 and 2.19, respectively, and included the dolomite end-member (+1.0, –1.66) as a datum. (B) Cross-plots of δ^{26}Mg *vs.* Mg/Ca (mol/mol). The hyperbolic relationship is demonstrative of two component mixing between limestone and dolomite. The dashed lines represent model mixing lines calculated using limestone and dolomite end-members for each carbonate unit using Equation 4.2 in the main text. Red colored symbols represent carbonate samples deposited before the Hirnantian glaciation, blue symbols represent carbonates deposited

during the glaciation, and green symbols represent carbonates deposited after the glaciation. (C) Cross-plot of $\delta^{26}Mg$ *vs.* Ca/Mg (mol/mol) for samples that were orthogonally projected onto their average mixing lines using Equations 4.3 and 4.4 in the main text (Table 4.3).

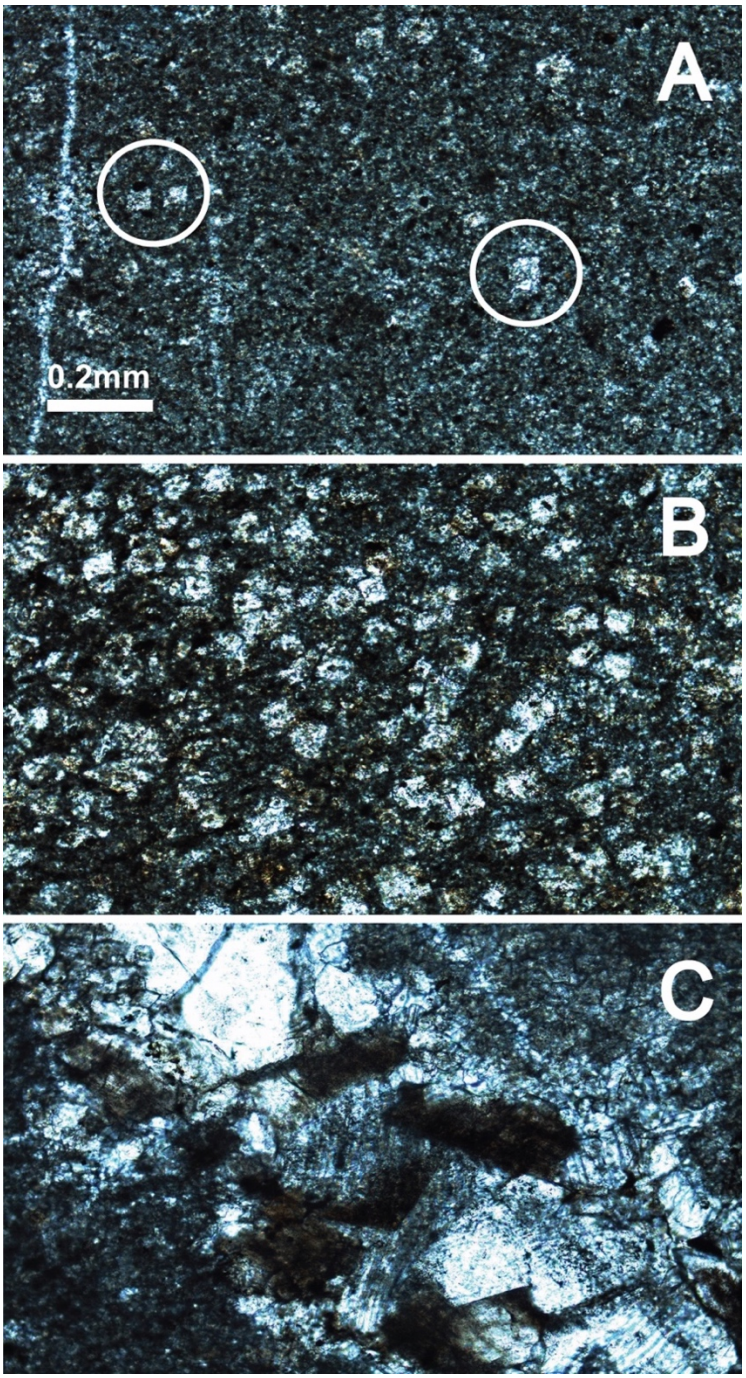

Figure 4.4 Thin-section images of three carbonate hand samples containing dolomite (highlighted in red in Fig. 4.2). Dolomite crystals show good rhombohedral habit indicating that the dolomite formed after the sediment was deposited. (A) Sample K45.5 at 171.5 m depth is a sample of mudstone with 16.1% dolomite. (B) Sample K56.5 at 182.5 m depth is a sample of oolitic limestone with 31.3% dolomite. (C) Sample K67.4 at 193.4 m depth is a sample of mudstone with chert nodules and 19.1% dolomite.

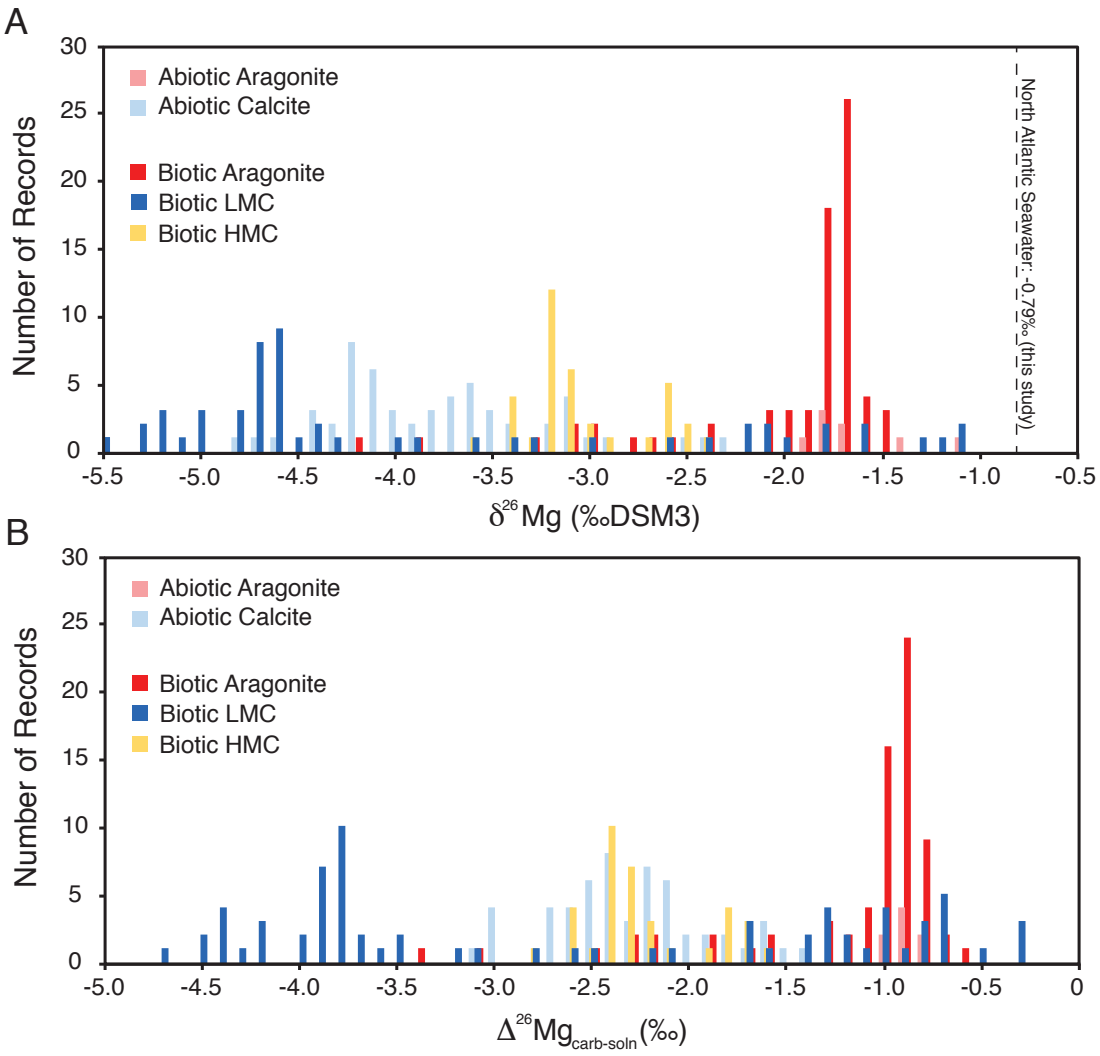

Figure 4.5 (A) Histogram of δ^{26}Mg values for abiotic aragonite (pink), abiotic calcite (light blue), biotic aragonite (red), biotic low magnesium calcite (dark blue), and biotic high magnesium calcite (yellow). Measured North Atlantic Seawater (this study) is shown as a dashed line. (B) Histogram of apparent Mg isotope fractionation factors ($\Delta^{carb}_{Mg\,(aq)}$) for abiotic aragonite (pink), abiotic calcite (light blue), biotic aragonite (red), biotic low magnesium calcite (dark blue), and biotic high magnesium calcite (yellow). Figures modified from Saenger and Wang (2014) reproduced in Supplementary Online Material.

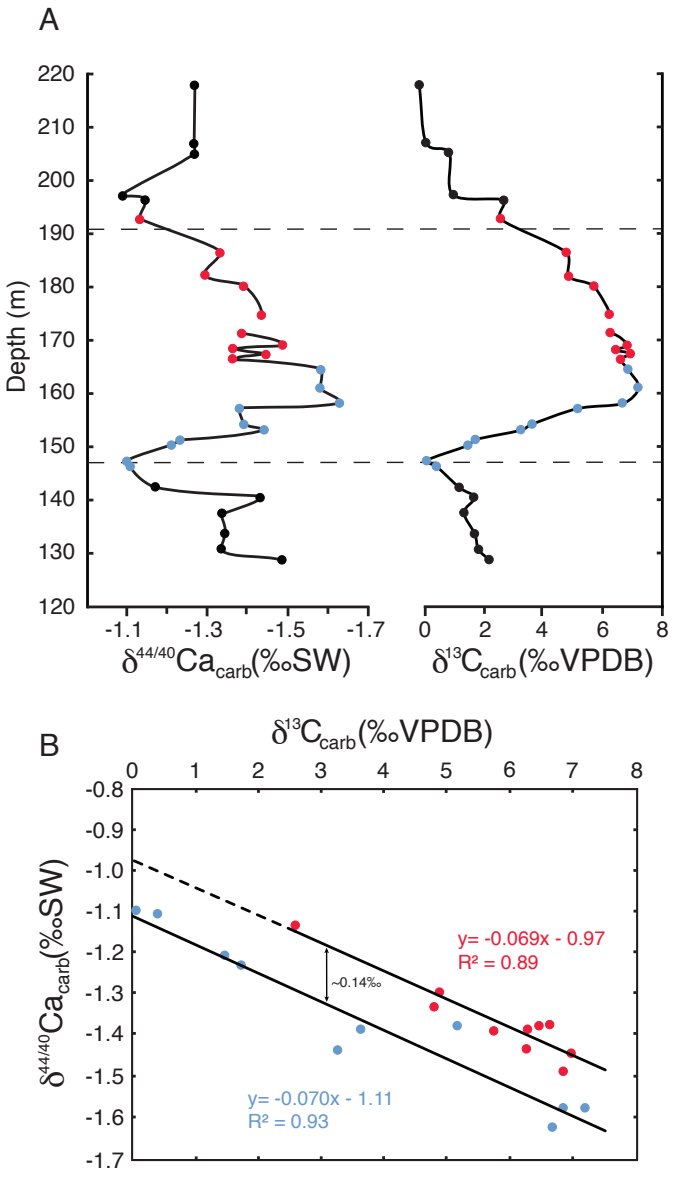

Figure 4.6 (A) Carbonate $\delta^{44/40}$Ca (Holmden at al., 2012a) and δ^{13}C (LaPorte et al., 2009) profiles for the Monitor Range section. Hirnantian sea-level lowstand interval is indicated with dashed lines. Sample K46.9 (172.9m) was removed as an outlier. Note that the scale is inverted for the $\delta^{44/40}$Ca profile. (B) Cross-plot of $\delta^{44/40}$Ca *vs.* δ^{13}C values showing strong linear correlations for samples deposited during the Hirnantian sea-level lowstand interval. Small arrows between the lower and upper mixing lines shows the 0.14‰ offset in $\delta^{44/40}$Ca values (see text for additional details). Symbols for samples from the lower part of the lowstand are blue and the equation of the best-fit line is y = –0.070x–1.11, R^2 = 0.93. Symbols for samples from the upper part of the lowstand are red and the best-fit line is y = –0.069x–0.97, R^2 = 0.89.

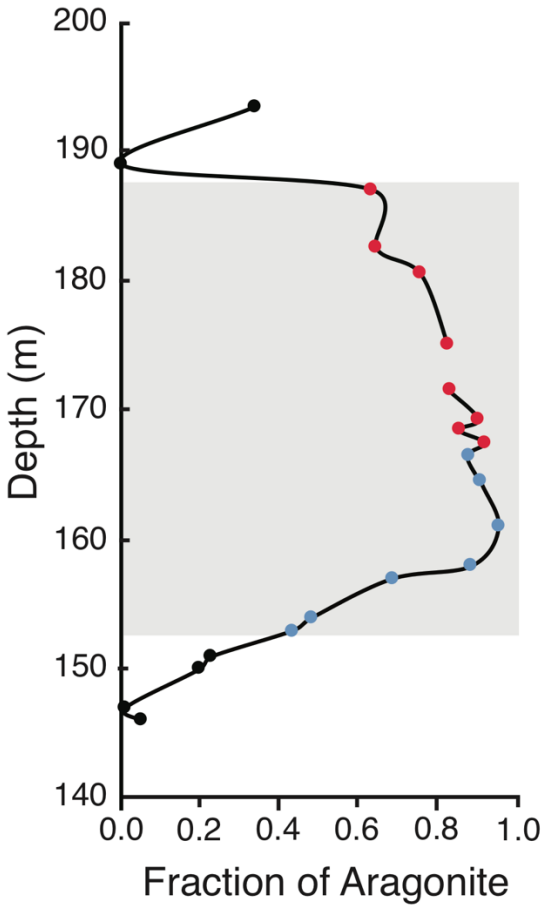

Figure 4.7 Calculated stratigraphic change in the inferred mole-fraction of aragonite in the Hirnantian sea-level lowstand carbonate (Table 4.4) as determined from the two regression lines in Figure 4.6a and Equation 4.6 in the main text. Symbols are the same as in Fig. 4.6.

4.9. Tables

Table 4.1 (part 1 of 2)

Sample	Depth (m)	N	δ^{26}Mg (‰ DSM3)	2σ	2se	δ^{25}Mg (‰ DSM3)	2σ	2se	δ^{13}C carb[a] (‰ VPDB)	$\delta^{44/40}$Ca[b] (‰ SW)	Calcite[b] (wt %)	Ca/Mg (mol/mol)	Sr/Ca (mmol/mol)	Ca (µmol/g)	Mg (µmol/g)	Sr (µmol/g)	Dolomite (mol %)
DSM3		59	-0.02	0.08		-0.01	0.05										
CAM1		123	-2.62	0.08		-1.35	0.04										
Mg Specpure		116	-3.80	0.11		-1.95	0.06										
OSIL		18	-0.79	0.08		-0.41	0.04										
K 2	128	4	-2.66		0.05	-1.40		0.01	2.19	-1.48	97	27.0	1.33	9781	362	13.0	4.12
K 4	130	3	-2.47		0.01	-1.30		0.04	1.83	-1.33	98	32.9	1.65	10819	329	17.8	2.94
K 7	133	4	-2.54		0.04	-1.34		0.02	1.71	-1.34	100	23.4	1.54	10000	428	15.4	5.14
K 11	137	4	-3.06		0.04	-1.59		0.04	1.35	-1.34	98	50.9	1.70	8384	165	14.2	0.984
K 14	140	4	-2.76		0.03	-1.44		0.01	1.66	-1.43	99	33.5	1.30	7725	230	10.0	2.83
K 15	141								1.26	-1.19	98	34.1	1.44	8982	263	13.0	
K 16	142	4	-2.81		0.04	-1.45		0.03	1.18	-1.17	98	25.2	1.40	9941	395	13.9	4.59
K 20	146	4	-3.63		0.04	-1.87		0.02	0.420	-1.11	98	40.4	1.55	9302	230	14.4	1.92
K 21	147	4	-4.07		0.02	-2.12		0.01	0.075	-1.10	98	63.6	1.40	10460	165	14.6	0.268
K 24	150	4	-1.76		0.05	-0.93		0.02	1.49	-1.21	82	3.60	0.542	9601	2666	5.20	39.8
K 25	151	4	-1.70		0.03	-0.89		0.04	1.74	-1.23	75	1.36	0.559	5389	3950	3.01	83.0
K 27	153	4	-1.90		0.02	-0.99		0.03	3.27	-1.44	96	11.1	1.49	8404	757	12.5	13.0
K 28	154	3	-1.96		0.02	-1.01		0.01	3.65	-1.39	97	13.9	1.38	8723	625	12.1	9.98
K 31	157	4	-1.97		0.01	-1.04		0.01	5.18	-1.38	96	14.7	1.51	8703	592	13.1	9.37
K 32	158	4	-2.08		0.05	-1.08		0.02	6.70	-1.63	98	24.0	2.84	8703	362	24.7	4.79
K 35	161	4	-2.49		0.05	-1.30		0.03	7.22	-1.58	99	57.7	1.75	9501	165	16.6	0.415

Table 4.1 (part 2 of 2)

Sample	Depth (m)	N	δ^{26}Mg (‰ DSM3)	2σ	2se	δ^{25}Mg (‰ DSM3)	2σ	2se	δ^{13}C carb[a] (‰ VPDB)	$\delta^{44/40}$Ca[b] (‰ SW)	Calcite[b] (wt %)	Ca/Mg (mol/mol)	Sr/Ca (mmol/mol)	Ca (µmol/g)	Mg (µmol/g)	Sr (µmol/g)	Dolomite (mol %)
K 38.5	164.5	3	-2.09		0.04	-1.13		0.04	6.87	-1.58	99	37.0	1.85	9741	263	18.0	2.19
K 40.5	166.5	4	-1.91		0.02	-1.00		0.02	6.64	-1.37	99	21.0	0.871	8284	395	7.21	5.86
K 41.5	167.5	3	-2.16		0.02	-1.12		0.02	6.97	-1.45	99	37.9	1.44	8743	230	12.6	2.06
K 42.5	168.5	4	-1.75		0.04	-0.92		0.03	6.47	-1.38	98	5.49	0.683	9222	1679	6.30	27.1
K 43.3	169.3	4	-2.13		0.05	-1.11		0.02	6.85	-1.49	100	51.9	1.18	3413	65.8	4.02	0.776
K 45.5	171.5	4	-1.70		0.04	-0.87		0.02	6.29	-1.38	99	9.15	0.597	9941	1086	5.93	16.1
K 46.9	172.9	3	-1.85		0.02	-0.96		0.02	1.38	-1.22	80	12.7	0.606	9641	757	5.84	11.1
K 49	175	3	-1.83		0.05	-0.95		0.02	6.26	-1.43	99	24.1	0.605	9501	395	5.75	4.79
K 54.5	180.5	4	-1.71		0.01	-0.88		0.02	5.74	-1.39	99	16.2	0.477	10140	625	4.84	8.28
K 56.5	182.5	4	-1.52		0.05	-0.79		0.02	4.89	-1.29	99	4.71	0.418	8523	1810	3.56	31.3
K 61	187	3	-1.85		0.03	-0.96		0.02	4.79	-1.33	99	23.0	0.471	9102	395	4.29	5.11
K 63.9	188.9									-1.28		6.81	0.439	8523	1251	3.74	
K 67.4	193.4	4	-1.79		0.03	-0.92		0.01	2.58	-1.13	94	7.79	0.879	8723	1119	7.67	19.1
K 71	197	2	-2.32		0.06	-1.26		0.02	2.69	-1.14	97	40.8	0.536	10739	263	5.75	1.78
K 72	198	4	-2.89		0.03	-1.51		0.00	0.980	-1.09	98	36.7	0.529	9661	263	5.11	2.28
K 80	206	3	-2.39		0.06	-1.26		0.03	0.820	-1.27	99	36.8	0.604	9681	263	5.84	2.27
K 82	208	4	-2.43		0.04	-1.28		0.02	0.049	-1.27	100	31.5	0.572	10380	329	5.93	3.08
K 93	219	4	-2.88		0.03	-1.52		0.03	-0.175	-1.27	99	61.6	0.594	10140	165	6.03	0.268
Full Mg Replicates																	
K 7 r		4	-2.53		0.05	-1.33		0.01									
K 42.5 r		4	-1.77		0.05	-0.92		0.03									
K 56.5 r		4	-1.52		0.03	-0.79		0.02									

[a]Carbon isotope data from LaPorte et al. (2009)

[b]Calcium isotope and calcite wt% data from Holmden et al. (2012a)

Multi-proxy elemental and isotopic data and calculated mol% dolomite for carbonates from the Monitor Range section, Nevada.

Table 4.2

	δ^{26}Mg (‰ DSM3)	Mg/Ca (mol/mol)	Ca/Mg (mol/mol)	Ca (μmol/g)	Mg (μmol/g)
After Hirnantian					
Limestone	-3.05	0.015	67.8	9855	145
Dolomite	-1.66	1.00	1.00	5423	5423
During Hirnantian					
Limestone	-2.54	0.015	66.7	9852	148
Dolomite	-1.66	1.00	1.00	5423	5423
Before Hirnantian					
Limestone	-4.45	0.014	69.9	9859	141
Dolomite	-1.66	1.00	1.00	5423	5423

Isotopic and elemental data for mixing end-members, calculated from model mixing lines in Fig. 4.3.

Table 4.3

Sample	Depth (m)	Measured δ^{26}Mg (‰ DSM3)	Measured Ca/Mg (mol/mol)	Measured Mg/Ca (mol/mol)	Projected δ^{26}Mg (‰ DSM3)	Projected Ca/Mg (mol/mol)	Projected Mg/Ca (mol/mol)
K2	128	-2.66	27.0	0.037	-2.71	27.0	0.037
K4	130	-2.47	32.9	0.030	-2.95	32.8	0.030
K7	133	-2.54	23.4	0.043	-2.56	23.4	0.043
K11	137	-3.06	50.9	0.020	-3.68	50.9	0.020
K14	140	-2.76	33.5	0.030	-2.98	33.5	0.030
K16	142	-2.81	25.2	0.040	-2.64	25.2	0.040
K20	146	-3.63	40.4	0.025	-3.25	40.4	0.025
K21	147	-4.07	63.6	0.016	-4.19	63.6	0.016
K24	150	-1.76	3.60	0.278	-1.69	3.60	0.278
K25	151	-1.70	1.36	0.733	-1.66	1.37	0.733
K27	153	-1.90	11.1	0.090	-1.79	11.1	0.090
K28	154	-1.96	13.9	0.072	-1.83	13.9	0.072
K31	157	-1.97	14.7	0.068	-1.84	14.7	0.068
K32	158	-2.08	24.0	0.042	-1.96	24.0	0.042
K35	161	-2.49	57.7	0.017	-2.41	57.7	0.017
K38.5	164.5	-2.09	37.0	0.027	-2.14	37.0	0.027
K40.5	166.5	-1.91	21.0	0.048	-1.92	21.0	0.048
K 41.5	167.5	-2.16	37.9	0.026	-2.15	37.9	0.026
K 42.5	168.5	-1.75	5.49	0.182	-1.72	5.49	0.182
K 43.3	169.3	-2.13	51.9	0.019	-2.33	51.8	0.019
K45.5	171.5	-1.70	9.15	0.109	-1.76	9.15	0.109
K46.9	172.9	-1.85	12.7	0.079	-1.81	12.7	0.079
K 49	175	-1.83	24.1	0.042	-1.96	24.1	0.042
K54.5	180.5	-1.71	16.2	0.062	-1.86	16.2	0.062
K56.5	182.5	-1.52	4.71	0.212	-1.70	4.71	0.213
K61	187	-1.85	23.0	0.043	-1.95	23.0	0.043
K67.4	193.4	-1.79	7.79	0.128	-1.80	7.79	0.128
K71	197	-2.32	40.8	0.025	-2.48	40.8	0.025
K72	198	-2.89	36.7	0.027	-2.40	36.7	0.027
K80	206	-2.39	36.8	0.027	-2.40	36.8	0.027
K82	208	-2.43	31.5	0.032	-2.29	31.5	0.032
K93	219	-2.88	61.6	0.016	-2.92	61.6	0.016

Measured Mg isotope data, Ca/Mg ratios and Mg/Ca ratios and adjusted data by orthogonal projection.

Table 4.4

Sample	Depth (m)	$\delta^{13}C$ carb[a] (‰ VPDB)	$\delta^{44/40}Ca$[b] (‰ SW)	$\delta^{13}C$ carb Projected	$\delta^{44/40}Ca$ Projected	Aragonite Fraction
K 20	146	0.420	-1.11	0.418	-1.14	0.055
K 21	147	0.075	-1.10	0.074	-1.12	0.010
K 24	150	1.49	-1.21	1.49	-1.21	0.197
K 25	151	1.74	-1.23	1.74	-1.23	0.230
K 27	153	3.27	-1.44	3.28	-1.34	0.433
K 28	154	3.65	-1.39	3.65	-1.36	0.482
K 31	157	5.18	-1.38	5.17	-1.47	0.684
K 32	158	6.70	-1.63	6.70	-1.58	0.885
K 35	161	7.22	-1.58	7.21	-1.61	0.953
K 38.5	164.5	6.87	-1.58	6.87	-1.59	0.908
K 40.5	166.5	6.64	-1.37	6.64	-1.43	0.877
K 41.5	167.5	6.97	-1.45	6.97	-1.45	0.921
K 42.5	168.5	6.47	-1.38	6.47	-1.41	0.854
K 43.3	169.3	6.85	-1.49	6.85	-1.44	0.905
K 45.5	171.5	6.29	-1.38	6.29	-1.40	0.830
K 49	175	6.26	-1.43	6.26	-1.40	0.828
K 54.5	180.5	5.74	-1.39	5.74	-1.36	0.758
K 56.5	182.5	4.89	-1.29	4.89	-1.31	0.646
K 61	187	4.79	-1.33	4.79	-1.30	0.633
K 63.9	188.9		-1.28		-0.97	0.003
K 67.4	193.4	2.58	-1.13	2.58	-1.15	0.341

[a]Carbon isotope data from LaPorte et al. (2009)

[b]Calcium isotope data from Holmden et al. (2012a)

Measured C and Ca isotope data and orthogonally projected data used to calculate the fraction of aragonite through the Hirnantian lowstand interval.

TRANSITION BETWEEN CHAPTERS 4 AND 5

As demonstrated up to this point, Mg isotopes serve as powerful tracers for geological processes as well as for paleo-ocean chemistry and ecology. Magnesium isotopes may also be applied to biological systems as important biogeochemical tracers of nutrient cycling, since Mg acts as a vital macronutrient for plants. Plants are expected to fractionate Mg isotopes as a result of uptake from the soil pool, as well as through a return flux to the soil, via litterfall decomposition. Due to these expected fractionation processes, the potential exists that densely vegetated areas can impact riverine Mg isotopic compositions, and consequently oceanic isotopic compositions. Chapter 5 will present findings on the overall extent of Mg isotope fractionation in a sugar maple (*Acer saccharum* Marsh.) dominated plot located in the Hermine Experimental Watershed, Québec, Canada. In addition, the impact of biogeochemical Mg-cycling on the continental weathering flux of Mg from the 'critical zone' to the ocean will be evaluated.

CHAPTER 5 – Magnesium isotope tracing of biogeochemical cycling of Mg in a forested ecosystem in Québec

Submitted as:

Kimmig S. R., Holmden C. and Bélanger N. Biogeochemical cycling of Mg and its isotopes in a sugar maple *(Acer saccharum* Marsh.) stand. *Geochim. Cosmochim. Acta.*

5.1. Abstract

Magnesium isotope fractionation is reported in a sugar maple (*Acer saccharum* Marsh.) stand in southern Québec, Canada, and on sugar maple seedlings grown from seeds in an artificial soil in the laboratory. Both mature trees and seedlings from the field, and the seedlings in the laboratory, show sizeable within-tree Mg isotope fractionation. However, only the laboratory seedlings show isotopic fractionation during Mg uptake into the fine roots from the soil substrate. By contrast, the fine roots of mature maple in the field have δ^{26}Mg values (–0.60 ± 0.34‰) that are identical to the plant-available Mg in the soils, as measured in soil solutions collected from three depths: 0, 15, and 50 cm, yielding –0.65 ± 0.15‰. Additionally, maple seedlings harvested from the forest floor were measured whole to discount the possibility that within-tree fractionation processes control the δ^{26}Mg value of fine roots. Three seedlings (two reconstructed and one digested whole) and the 0 cm lysimeter, placed beneath the forest floor, yield identical δ^{26}Mg values. Differences in Mg isotope fractionation between field and laboratory grown maple due to uptake is reminiscent of conflicting literature reports of this process in various plants. In the present study, the difference is attributed to the presence or absence of arbuscular mycorrhizal fungi. The finding that Mg isotopes are not fractionated by maple has implications for the export flux of weathered Mg to first-order streams, rivers, and eventually oceans, where it is a key component flux of the ocean Mg cycle. It has been reported that the Mg flux from continental weathering may be isotopically light compared to bedrock sources, due to plant or secondary mineral formation favoring retention of heavy isotopes in weathering environments. Some support for the heavy isotope retention in vegetation comes from laboratory grown plants that may behave differently than plants in the field. Precipitation at the study site has a very low δ^{26}Mg value –1.66 ± 0.21‰, decreasing to –2.22‰ ± 0.15‰ during hurricane Irene, which passed over the study site in 2011. These values may be indicative of carbonate dust as a source of Mg in precipitation. The 1N HNO_3

leach of the parent C mineral soil, which is often used to identify of minerals that may be releasing Mg and other base cations into plant-available soil pools, has nearly the same δ^{26}Mg value (–0.66‰) as the Mg dissolved in soil solutions (–0.65 ± 0.15‰), and the bulk forest floor (–0.64‰). Even more revealing is that the Mg/Ca molar ratio of this acid leach (0.17) is nearly identical to the bulk Mg/Ca ratio of the plant aboveground biomass in the study plot (0.14). This treatment is therefore not releasing Mg from primary minerals in the soil, but rather from secondary minerals (clays) that have taken up plant-recycled Mg and Ca that has filtered down through the soil profile from the forest floor. This finding attests to the dominance of the cache of plant-recycled Mg as a source of Mg to sustain the nutritional requirements of the forest.

5.2. Introduction

Magnesium (Mg) is a major element, the 8th most abundant in continental crust (Taylor and McLennan, 1985), the 4th most abundant species in seawater (Millero, 1974), and an essential macronutrient for plants. Magnesium is the coordinating cation of the chlorophyll molecule, an enzyme activator for energy metabolism and synthesis of organic molecules, is required for the formation of RNA in the nucleus, aids in phosphate metabolism (ATP) and plant respiration, and is involved in cellular pH regulation and cation–anion balance (Wilkinson et al., 1990; Marschner, 1995; Epstein and Bloom, 2005; Barker and Pilbeam, 2007). Magnesium is found in the plant available exchange pools in soils (Wilkinson, 1990), where it is taken up by fine roots of plants as an aqueous complex ($Mg(H_2O)_6)^{2+}_{(aq)}$). Inside the plant, Mg exists in both the free ion and chelated forms, and is translocated when needed from older plant tissues to younger growing leaves, seeds and roots (Wilkinson, 1990; Marschner, 1995; Barker and Pilbeam, 2007; Black et al., 2008).

The isotopes of Mg (^{26}Mg/^{24}Mg and ^{25}Mg/^{24}Mg expressed as δ^{26}Mg and δ^{25}Mg, respectively) can be used to trace elemental Mg cycling in Earth surface environments, due to isotopic fractionations that result from processes affecting Mg, such as diffusion, ion exchange, and mineral precipitation reactions. On the continents, weathering of Mg and Ca silicate minerals is an important regulator of atmospheric CO_2 and climate on million-year timescales (Eq. 5.1) (Berner et al., 1983).

$$(Mg, Ca)SiO_3 + 2CO_2 + 3H_2O \rightarrow (Mg, Ca)^{2+} + 2HCO_3^- + Si(OH)_4 \quad (5.1)$$

Mineral weathering provides vital nutrients to vegetative growth, which regulates atmospheric CO_2 on shorter time-scales and neutralizes acidic deposition. Processes that accelerate mineral weathering include: (1) physical and biochemical changes in soils by the rooting activity of plants, (2) cycling of vegetative organic matter, and (3) oxidation of organic matter to generate soil CO_2 and carbonic acid (Drever, 1994; Berner 1997; Walker et al., 2003; Derry et al., 2005).

Field and laboratory studies demonstrate that plants and fungi can fractionate Mg isotopes (Black et al., 2008; Bolou-Bi et al., 2010, 2012, 2016; Fahad et al., 2016; Tipper et al., 2010, 2012b; van der Heijden et al., 2013, 2014a, b; Opfergelt et al., 2012, 2014; Mavromatis et al., 2014, 2016). Fractionation occurs where Mg is drawn into the plant, between the fine roots and nutrient solution source, and within the plant between different tissues (e.g., roots, shoots/stem and leaves). Fractionated Mg isotopes are returned to soil nutrient pools in litterfall. Some of this Mg is recycled back into the plant after its release to soil waters through litter degradation, and some is lost to groundwater, streams, and rivers. A question of importance in Mg isotope research relates to the δ^{26}Mg value of the continental weathering flux of Mg to the oceans on a global scale. Is it a reflection of mineral weathering processes or nutritive Mg-cycling processes in vegetated landscapes?

Mineral weathering contributions of Mg and its isotopes to rivers have been evaluated in sparsely vegetated environments. Tipper et al. (2006a) investigated mineral fractionation in river water from a site in the Southern Tibetan Plateau and found that heavy Mg isotopes are retained in secondary minerals (clays) during silicate weathering while the companion waters are driven to lighter Mg isotope values. Wimpenny et al. (2011) confirm that rivers located in areas of sparse vegetation in Greenland record lower δ^{26}Mg values than bedrock. However, in this case, they attribute the fractionation to incongruent mineral weathering of carbonates and silicates rather than clay mineral formation. Several other studies have demonstrated that rivers in silicate catchments usually record lower δ^{26}Mg values than parent silicate bedrock with light Mg isotope enrichment in both rivers and soil solutions commonly attributed to the incorporation of heavy Mg isotopes into secondary silicate phases such as clays, oxides, or amorphous phases (e.g., Brenot et al., 2008; Tipper et al., 2006b, 2008, 2010, 2012a,b; Teng et al., 2010; Opfergelt et al., 2012; Wimpenny et al., 2014a; Mavromatis et al., 2014), or the preferential adsorption of heavy Mg isotopes into the exchangeable sites of secondary silicates formed in the weathering environment (Pogge von Strandmann et al., 2012; Huang et al., 2012).

Biogeochemical cycling of Mg by vegetation may also result in the light isotope enrichment of environmental waters due to heavy isotope uptake in plants. For example, Black (2008) showed that a nutrient solution with a known initial Mg isotopic composition used to grow wheat, hydroponically, shifted to lower δ^{26}Mg values over the course of plant growth. However, contrasting results have been reported in the field. Using isotopically enriched Mg isotope tracers, van der Heijden et al. (2013) reported that fine roots were enriched in light Mg isotopes compared to soil solutions and the plant-available cation exchange pool, with which the soil solutions were in equilibrium, in the soils of a beech tree stand. They attributed their findings to Mg isotope fractionation occurring during uptake of Mg into tree fine roots, but recognized that uptake related fractionation alone couldn't account for the magnitude of the effect that they observed. Instead, they suggested that the light Mg isotope enrichment in the roots could be attributed to an uptake of Mg from an unidentified nutrient source, such as Mg from the weathering of biotite, mediated to the roots by mycorrhizal fungi activity in the soil. Alternatively, they suggested that an originally heavy signature within the roots could be lost to mixing with unlabeled phloem sap moving down into the roots during Mg-cycling within the tree (van der Heijden et al., 2013).

Xylem flow is uni-directional along the transpiration stream (from roots to foliage) and appears to favor light isotopes of Mg, as rye grass and clover plants exhibit an enrichment in light isotopes from roots to shoots, and in spruce trees, foliage is lower in δ^{26}Mg value than roots and stemwood (Bolou-Bi et al., 2010, 2012). By contrast, xylem exudates and leaves are higher in δ^{26}Mg values than roots in wheat plants studied by Black et al. (2008). Fractionation of Mg isotopes during the translocation (phloem flow) of Mg between plant tissues may be thought of as an ion exchange process involving a mobile phase (aqueous Mg ions) and an immobile ion exchange complex. However, not much is presently known about the speciation of Mg during these processes of internal transport between plant tissues. In addition to translocation, the formation of chlorophyll may contribute to the low δ^{26}Mg values in leaves by the incorporation of light Mg isotopes into chlorophyll during synthesis (Galy et al., 2001; Young and Galy, 2004; Black et al., 2006, 2008; Ra and Kitagawa, 2007; Ra, 2010). The fractionating step might occur during chelation by the enzyme Mg-chelatase, which could favor a kinetic isotope driven enrichment of light isotopes in the Mg-bearing precursor to the chlorophyll molecule (Walker and Willows, 1997; Willows, 2003). On the other hand, the chlorophyll extracted from English Ivy is

higher in δ^{26}Mg than whole leaves (Black et al., 2007), indicating that species-dependent fractionation effects are real and should be considered carefully.

In this paper, Mg isotope fractionation in sugar maple (*Acer saccharum* Marsh.), an emblematic tree species in Canada, is investigated in the field and laboratory. The aim of the study is to evaluate the relative importance of plant *vs.* soil mineral weathering induced fractionation of Mg isotopes in a first-order stream exporting Mg from the 'critical zone'. Measurements of δ^{26}Mg values in fine roots, stemwood, xylem exudates (sap), foliage (senescent and photosynthesizing), and litterfall from mature sugar maple trees and seedlings are presented, as well as soil (solid and liquid phases), rock, throughfall, bulk precipitation, and stream water. In addition, sugar maple seedlings were cultivated in the laboratory to help isolate the tree induced fractionations of Mg isotopes from other sources of fractionation that might be occurring in the field.

5.3. Study site and sampling methods

5.3.1. Study site description

The study was conducted in the Hermine Experimental Watershed (HEW), a first-order spring-fed catchment located within an unmanaged northern hardwood forest of the *Station de Biologie des Laurentides* (SBL) of *Université de Montréal*, approximately 80 km north of Montréal, Québec, Canada, near the town of Saint-Hippolyte in the Lower Laurentians (Fig. 5.1). The forest has a mean basal area of approximately 29 m^2 ha^{-1} with a mean overstory age of ~ 90 years and heights ranging from 20 to 25 m (Courchesne et al., 2005). The present day forest is the result of secondary succession following a fire disturbance in the 1920s (Bélanger et al., 2004). Mean July and December air temperatures are 19ºC and –10ºC, respectively, with mean annual precipitation of 1100 mm, 30% of which falls as snow. Overstory vegetation is ~ 65% sugar maple, with subsidiary populations of American beech (*Fagus grandifolia* Ehrh.), red maple (*Acer rubrum* L.), yellow birch (*Betula alleghaniensis* Britt.), paper birch (*Betula papyrifera* Marsh.), balsam fir (*Abies balsamea* (L.) Mill.), and bigtooth aspen (*Populus grandidentata* Michx.) (Liu and Côté, 1993; Vizcayno-Soto and Côté, 2004; Bélanger et al., 2004). Understory vegetation consist primarily of striped maple (*Acer pennsylvanica* L.), hobble-bush (*Viburnum lantanoides* Michx.), wood fern (*Dryopteris* sp.), and lycopods (*Lycopodium* sp.).

The bedrock of the watershed is an anorthosite of the Morin anorthosite-charnockite complex within the Grenville Province with ages between 1165 Ma and 1135 Ma (Doig, 1991;

Friedman and Martignole, 1995). The study site is situated approximately five kilometers west of an anorthosite-orthopyroxene granitoid contact zone and southeast of a series of banded granitic gneisses, charnockite gneiss, orthopyroxene bearing granitoids, and marble (Martignole and Schrijver, 1970; Emslie, 1975). During the last glaciation, ice sheets covered the landscape, advancing from the northwest. The forests are developed on allochthonous glacial till, with a mineralogical makeup and chemical composition differing greatly from the underlying anorthosite bedrock (e.g., Bélanger et al., 2012), which outcrops in a few areas within the watershed. The soils are fairly thin (< 2 m to the bedrock) and consist mostly of Orthic Humo-Ferric Podzols (SCWG, 1998). The dominant Mg-containing minerals in the soil are chlorite and vermiculite, which likely weathered from biotite. The latter is not a primary mineral constituent of the anorthosite, and so must be contributed by the till. These alteration products were determined from strong acid leaches of the till reported by Bélanger et al. (2012), who found evidence for very high $^{87}Sr/^{86}Sr$ ratios indicative of Rb-containing biotite, as radioactive ^{87}Rb decays slowly to ^{87}Sr over long periods of geological time.

A permanent plot was established in the summer of 2010 located at 45.984°N and 074.014°W, 387 ± 11 m in a part of the HEW with overstory vegetation consisting primarily of sugar maple. This sugar maple dominated 'plot 0' is located just south of a previously established 'plot 1' weir (Courchesne et al., 2001; Bélanger et al., 2004), (Figs. 5.1, 5.2).

5.3.2. Sample collection

Zero-tension 'nested' lysimeters were installed in plot 0 of the HEW in June 2010 following the protocols detailed in MacDonald et al. (2007) at depths corresponding to directly below the forest floor (0 cm), upper B horizon (15 cm), and BC horizon (50 cm), which is below the rooting zone. Following installation, the lysimeters were allowed to equilibrate with soil solutions over several months during which time they were purged of water. Lysimeters were sampled for this study in October 2010, May 2011, and October 2012 using trace metal clean high density polyethylene (HDPE) bottles. Soils were identified and sampled during the installation of the lysimeters in plot 0 in June of 2010. The soil was visually confirmed to be an Orthic Humo-Ferric Podzol and consisted of five identified soil horizons in the following sequence: FH, Ae, Bhf (thin), Bf, BC, and C. The forest floor (FH horizon), lower podzolic horizon (Bf-BC), and mineral soil horizon (C) were sampled for Mg isotope study. A piece of exposed anorthosite bedrock was

also sampled from within the HEW.

Groundwater was collected in the autumn of 2009 from the spring source of the stream using trace metal clean HDPE bottles. Stream waters were also collected at low and high (following a rain event) flows in September 2010 just upstream from plot 0, near the HEW weir, as well as bulk sample collection during the months of July, August, and June of the following year. Lake water from Lac Triton, located ~ 0.5 km northeast of plot 0 (Fig. 5.1) was sampled at low and high levels with trace metal cleaned HDPE bottles. Rainwater was collected as bulk (wet and dry) deposition in a shielded funnel collector between July and September 2010 from continentally derived storm systems. The collector consists of funnels attached with Tygon® tubing to sample bottles contained within a cooler, and suspended on a tower at a height of 20 m to limit contamination from the canopy. The tower is located 500 m outside of the HEW. The sample bottles were completely covered with exception of the funnel inlet in order to limit evaporation prior to retrieval. Samples were collected in 1 L trace metal cleaned low density polyethylene (LDPE) bottles, filtered with 0.45 μm polycarbonate membranes, and acidified to ~ 0.2N HNO_3 with the addition of ultrapure 15N HNO_3. In August of 2011, hurricane Irene passed through the field site and was sampled as a separate event. Throughfall samples were collected in September of 2010 using temporary collectors in two locations within plot 0. The collectors consisted of funnels attached with Tygon® tubing to HDPE bottles on the ground. A plug of trace metal cleaned fibrous polyester was used in the neck of the funnel collector to block particulate matter from entering the collection bottle. Funnels, bottles, and Tygon® tubing for the collectors were trace metal cleaned in the laboratory prior to installation.

All mature sugar maple vegetation samples (foliage, stemwood, fine roots) were collected from the same tree, identified as 'Sugar Maple 3' (SM3). Diameter at breast height (DBH) (height at 1.3 m from the ground) of SM3 was 10.2 cm. Foliage from SM3 located in the upper half of the canopy was sampled in September of 2010 with a telescopic pole pruner prior to and during multiple stages of leaf senescence, as well as from the following year early spring canopy. Foliage samples were collected throughout the senescent period of SM3 and categorized by color, including (1) green foliage, (2) yellow/green foliage, and (3) yellow foliage. Stemwood was sampled in September of 2010, at ~ 1.3 m aboveground with a 4.1 mm-diameter Haglöf® increment borer. The wood cores were stored in the field in plastic drinking straws prior to being transported back to the lab for processing. Fine roots (< 2 mm diameter) were sampled at the base of SM3.

Fine root samples were taken in June of 2010 during the installation of the nested lysimeters, and again in September of 2010, by sampling a shallow pit dug at the base of SM3.

Leaf litterfall was collected in September of 2010. Only pristine sugar maple leaves without any evidence of decomposition were chosen for sampling. Throughout leaf senescence, litterfall was categorized by color denoted as yellow and red leaves. Yellow leaves were sampled as both attached to the tree and as leaf litter on the ground. Red leaves that were still attached to the tree could not be sampled as they were out of reach of the pole pruner, and so were collected only on the ground as litterfall. Sugar maple seedlings from the understory were also collected in September of 2010. Sugar maple xylem exudates (saps) were collected in April of 2011 during early, middle, and late harvest season from four individual adult sugar maple trees located within the study plot, with the exception of one tree that yielded samples only during the middle and late season. All saps were collected with polyethylene trace metal clean spouts and pails (Dominion & Grimm Inc., Montréal, Québec). Saps were filtered and refrigerated for transport, with long-term refrigerated storage in the laboratory.

In addition to the field study samples, two sugar maple seedlings were cultivated *in vivo* at the *Université du Québec à Montréal* (UQAM) to compare the findings in the watershed to a laboratory controlled setting. The seedlings were grown on a finely crushed and homogenized quartz/basalt (3:1) mixture. Seedlings were grown from non-germinated sugar maple seeds. A Mg-free standard Hoagland-type solution served as nutrient supply to the seedlings, making the basalt and the original seed stores the only Mg source available for the uptake by the seedlings during their growth. The seedlings were watered with 30 ml of the solution every other day. Both seedlings were harvested after five months of growth. One seedling was sectioned into roots, stem, and leaves, whereas the other was digested in bulk for comparison. The quartz/basalt growth mixture was also sampled for bulk digestion and sequential extraction.

5.4. Analytical methods

5.4.1. Sample laboratory preparation

All samples were transported to a class 10,000 trace metal clean room at the Saskatchewan Isotope Laboratory (SIL) for elemental and isotopic preparation. All solutions were filtered with a 0.45 μm polycarbonate membrane. Filters were pre-cleaned with 200 ml of ultrapure 0.3N HNO_3, followed by a rinse with 200 ml of ultrapure Milli-Q (18.2 MΩ·cm) water. Filter Mg blanks for

the initial HNO_3 and subsequent ultrapure water rinses were 0.005 μg/ml and 0.0008 μg/ml, respectively.

Prior to acid digestion, all vegetation samples were oven dried at 50ºC for 48 h and dry masses were recorded. Vegetation samples were digested in ultrapure 15N HNO_3 using polytetrafluoroethylene (PTFE) beakers covered with PTFE 'watch glasses', heated to 130ºC for 72 h. Following digestion, the sample solutions were dried down at 80ºC and reconstituted in a final sample stock solution volume of 30 ml in 0.3N HNO_3. Dried sap samples were treated with a mixture of high purity 30% hydrogen peroxide (H_2O_2) and 15N HNO_3 and refluxed for an additional 24 hours at 130ºC to assist in the degradation of complex organics. All sample solutions were then transferred to trace metal cleaned fluorinated ethylene propylene (FEP) bottles and exposed to simultaneous 185 nm and 125 nm ultraviolet (UV) radiation for a minimum of 72 h to assist in the degradation of residual organics in solution prior to elemental and Mg isotopic analysis. Clear solutions were obtained following UV exposure.

Foliage and litter sample whole leaf digestions were carried out in duplicate. Stemwood whole core samples were rinsed with ultrapure water to remove any surface particulates prior to being dried. Fine roots (< 2 mm) were rinsed and ultra-sonicated in Milli-Q water to remove any traces of soil from the root surface prior to being dried. Roots were visually inspected under a binocular microscope to check for attachment of surface particles (none were observed). Approximately 30 ml of each sap sample was aliquoted for elemental and isotopic analysis (0.4–1.5 g dried material). An additional aliquot of each sap was analyzed for sugar content (% Brix) analysis using a Hanna HI96811 digital refractometer. Seedlings from within plot 0 were sampled whole and rinsed with ultrapure water. The roots were cleaned following the previously described method. One seedling was acid digested whole, while the other two were sectioned by root (fine root and radicle), stem, and leaves. All water samples were filtered and acidified to ~ 0.2% HNO_3 with ultrapure 15N HNO_3 prior to elemental analyses.

Soils were oven-dried in the laboratory at 50ºC for 48 h to eliminate weighing uncertainties associated with evaporation from wet samples. The soils were then gently disaggregated to break up coarse pieces to a ≤ 2 mm fraction, which was assumed representative of the bulk soil. Approximately 3 g samples of the forest floor (FH horizon), and Bf-BC and C mineral soil horizons were subjected to a sequential chemical leach following protocols described in Bélanger and Holmden (2010) and Holmden and Bélanger (2010). The sequential extractions used in this study

are as follows: (1) 30 ml 0.1N $BaCl_2$ solution in a 50 ml trace metal cleaned centrifuge tube, (2) 30 ml 0.1N HCl extraction at room temperature (20–21ºC), (3) 30 ml 1N HNO_3 extraction at room temperature, and (4) treatment with 15N HNO_3 at 80ºC for ~ 10 h. For each of the first three steps of the extraction procedure, solutions were gently shaken for two hours. The $BaCl_2$ extractions were subsequently treated with an ultrapure $NaSO_4$ solution to remove Ba. Finally, a 150 mg aliquot of the residue was acid digested in a 2.5:1 mixture of concentrated HF–HNO_3 at ~ 120°C for 48 h, and then refluxed in 6N HCl several times after dissolution to remove fluorides. In addition, untreated samples from each soil horizon were also bulk digested using HF–HNO_3 acids and refluxed several times with 6N HCl. A finely powdered sample of anorthosite bedrock was also subjected to the sequential extraction procedure, as was the quartz/basalt growth mixture used in the laboratory pot experiment.

All sequential extraction solutions were filtered with trace metal cleaned 0.2 μm Teflon™ membrane syringe filters. The solutions were then transferred into acid cleaned FEP bottles and treated extensively with UV radiation (until the solutions cleared), followed by dry-down and reconstitution in 0.3N HNO_3 for elemental analysis, which also served as a stock solution for further purification of Mg from matrix elements prior to mass spectrometry. The 0.1N $BaCl_2$ extraction serves as a proxy for exchangeable cations, including Mg, Ca, and Sr. Drouet et al. (2005) proposed that the 0.1N HCl leach dissolves calcite, although Miller et al. (1993) initially proposed this treatment as an effective simulation of the weathering signature of the anorthosite bedrock. The 1N HNO_3 leach is believed to release some Mg from phyllosilicates (e.g., biotite, chlorite, vermiculite) and amphibole minerals (Nezat et al., 2007, 2008; Bélanger and Holmden, 2010), however, the 15N HNO_3 leach leaches more resilient minerals, such as feldspars, but mostly causes a more complete degradation of phyllosilicates. The residues following the concentrated HNO_3 leach were completely digested with concentrated HF–HNO_3 acids and refluxed several times with 6N HCl, in order to release Mg contained within feldspars.

5.4.2. Elemental concentrations and Mg isotope analyses

Vegetation digests were analyzed for trace and major elements by Perkin Elmer Inductively Coupled Plasma Optical Emissions Spectrometer (ICP-OES) using a 5–8 point calibration curve in the University of Michigan Biogeochemistry and Environmental Isotope Geochemistry Laboratory (BEIGL), with analytical uncertainties generally less than ± 10% (2σ). All other

sample solutions were analyzed by Thermo Scientific Element 2 HR-ICP-MS at the University of Michigan Keck Elemental Geochemistry Laboratory (KEGL), with analytical uncertainties generally less than ± 5% (2σ).

Aliquots of each sample solution corresponding to 30 μg of Mg were purified using gravity-flow cation exchange columns packed with 2 ml of BioRad® AG® MP-50 resin. Some samples with lower concentrations of Mg (e.g., rainwater) were processed at the 10 μg level. Most Mg samples were eluted through two sets of cation exchange columns, as described in Kimmig and Holmden (2017), with the exception of those that were notably high in transition metals (soil and rock sequential extractions). Due to the high Fe content of the soil digests and sequential leaches, these solutions were dissolved in 6N HCl and eluted through an anion exchange column (0.5 ml BioRad® AG® 50X8) to remove both Fe and Mn from the sample solution prior to cation exchange chemistry for the separation of Mg, then passed through the standard two column separation procedure.

Samples of approximately 1 ppm Mg dissolved in 0.3N HNO_3 were measured using a Thermo Scientific Neptune MC-ICP-MS instrument, housed in the Saskatchewan Isotope Laboratory (SIL), using specifications described in Kimmig and Holmden (2017). The $^{26}Mg/^{24}Mg$ ratios are reported in the conventional delta notation as permil (‰) deviations of the sample isotope ratios relative to the standard Dead Sea Metal 3 (DSM3) (Galy et al., 2003). The $^{25}Mg/^{24}Mg$ ratios were also measured to demonstrate the mass-dependently fractionating behavior of the samples in nature and in the mass spectrometer, thus, ensuring that the measurements are not affected by isobaric interferences (Equation 5.2, where x = 25 or 26; Fig. 5.3a, b). The long-term precision and accuracy of the measurements was monitored across differently tuned analytical sessions using interlaboratory standards Cambridge-1 (CAM1) with a $\delta^{26}Mg$ value of –2.62 ± 0.08‰ (2σ, n = 123) and DSM3 with a $\delta^{26}Mg$ value of –0.02 ± 0.09‰ (2σ, n = 103) (Galy et al., 2003), as well as an in-house mono-elemental standard solution (Mg Alfa Aesar Specpure), which is isotopically distinct from CAM1 and DSM3 with a $\delta^{26}Mg$ value of –3.80 ± 0.11‰ (2σ, n = 116). In addition, four sample solutions were processed as duplicates through the entire Mg separation and isotope analysis procedure (indicated as 'Mg duplicate' in Table 5.1). In instances where sample material was digested, purified and measured more than once, 'duplicate digest' is indicated in Table 5.1. Uncertainties associated with the measurements of samples within the same mass spectrometry session are reported as two standard errors of the mean (2 se), whereas errors from data collected

over multiple mass spectrometry sessions are reported as two standard deviations (2σ). Total procedural blank for Mg chemical separations was < 16 ppb.

$$\delta\ {}^{x}\mathrm{Mg}_{\mathrm{smp}} = \left(\frac{\left({}^{x}\mathrm{Mg}/{}^{24}\mathrm{Mg} \right)_{\mathrm{smp}}}{\left({}^{x}\mathrm{Mg}/{}^{24}\mathrm{Mg} \right)_{\mathrm{DSM3}}} - 1 \right) \times 1000 \qquad (5.2)$$

5.5. Results

The total range in δ^{26}Mg values is 2.75‰ within the HEW (Table 5.1, Fig. 5.3a). All samples are mass dependently fractionated as indicated by the correlation between δ^{26}Mg and δ^{25}Mg with a slope of 0.516 ± 0.006 (2σ), compared to the theoretical equilibrium fractionation slope of 0.521 (Young and Galy, 2004). Deviation from the equilibrium fractionation line is reported as Δ^{25}Mg' (Table 5.1). The 15N HNO_3 leach of the C horizon mineral soil yielded the highest δ^{26}Mg value of the studied samples yielding –0.01‰. Throughfall yielded the lowest value of –2.76‰.

The total range of δ^{26}Mg values for maple seedlings grown in the pot experiment is 1.72‰ (Table 5.2). These samples yielded a slope of 0.514 ± 0.010 (2σ) on the three isotope plot (Fig. 5.3b). The seedlings were grown in a mixture of ground basalt and quartz sand. The HF–HNO_3 digest of the quartz/basalt residue (after sequential leaching) yielded the highest δ^{26}Mg value in the pot study of +0.43‰. A sugar maple seed yielded the lowest value of –1.30‰.

The following sections report the results obtained for δ^{26}Mg and elemental concentrations in each of the studied compartments of the HEW and pot experiment.

5.5.1. Vegetation

Isotopic and elemental data for vegetation, including fine roots, stemwood, foliage, litterfall, seedlings, and xylem exudates (saps), are reported in Table 5.1, for dry sample masses. Averages for each vegetation type are illustrated in Figure 5.2. Fine roots yielded an average δ^{26}Mg value of –0.60 ± 0.34‰ (2σ, n = 2) and an average Mg concentration of 1015 μg/g. Stemwood δ^{26}Mg values yielded an average δ^{26}Mg value of –0.70 ± 0.18‰ (2σ, n = 2) and an average Mg concentration of 174 μg/g. Foliage exhibits the greatest variability in δ^{26}Mg values, ranging between –1.32‰ and –0.86‰. Categorized by leaf color and whether the leaves were sampled

attached to the tree or as litterfall, the autumn 2010 sampling period yielded: (1) red litterfall with an average δ^{26}Mg value of –1.19 ± 0.36‰ (2σ, n = 2) and an average Mg concentration of 1089 μg/g, (2) green (autumn) leaves with an average δ^{26}Mg value of –1.12 ± 0.20‰ (2σ, n = 2) and an average Mg concentration of 1613 μg/g, (3) yellow/green leaves with an average δ^{26}Mg value of –0.98 ± 0.34‰ (2σ, n = 2) and an average Mg concentration of 1124 μg/g, (4) yellow leaves with an average δ^{26}Mg value of –0.96 ± 0.22‰ (2σ, n = 2) and an average Mg concentration of 1578 μg/g, and (4) yellow litterfall with a δ^{26}Mg value of –0.90‰ and Mg concentration of 970 μg/g. Green leaves from the same tree sampled the following spring (June 2011) yielded an average δ^{26}Mg value of –0.27 ± 0.38‰ (2σ, n = 2) and average Mg concentration of 1303 μg/g. Sugar maple saps collected at the beginning, middle, and end of the standard harvesting season in 2011 yielded δ^{26}Mg ranging between –1.10‰ and –0.79‰, with an average value of –0.95 ± 0.24‰ (2σ, n = 11) and an average Mg concentration of 274 μg/g. There is no correlation between δ^{26}Mg, Mg concentration, total sugar content, and time of harvest for the sugar maple saps.

One sugar maple seedling sampled from the understory in plot 0 was completely digested, yielding a δ^{26}Mg value of –0.60‰. The two other seedlings were sampled and sectioned into roots, stems, and leaves, and revealed increasing ^{26}Mg-depletion along the transpiration stream (roots > stems > leaves) (Table 5.1), in agreement with a study of Norway spruce (Bolou-Bi et al., 2012). Considering mass balance and using Eq. 5.3, where subscript *w* refers to the whole plant, *r* to root, *s* to stem, and *l* to leaves, and superscript *c* refers to Mg concentrations (μg/g), the weighted δ^{26}Mg of the whole seedling was calculated from the sectioned seedling.

$$\delta^{26}\mathrm{Mg_w} * \mathrm{Mg_w^c} = \delta^{26}\mathrm{Mg_r} * \mathrm{Mg_r^c} + \delta^{26}\mathrm{Mg_s} * \mathrm{Mg_s^c} + \delta^{26}\mathrm{Mg_l} * \mathrm{Mg_l^c} \quad (5.3)$$

Allometric equations (reported in Lambert et al. (2005)) were applied for estimating the aboveground dry biomass compartments of sugar maple, using the diameter at breast height (DBH) measurement recorded during sampling to calculate the total woody component biomass (stemwood and bark) as well as tree crown biomass (foliage and branches) of the studied SM3 tree in plot 0. Total nutrient mass (g) was assessed for each aboveground compartment using average stemwood and foliage concentrations from Table 5.1 and estimates for bark and branches provided in the literature (Chatarpaul et al., 1985). The results are reported in Table 5.3. Stemwood and bark

retain 57% of the Mg in sugar maple trees (33% and 24%, respectively) while foliage and branches contain 43% (20% and 23%, respectively). When considering that roots may contain up to ~ 15% of the total nutrient content of a sugar maple tree (Whittaker et al., 1974), the values for the aboveground inventory of Mg are reallocated to ~ 50% for stemwood and bark (29% and 20%, respectively), and to ~ 36% for foliage and branches (16% and 19%, respectively).

The DBH measurements from every tree (sugar maple and others) within plot 0 were also collected, with which the basal area for the study plot was calculated (19.2 m^2 ha^{-1}). Using the basal area for each tree and the entire plot, the total mass of nutrients per hectare may be calculated. Total foliage inventory of the trees in plot 0 was used as a representative estimation of the uptake rate of Mg on an annual basis (296.2 ± 184 mol ha^{-1} yr^{-1}). Allometric equations developed by Lambert et al. (2005) were also applied to every tree in plot 0 in order to determine the total elemental content of base cations stored in the aboveground biomass nutrient compartments, the results of which yielded 3,068 g (126 mol) of Mg and 36,004 g (898 mol) of Ca in the study plot.

5.5.2. Water samples

Isotopic and elemental data for bulk precipitation, throughfall, stream water, and soil solutions are listed in Table 5.1, with average δ^{26}Mg values illustrated in Fig. 5.2. Bulk precipitation δ^{26}Mg values range between –1.73‰ and –1.58‰, with an average value of –1.66 ± 0.20‰ (2σ, n = 2) and an average Mg concentration of 0.057 μg/ml. Hurricane Irene, which passed through the HEW in August of 2011, yielded a δ^{26}Mg value of –2.22 ± 0.15‰ (2σ, n = 2) and Mg concentration of 0.041 μg/ml. The $^{87}Sr/^{86}Sr$ ratio of hurricane Irene precipitation is 0.7089. Throughfall samples from two separate collectors in plot 0 yielded δ^{26}Mg values of –2.76‰ and –1.30‰ with an average Mg concentration of 0.066 ± 0.02 μg/ml. Stream water δ^{26}Mg values range between –0.77‰ and –0.43‰, with an average value of –0.59 ± 0.22‰ (2σ, n = 8) and average Mg concentration of 0.36 ± 0.10 μg/ml. Stream waters collected at low flow conditions may be used as a proxy for bedrock anorthosite weathering due to the stream being fed entirely by shallow groundwater which apparently flows through bedrock, while stream waters collected at high flow may be used as a more representative sampling of subsurface (soil water) flow into the stream (O'Brien and Hendershot, 1993; Bélanger et al., 2012). Despite this distinction, there is no correlation between high and low stream water flows and δ^{26}Mg values during the sampling period.

Water in the spring source to the stream yielded a $\delta^{26}Mg$ value of –0.52‰. Soil water $\delta^{26}Mg$ values range between –0.75‰ and –0.51‰ with an average of –0.65 ± 0.15‰ (2σ, n = 14) and an average Mg concentration of 0.39 ± 0.27 μg/ml, with no systematic trends with depth or season of sampling. Sampling of Lac Triton, a small lake in close proximity to plot 0 (Fig. 5.1), at low and high water levels yielded $\delta^{26}Mg$ values of –1.64‰ and –1.13‰ and an average Mg concentration of 0.38 ± 0.20 μg/ml.

5.5.3. Soils and bedrock

Isotopic and elemental data for bulk soil and bedrock acid digestions as well as sequential leach extractions are reported in Table 5.1. Effective cation exchange capacity (CEC_e) for soil horizons is reported in Table 5.4. The CEC_e quantifies the number of exchange sites on the surfaces of soil particles that have the ability to adsorb cations. These cations are easily exchanged with dissolved cations in soil solutions, and together constitute plant-available pools of base metal cations (Ross, 1995). Duplicate digestions of the anorthosite bedrock yielded an average $\delta^{26}Mg$ value of –0.21‰ ± 0.0‰ (2σ, n = 2). Bulk digests of each soil horizon yielded the following $\delta^{26}Mg$ values: Forest floor –0.64‰, Bf-BC horizon –0.75‰, and C horizon –0.71‰. The $\delta^{26}Mg$ values of the C mineral soil is significantly isotopically lighter than the anorthosite bedrock, which supports the notion that the soils are not derived from the weathering of the bedrock but are, rather, from glacial till (Bélanger et al., 2012). The CEC_e is (reported in cmol/kg) calculated from the elemental concentrations in the 0.1N $BaCl_2$ extractions using conversion factors and calculations provided in Hendershot et al. (2007) (Table 5.4).

The CEC_e of the forest floor (FH horizon) (16.5 cmol/kg) is much higher than those of the underlying mineral soils (Bf-BC horizon 0.415 cmol/kg, C horizon 0.353 cmol/kg) or the anorthosite bedrock (1.51 cmol/kg), indicating that a large fraction of the exchange sites is hosted by organic matter (Table 5.4) (Ross, 1995). The $\delta^{26}Mg$ values for the CEC_e pools in each soil horizon (equivalent to the 0.1N $BaCl_2$ extracts) are: Forest floor (–0.59‰), Bf-BC (–1.65‰), and C (–2.07‰). The $\delta^{26}Mg$ values of the 0.1N HCl extracts are: Forest floor (–0.74‰) and C (–0.80‰). No $\delta^{26}Mg$ value is reported for the 0.1N HCl extract of the Bf-BC horizon due to its low concentration. The $\delta^{26}Mg$ values of the 1N HNO_3 extracts are: Forest floor (–0.30‰), Bf-BC (–0.66‰), and C (–0.66‰). The $\delta^{26}Mg$ values of the 15N HNO_3 extracts are: Forest floor (–0.43‰),

Bf-BC (–0.08‰), and C (–0.03‰ ± 0.06‰ 2σ (n=2)). The HF–HNO_3 digestion of the residues are: Forest floor (–0.37‰), Bf-BC (–0.69‰), and C (–0.65‰). The mass fractions of Mg for each of the applied minerals soil (Bf-BC and C horizon) sequential leaches (0.1N $BaCl_2$ through the 15N HNO_3 leaches) are reported in Table 5.5, with > 97% of the total amount of Mg contained within the 15N HNO_3 leach for both horizons.

5.5.4. Laboratory pot experiment

Isotopic and elemental data from the laboratory controlled pot experiment used to cultivate sugar maple seedlings are reported in Table 5.2 and Figure 5.4. Data include analyses of sugar maple seeds, roots, stems, and leaves of seedlings, a whole seedling and growth medium (quartz/basalt mixture), as well as as sequential leach extracts of the bulk soil mixture. Two individual sugar maple seeds yielded an average δ^{26}Mg value of –1.22 ± 0.22‰ (2σ, n = 2). Seedling roots (fine roots and radicle combined) yield a δ^{26}Mg value of –0.02‰, while the stem and leaves yielded δ^{26}Mg values of –0.52‰ and +0.01‰, respectively. The complete digestion of a whole seedling yielded a δ^{26}Mg value of –0.70‰. Applied to the quartz/basalt soil mixture, the sequential extraction procedure yielded: 0.1N $BaCl_2$ (–1.01‰), 0.1N HCl (–1.08‰), 1N HNO_3 (+0.07‰), 15N HNO_3 (+0.32‰), and the HF–HNO_3 digest of the residue (+0.43‰). The δ^{26}Mg value of a bulk digest of the quartz/basalt soil mixture yielded +0.13‰. The mass fractions of Mg in the applied sequential leaches of the quartz/basalt mixture are reported in Table 5.5, with the majority of Mg (> 86%) contained in the 15N HNO_3 leach.

5.6. Discussion

5.6.1. Bulk precipitation contributions of Mg to the forest

The HEW records the lowest reported Mg isotopic composition for rainfall to date, yielding –2.22 ± 0.15‰ (2σ, n = 2), collected during hurricane Irene in August of 2011. This compares to an average background δ^{26}Mg value for rainfall at the study site of –1.66 ± 0.21‰ (2σ, n = 2) (Figs. 5.3, 5.5, Table 5.1). Hurricane Irene was named as the first hurricane of the Atlantic Ocean 2011 season, which made landfall in North Carolina. From there, the storm moved north-northwest along the east coast of the United States, eventually crossing the international boundary with Canada where it delivered large amounts of precipitation to southern Québec (Fig. 5.6).

There appears to be little seawater-derived Mg in the precipitation delivered by Irene, at

least over the study area. As a case in point, coastal precipitation near Santa Cruz has a $\delta^{26}Mg$ value of –0.79 ± 0.05‰ (2σ, n = 5), which is nearly identical to the $\delta^{26}Mg$ value of seawater of –0.83 ± 0.09‰ (2σ, n = 90) (Tipper et al., 2010; Ling et al., 2011). Irene travelled over the Atlantic Ocean for days before making landfall, but it appears that any sea salts that the storm whipped into the atmosphere rained out before reaching Québec. As an additional test, the $^{87}Sr/^{86}Sr$ ratio of Irene precipitation was measured, yielding 0.7089. This is also different from seawater $^{87}Sr/^{86}Sr$ of 0.7092. In fact, it falls within the range of $^{87}Sr/^{86}Sr$ ratios in background precipitation at the study site, which averages 0.7104 ± 0.0030 (2σ, n = 14) (Bélanger et al., 2012). In addition, the Sr/Ca ratio of Irene precipitation is ~ 0.9 mmol/mol, which is also very different from the seawater Sr/Ca of ~ 8.5 mmol/mol.

The low $\delta^{26}Mg$ value of –2.22‰ for Irene precipitation is reminiscent of the low $\delta^{26}Mg$ values that characterize marine carbonate minerals such as aragonite (~ –1.8‰) and calcite (~ –2.0 to –4.0‰) (Saenger and Wang, 2014; and references therein), thus prompting the consideration of whether carbonate dust may have been the source of dissolved Mg in Irene precipitation. The storm track of hurricane Irene passed directly over several shallow Caribbean islands and the Bahamas where shallow water carbonates form at the present day. However, the Mg/Ca ratio of Irene precipitation (0.38) is too high to be aragonite (~ 0.003) (Veizer, 1983), which is the most voluminous polymorph of $CaCO_3$ produced in these settings, and the Sr/Ca ratio (~ 0.9) is too low as well. If carbonate is the source of Mg in precipitation over the study area, then the source of carbonate dust must be more locally derived; e.g., from the extensive outcroppings of lower Paleozoic carbonate in the St. Lawrence Lowlands, many of which are dolomitized. A simple apportionment calculation based on Mg/Ca ratios (assuming Mg/Ca is 1 for stoichiometric dolomite and ~ 0.07 for low magnesium calcite (LMC)) indicates that dolomite dissolution in the atmosphere may have contributed ~ 33% of the Mg to Irene precipitation. This in turn can be used to determine the $\delta^{26}Mg$ value of the contribution of dissolved calcite in Irene precipitation, yielding –2.46‰, if it is assumed that $\delta^{26}Mg$ value of dolomite is close to the average value of ~ –1.75 ± 1.08‰, n = 42, using data reported in Geske et al. (2015a).

The calculated value of the inferred calcite is consistent with the known range of $\delta^{26}Mg$ values in calcite (~ –2.0 to –4.0‰). However, the calculation only demonstrates the plausibility of the argument that Mg in precipitation may be mostly derived from the dissolution of carbonate dust in the atmosphere. Dry deposition collectors would need to be installed to test this hypothesis.

Besides marine carbonate, there are virtually no other known sources of Earth surface materials with such low δ^{26}Mg values. The main assumption is that there is no process associated with the transfer of Mg into and out of precipitation that fractionates Mg isotopes. Prior to this study, the lowest δ^{26}Mg value for precipitation was –1.44 ± 0.42‰ (2σ) measured in the Swiss Alps (Tipper et al., 2012b), which the authors also attributed to carbonate dust. There are few literature values for δ^{26}Mg in precipitation to compare. The range in published values (not including this study) is –1.59‰ to –0.51‰, which gives an average value of –0.85 ± 0.58‰ (2σ, n = 17), and is similar to the δ^{26}Mg value of seawater (Pogge von Strandmann et al., 2008a; Tipper et al., 2010, 2012b; Riechelmann et al., 2012; Bolou-Bi et al., 2012; Mavromatis et al., 2014; Teng, 2017).

5.6.2. Source apportionment of Mg to Lac Triton

Despite the low average δ^{26}Mg value (–1.66 ± 0.21‰) of precipitation at the study site, there is little direct evidence for an atmospheric fingerprint of Mg in surface and shallow groundwater (i.e., soil, stream and spring water), which averages –0.63 ± 0.18‰ (2σ, n = 21). The one exception is Lac Triton, which has a δ^{26}Mg value of –1.38‰ ± 0.73‰ (Fig. 5.1, Table 5.1). Assuming that the δ^{26}Mg value of Lac Triton is controlled by two-component mixing between rainfall and shallow groundwater, the volume fraction of rainfall in Lac Triton may be calculated using the mass balance Equation 5.4, where rainfall (not including Irene) is denoted (*atm*), shallow groundwater is (*lys*) because the shallow groundwater composition is collected by the lysimeters, and Lac Triton is denoted (*triton*). A derivation of Equation 5.4 may be found in Stewart et al. (1998). Substituting the average values for the compositions of the mixing end-members (δ^{26}Mg and Ca/Mg molar ratios) into Eq. 5.4 (Table 5.1), it is found that 81% of the water in Lac Triton is derived from rainfall.

$$\frac{Mg_{atm}}{Mg_{triton}} = \frac{Mg_{atm}}{Mg_{atm}+Mg_{lys}} = \frac{\left(\frac{Ca}{Mg}\right)_{lys}\left(\delta^{26}Mg_{lys} - \delta^{26}Mg_{triton}\right)}{\left(\frac{Ca}{Mg}\right)_{atm}\left(\delta^{26}Mg_{triton} - \delta^{26}Mg_{atm}\right)+\left(\frac{Ca}{Mg}\right)_{lys}\left(\delta^{26}Mg_{lys} - \delta^{26}Mg_{triton}\right)} \quad (5.4)$$

This is not the case, however, for water in the first-order stream which yields a small range of δ^{26}Mg values (–0.60 ± 0.23‰) at high and low flows that is indistinguishable from soil solutions (–0.65 ± 0.15‰). It is concluded that most of the water in Lac Triton (81%) must originate from

precipitation falling directly into the lake, and possibly from snow melt in the spring. It is observed that the lake level rises and falls with precipitation, although only a small fraction of this change can be ascribed to the seepage of shallow soil solutions at the lake margins. This calculation is, however, contingent upon the lake being well mixed. Alternatively, the samples collected from Lac Triton may simply represent a stratified water body. The sampling of Lac Triton was performed in the uppermost layer (epilimnion) of the water body. The possibility exists that the samples collected are not representative of a homogenous lake signal, but rather a sub-sampling of atmospherically derived Mg near the surface while at depth, the waters consist primarily of a groundwater signature. Additional sampling would be required to test this hypothesis.

5.6.3. Mg isotope fractionation during leaf senescence

Studies have demonstrated that 6–25% of total Mg in plants is associated with chlorophyll (Marschner, 1995). Another 5–10% of Mg in leaves is immobilized in the pectate of cell walls or precipitated as soluble salts (phosphates). The remaining 60–90% of Mg in leaves is extractable with water (Marschner, 1995). From these data it can be seen that plants require Mg for purposes other than the synthesis of chlorophyll, such as the activation of enzymes in energy metabolism, formation of RNA, activation of amino acids by ATP, plant respiration, and the regulation of cellular pH regulation as well as for cation–anion balance (Wilkinson et al., 1990; Marschner, 1995; Epstein and Bloom, 2005; Barker and Pilbeam, 2007). Magnesium is also present in both the mobile free ionic state as well as a complex with organic ligands (Mengel and Kirkby, 2001). Despite only a fraction of the Mg in foliage devoted to chlorophyll, the majority of studies measuring chlorophyll report low δ^{26}Mg values, an indication that the molecule incorporates isotopically light Mg during its synthesis (Galy et al., 2001; Young and Galy, 2004; Black et al., 2006, 2008; Ra and Kitagawa, 2007; Ra, 2010). In this study, and in a study of Norway spruce (Bolou-Bi et al., 2012), leaves are the lightest tissues of the plant, a result consistent with chlorophyll being low in δ^{26}Mg value. However, there are also exceptions to this rule, English Ivy and marine phytoplankton appear to sequester heavy Mg isotopes during chlorophyll synthesis (Black et al., 2007; Ra and Kitagawa, 2007). It was suggested by Black et al. (2006) that the low δ^{26}Mg value for chlorophyll in wheat grass might be due to the preferential binding of light isotopes of Mg to the protein backbone of Mg-chelatase, which is then transferred to chlorophyll molecule. This mechanism is supported by the known preference for light isotopes of Mg on

organic exchange sites of the cation exchange AG®50W-X12 resin (e.g., Chang et al., 2003).

Senescence is the final stage of leaf development. It is marked in deciduous trees by dramatic changes in the color of leaves before the onset of winter as a result of chlorophyll and chloroplast breakdown (Langmeier et al., 1993; Decoteau, 2005; Pessarakli, 2016). The breakdown of chlorophyll and chloroplast is so prominent during leaf senescence that progress is generally measured in terms of chlorophyll loss (Noodén et al., 1997). The benefit imparted to the tree by senescence is the translocation of nutrients into perennial tissues of the stemwood, which appears to give over-wintering species a cache of nutrients that can be utilized the following spring when the canopy is being reconstructed (Collier and Thibodeau, 1995). Chlorophyll is broken down during senescence, and the Mg is recovered from the leaves by organic acids and translocated by the phloem sap into the stemwood for storage (Black et al., 2008; Bolou-Bi et al., 2012, 2016). However, not all nutrients are resorbed and what remains in the leaves is returned to the forest floor as litterfall.

The removal of isotopically light chlorophyll-bound Mg is expected to drive leaves towards higher δ^{26}Mg values, and this is generally what is observed in the HEW with changes in leaf color: δ^{26}Mg values in yellow leaves > mixed yellow/green leaves > green leaves > red leaves. However, the unexpectedly low δ^{26}Mg values in red leaves requires further discussion. The red pigment, anthocyanin, belongs to a class of flavonoids which are water soluble vascular pigments usually responsible for red/violet colors in many flowers and fruits, and leaves in the case of higher plants (Davies, 2004). Anthocyanin production starts shortly after chlorophyll degradation begins. It is believed to serve as 'sunscreen' for the leaves, which helps to lengthen the time available for resorption of nutrients during the senescence period in elevated UV exposure environments (Hoch et al., 2001, 2003). As a result, the chlorophyll is actively photosynthesizing in red foliage late into the senescent period, which at least partly explains their low δ^{26}Mg values, though it is unknown why they are isotopically lighter than green leaves. However, δ^{26}Mg values in green leaves can also vary depending on the time of year.

Young leaves sampled in the spring of 2011 yield very high δ^{26}Mg values ranging from –0.40 to –0.13‰. These are the highest leaf values observed at the study site (Figs. 5.3, 5.5). Interestingly, the Mg concentrations in these leaves (~ 1300 μg/g) are similar to the concentrations in mature green leaves (~ 1600 μg/g), although the Ca concentrations are nearly 60% lower (Table 5.1). These data indicate that Ca and Mg are highly mobile between leaves and other tissues of the

tree during the early stages of leaf growth. One explanation, and the most likely scenario, is that the low δ^{26}Mg values of the autumn leaves may be the result of an increase of leaf chlorophyll content. The capacity for leaves to photosynthesize is contingent upon the season, and the concentration of chlorophyll increases from the spring until the autumn, which was observed for mature Sitka spruce trees (Lewandowska and Jarvis, 1977). The lower δ^{26}Mg values of the autumn green foliage compared to the heavy values obtained from the spring foliage could simply be the result of the increase in chlorophyll content over the course of the growing season, as chlorophyll production can increase by up to four-fold over the typical growing season from spring through autumn (Lewandowska and Jarvis, 1977). By applying mass-balance to this scenario (Eq. 5.5, where subscripts *gl, sl,* and *chl* refer to green autumn leaves, spring leaves, and chlorophyll, respectively), assuming 25% of the Mg content in the green autumn leaves is attributed to the presence of chlorophyll (400 μg/g), and using the δ^{26}Mg values for spring foliage (as containing little chlorophyll) and green leaves (as containing abundant chlorophyll) as end-members, it is determined that the δ^{26}Mg value of chlorophyll in the sugar maple leaf is –3.67‰. Considering the δ^{26}Mg values previously reported for chlorophyll-a in spinach (–3.01‰) and for *Anacystis nidulans* algae (–3.55‰) (Ra and Kitagawa, 2007), the value obtained in this study for chlorophyll in sugar maple leaves is not outside of the realm of possibilities.

$$\delta\,^{26}\mathrm{Mg}_{\mathrm{gl}} = \delta\,^{26}\mathrm{Mg}_{\mathrm{chl}} * f_{\mathrm{chl}} + \delta\,^{26}\mathrm{Mg}_{\mathrm{sl}}(1 - f_{\mathrm{chl}}) \qquad (5.5)$$

Alternatively, the initially heavy isotopic composition of spring leaves could be due to an isotopic gradient in leaves that develops as they grow, with later stages of leaf growth being isotopically lighter than earlier stages. Because only whole leaves were measured, including the stems, further evaluation of these hypotheses is not possible at this time. One additional consideration is the overwintering pool of Mg in the stemwood. If this cache of Mg is mostly derived from chlorophyll, which seems unlikely considering that only up to 25% of Mg in the leaf would be contained in the molecule, then early spring leaves should be isotopically lighter than autumn leaves, which is not what is observed. Another conceivable alternative is that a large fraction of the Mg in spring leaves comes directly from soil solutions (–0.65 ± 0.15‰), unfractionated, through the xylem flow. The average δ^{26}Mg value for sugar maple sap collected in 2011 is –0.95 ± 0.24‰, which is still too low to be the source of Mg to spring leaves unless there is a large fractionation effect favoring

heavy isotope enrichment in leaves, and is also at odds with the fact that leaves have the lowest δ^{26}Mg of any of the plant tissues.

5.6.4. Uptake fractionation of Mg isotopes by sugar maple

Holmden and Bélanger (2010) showed that tree fine roots preferentially take up light Ca isotopes, thus driving plant-available Ca in the soils to higher δ^{44}Ca values. This finding has been replicated in a number of other studies and appears to be robust (Farkaš et al., 2011, Cobert, 2011a; Hindshaw et al., 2011, 2013; Schmitt et al., 2012, 2013; Bullen and Chadwick, 2016). Mg isotopes are more complicated. Some authors have presented evidence that fractionation during uptake of Mg into plants is opposite to that of Ca isotopes (Black et al., 2008; Bolou-Bi et al., 2010; Tipper et al, 2010, 2012b; Bolou-Bi et al., 2012, 2016; Opfergelt et al., 2014; Mavromatis et al., 2014). One exception is a study by van der Heijden et al. (2013), who showed that beech trees in an experimental plot in France took up light isotopes of Mg, similar to Ca. Although there seems to be a consensus that heavy isotope fractionation during uptake of Mg into plants is more prevalent, most of these studies did not show the corresponding expected light isotope enrichment of Mg in soil pools that would accompany this sense of fractionation. The one exception is Black et al. (2008) who grew wheat plants on a Mg-limited hydroponic solution. They found that as Mg decreased in the solution (due to removal by the plants) the δ^{26}Mg value of the solution also decreased.

In contrast to the above studies, sugar maple in the HEW show no evidence for isotopic fractionation of Mg during uptake from soil solutions. While there exists plenty of within-tree fractionation in sugar maples, as with other trees and plants, the fine roots (–0.60 ± 0.30‰) and soil solutions (–0.65 ± 0.15‰) have nearly the same δ^{26}Mg values (Table 5.1). This finding raises the possibility that most of the Mg isotope fractionation observed in sugar maple, and perhaps for other tree species as well, reflects processes occurring within trees, rather than between trees and soil solutions during uptake of Mg at the root-tip. Recognizing this possibility, van der Heijden et al. (2013) suggested that the light isotope enrichment in the fine roots of their beech trees could simply reflect transport related fractionation of Mg isotopes in phloem sap as a result of its translocation along with other nutrients from the canopy down to the fine roots.

It is generally accepted that fibrous roots are concentrated in the uppermost 5–25 cm of the soil, including the litter layer on the forest floor (van der Heijden, 2014b). As a further test of the

hypothesis that tree fine roots of mature sugar maple do not fractionate Mg isotopes during uptake of Mg from soil solutions, sugar maple seedlings collected from the study plot were analyzed whole. The seedlings were rooted in the forest floor horizon where plant-available Mg (0cm lysimeter) has an average δ^{26}Mg value of –0.66 ± 0.13‰ (2σ, n = 6) (Table 5.1). One completely digested seedling yielded a nearly identical δ^{26}Mg value of –0.60‰ (Table 5.1, Fig. 5.3). Two other seedlings were dissected into roots, stem, and leaves with dry masses recorded. The roots yielded the highest δ^{26}Mg values (–0.41 ± 0.17‰, 2σ, n = 2) and the leaves the lowest values (–0.78 ± 0.11‰, 2σ, n = 2), thus replicating the within-tree fractionation of Mg isotopes observed for the mature sugar maples. However, the weighted average δ^{26}Mg values of the two seedlings (–0.66‰ and –0.73‰, calculated using Eq. 5.3) show that there is no net fractionation between the whole seedlings and the environment (Table 5.1). These findings confirm that the increase in δ^{26}Mg values of tree tissues sampled along the transpiration stream (roots/stemwood relative to canopy) is due to fractionation processes occurring within the tree rather than between the tree and the soil solutions surrounding the root tips.

Stemwood, bark, and branches of sugar maple account for ~ 81% of the Mg in the studied tree (Table 5.3), with the remainder retained in the foliage. The immobilization of Mg in stemwood and branches (and bark to a lesser extent) represents a net sink of Mg over the time scale of forest growth, since it is not returned to soil each year in litterfall. Although bark was not measured in this study, stemwood and roots have nearly identical δ^{26}Mg values of ~ –0.65‰ (Table 5.1). Because stemwood (the largest pool of Mg in sugar maple trees) is unfractionated relative to soil solutions (–0.70 ± –0.19‰), and autumn foliage (–1.12 ± 0.19‰) is isotopically lighter than stemwood, there must be a small but isotopically heavy pool of Mg in the tree that is fractionated in the opposite direction to the leaves. Another perspective on the same problem is the ~ 0.3‰ difference between yellow leaves (–0.94 ± 0.17‰), measured in the early autumn, and the Mg released from the litter on the forest floor in the 0cm lysimeter (–0.66 ± 0.13‰). One possibility is that sugar maple seeds, which are not considered in the allometric equations that partition Mg between different tree tissues (Lambert et al., 2005), are isotopically heavier than leaves. A literature search shows that maple seeds contain ~ 3000 μg/g of Mg (Cleavitt et al., 2011), which is ~ 2-times greater in Mg concentration than green leaves. In their study of hydroponically grown wheat, Black et al. (2008) showed that seeds do in fact have higher δ^{26}Mg values than leaves. The

missing pool of heavy Mg isotopes may also be sequestered into the bark and branches, which were not sampled as part of this study. The forest floor contains organic material other than leaves, such as seeds mentioned above, and other plant species (29% of the vegetation in the study plot is not sugar maple) which may be higher in δ^{26}Mg value than sugar maple leaves in summer and early autumn. However, despite the presence of other tree species in plot 0, the lysimeters were installed in an area occupied predominately by sugar maple. Lastly, the leaves measured in the early autumn may not be fully representative of the leaves that will drop in the late autumn.

5.6.5. Atmospheric dust and mineral weathering contributions of Mg to the forest

Using $^{87}Sr/^{86}Sr$ as a tracer, Bélanger et al. (2012) argued that only ~ 15 mol% of the plant-available pool of Ca in the HEW is from atmospheric sources. The remaining 85 mol% was released during weathering of soil minerals, mostly calcite and apatite, as determined from sequential leaches of the mineral soil. The C horizon is targeted for this purpose because the most soluble minerals would be prone to dissolution in the upper soils, particularly in the finely rooted horizons where organic matter is concentrated and the metabolic activity of the microbiome increases the acidity of the soil solutions, increasing the rate of mineral dissolution.

An alternative Ca apportionment model was also presented wherein the atmospheric sources of Ca were considered negligible, and the range in $^{87}Sr/^{86}Sr$ in soil leachates was attributed to the weathering of two groups of minerals: (1) calcite and apatite releasing Sr with low $^{87}Sr/^{86}Sr$ of ~ 0.7070, and (2) and biotite/chlorite releasing Sr with high $^{87}Sr/^{86}Sr$. McCourt (1993) reports a semi-quantitative mineral composition of the whole B horizon soil, determined by X-ray diffraction using the < 0.2 μm size fraction (Kittrick and Hope, 1963), yielding: 45.4% quartz, 15% plagioclase, 19% chlorite, 10% muscovite, 4% hornblende, 4% vermiculite, 1.5% biotite, 1% garnet and 0.1% apatite. Calcite was not found in the XRD analysis, possibly a result of it being completely dissolved. The soil protolith is the till left behind from the last glacial retreat in the region, approximately ten thousand years ago (Dyke and Prest, 1987; Dyke, 2004). The evidence for calcite comes from weak acid leaches of the deeper C horizon soil. Here, the 0.1N HCl treatment yielded a high Ca/Sr molar ratio of ~ 1600, which is typical of calcite of marine origin that may have become mixed into the till during glacial grinding. Alternatively, the calcite may have come from local deposits of Proterozoic marble belonging to the Morin terrain into which the Morin Anorthosite Suite intruded (Bélanger et al. (2012) Fig. 1). The $^{87}Sr/^{86}Sr$ ratio of the

inferred carbonate is 0.7070, which is determined from the y-intercept on plots of $^{87}Sr/^{86}Sr$ *vs.* Rb/Sr and $^{87}Sr/^{86}Sr$ *vs.* Ca/Sr, which denotes the end-member with the least radiogenic composition. The local marbles of middle Proterozoic age have not been measured, locally, but marble from similar age basement rocks of the Central Metasedimentary Belt of the Grenville Province in nearby Eastern Ontario fall in the range of 0.704–0.705 (Krogh and Hurley, 1968). These $^{87}Sr/^{86}Sr$ ratios are lower than the 0.707 signature of the inferred calcite in HEW soils, indicating that marble may not be the source of calcite. Alternatively, the partial dissolution of another mineral with higher $^{87}Sr/^{86}Sr$ may be driving the weak acid leach towards the more radiogenic composition observed. For example, a small release of radiogenic Sr from biotite could easily shift the $^{87}Sr/^{86}Sr$ of the marble from 0.704 to 0.707.

It could be argued that apatite, rather than calcite, is the main source of Ca in the weak 0.1 N HCl leach. Indeed, Bélanger et al. (2012) reported a strong correlation between $^{87}Sr/^{86}Sr$ and Ca/P in this leach ($R^2 = 0.98$), yielding an end-member apatite $^{87}Sr/^{86}Sr$ ratio of 0.7071 and a Ca/P ratio of 1.61. The leachate with the highest $^{87}Sr/^{86}Sr$ on this diagram ($^{87}Sr/^{86}Sr$ *vs.* Ca/P) yielded 0.7092. Again, there must be a mineral more radiogenic than the apatite in the soil that is liberating Sr simultaneously to the dissolution of apatite. There is also evidence for apatite dissolution in the stronger leaches (from Ca/P ratios), suggesting that some of the apatite may be mantled by minerals, such as biotite, and thus the crystal lattice structure of the biotite must be degraded by the acid attack before the inclusions of apatite are able to fully dissolve.

The Ca apportionment constraints utilizing $^{87}Sr/^{86}Sr$ as a proxy yield some insights into sources of Mg in the trees of the HEW. Calcite and apatite contain plenty of Ca but are low in Mg, and as such, these minerals cannot be the soluble source of Mg in HEW soils with low $^{87}Sr/^{86}Sr$. Dolomite has equal abundances of Ca and Mg but there is no evidence that it is present in the C horizon as an original component of the till. The Mg/Ca molar ratio of the 0.1N HCl leach of the C horizon gave ~ 0.004, which fingerprints calcite rather than dolomite. Instead, dolomite may be supplied to the surface soils in the HEW in the form of dust from local outcropping sources (section *5.6.1*). Rapid dissolution of dolomite dust in the acidic podzolic soils of the HEW would make it difficult to detect, even though it may be continuously supplied. Dolomite bedrock is fairly widespread in the St. Lawrence Lowlands and in Southern Ontario. Additional support for the dry deposition of dolomite into the HEW may be gleaned from the throughfall samples. Throughfall is defined as rain water that has percolated through the forest canopy, where dust and dry aerosols

containing Mg may be washed from the surfaces of foliage and branches (Lovett et al., 1985; Ragsdale et al., 1992). The low δ^{26}Mg value of throughfall (the lowest being –2.76‰) (Fig. 5.5) again suggests that carbonate dust may be a source of Mg, this time deposited on foliage and branches, with the more insoluble fraction (dolomite) subsequently washed into the underlying soil pools where it can dissolve at a later time in the acidic (pH < 5) podzolic soil water environment. Alternatively, the low δ^{26}Mg value of throughfall could reflect leaching of isotopically light Mg from leaf tissues. Because the δ^{26}Mg value of throughfall is lower than the whole leaves, the released Mg would have to be derived from a light component of Mg in leaves, such as chlorophyll, or there is fractionation of Mg isotopes associated with this release by an unknown mechanism.

The mineral weathering end-member with high $^{87}Sr/^{86}Sr$ is identified as biotite, with potential contributions from chlorite and vermiculite (Bélanger et al., 2012). These phyllosilicate minerals contain very little Ca in comparison to calcite and apatite, but they contain high concentrations of Mg. A positive covariance between $^{87}Sr/^{86}Sr$ and Mg/Sr ratios in the 1N and 15N HNO_3 leaches of the C horizon appears to target these minerals, with the Mg coming mostly from chlorite and vermiculite, and the radiogenic Sr component from biotite (Bélanger et al., 2012). The 15N HNO_3 treatment performed in this study released large quantities of Fe, in addition to Mg, which is another element that is concentrated in these minerals (Table 5.1). This raises the question, can the δ^{26}Mg values of the soil leaches fingerprint these phyllosilicate weathering sources of Mg in the HEW soils, and perhaps even help to identify which of these minerals has contributed the most Mg to the trees? A granite weathering experiment by Ryu et al. (2011) offers some important clues that can assist in answering this question.

Ryu et al. (2011) performed a simulated weathering experiment on the Boulder Creek granodiorite, which was crushed, cleaned, and sieved to produce a powder with grain size ranging between 45 and 850 μm. The sample powder was then packed into a flow-through column reactor maintained at pH = 1 (Ryu et al., 2011). A major aim of the study was to relate time-dependent changes in δ^{26}Mg, $\delta^{44/40}$Ca, and $\delta^{44/42}$Ca values in the output of the reactor to the sequential dissolution of minerals in the granodiorite powder, which contained: plagioclase (29.8 wt.%), quartz (29.0 wt.%), K-feldspar (10.4 wt.%), biotite (8.4 wt.%), chlorite (1.5 wt.%), hornblende (1.0 wt.%), titanite (0.9 wt.%), epidote (0.7 wt.%), apatite (0.3 wt.%), and calcite (0.2 wt.%). What is particularly relevant to this study is the fact that ~ 96% of the Mg in the granodiorite is distributed

between only three minerals with their respective δ^{26}Mg values listed in parentheses: biotite (–0.29‰), hornblende (–0.32‰) and chlorite (–1.82‰). The chlorite has a considerably lower δ^{26}Mg value than the other two minerals, which exhibit mantle-like δ^{26}Mg values. The average δ^{26}Mg value of mantle rocks and minerals is –0.25 ± 0.07‰ (2σ) (Teng et al., 2010), indicating that the Mg isotopes in biotite and hornblende were fractionated during igneous differentiation, and that chlorite alone must be responsible for the low δ^{26}Mg value of the whole-rock graonodiorite (–0.77‰). Chlorite, however, is not a magmatic mineral. It forms by chloritization of biotite, indicating that hot fluids passed through the rock at some stage in its history (Ryu et al., 2011). It is unclear whether the low δ^{26}Mg value of the chlorite is due to fractionation of Mg isotopes during the formation of chlorite or whether the Mg-bearing fluids were themselves low in δ^{26}Mg value.

The complete digest of the C horizon in the HEW is –0.71‰, which is also lower than the mantle inventory value, most likely due to the presence of chlorite in the till soil. Using the following fractions of mafic minerals from the XRD analysis of the B horizon: (1) chlorite (19%), (2) biotite/vermiculite (5.5%), and (3) hornblende (4%); and the Mg stoichiometry for chlorite, biotite, and hornblende from Ryu et al. (2011), it is determined that ~ 79% of the Mg in the HEW soil is in chlorite, ~ 14% is in biotite/vermiculite, and ~ 8% is in hornblende. Considering that hornblende is fairly resistant to weathering compared to chlorite and biotite, 87% of the easily weatherable Mg is in chlorite. Assuming that biotite/vermiculite and hornblende have mantle-like δ^{26}Mg values of –0.25‰, the δ^{26}Mg value of chlorite is determined to be –0.78‰, from isotope mass balance considerations.

The δ^{26}Mg values for the chlorite reported by Ryu et al. (2011), and a kaolinite reported in Wimpenny et al (2014a), are the lowest δ^{26}Mg values reported for silicate minerals to date. Ryu et al. (2011) found that their reactor released a pulse of Mg very early in the experiment, which they attributed to selective dissolution of the brucite interlayer in chlorite, noting that brucite ($Mg(OH)_2$) is 10^7 times more soluble than chlorite. Their reactor was held at the same pH as the 0.1N HCl leach employed in this work (pH = 1). It therefore follows that chlorite can also release large quantities of Mg to plant-available soil pools in the HEW at typical podzolic soil pH values (pH ~ 4–5, Courchesne et al., 2005). In addition, because chlorite and carbonate sources of Mg are both low in δ^{26}Mg value (compared to mantle-derived rocks) it will be difficult to distinguish

chlorite and dolomite sources of Mg to plant available soil pools in the HEW (the average δ^{26}Mg value for dolomite is –1.75; Geske et al., 2015a).

One puzzling feature of the sequential leach data for the HEW soils is the 0.1N $BaCl_2$ extraction, which yields very low δ^{26}Mg values (–2.07 to –1.65‰) (Table 5.5, Fig. 5.7). Wimpenny et al. (2014a) demonstrated that the exchangeable pool of Mg released from an acetic acid leach of illite, montmorillonite, and kaolinite is isotopically light (< –1.5‰). This may explain the low δ^{26}Mg values for the 0.1N $BaCl_2$ extractions performed in this study, if there are clays in the mineral soils of the HEW, which is likely given the warm humid summer climate of the study site. The amount of Mg liberated by both the 0.1N $BaCl_2$ and 0.1N HCl extraction is very small (< 0.2 wt.%) compared to the 1N HNO_3 (~ 2 wt.%) and 15N HNO_3 (~ 98%) extractions (Table 5.5). More importantly, the δ^{26}Mg values for the 1N HNO_3 treatments of the Bf-BC and C horizons (–0.66 ± 0.0‰, 2σ) are similar to the average δ^{26}Mg values for the forest floor bulk digest (–0.64‰) and the soil solutions (–0.65 ± 0.15‰, 2σ) (Figs. 5.5, 5.7, 5.8, Table 5.1). In addition, the Mg/Ca molar ratio of the 1N HNO_3 leach of the Bf-BC and C horizon (0.17 ± 0.01, 2σ) is nearly identical to the Mg/Ca ratio in leaves (0.15 ± 0.05, 2σ), forest floor (0.18), and soil solutions (0.18 ± 0.11, 2σ) (Fig. 5.8). In fact, it is basically the same Mg/Ca molar ratio as the entire aboveground biomass in the study plot, which is 0.14, as determined from the Mg and Ca allometry using all of the trees in plot 0. This Mg/Ca ratio of 0.14 has special significance. It describes the Ca and Mg nutritional requirement of the plants, i.e., plants in the study site require ~ 7 times more Ca than Mg. However, these are also the same relative proportions of Ca and Mg released by the 1N HNO_3 attack of the C horizon (~ 0.17). In the previous discussion, the 1N HNO_3 leach is used to identify the minerals that are most likely liberating Mg to the soil solutions. What is found here, however, is that the minerals are liberating Mg and Ca in exactly the proportions needed by the plants, which seems highly unlikely. There is no primary mineral identified from which Mg and Ca can be released with a Mg/Ca molar ratio of 0.17 in the study site. However, the formation of secondary clay minerals such as smectites could serve as an explanation. In forests under low pH conditions and where organic matter contents are high, such as the podzols of the HEW, mica minerals can transform to smectites (beidellite or montmorillonite) as a result of acid leaching (Churchman, 2012). The HEW soils have been described as containing up to 20% clays in the B and C horizons (Courchesne et al., 2005). The incorporation of the biologically-labeled δ^{26}Mg value and Mg/Ca

molar ratio into the clay interlayers, and subsequent release during the 1N HNO_3 extraction, could explain why the $\delta^{26}Mg$ value and the Mg/Ca ratio mirror that of the forest floor and soil solutions.

This brings into question the fact that the 1N HNO_3 leach is releasing Ca (and Mg) from apatite (and biotite), on the basis of the range of observed $^{87}Sr/^{86}Sr$ ratios in leachates performed by Bélanger et al. (2012). It now seems more apparent that presently unidentified secondary clay minerals, formed as a result of selective weathering of the multi-mineralic soil, are releasing the Ca and Mg captured in this leachate rather than primary igneous, metamorphic, and/or sedimentary minerals, and that radiogenic Sr has also been incorporated into these alteration products. The secondary minerals, formed by the weathering of the primary silicate minerals, are of greater significance to influencing the chemistry of the acid leaches used to examine the sources of metal base cation nutrients to plant-available soil pools over long periods of time, an impact that has previously been overlooked. The finding in this study emphasizes the role of the forest floor, and the overall aboveground biomass of the forest itself, as a cache of nutrient Mg and Ca that is tightly recycled over timescales of thousands of years. As a testament to the importance of recycled Mg and Ca in this system, altered soil minerals such as clays are completely overprinted by fluxes of Ca and Mg that are filtering down through the soil profile from the decomposing litter, capturing the recycled, forest-labeled signature. This biologically-labeled signature is subsequently released by the 1N HNO_3 extraction (Fig. 5.8). This mechanism also accounts for the fact that the soil solutions from the Bf-BC and C horizons have the same $\delta^{26}Mg$ value as the soil solutions from the forest floor, as well as similar Mg/Ca molar ratios. The succeeding treatment, the more aggressive 15N HNO_3 leach, yields Mg/Ca ratios > 10 for the Bf-BC and C horizons and very high $^{87}Sr/^{86}Sr$ ratios (Bélanger et al., 2012), indicative of a stronger dissolution of chlorite, biotite, and vermiculite.

5.6.6. Mg isotope signature of environmental waters exported from the watershed

Stream water exhibits fairly uniform $\delta^{26}Mg$ values at all times of the year sampled, as well as at high and low flows. The dissolved Mg in the stream water is isotopically heavier than bulk precipitation and throughfall (Table 5.1, Fig. 5.3), and similar to $\delta^{26}Mg$ values in soil solutions collected at all depths in the soil profile (Fig. 5.5). This is evidence that the stream water is mainly derived from the soil solutions. Bélanger et al. (2012) measured stream water $^{87}Sr/^{86}Sr$ ratios from samples collected at three times of the year yielding 0.70764, 0.70761, and 0.70791, for low,

medium, and high stream flows, respectively. They attributed the low $^{87}Sr/^{86}Sr$ ratios at low stream flow to anorthosite weathering and high stream flow characterized by high $^{87}Sr/^{86}Sr$ to larger Sr inputs from forest floor and mineral soil solutions. In contrast, a shift between low and high flow events for Mg isotopes that might indicate a change in the apportioning of Mg between bedrock weathering sources and shallow soil water sources is not observed. At all times of the year, soil solutions are the dominant source of Mg to the stream.

The forest floor (FH horizon) has the largest CEC_e in the soil profile and it has the highest Mg concentration (Tables 5.1, 5.4). As discussed above, this finding and the similarity in $\delta^{26}Mg$ values in all of the lysimeters below the forest floor is evidence that the Mg in the forest floor has mobilized downwards into the underlying soil horizons. Indeed, this process has been documented previously for Ca (using Ca isotopes) in base poor soils in a forest ecosystem in northern Saskatchewan (Holmden and Bélanger, 2010) and for Mg (using Mg isotopes) in a granitic forested catchment in the Vosges Mountains in northeast France (Bolou-Bi et al., 2016). Soil solutions are generally affected by the acidifying nature of decomposing litter, especially litter produced by sugar maple (Côté and Fyles, 1994) and acidity introduced via atmospheric deposition (e.g., Likens et al., 1996; Courchesne et al., 2002, Duchesne et al., 2010). In forest ecosystems with base-poor soils, biological cycling generates a greater pool of nutrients than the mineral soil pools (van der Heijden et al., 2014b), and plants retrieve the majority of their nutrients from the uppermost organic soil horizons via the exchangeable pool, including sugar maple trees (Chen et al., 2013). The degree of Mg isotope fractionation of litterfall decomposition is believed to be minimal, analogous to Ca isotopes studied in vegetation of the Central Siberian Plateau (Bagard et al., 2013; Mavromatis et al., 2014). Evidence of a lack of fractionation associated with litterfall degradation is provided by the bulk digest of the forest floor, which is representative of a long-term amalgamation of litterfall with various degrees of decomposition, yielding a $\delta^{26}Mg$ value identical to the soil solutions (–0.64‰) (Figs. 5.5, 5.8). However, freshly fallen leaf litter yields lower $\delta^{26}Mg$ values (< 0.9‰) than the forest floor (Fig. 5.5), a discrepancy which could be explained by the amount of isotopically light chlorophyll-bound Mg retained in the leaves after abscission during autumnal senescence (section *5.6.3*).

Ultimately, the stream waters reflect Mg returned to the soil pool by litterfall and recycled by vegetation, with minimal contributions from anorthosite bedrock weathering and bulk precipitation. Silicate weathering in the mineral soil horizons also contributes Mg to the stream.

However, Bélanger et al. (2012) estimated with the SAFE model that (at most) the Mg flux is 10% of the total amount of base cations (~ 100 mol ha^{-1} yr^{-1}). Atmospheric deposition contributes ~ 25 mol of Mg ha^{-1} yr^{-1}, and 400 mol ha^{-1} yr^{-1} of Mg returns annually to the forest floor as litterfall (Bélanger et al., 2002a). The average uptake rate of Mg in plot 0 of the HEW is ~ 296 mol ha^{-1} yr^{-1}, based on the inventory of Mg stored in the mature tree foliage in the study plot on an annual basis. This demonstrates that the litterfall return flux of Mg is nearly four times larger than the soil mineral weathering Mg-flux to the vegetation. This is a substantial amount of Mg returned to the soil pool in the HEW, and may lend support as to why the soil pools at each lysimeter depth record identical δ^{26}Mg values. As a result of these litter additions, the forest floor pool has accumulated a Mg repository of 7.5 to 9 kmol ha^{-1} over time, determined using a forest floor exchangeable Mg concentration of 0.025 mol kg^{-1} and a bulk forest floor density of 300 kg m^{-3}, corrected by depth to a density of 30 to 36 kg m^{-1}. This means that mineral weathering and atmospheric deposition contribute only ~ 1% and ~ 0.3% of Mg to that pool annually, respectively, while the litterfall Mg-flux contributes ~ 5%. The total uptake of Mg by the forest annually is ~ 3–4% of the total available Mg pool in the forest floor.

5.6.7. Sugar maple seedlings and Mg uptake, insights from a laboratory pot experiment

The field-based finding that there is no apparent isotopic fractionation of Mg during uptake into sugar maple trees is not validated by the laboratory pot experiment. The sugar maple seedlings grown in the laboratory are enriched in heavy isotopes compared to the plant-available Mg in the mixture of crushed basalt and quartz that was prepared as an artificial growth substrate. The complete digestion of one of the seedlings gave a δ^{26}Mg value of –0.70‰ while the plant-available Mg released by the weak 0.1N $BaCl_2$ and 0.1N HCl extractions of the artificial soil gave similar δ^{26}Mg values of –1.01‰ and –1.08‰, respectively (Table 5.2). These are somewhat surprising results given that basalt typically has a δ^{26}Mg value of –0.2 to –0.4‰ (Teng, 2017). It indicates that the basalt contains secondary clay minerals and possibly chlorite that formed through water rock interaction and/or metamorphism. The amount of Ca released in the 0.1N HCl leach suggests that there is also calcite in the sample. The stronger 1N HNO_3 leach yielded a δ^{26}Mg value (+0.07) that is more typical of basalt, and so the inferred calcite and chlorite are determined to be minor constituents of the basalt. Nevertheless, these low abundance minerals appear to control the δ^{26}Mg values of the 0.1N $BaCl_2$ and 0.1N HCl extractions, and the Mg released by these weak

treatments is the most likely accessible fraction available to the plants. The apparent fractionation factor is ~ 0.4‰, calculated from the difference in δ^{26}Mg values between the whole seedling (–0.70‰) and the pool of plant available Mg in the artificial soil (*avg*. –1.08‰). This value, however, assumes that all of the Mg in the seedling is derived from the artificial soil, but there is also the original store of Mg in the seed from which the plant grew that must be considered.

Two sugar maple seeds analyzed in this study yielded an average Mg concentration of 2227 ± 1317 μg/g (2σ) (Table 5.2). The average δ^{26}Mg value of the seeds is –1.22 ± 0.23‰ (2σ), which is low compared to the bulk digest of the whole seedling (–0.70‰). Another seedling grown in the lab was sectioned into roots (fine root and root radicle), stem, and leaves. Using Eq. 5.3, the reconstructed δ^{26}Mg value of the whole seedling is –0.36‰, which is also enriched in ^{26}Mg compared to the seeds. Assuming that the two seeds measured in this study are representative of the Mg concentrations of the seeds used to grow the seedlings, and that none of this Mg is lost from the seedlings, the fractions of Mg in each seedling contributed by the seeds is 0.79 (whole seedling) and 0.60 (reconstructed sectioned seedling). Accordingly, a large amount of the Mg originally contained within the seeds remains within each plant at the time of harvesting. The sectioned seedling is the larger plant, and this accounts for its lower fraction of seed-derived Mg. Using an isotope mass balance equation, the δ^{26}Mg value of the Mg taken up from the quartz/basalt soil can be calculated for each seedling, yielding +0.9‰ and +1.3‰. Ideally, these values should be identical if the two seedlings behaved similarly with respect to uptake related Mg isotope fractionation effects. However, this expectation must be considered in light of the assumptions regarding the original Mg concentrations in the seeds and their δ^{26}Mg values, which are based on measurements of representative seeds, not the exact seeds that were planted for study. The apparent uptake related Mg isotope fractionation factor $\left(\Delta^{26}\mathrm{Mg}_{soil}^{plant}\right)$ is ~ +2.0–2.3‰, where the subscript '*soil*' refers to the average δ^{26}Mg value (–1.08‰) for the 0.1N $BaCl_2$ and 0.1N HCl leaches of the quartz/basalt mixture. This calculated value for the Mg uptake related fractionation factor is the largest reported, thus far, in the literature. Even if the isotopically heavy Mg released by the 1N HNO_3 leach is combined with the Mg released from the first two treatments (0.1N $BaCl_2$ and 0.1N HCl), yielding a δ^{26}Mg value of –0.51‰ for the plant available pool of Mg in the artificial soil, the uptake related fractionation factor becomes ~ +1.45–1.8‰, which is still very positive.

The contrasting findings between the field and laboratory studies regarding uptake related Mg isotope fractionation in sugar maple requires an explanation. The most obvious one relates to

the sterile growth medium used in the pot experiment, which does not contain mycorrhizal fungi. These fungi have been shown to facilitate uptake of nutrients into the fine roots of plants, while the fine roots, in turn, exude carbohydrates to help support the growth of the fungi in what is widely considered to be a mutualistic symbiotic relationship (Smith and Read, 1997). For example, it has been reported that arbuscular mycorrhizae in the roots of sugar maple help the trees survive in acidic podzol environments where they would not normally thrive (Klironomos, 1995). Jones (1998) suggests that laboratory grown vegetation, especially vegetation grown hydroponically, can exhibit stresses not usually observed with vegetation grown on natural soils, and that this can result in morphological and physiological changes to the roots that negatively affect nutrient uptake. In practice, plants grown on sterile soil often fail to thrive, possibly accredited to the absence of symbiotic fungi in the growth medium. Only two of the six sugar maples seeded at the beginning of this study survived. The surviving plants exhibited signs of stress under the applied growth conditions and were quickly harvested before they also perished. This raises the question, is the lack of fractionation of Mg isotopes observed in the field study of sugar maple somehow related to the activities of the mycorrhizal fungi?

Ectomycorrhizal fungi have been shown to fractionate Mg isotopes. Fahad et al. (2016) cultured ectomycorrhizal fungi and non-mycorrhizal fungi in the laboratory on growth substrates including granite, the forest floor of a boreal forest podzol, and Modified Melin-Norkrans (MMN) fungal culture medium in order to measure the Mg isotopic fractionation effects associated with fungal uptake of Mg. They found that the magnitude and sign of the Mg isotope fractionation depended on the species of fungi cultured and the culture medium. For example, on the granite, the ectomycorrhizal fungi largely sequestered light isotopes, while on the forest floor substrate, the magnitude of the fractionation decreased and some species even switched toward taking up heavy isotopes of Mg. Non-mycorrhizal fungi largely sequestered heavy Mg isotopes with the exception of *Heterobasidion parviporum*, which exhibited a light Mg isotope preference, or no fractionation at all (Fahad et al., 2016).

Sugar maple is not known to form symbiotic relationships with ectomycorrhizal fungi (Klironomos, 1995), which are fungi that cover the surfaces of the roots. Therefore, the study of Fahad et al. (2016) is not directly applicable to the present study. However, the arbuscular mycorrhizae, which are fungi that penetrate the fine roots, commonly form symbiotic relationships with sugar maple. It is therefore tempting to conclude that the lack of Mg isotope fractionation

with uptake into sugar maple in the field is due to the colonization of these fungi, which pass unfractionated Mg isotopes from soil solutions to the fine roots of trees. A similar suggestion has been recently made by Pokharel et al. (2017), that Mg isotope fractionation induced by plant uptake could simply reflect a prior uptake of Mg into mycorrhizal fungi. It is recalled that wheat grass grown hydroponically by Black et al. (2008) also exhibited a clear signal of heavy isotope enrichment during uptake of Mg into the plant of ~ 0.5‰. Fields of wheat grass also form symbiotic relationships with arbuscular mycorrhizae, and the practice of inoculating wheat fields with arbuscular mycorrhizal fungi helps to reduce drought stress and increase overall productivity of the crop (Al-Karaki et al., 2004). By analogy with sugar maple grown in the field, the uptake related fractionation found under laboratory hydroponic growth conditions may also be absent in the field.

5.7. Conclusion

Translocation of Mg in sugar maple trees causes significant isotopic fractionation, as evidenced from differences in δ^{26}Mg values between roots, stemwood, and foliage within both juvenile (seedlings) and mature sugar maple trees. Photosynthesizing foliage collected from a mature sugar maple tree during autumnal senescence yields the lowest δ^{26}Mg values, followed by isotopically heavier values for stemwood and fine roots, which yield similar results. The δ^{26}Mg value of chlorophyll appears to be isotopically light compared to whole leaves, which is based on the finding that new leaves in the spring canopy are much higher in δ^{26}Mg value than mature leaves in the fall, a pattern that appears to reflect the known increase in chlorophyll concentration of leaves as the growing season progresses. In addition, leaves become heavier yet again during autumnal senescence, which is interpreted to reflect the breakdown of chlorophyll and the translocation of the isotopically light Mg into the stemwood, where it is stored for the winter and presumably used the following spring to help regrow the canopy. Bulk precipitation over the study site is low in δ^{26}Mg value, which is tentatively attributed to local/regional sources of carbonate dust, particularly dolomite, which is high in Mg. A Mg isotope apportionment calculation reveals that the vast majority of the Mg in a small lake located near the study site (Lac Triton) is directly sourced from rainfall and snow melt. However, results may also be contingent upon stratification of the lake layers.

There is no uptake related fractionation of Mg isotopes into sugar maple tree fine roots at the study site in the HEW. In addition, the Mg/Ca molar ratios of soil solutions and the first-order stream are nearly identical to the Mg/Ca ratio of aboveground plant biomass, indicating that plant-recycled fluxes of Mg and Ca completely mask the much smaller annualized input fluxes of Mg from atmospheric deposition and soil mineral weathering. In fact, even the 1N HNO_3 leach of the mineral soil in the C horizon yields the ~ 7:1 ratio of Ca to Mg observed in the vegetation at the study site, which is interpreted to be indicative of clay formation in the mineral soil that has captured a plant-derived ratio of the two cations. In other words, the 1N HNO_3 leach does not capture a primary mineral weathering signature, which is often assumed to be the case with this treatment.

Consistent with previous studies of uptake related fractionation of Mg isotopes in plants (e.g., Black et al., 2008; Bolou-Bi et al., 2010), sugar maple seedlings grown on sterile artificial soil in the laboratory take up heavy Mg isotopes over light Mg isotopes. This is not the case, however, for sugar maple grown in the field, where no uptake related Mg isotope fractionation is observed. The different behavior is attributed to the presence of arbuscular mycorrhizal fungi which colonize sugar maple roots in the field. It is proposed that forest stands of sugar maple receive much of their required nutrient load of Mg from the symbiotic relationship with these fungi, and that the fungi do not fractionate Mg isotopes. Thus, the uptake related fractionation of Mg isotopes in the laboratory grown seedlings reflects the absence of these fungi, serving as intermediaries in the transfer of Mg into the roots. The implication is that findings from laboratory studies of plant growth using sterile growth mediums may not be applicable to their field-based counterparts.

5.8. Figures

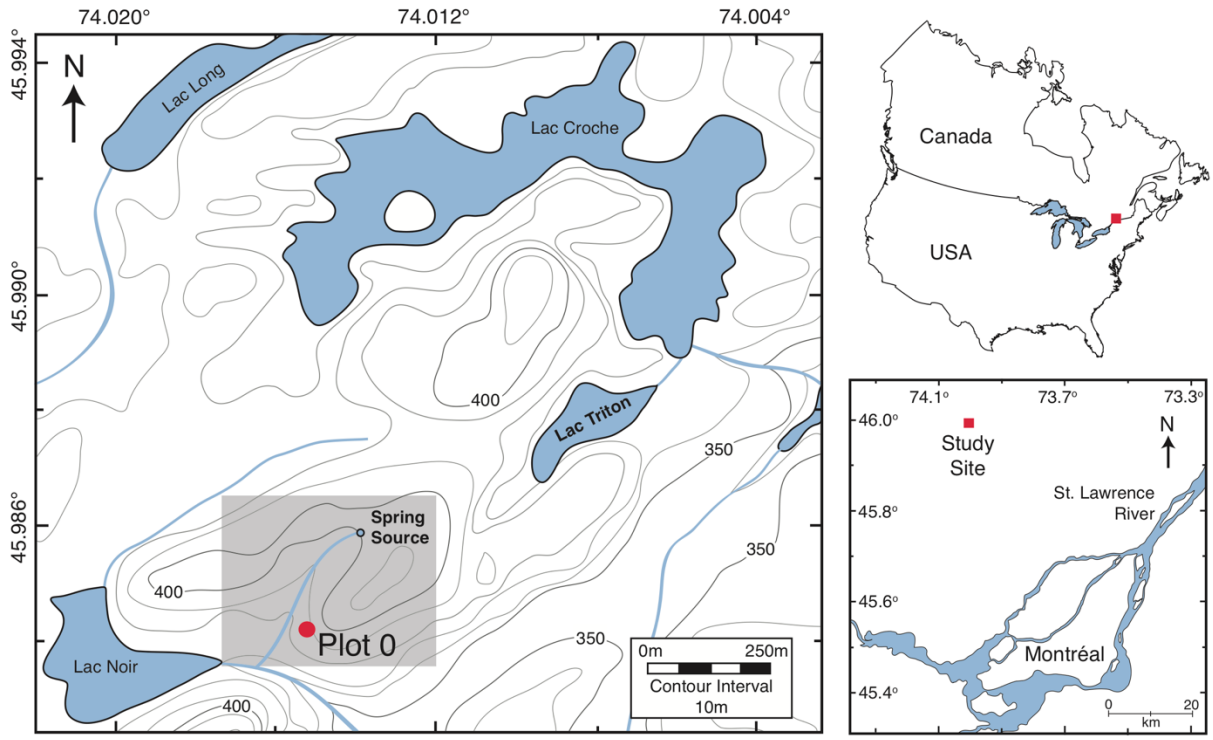

Figure 5.1 Maps showing the location of the study site in northeastern North America, located approximately 80 km north of the city of Montréal, Québec, Canada. The topographic map location of the study location is indicated by the red boxes, plot 0 is indicated by a red circle in the Hermine Experimental Watershed (HEW), shown as a gray shaded box.

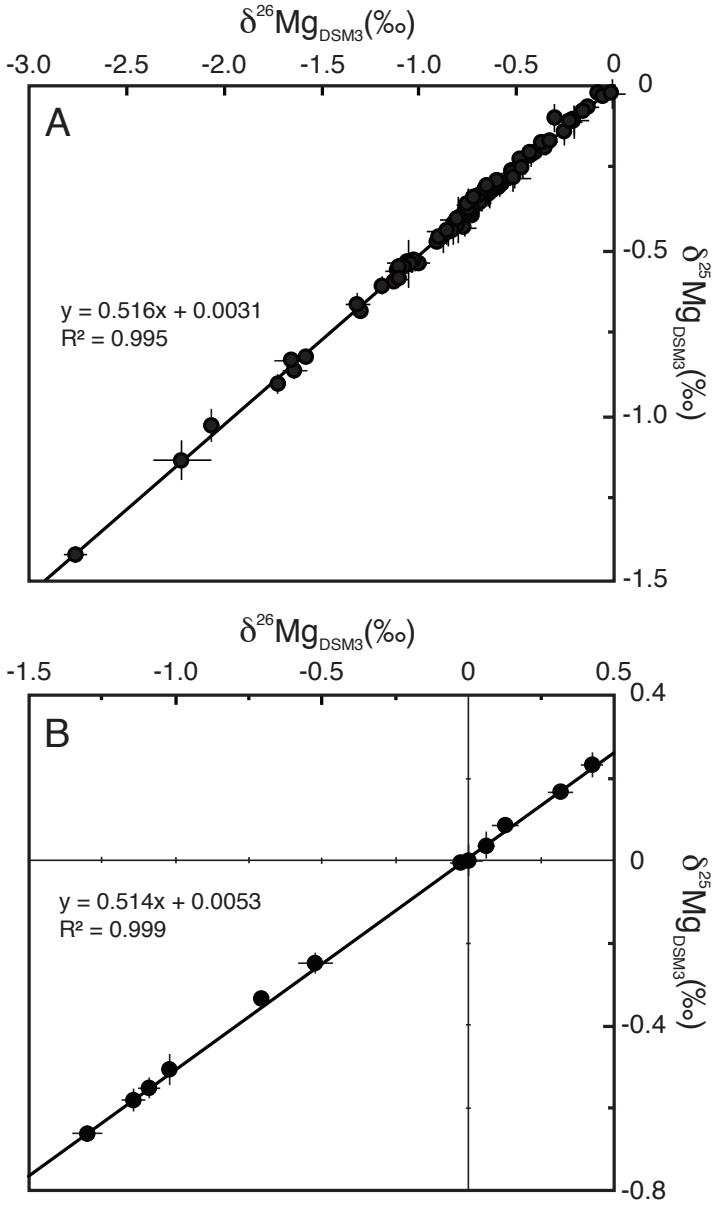

Figure 5.2 (A) A three-isotope plot for all data listed in Table 5.1 for the HEW. (B) A three-isotope plot for all data listed in Table 5.2 for the laboratory cultivated sugar maple trees grown in the laboratory during a pot experiment. The Mg isotope ratios demonstrate mass dependent behavior. Error bars shown are ± 2se in the cases where the sample was analyzed during one mass spectrometry session and ± 2σ in cases where the sample was analyzed in more than one mass spectrometry session. For additional details, refer to the main text.

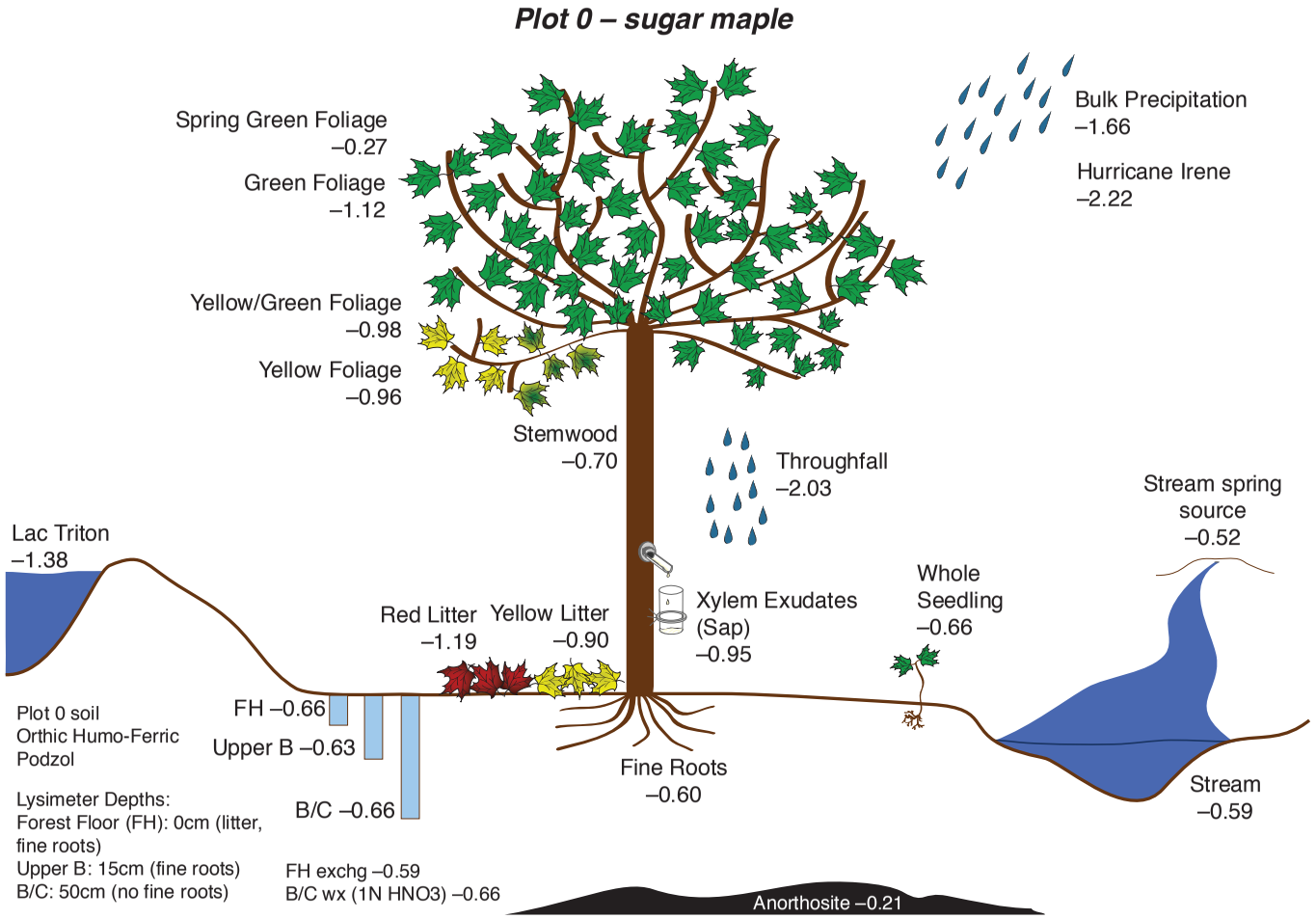

Figure 5.3 Schematic illustration of plot 0 in the HEW hardwood forest study site. The illustration shows the first-order, spring-fed stream, the nearby spring source for the stream, the precipitation-groundwater recharged lake (Lac Triton) located near the HEW (Fig. 5.1), soil type, and dominant tree species (sugar maple). Also shown are the δ^{26}Mg values for bulk precipitation, event precipitation, vegetation, throughfall, soil solutions, stream water, lake water, anorthosite bedrock, forest floor (FH horizon) exchangeable (0.1N $BaCl_2$) extract and Bf-BC and C horizon (denoted as B/C) weathering signature (1N HNO_3) extract.

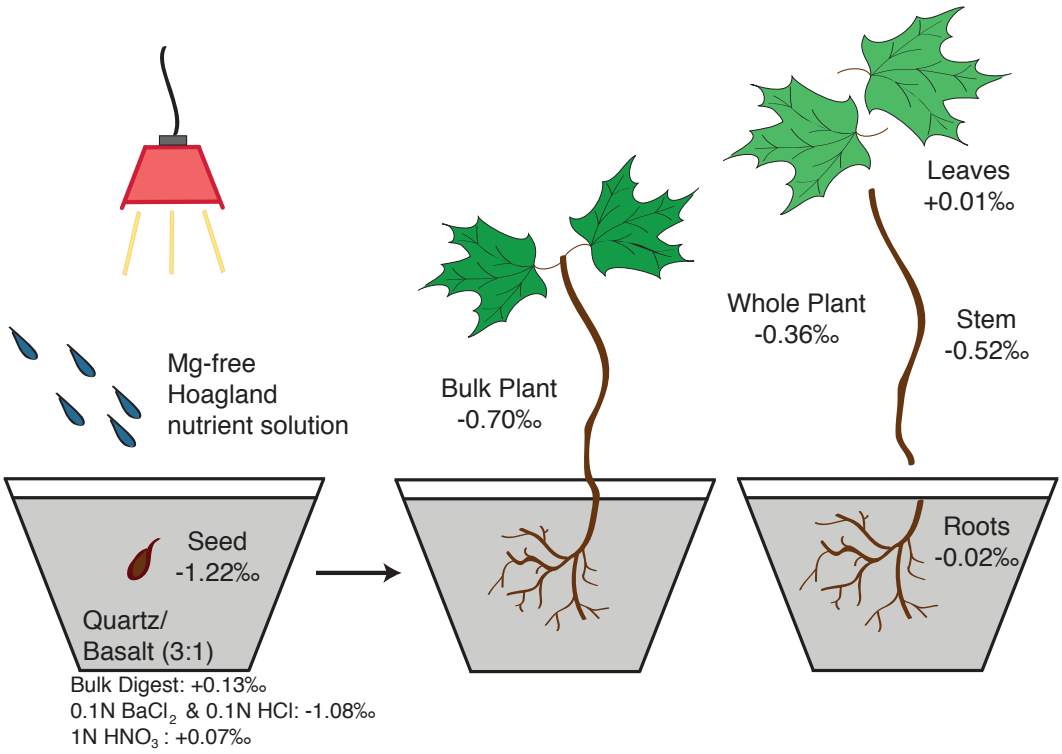

Figure 5.4 Pot experiment used for growing sugar maple seedlings in the laboratory. A Mg-free Hoagland-type nutrient solution was used to water the plants, resulting in the plant-available Mg pool limited to both Mg stored within the seed prior to planting and the quartz/basalt (3:1) growth substrate exchangeable fraction (0.1N $BaCl_2$ and 0.1N HCl extractions). Average δ^{26}Mg values are shown as well as a bulk plant digest, and a weighted whole-plant value calculated for the seedling that was sectioned into root, stem, and leaves using Equation 5.3.

Figure 5.5 Magnesium isotope (δ^{26}Mg ‰DSM3) distribution in the water, vegetation, and soil/rock samples collected from plot 0 of the HEW. Values with associated errors are shown in Table 5.1 and the main text. The number of analyzed samples used for each compartment is indicated by n. Total range of values is 2.75‰.

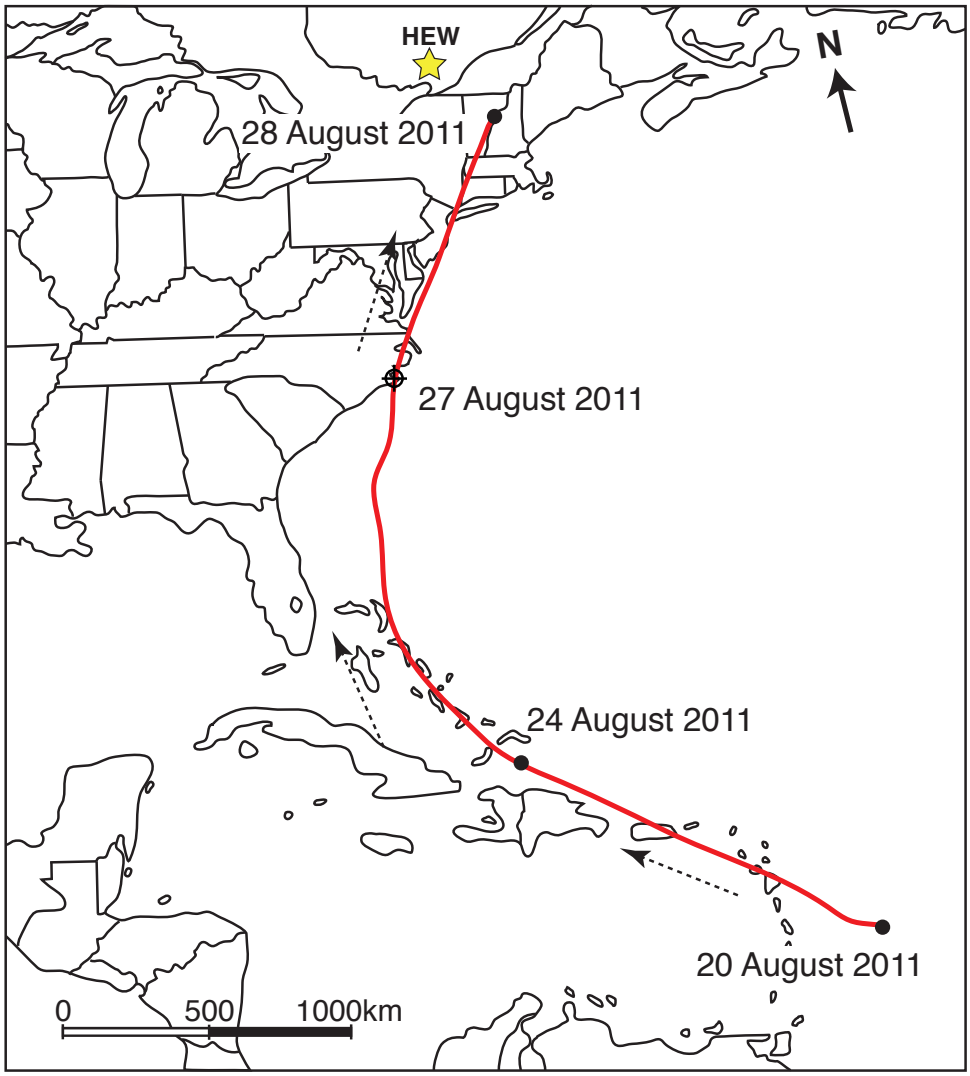

Figure 5.6 Hurricane Irene storm track in August of 2011. The storm track is indicated by a red line while the direction of movement is indicated by dashed arrows. Based on data provided in Avila and Cangialosi (2011). The target symbol denotes landfall on August 27th, 2011 near Cape Lookout, North Carolina. The HEW is shown as a yellow star.

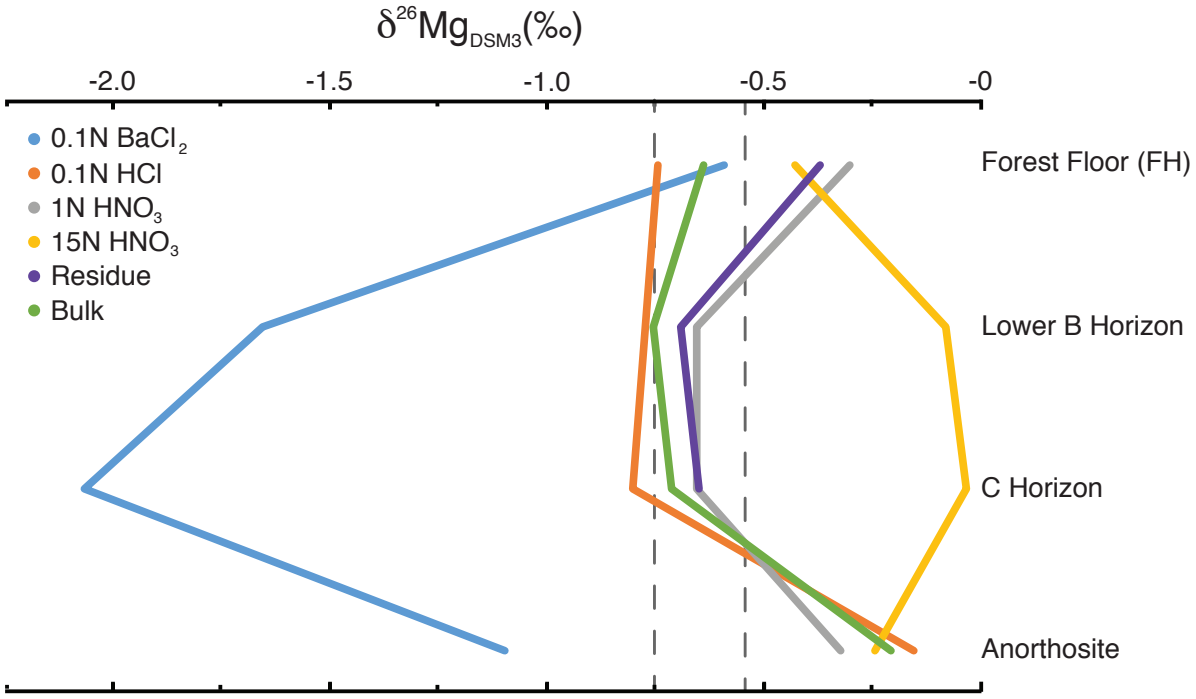

Figure 5.7 Magnesium isotope (δ^{26}Mg ‰DSM3) compositions of the soil sequential leaches and digests plotted according to relative position in the soil sampling column. Samples are shown as solid color-coded lines according to each leach/digest as follows: light blue for the 0.1N $BaCl_2$ leach, orange for the 0.1N HCl leach, light gray for the 1N HNO_3 leach, yellow for the 15N HNO_3 leach, purple for the HF–HNO_3 digest of the leach residues, and green for the bulk soil/rock HF–HNO_3 digest. Vertical dashed lines correspond to the range of lysimeter δ^{26}Mg values.

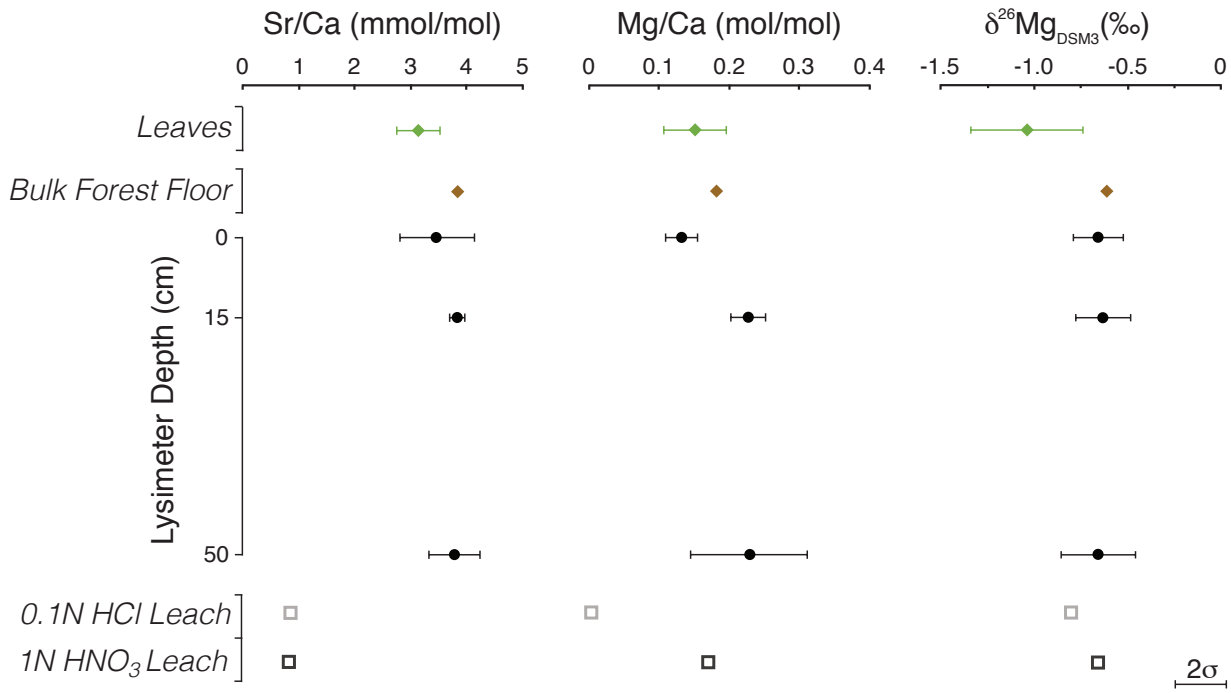

Figure 5.8 Depth profile of average Sr/Ca (mmol/mol) ratios, Mg/Ca (mol/mol) ratios, and $\delta^{26}Mg$ (‰DSM3) values of autumn leaves collected from SM3 in plot 0 of the HEW shown as green diamonds, a bulk forest floor (FH horizon) digest shown as a brown diamond, lysimeters collecting soil solutions at 0 cm, 15 cm, and 50 cm in plot 0 shown as black circles, and the 0.1N HCl and 1N HNO_3 leaches of the C horizon shown as an open light gray square and an open dark gray square, respectively. Error bars are shown as ± 2σ for each sample grouping.

5.9. Tables

Table 5.1 (part 1 of 3)

Sample ID	Sample Type	Sample Description	N	δ^{26}Mg (‰ DSM3)	2SE	2σ	δ^{25}Mg (‰ DSM3)	2SE	2σ	Δ^{25}Mg' [a]	^{87}Sr/^{86}Sr	Ca (ppm)	Mg (ppm)	Sr (ppm)	Fe (ppm)	Ca/Mg (mol/mol)	Mg/Ca (mol/mol)	Sr/Mg (mmol/mol)	Sr/Ca (mmol/mol)	Fe/Mg (mol/mol)
Bulk Precipitation																				
W18	Rain water	July Bulk	2	-1.73		0.04	-0.90		0.03	0.00		0.236	0.043	0.0005		3.33	0.300	3.50	1.05	
W23	Rain water	August/September Bulk	4	-1.58	0.02		-0.82	0.02		0.00		0.450	0.071	0.0011		3.85	0.259	4.27	1.11	
		average	*2*	*-1.66*		*0.21*	*-0.86*		*0.12*			*0.34*	*0.06*	*0.00*		*3.59*	*0.278*	*3.89*	*1.08*	
Hurricane Irene																				
W34	Event rain water	Bulk Precipitation 2011	2	-2.22		0.15	-1.13		0.06	0.02	0.708893	0.176	0.041	0.0004		2.64	0.379	2.40	0.91	
Throughfall																				
W09	Throughfall	Collector 2	2	-2.76		0.06	-1.42		0.03	0.02		0.703	0.073	0.0028		5.86	0.171	10.8	1.83	
W10	Throughfall	Collector 1	4	-1.30	0.02		-0.68	0.01		-0.01		0.475	0.059	0.0018		4.86	0.206	8.19	1.69	
		average	*2*	*-2.03*		*2.07*	*-1.05*		*1.04*			*0.59*	*0.07*	*0.0023*		*5.36*	*0.188*	*9.47*	*1.76*	
Lakewater																				
W07	Lake water	Lac Triton - High Level	4	-1.13	0.02		-0.59	0.01		-0.01		2.23	0.448	0.0152		3.02	0.331	9.40	3.11	
W33	Lake water	Lac Triton - Low Level	4	-1.64	0.06		-0.86	0.02		-0.01		1.84	0.308	0.0121		3.62	0.276	10.9	3.00	
		average	*2*	*-1.38*		*0.73*	*-0.73*		*0.38*			*2.03*	*0.38*	*0.01*		*3.32*	*0.301*	*10.1*	*3.05*	
Groundwater																				
KETTLE	Groundwater	Spring Source Autumn 2009	4	-0.52	0.04		-0.26	0.02		0.01		2.49	0.230	0.0203		6.57	0.152	24.5	3.73	
Stream Water																				
W05	Stream water	Low Flow September	4	-0.60	0.03		-0.31	0.03		0.01		2.70	0.463	0.0181		3.53	0.283	10.8	3.06	
W06	Stream water	High Flow September	4	-0.77	0.04		-0.40	0.02		0.00		2.33	0.370	0.0165		3.82	0.261	12.4	3.23	
W16	Stream water	July Bulk	3	-0.57	0.04		-0.30	0.01		0.00		2.14	0.351	0.0147		3.71	0.270	11.6	3.14	
W20	Stream water	August Bulk	4	-0.51	0.01		-0.27	0.02		0.00		2.56	0.328	0.0175		4.74	0.211	14.8	3.13	
W22	Stream water	August/Sept Bulk	4	-0.43	0.05		-0.21	0.03		0.01		2.07	0.362	0.0135		3.48	0.288	10.3	2.98	
W24	Stream water	Low Flow June 2011	4	-0.58	0.01		-0.30	0.02		0.01		2.03	0.320	0.0145		3.85	0.260	12.6	3.27	
W30	Stream water	Low Flow June 2011	3	-0.72	0.02		-0.40	0.02		-0.02		2.13	0.345	0.0151		3.75	0.266	12.2	3.24	
		average	*7*	*-0.60*		*0.23*	*-0.31*		*0.13*			*2.28*	*0.36*	*0.0157*		*3.84*	*0.260*	*12.1*	*3.15*	
Soil Solutions																				
W11	Lysimeter	0cm - Autumn 2010	4	-0.73	0.03		-0.38	0.02		0.00		6.64	0.571	0.0499		7.06	0.142	24.3	3.44	
W11d	Lysimeter	0cm - Mg duplicate	3	-0.64	0.01		-0.33	0.02		0.01										
W25	Lysimeter	0cm - Spring 2011	4	-0.59	0.04		-0.31	0.02		0.00		4.50	0.398	0.0329		6.86	0.146	23.0	3.34	
W31	Lysimeter	0cm - Spring 2011	4	-0.63	0.04		-0.33	0.01		0.00		3.88	0.305	0.0254		7.73	0.129	23.2	3.00	
W36	Lysimeter	0cm - Autumn 2012	3	-0.61	0.04		-0.31	0.01		0.00		4.32	0.327	0.0356		8.01	0.125	30.2	3.77	
W39	Lysimeter	0cm - Autumn 2012	4	-0.75	0.03		-0.38	0.05		0.01		4.24	0.304	0.0354		8.46	0.118	32.3	3.82	
W12	Lysimeter	15cm - Autumn 2010	3	-0.69	0.06		-0.35	0.03		0.01		4.32	0.597	0.0356		4.39	0.228	16.5	3.77	
W12d	Lysimeter	15cm - Mg duplicate	3	-0.65	0.05		-0.33	0.03		0.01										
W26	Lysimeter	15cm - Spring 2011	4	-0.66	0.05		-0.32	0.01		0.02		3.59	0.525	0.0302		4.14	0.241	16.0	3.86	
W40	Lysimeter	15cm - Autumn 2012	4	-0.52	0.07		-0.26	0.06		0.01		4.45	0.583	0.0380		4.63	0.216	18.1	3.91	
W13	Lysimeter	50cm - Autumn 2010	4	-0.72	0.02		-0.38	0.02		-0.01		1.79	0.255	0.0157		4.24	0.236	17.1	4.03	
W27	Lysimeter	50cm - Spring 2011	4	-0.72	0.02		-0.36	0.01		0.01		1.77	0.307	0.0151		3.50	0.286	13.6	3.89	
W32	Lysimeter	50cm - Spring 2011	4	-0.68	0.05		-0.36	0.03		0.00		2.18	0.306	0.0167		4.32	0.231	15.1	3.50	
W41	Lysimeter	50cm - Autumn 2012	3	-0.51	0.09		-0.28	0.03		-0.01		2.19	0.245	0.0179		5.42	0.184	20.3	3.74	
		average	*14*	*-0.65*		*0.15*	*-0.33*		*0.07*			*3.66*	*0.39*	*0.03*		*5.73*	*0.175*	*20.8*	*3.67*	

Table 5.1 (part 2 of 3)

Sample ID	Sample Type	Sample Description	N	δ^{26}Mg (‰ DSM3)	2SE	2σ	δ^{25}Mg (‰ DSM3)	2SE	2σ	Δ^{25}Mg' [a]	^{87}Sr/^{86}Sr	Ca (ppm)	Mg (ppm)	Sr (ppm)	Fe (ppm)	Ca/Mg (mol/mol)	Mg/Ca (mol/mol)	Sr/Mg (mmol/mol)	Sr/Ca (mmol/mol)	Fe/Mg (mol/mol)
Roots																				
V25	Sugar maple 3	Fine Roots - June 2010	1	-0.48			-0.23			0.02		11014	1341	115.1		4.98	0.201	23.8	4.78	
V49	Sugar maple 3	Fine Roots - September 2010	4	-0.72	0.02		-0.37	0.01		0.01		5411	688	53.6		4.77	0.210	21.6	4.53	
		average	*2*	*-0.60*		*0.34*	*-0.30*		*0.20*			*8213*	*1015*	*84.37*		*4.87*	0.205	*22.7*	*4.66*	
Stemwood																				
V42	Sugar maple 3	Core1	3	-0.76	0.06		-0.43	0.02		-0.03		2739	115	25.1		14.48	0.069	60.8	4.20	
V43	Sugar maple 3	Core2	2	-0.63		0.01	-0.31		0.02	0.01		3477	233	28.7		9.07	0.110	34.2	3.77	
		average	*2*	*-0.70*		*0.19*	*-0.37*		*0.17*			*3108*	*174*	*26.91*		*11.77*	0.085	*47.5*	*3.99*	
Autumn Foliage																				
V51	Sugar maple 3	Green Foliage	3	-1.19	0.03		-0.60	0.03		0.02		16715	1641	120		6.18	0.162	20.2	3.27	
V51-2	Sugar maple 3	Green Foliage	4	-1.05	0.03		-0.54	0.02		0.01		16322	1585	108		6.24	0.160	19.0	3.04	
V52	Sugar maple 3	Yellow/Green Foliage	4	-1.10	0.07		-0.56	0.04		0.01		12533	853	91.0		8.92	0.112	29.6	3.32	
V52-2	Sugar maple 3	Yellow/Green Foliage	4	-0.86	0.05		-0.45	0.03		0.00		12584	1396	90.0		5.47	0.183	17.9	3.27	
V53	Sugar maple 3	Yellow Foliage	3	-0.88	0.05		-0.46	0.04		0.00		17278	1416	124		7.40	0.135	24.2	3.28	
V53-2	Sugar maple 3	Yellow Foliage	4	-1.03	0.03		-0.54	0.02		0.00		17820	1740	121		6.21	0.161	19.3	3.11	
		average	*6*	*-1.02*		*0.25*	*-0.53*		*0.12*			*15542*	*1439*	*109*		*6.74*	0.148	*21.7*	*3.22*	
Leaf Litter																				
V33	Sugar maple	Red Litter	4	-1.32	0.06		-0.66	0.04		0.02		12335	1150	81.2		6.51	0.154	19.6	3.01	
V33-2	Sugar maple	Red Litter	3	-1.06	0.11	0.11	-0.54	0.07	0.07	0.01		13822	1027	82.0		8.16	0.123	22.2	2.71	
V34	Sugar maple	Yellow Litter	4	-0.90	0.01		-0.47	0.01		0.00		9824	970	66.6		6.14	0.163	19.1	3.10	
		average	*3*	*-1.09*		*0.42*	*-0.56*		*0.19*			*11994*	*1049*	*76.61*		*6.94*	0.144	*20.3*	*2.94*	
Spring foliage																				
V55	Sugar maple 3	Spring Green Foliage	4	-0.13	0.06		-0.06	0.03		0.01		4142	1333	25.8		1.88	0.531	5.36	2.84	
V55-2	Sugar maple 3	Spring Green Foliage	4	-0.40	0.02		-0.20	0.02		0.00		4006	1273	25.7		1.91	0.524	5.60	2.94	
		average	*2*	*-0.27*		*0.37*	*-0.13*		*0.20*			*4074*	*1303*	*25.73*		*1.90*	0.527	*5.5*	*2.89*	
Seedlings																				
V35	Sugar maple	Autumn Seedling (whole)	4	-0.60	0.02		-0.30	0.02		0.01		6341	919	54.2		4.18	0.239	16.4	3.91	
V35r-1	Sugar maple	Autumn Seedling Root	4	-0.47	0.01		-0.25	0.03		-0.01		9798	695	89.2		8.55	0.117	35.6	4.16	
V35s-1	Sugar maple	Autumn Seedling Stem	4	-0.64	0.04		-0.33	0.04		0.00		2415	609	28.7		2.40	0.416	13.1	5.44	
V35l-1	Sugar maple	Autumn Seedling Leaves	4	-0.74	0.03		-0.38	0.02		0.01		12816	1970	75.5		3.95	0.253	10.6	2.69	
V35-1		Whole (calculated) seedling		-0.66			-0.34													
V35r-2	Sugar maple	Autumn Seedling Root	4	-0.35	0.02		-0.19	0.02		-0.01		6348	507	61.0		7.59	0.132	33.4	4.40	
V35s-2	Sugar maple	Autumn Seedling Stem	4	-0.78	0.05		-0.40	0.04		0.01		2772	564	31.0		2.98	0.336	15.2	5.12	
V35l-2	Sugar maple	Autumn Seedling Leaves	4	-0.82	0.04		-0.42	0.02		0.01		11592	1732	82.3		4.06	0.246	13.2	3.25	
V35-2		Whole (calculated) seedling		-0.73			-0.37													
		average (whole)	*3*	*-0.66*		*0.13*	*-0.34*		*0.07*											
Xylem Exudates (Saps) - Sugar Maple																				
SBL01	Early season sap	1.5°Bx sugar content	4	-0.79	0.06		-0.41	0.03		0.00		2180	253	15.0		5.23	0.191	16.4	3.14	
SBL01	Mid season sap	3.4°Bx sugar content	4	-0.99	0.03		-0.54	0.01		-0.02		1144	174	8.12		4.00	0.250	13.0	3.25	
SBL01	Late season sap	3.3°Bx sugar content	4	-0.80	0.03		-0.42	0.01		-0.01		1694	243	10.8		4.23	0.236	12.3	2.91	
SBL02	Early season sap	1.8°Bx sugar content	4	-0.89	0.04		-0.46	0.01		0.01		2119	259	13.8		4.96	0.202	14.8	2.98	
SBL02	Mid season sap	4.4°Bx sugar content	4	-1.02	0.04		-0.53	0.03		0.00		1821	222	11.7		4.98	0.201	14.6	2.93	
SBL02	Late season sap	2.1°Bx sugar content	4	-1.03	0.05		-0.54	0.02		0.00		2173	272	15.0		4.85	0.206	15.3	3.15	
SBL03	Early season sap	1.7°Bx sugar content	4	-1.07	0.03		-0.55	0.03		0.01		1580	191	10.9		5.01	0.200	15.8	3.15	
SBL03	Mid season sap	2.1°Bx sugar content	4	-0.83	0.02		-0.44	0.04		-0.01		3005	348	19.5		5.24	0.191	15.6	2.97	
SBL03	Late season sap	2.1°Bx sugar content	4	-0.86	0.10		-0.44	0.04		0.00		3633	431	23.6		5.12	0.195	15.2	2.98	
SBL04	Mid season sap	2.4°Bx sugar content	4	-1.10	0.01		-0.57	0.01		0.00		2722	279	17.0		5.92	0.169	16.9	2.85	
SBL04	Late season sap	1.5°Bx sugar content	4	-1.10	0.03		-0.55	0.02		0.02		3234	349	20.8		5.62	0.178	16.5	2.94	
		average	*11*	*-0.95*		*0.24*	*-0.50*		*0.12*			*2300*	*274*	*15.1*		*5.02*	0.199	*15.1*	*3.02*	

Table 5.1 (part 3 of 3)

Sample ID	Sample Type	Sample Description	N	δ^{26}Mg (‰ DSM3)	2se	2σ	δ^{25}Mg (‰ DSM3)	2se	2σ	Δ^{25}Mg'[a]	^{87}Sr/^{86}Sr	Ca (ppm)	Mg (ppm)	Sr (ppm)	Fe (ppm)	Ca/Mg (mol/mol)	Mg/Ca (mol/mol)	Sr/Mg (mmol/mol)	Sr/Ca (mmol/mol)	Fe/Mg (mol/mol)
Soil Extracts - Forest Floor (FH) Horizon																				
S06	FH	Bulk digest	4	-0.64	0.07		-0.32	0.04		0.02		8363	917	71.1	5246	5.53	0.181	21.5	3.89	2.49
S06	FH	0.1N $BaCl_2$ Leach	4	-0.59	0.02		-0.29	0.03		0.02		2841	103	35.2	9.47	16.6	0.060	94.4	5.67	0.040
S06	FH	0.1N HCl Leach	4	-0.74	0.07		-0.37	0.04		0.01		977	38.4	4.02	128	15.4	0.065	29.0	1.88	1.45
S06	FH	1N HNO_3 Leach	4	-0.30	0.02		-0.10	0.04		0.06		284	11.3	2.81	544	15.3	0.065	69.4	4.53	21.0
S06	FH	15N HNO_3 Leach	4	-0.43	0.01		-0.21	0.02		0.02		204	74.8	2.27	2259	1.65	0.605	8.41	5.09	13.1
S06	FH	Residue digest	4	-0.37	0.02		-0.18	0.02		0.02		4761	2129	89.1	9388	1.36	0.737	11.6	8.56	1.92
Soil Extracts - Bf-BC Horizon																				
S10	Bf-BC	Bulk digest	4	-0.75	0.06		-0.36	0.05		0.03		18572	6663	212	27159	1.69	0.592	8.84	5.23	1.77
S10	Bf-BC	0.1N $BaCl_2$ Leach	2	-1.65	0.09		-0.83	0.00		0.03		20.2	0.77	8.39	0.578	15.9	0.063	3022	190	0.326
S10	Bf-BC	0.1N HCl Leach										473	1.14	1.10	20.2	252	0.004	269	1.07	7.72
S10	Bf-BC	1N HNO_3 Leach	4	-0.66	0.03		-0.32	0.02		0.02		249	24.7	0.462	816	6.12	0.164	5.18	0.85	14.4
S10	Bf-BC	15N HNO_3 Leach	4	-0.08	0.03		-0.03	0.02		0.02		168	1270	0.995	4905	0.080	12.4	0.22	2.70	1.68
S10	Bf-BC	Residue digest	4	-0.69	0.03		-0.33	0.02		0.02		16505	6341	198	24426	1.58	0.634	8.65	5.48	1.68
Soil Extracts - C Horizon				0.00																
S11	C	Bulk digest	4	-0.71	0.04		-0.34	0.02		0.03		23963	8032	220	31558	1.81	0.553	7.58	4.19	1.71
S11	C	0.1N $BaCl_2$ Leach	3	-2.07	0.04		-1.03	0.05		0.05		25.7	1.03	11.0	0.618	15.2	0.066	2957	195	0.261
S11	C	0.1N HCl Leach	3	-0.80	0.09		-0.40	0.07		0.01		719	1.84	1.37	47.5	237	0.004	206	0.872	11.2
S11	C	1N HNO_3 Leach	4	-0.66	0.02		-0.31	0.02		0.03		309	31.9	0.573	473	5.89	0.170	4.98	0.847	6.46
S11	C	15N HNO_3 Leach	4	-0.05	0.04		-0.03	0.01		-0.01		235	1533	1.47	5455	0.0931	10.7	0.266	2.86	1.55
S11d	C	15N HNO_3 Mg duplicate	3	-0.01	0.07		-0.02	0.05		-0.02										
S11	C	Residue digest	4	-0.65	0.01		-0.30	0.01		0.03		21496	7163	222	26375	1.82	0.549	8.60	4.72	1.60
Bedrock Extracts																				
R01	Anorthosite	Bulk digest	4	-0.21	0.08		-0.10	0.04		0.01		78965	13470	650	17939	3.56	0.281	13.4	3.77	0.580
R01-2	Anorthosite	Bulk full duplicate digest	3	-0.21	0.04		-0.11	0.05		0.00		80977	13704	623	17837	3.58	0.279	12.6	3.52	0.566
R01	Anorthosite	0.1N $BaCl_2$ Leach	4	-1.10	0.04		-0.58	0.01		-0.01		233	12.4	12.1		11.4	0.088	271	23.7	
R01	Anorthosite	0.1N HCl Leach	3	-0.15	0.03		-0.08	0.00		0.00		1372	167	4.90	284	4.97	0.201	8.11	1.63	0.737
R01	Anorthosite	1N HNO_3 Leach	4	-0.32	0.03		-0.17	0.02		0.00		607	177	4.11	284	2.08	0.480	6.45	3.10	0.700
R01	Anorthosite	15N HNO_3 Leach	4	-0.26	0.03		-0.13	0.05		0.00		7484	2321	51.7	3242	1.96	0.511	6.18	3.16	0.608
R01d	Anorthosite	15N HNO_3 Mg duplicate	4	-0.22	0.02		-0.11	0.02		0.01										

[a] Calculated using methods from Young and Galy (2004)

Magnesium isotope data, Ca, Mg, and Sr concentrations as well as elemental molar ratios for precipitation, throughfall, stream water, lake water, soil solutions, plant tissues (foliage, stemwood, roots, seedlings), xylem exudates (saps), soil and rock extracts/digests at plot 0 in the HEW. 'Mg duplicates' refer to sample solutions duplicated through chemical separation and analysis. Prepared Mg solutions that were analyzed in separately tuned mass spectrometry sessions are shown with 2 standard deviations (2σ) error. Those analyzed within the same tuned sessions are denoted by 2 standard errors of the mean (2se).

Table 5.2

Sample ID	Sample Type	Sample Description	N	δ^{26}Mg	2SE	δ^{25}Mg	2SE	Δ^{25}Mg' [a]	Ca (ppm)	Mg (ppm)	Sr (ppm)	Fe (ppm)	Ca/Mg (mol/mol)	Mg/Ca (mol/mol)	Mg/Sr (mol/mol)	Sr/Ca (mmol/mol)	Fe/Mg (mol/mol)
Vegetation																	
V79	Sugar maple	Seed	3	-1.14	0.04	-0.59	0.03	0.00	44419	1761	207		15.3	0.065	30.7	2.13	
V80	Sugar maple	Seed	4	-1.30	0.05	-0.67	0.02	0.01	19969	2693	67.5		4.50	0.222	144	1.55	
V81	Sugar maple	Roots	4	-0.02	0.04	-0.01	0.01	0.00	11319	2240	16.4		3.06	0.326	493	0.662	
V82	Sugar maple	Leaves	4	0.01	0.05	0.00	0.04	-0.01	8191	238	9.28		20.9	0.048	92.4	0.518	
V83	Sugar maple	Stem	4	-0.52	0.06	-0.25	0.02	0.02	89694	7100	93.7		7.66	0.131	273	0.478	
V84	Sugar maple	Whole Seedling	4	-0.70	0.03	-0.34	0.02	0.03	30962	2210	26.0		8.49	0.118	306	0.385	
Growth Mix Extracts																	
S13	Quartz/Basalt	Bulk digest	4	0.13	0.05	0.08	0.02	0.01	2354	3535	13	8518	0.404	2.48	998	2.48	1.05
S13	Quartz/Basalt	0.1N $BaCl_2$ Leach	4	-1.01	0.01	-0.51	0.04	0.02	206	5.51	9.28	1.69	22.6	0.044	2.14	20.7	0.134
S13	Quartz/Basalt	0.1N HCl Leach	4	-1.08	0.04	-0.55	0.02	0.01	435	135	0.635	237	1.96	0.510	764	0.668	0.766
S13	Quartz/Basalt	1N HNO_3 Leach	4	0.07	0.03	0.03	0.03	0.00	51.6	140	0.114	410	0.223	4.48	4433	1.01	1.27
S13	Quartz/Basalt	15N HNO_3 Leach	4	0.32	0.04	0.16	0.02	0.00	116	1727	0.401	4354	0.041	24.5	15540	1.58	1.10
S13	Quartz/Basalt	Residue digest	4	0.43	0.04	0.23	0.03	0.01	1799	860	11.6	2328	1.27	0.788	268	2.94	1.18

[a] Calculated using methods from Young and Galy (2004)

Detailed Mg isotope data, Ca, Mg, and Sr concentrations and elemental molar ratios for sugar maple seedlings grown during the laboratory controlled pot experiment using a Mg free Hoagland-type nutrient solution.

Table 5.3

Sugar Maple (*Acer saccharum* Marsh.)	Mg (g/kg)	Dry Biomass (kg)	Mg per Compartment (g)	Total Mg (%)
Stemwood	0.174[a] (0.17)	28.3	4.92	34%
Stembark	0.64[b] (0.12)	5.50	3.52	24%
Branches	0.42[b] (0.08)	8.19	3.44	23%
Foliage	1.4[a] (0.55)	2.00	2.81	19%
DBH (cm)	10.2[a]			

[a]Data collected during this study and provided in Table 5.1 and the main text

[b]Data reported in Chatarpaul et al. (1985)

Mg concentrations in sugar maple tree 3 (SM3) components used to estimate aboveground Mg compartments in the HEW using equations in Lambert et al. (2005). Values shows in parentheses represent ± 2σ errors.

Table 5.4

Sample ID	Horizon	Sample Mass (g)	Total Solution (ml)	CEC_e[a] (cmol/kg)	$\delta^{26}Mg$ (‰ DSM3)	Na (cmol/kg)	Mg (cmol/kg)	Al (cmol/kg)	K (cmol/kg)	Ca (cmol/kg)	Mn (cmol/kg)	Fe (cmol/kg)
S06	Forest floor (FH)	3.06	24.8	16.5	-0.59	0.036	0.852	1.01	0.318	14.2	0.028	0.017
S10	Bf-BC	3.02	29.0	0.415	-1.65	0.016	0.006	0.282	0.007	0.101	0.002	0.001
S11	C	2.88	29.6	0.353	-2.07	0.022	0.008	0.177	0.009	0.129	0.006	0.001
R01	Anorthosite	2.84	32.2	1.51	-1.10	0.161	0.102	0.014	0.066	1.16	0.002	0.000

[a] Calculated using equations and conversion factors provided in Hendershot et al. (2007) and defined as Σ of Ca^{2+}, Mg^{2+}, K^{+}, Na^{+}, Fe^{2+}, Al^{3+}, and Mn^{3+}; H^{+} was not included in the calculation.

Dry sample mass (g), total solution volume (ml), Effective cation exchange capacity (CECe), $\delta^{26}Mg$ values (‰DSM3), and elemental concentrations (cmol/kg) for soil horizons and bedrock 0.1N $BaCl_2$ leach solutions in the HEW plot 0.

Table 5.5

HEW Mineral Soil - Plot 0

Bf-BC Horizon	0.1N $BaCl_2$	0.1N HCl	1N HNO_3	15N HNO_3	Residue digest	Weighted Bulk
δ^{26}Mg (‰ DSM3)	-1.65	-	-0.66	-0.08	-0.69	-0.59
Mg (ppm)	0.77	1.14	24.7	1270	6341	
Mass Fraction (Mg)	0.001	0.001	0.019	0.979		
C Horizon						
δ^{26}Mg (‰ DSM3)	-2.07	-0.80	-0.66	-0.03	-0.65	-0.54
Mg (ppm)	1.03	1.84	31.9	1533	7163	
Mass Fraction (Mg)	0.001	0.001	0.020	0.978		

Pot Experiment

Quartz/Basalt	0.1N $BaCl_2$	0.1N HCl	1N HNO_3	15N HNO_3	Residue digest	Weighted Bulk
δ^{26}Mg (‰ DSM3)	-1.01	-1.08	0.07	0.32	0.43	0.00
Mg (ppm)	5.51	135	140	1727	860	
Mass Fraction (Mg)	0.003	0.067	0.070	0.860		

Summary of the Mg mass fractions for each sequential leach of the mineral soil horizons in the HEW plot 0 and the quartz/basalt growth mixture in the laboratory pot experiment.

CHAPTER 6 – Conclusion

6.1. Thesis summary

Magnesium (Mg) is an important, highly mobile element in the environment. It is an abundant aqueous cation in natural waters, a significant component of rocks and minerals in the Earth's crust, and a vital macronutrient for plants. With the advent of modern, high precision analytical techniques, Mg isotopes have been successfully tested and applied as a novel tool for the investigation of mass dependent differences in terrestrial samples and the complex nature of Mg-exchange within and between each of the lithosphere, hydrosphere, and biosphere in the geochemical cycle (Fig. 1.1). The isotopes of Mg ($^{26}Mg/^{24}Mg$ and $^{25}Mg/^{24}Mg$ expressed as $\delta^{26}Mg$ and $\delta^{25}Mg$, respectively) are demonstrated in this thesis to be useful tracers of elemental Mg-cycling in Earth's exogenic system. The findings reported herein contribute original and important new information regarding Mg isotope fractionation related to the process of dolomitization of marine carbonate sediment, the oscillations in primary mineralogy of inorganic marine carbonate precipitates through geological time, and the biogeochemical cycling of Mg in the 'critical zone.'

Evidence was presented in Chapter 2 for the homogenization of $\delta^{26}Mg$ values in three types of dolomite: (1) burrow, (2) matrix, and (3) saddle (Qing et al., 2001) at the hand-sample scale in the Home Dome Torquay well core of the Red River Formation in the Williston Basin, collected in southeastern Saskatchewan. Based on textural evidence and regional trends, the three types of dolomite appear to reflect three episodes of dolomitization, with the burrow dolomite forming first, followed by matrix and saddle dolomite. Saddle dolomite, being the last type to form and with a peculiar crystal habit, is generally interpreted as evidence for rapid precipitation from higher temperature fluids. It is also possible that the three types of dolomite may reflect dolomitization at increasing burial temperatures. The finding that the three types of dolomite yielded nearly identical $\delta^{26}Mg$ values at the hand-sample scale appears to be at odds with the interpretation that the paragenetic sequence of the three dolomite types reflects three different dolomitization events, and the implied differences in conditions of the dolomite formation associated with each dolomite type. These findings suggest instead that each dolomitization event overprinted the $\delta^{26}Mg$ values of the earlier formed dolomite. Recrystallization of older (poorly ordered) dolomite at elevated temperatures has been previously discussed in the literature for both field and laboratory studies (e.g., Malone et al., 1996; Warren, 2000; Geske et al., 2012; Kaczmarek and Sibley, 2014; Hu et

al., 2017). Although δ^{26}Mg values are quite uniform between the three types of dolomite at the hand-sample scale in the studied 'Home Dome Torquay' core, there is also limited evidence for variation in average δ^{26}Mg values between hand-samples at different depths. This is highlighted in Figs. 2.2 and 2.3 of Chapter 2, where the average δ^{26}Mg value of one group of hand-samples is –1.34 ± 0.12‰ 2σ (~ 3196 to 3209 m depth) and the other is –1.55 ± 0.11‰ 2σ (~ 3193 m depth). This is the maximum variation observed between burrow, matrix, and saddle dolomite in the core (Appendix B). This finding seemed significant but was difficult to interpret. Could it reflect changes in the Mg isotope composition of the dolomitizing fluid along a flow path? Or perhaps spatial variations in dolomite precipitation rate? The two explanations are not mutually exclusive.

Future investigations of the Home Dome Torquay well core dolomite types are warranted. The burrow, matrix, and saddle dolomite that was collected for geochemical analysis was sampled as powders, as such, in depth petrographic analyses (cathodoluminescence) that may be used to test the hypothesis of overprinting of dolomitization events were unable to be conducted. The interpretation of overprinting of dolomite fabrics during subsequent episodes of dolomitization was offered on the basis of the similar dolomite δ^{26}Mg values yielded at the hand sample scale. Presented with the new information that each 'episode' of dolomitization records the same Mg isotopic composition, it would be beneficial to revisit the sampling locations of the Home Dome core for the strict purpose of collecting samples for petrographic analysis. More detailed petrographic investigation would be necessary to assist in deciphering the mechanism by which overprinting of isotopic signals may take place (dissolution-recrystallization or diffusion), if it has at all, and will be able to assist in unraveling the complex diagenetic history of other pervasively dolomitized cores within the Williston Basin. Additionally, microsampling of the different dolomite types found in the Home Dome core would be useful to discern whether or not there are actually three distinct types of dolomite, or if even more exist at smaller scales, such as within the *Thalassinoides* type burrows. Previous investigation of the burrows has shown that the burrow features exhibit different dolomite fabrics from burrow center to the edges, these attributed to the behavior of the burrowing organisms in 'cleansing' the areas surrounding the initial burrow and inducing a dolomite-mottle surrounding the burrow edges while the primary burrow is filled with blocky dolomite cement (Jin et al., 2012). Future investigation involving the microsampling and Mg isotope analysis, in addition to more detailed petrographic analysis, of dolomite from burrow center to edge could be useful to describe whether the burrows record a diagenetically altered

dolomite signal from LMC or HMC originally contained within the burrows or from a primary precipitation of dolomite as blocky crystals within the primary burrow feature. This would have implications for the amount of Mg ions available for late-stage diagenesis during the burial history of the Williston Basin.

Replacement dolomitization is essentially a hydrogeological process that requires subsurface fluid flow to deliver reactive Mg to the sites of dolomitization and remove product Ca. Because dolomite preferentially sequesters light isotopes of Mg during its formation from aqueous solutions, both the dolomitizing fluid and dolomite produced along the fluid migration pathway were expected to increase in δ^{26}Mg value in the direction of fluid flow. There are other factors to consider as well, such as the rate of dolomite precipitation. If dolomite precipitation rate is fast compared to fluid flow rate, the Mg isotopic fractionation between the fluid and dolomite is minimized. The opposite is the case if fluid flow rate is fast compared to a slower dolomite precipitation rate. These questions led to the consideration of a new study described in Chapter 3 aimed at addressing spatial variation in δ^{26}Mg values in Red River dolomite on a basin-scale. This type of study is impossible to perform on a single core because dolomitizing fluids are expected to move laterally across a single cored interval; i.e., up or down the paleo-dip slope of the sedimentary beds. Accordingly, it was necessary to sample the Red River dolomite along the strike of the beds. Furthermore, in order to avoid the added complexity of dealing with multiple dolomitization events, cores were chosen where only the burrows were dolomitized and the matrix remained undolomitized. Sixteen cores and an outcrop sample meeting this criterion were chosen, and were located and sampled from the basin edge to the basin center. Sampling was focused on the burrowed 'C' member carbonate of the Red River, which is stratigraphically equivalent to the studied 'Yeoman Formation' interval of the Home Dome Torquay core.

The findings (reported in Chapter 3) show that burrow-dolomite δ^{26}Mg values increase from the center of the basin towards the edges, in all directions. Applying the interpretive framework, the gradient in burrow-dolomite δ^{26}Mg values reveals that the burrows channelized the flow of dolomitizing fluids up-dip through the 'C' member carbonate, which is confined over much of its extent by anhydrite above and the Winnipeg shale below. A similar gradient in burrow dolomite $^{87}Sr/^{86}Sr$ ratios supports the Mg isotope interpretation. Burrow-dolomite is most radiogenic in the center of the basin (~ 0.7090) and least radiogenic towards the more shallowly buried edges of the basin (~ 0.7081). This pattern of decreasingly radiogenic Sr isotope

compositions away from the center of the basin is consistent with large concentrations of Ordovician seawater-derived Sr (0.7080) that would have been released from marine carbonates undergoing progressive dolomitization along the fluid flow path. Undolomitized matrix limestone sampled from the basin edge in outcrop (Garson Quarry Tyndall Stone) supports this interpretation by yielding $^{87}Sr/^{86}Sr$ ratios of ~ 0.7080, with burrow dolomite yielding $^{87}Sr/^{86}Sr$ ratios of ~ 0.7081 (Table 3.2 in Chapter 3, Appendix B).

Burrow dolomitization of Red River carbonate has most often been attributed to the passage of evaporatively concentrated seawater through the burrows, which filtered downward into the carbonate during periods of basin restriction and evaporite formation (Longman et al., 1983; Longman and Haidl, 1996). Although the gradient in $\delta^{26}Mg$ values clearly shows that dolomitizing fluids must have ascended through the burrowed carbonate in the up-dip direction, one of the lessons to be learned from Chapter 2 is that this is likely to be the *last* dolomitization event to affect the burrows, not necessarily the *only* dolomitization event. It is possible, for example, that the burrows formed a precursor 'protodolomite' (poorly ordered dolomite) by other processes earlier in the diagenetic history of the Red River, but that these dolomites re-equilibrated with Mg-bearing fluids ascending through the burrows at a younger age, and only at that time did the Mg/Ca ratio of the dolomite reach the stoichiometric molar ratio of 1.0. If this is true, the earlier formed dolomite would have been open to Sr-isotope exchange with later dolomitizing fluids as well.

Although it is impossible at this time to know whether there were dolomitization events that predated the formation of the burrow-dolomite, the earliest dolomite type recognized in the Red River strata, there is some additional data presented in Appendix B that can be marshalled to support the idea that the same event that dolomitized the burrows also dolomitized the matrix carbonate in some locations in the basin, as well as the directly overlying layer of laminated dolomite. The average $\delta^{26}Mg$ value for all sampled dolomite in the Home Dome Torquay core is $-1.49 \pm 0.23‰$ (2σ, n = 24), which is exactly the value of burrow-dolomite predicted for that location using the contour map of burrow-dolomite $\delta^{26}Mg$ values (Fig. 3.4, Chapter 3). In addition, one sample of laminated dolomite from the Home Dome core overlying the burrowed member yielded –1.43‰, which suggests that the laminated carbonate was dolomitized at the same time as the burrows and matrix dolomite in the Red River.

The 'C' member carbonate and laminated dolomite are directly overlain by anhydrite over

a large area that encompasses the center of the basin, which is why the brine reflux model of dolomitization has factored so prominently in dolomitization models of the Red River carbonate. In fact, there are 'B' and 'A' member carbonates to consider as well, and each of these is also overlain by laminated carbonate and anhydrite. It seems reasonable to conclude that the 'B' and 'A' member carbonates were dolomitized at the same time as the 'C' member carbonates. Admittedly, it also appears inevitable that Mg-rich brines must have filtered down through the burrows during each of three successive episodes of evaporite formation in the Williston Basin in the Late Ordovician, but on the basis of the Mg and Sr isotope evidence presented in Chapter 3, it seems unlikely that dolomite formed at this time. Reasoning for this statement is that if Mg were consumed from solution by dolomitizing carbonate during brine descent to the center of the basin, there would be too little Mg remaining to dolomitize carbonates when these brines ascended through the burrows later in the history of the basin.

The timing of burrow dolomitization is unknown, but two periods of anomalously high heat flow punctuate the subsidence history of the Williston Basin and are potential candidates, one in Late Devonian to early Carboniferous time and the other in the Late Cretaceous–Paleogene. These events are constrained by evidence from apatite fission track (AFT) studies, thermal remnant magnetizations of carbonate and evaporite, K/Ar dating and fluid inclusion study of the Devonian Prairie Evaporite Formation, and radiometric dating of MVT ores at Pine Point, in the nearby Alberta Foreland Basin (Chipley and Kyser, 1992; Koehler et al., 1997; Leach et al., 2001; Osadetz et al., 2002; Cioppa, 2003; Szabo and Cioppa, 2006; Feinstein et al., 2009). The late Paleozoic event has been linked to the Antler Orogeny, and the Late Cretaceous–Paleogene event to the Laramide Orogeny. Fluid flow during the Cretaceous event is attributed to the creation of a high elevation head along the southern margin of the Williston Basin during the emplacement of Paleogene-age intrusions (e.g., the Black Hills and the Little Rocky Mountains), most likely as a consequence of the Laramide Orogeny occurring further to the west. However, topographically-driven recharge in the Black Hills would drive basin fluid flow roughly north to south across the Williston Basin, which is the dominant pattern of fluid flow in the present day. This is discordant with the radially concentric pattern of fluid flow recorded in the burrow dolomite of the Red River. If dolomitization occurred during one of these two heating events, then on the basis of the previous discussion, it would have to be the Late Paleozoic event. This activity also coincides with the maturation of source rocks in the Williston Basin (Osadetz et al., 2002).

There are only two classes of fluid flow models that can explain dolomitization by ascending fluids from the deep center of an intracratonic basin. The first model, sediment compaction, creates fluid overpressures in the deep basin through the reduction of pore volume in shale. Applied to the Williston Basin, the underlying Winnipeg shale is a candidate for dewatering during compaction, and it directly underlies the Red River. However, sediment compaction generates exceptionally low fluid flow velocities (e.g., Bethke, 1985) compared to other hydrogeological drives (Whitaker et al., 2004). It requires a consistently subsiding basin over long periods of geologic time (tens of millions to hundreds of millions of years), otherwise the flow is easily overcome by nearly all other drivers of fluid flow. The second class of fluid flow model creates fluid overpressures by increasing the fluid volume, which includes generation of hydrocarbons (capillary seals), mineral dewatering, forced thermal convection (in association with magmatic intrusions in the crust), and increased geothermal heat flow from the mantle. In all of these cases, thermal expansion of existing fluids, or the introduction of new fluids, causes their upward migration due to buoyancy forces. The deep center of the Williston Basin is riddled with faults penetrating from the basement through the overlying sedimentary units. Because of this, there is plenty of scope for over-pressurized fluids to use vertical faults to flow across the basement-cover contact and enter the bottom of the Williston Basin. The expulsion of crustal fluids into the deep basin center could, in turn, drive Mg-bearing fluids upwards along vertical faults between the basal aquifer and the Red River, and in the Red River these fluids could flow up-dip through the burrows towards the edges of the basin.

Additional work is required in order to discern the mechanism(s) by which the burrowed ‘C member’ carbonate was dolomitized, as well as to decipher the source of the large quantities of Mg required for dolomitization of such a large amount of carbonate. The model of ascending fluid flow through the burrows could be explored further with a reactive transport model. This could help to determine the conditions of dolomitization, the flow rates of the dolomitizing fluids, the fractionation factor accompanying the formation of dolomite along the flow path, and even the mechanism by which calcite becomes dolomite.

Chapter 4 reported on the large effects that only a few mol% dolomite can have on the attempt to reconstruct stratigraphic changes in $\delta^{26}Mg$ values of whole-rock limestone in marine carbonate successions from the geological past, and applying a graphical technique to correct for these effects. The study section is the largely mudstone succession of marine limestone in the

Monitor Range of Nevada, which records the Late Ordovician (Hirnantian) glaciation and mass extinction event. Previous studies have reported excursions in sedimentary $\delta^{13}C$ and $\delta^{44/40}Ca$ values in the same section, consistent with lithofacies and biofacies indicators of sea-level change (Finney et al., 1997; LaPorte et al., 2009; Holmden et al., 2012a). The 2–3‰ positive excursion in $\delta^{26}Mg$ values that was found is attributed to a small (~ 12 mol% average) increase in dolomite abundance in the limestone in the sea-level lowstand interval. The effect of the dolomite was corrected for using a mixing analysis and graphical technique, which divulged a significant positive excursion in $\delta^{26}Mg$ values in the originally deposited glacial-age limestone, yielding –2.54‰ ± 0.23‰ (2σ). By contrast, the dolomite-corrected limestone deposited before the glaciation yielded –4.45‰ ± 0.82‰ (2σ), and the limestone deposited after the glaciation yielded –3.05‰ ± 0.27‰ (2σ). Shifts of this magnitude in $\delta^{26}Mg$ values are consistent with changes in carbonate mineralogy. It was therefore hypothesized that aragonite may have precipitated in this tropical-shelf setting during the Hirnantian glaciation, with calcite precipitation dominating during the pre-glacial and post-glacial sea-level highstands. The Mg isotope evidence for aragonite is unexpected because the Late Ordovician lies in the midst of a long period of 'calcite seas,' a time in Earth history during which the chemistry of seawater favored the precipitation of primary calcite over primary aragonite. However, when it is considered that the limestone in the study section is altered to an unknown extent by diagenesis, the Mg isotopes alone do not permit a definitive interpretation of changes in carbonate polymorph mineralogy, as diagenetic effects on $\delta^{26}Mg$ values in carbonate sediment are often difficult to predict. Although this complexity is acknowledged, there is additional evidence for aragonite in the study section from stratigraphic shifts to lower $\delta^{44/40}Ca$ values, higher $\delta^{13}C$ values, and intermittently higher Sr/Ca ratios in the carbonates deposited during the glacial interval, thus strengthening the case for Mg isotopes recording a similar shift in carbonate mineralogy in these deposits. Although aragonite and calcite are carbonate polymorphs with the same chemical formula, the minor elemental and isotopic geochemistry of the two minerals can be substantially different. It is therefore important when using marine carbonate successions to reconstruct potential changes in seawater $\delta^{13}C$, $\delta^{44/40}Ca$, and $\delta^{26}Mg$ values, to properly evaluate the extent to which the observed changes might be due to either a true secular change in the isotopic signatures of C, Ca, and Mg in contemporaneous seawater, or a change in the abundance of calcite and aragonite (having inverted to calcite during

diagenesis) in the original depositional setting. Carbonate mineralogical changes should be suspected when these aforementioned tracers change synchronously in a sedimentary carbonate succession due to the differences in oceanic residence times of C, Ca, and Mg, which would not normally permit synchronous changes in the oceanic cycles of these elements encoded to carbonate rocks.

In Chapter 5, the focus shifted to biogeochemical cycling of Mg in a forested first-order catchment in southern Québec, located in the Hermine Experimental Watershed (HEW). Biogeochemical cycling within a stand of sugar maple trees in the HEW demonstrated significant within-tree Mg isotope fractionation, as evidenced from the differences in δ^{26}Mg values between roots, stemwood, and foliage, with autumn foliage recording the lowest δ^{26}Mg values, and roots recording the highest δ^{26}Mg values for both juvenile (seedlings) and mature sugar maple trees. Internal processes resulting in mass dependent fractionation in sugar maple include the synthesis of chlorophyll in photosynthesizing leaves, the breakdown of chlorophyll in the leaves during autumnal senescence, and the translocation of Mg between various tree tissues. The overall range in δ^{26}Mg values in the studied forest was 2.75‰, with contributions of Mg from bulk precipitation and throughfall yielding the lowest δ^{26}Mg values (< –1.5‰) and mature tree spring foliage yielding the highest δ^{26}Mg values (up to –0.13‰).

The δ^{26}Mg of chlorophyll in sugar maple appears to be isotopically light compared to whole leaves, which was based on the finding that new leaves in the spring canopy are much higher in δ^{26}Mg value than mature leaves in the fall, a pattern that appears to reflect a known increase in chlorophyll concentration of leaves as the growing season progresses from spring through autumn (Lewandowska and Jarvis, 1977). Applying a mass balance approach, the sugar maple chlorophyll δ^{26}Mg value was determined to be –3.67‰, while the whole leaf value for photosynthesizing autumn leaves averaged –1.12 ± –0.19‰. Sugar maple leaves become heavier yet again during autumnal senescence, an interpretation based on the breakdown of chlorophyll and the translocation of the isotopically light Mg into the stemwood, where it is presumably stored for the winter and used the subsequent spring to assist in canopy regrowth. Bulk precipitation over the study site was low in δ^{26}Mg value (–1.66 ± 0.21‰), a result tentatively attributed to local/regional sources of carbonate dust, particularly dolomite, which is high in Mg. Analysis of hurricane Irene, which passed over the HEW in August of 2011, revealed the lowest δ^{26}Mg value for precipitation

in the literature to date (–2.22 ± 0.15‰), a result also attributed to the influence of carbonate dust picked up by the storm en route to the study site. A Mg isotope apportionment calculation revealed that the vast majority (~ 81%) of the Mg in a small lake located near the study site (Lac Triton) is directly sourced from rainfall and snow melt, as opposed to shallow ground water (soil solutions). However, lake stratification could have resulted in an atmospheric signature bias on the samples collected from the uppermost lake layer.

There was no observed uptake related fractionation of Mg isotopes into sugar maple tree fine roots at the study site in the HEW from the plant-available soil pool. The finding that Mg isotopes are not fractionated by sugar maple has implications for the export flux of weathered Mg to first-order streams, rivers, and eventually the oceans, where it is a key component flux of the ocean Mg-cycle. These results are further supported by soil solutions collected at three depths within the plot (0 cm, 15 cm, 50 cm) as well as fine root (< 2 mm diameter) samples from a mature sugar maple tree and whole sugar maple seedlings collected from the forest floor, yielding identical isotopic compositions. Whole seedlings grown in the laboratory on a quartz/basalt artificial soil, on the other hand, yield contrasting results. The laboratory grown seedlings demonstrated a preference for heavy Mg isotope uptake from the nutrient source, results in agreement with previously reported laboratory and field-based observations (e.g., Black et al., 2008; Bolou-Bi et al., 2010; Tipper et al., 2010). The discrepancy between sugar maple collected in the field *vs.* laboratory fostered plants was attributed to the absence of mycorrhizal fungi in laboratory artificial growth substrates (soils and/or hydroponic solutions). It was proposed that forest stands of sugar maple receive much of their required nutrient load of Mg through a symbiotic relationship with arbuscular mycorrhizal fungi, and that the fungi do not fractionate Mg isotopes during this nutrient mediation. Thus, the uptake related fractionation of Mg isotopes in the laboratory grown seedlings reflects the absence of these fungi, serving as intermediaries in the transfer of Mg and other nutrients into the roots. The implication is that findings from laboratory studies of plant growth using sterile growth mediums may not be applicable to their field-based counterparts. It was tentatively concluded that fine roots of sugar maple preferentially sequester heavy isotopes of Mg over light isotopes when mycorrhizal fungi are absent, such as when fostered in the laboratory. However, additional studies are required to better constrain how laboratory grown plant biogeochemical cycling may differ from results procured from the field.

The absence of a primary fractionation step between the soil pool and fine roots at the study

site suggests that uptake by plants does not impact the Mg isotopic composition delivered from the 'critical zone' to the first-order stream. However, plant Mg-cycling nevertheless plays an active role in driving the chemical composition of stream water through the substantial amount of biologically fractionated Mg returned to the soil pool via the litterfall flux, and tightly recycled by the forest. In support of this interpretation, the chemistry of the 1N HNO_3 leach of the C horizon mineral soil, which is often used to reveal the identity of minerals that may be releasing Mg and other base cations into the plant-available soil pool, yielded nearly the same δ^{26}Mg value (–0.66‰) as the Mg dissolved in soil solutions (–0.65 ± 0.15‰), and the bulk forest floor (–0.64‰). Even more revealing was that the Mg/Ca molar ratio of this acid leach (0.17) yielded a nearly identical value to the bulk Mg/Ca molar ratio of the plant aboveground biomass in the study plot (0.14), which is dominated by sugar maple. It is unlikely that the ~ 7:1 ratio of Ca to Mg required to sustain plant growth is the same ratio released by the 1N HNO_3 acid attack of the soils, considering the mineralogy of the soils previously reported in the literature (McCourt, 1993; Bélanger et al., 2012). Due to the complexity associated with the multi-mineralic nature of the soil, it is proposed that alteration products (clays), formed from the weathering of primary silicates in the mineral soil horizons, captured a forest-labeled Mg isotope signature and Mg and Ca in the same proportion recorded in the soil pool as a result of the downward transport of soil solutions from the forest floor. This captured plant-recycled signature was then released by the weathered alteration products in the 1N HNO_3 extraction, yielding a Mg isotope signature and Mg/Ca molar ratio that is the same as the forest floor. The similar δ^{26}Mg values of bulk plants, soil solutions and the first-order stream further support this interpretation. Despite the evidence that the Mg/Ca ratios have been extensively modified by this cycling, it must be noted once again that there exists no evidence for any net fractionation of Mg isotopes during uptake in tree fine roots.

This study emphasizes the dominance of the forest floor as a source of Mg to sustain the nutritional requirements of the vegetation within the forest. Additionally, the large role of the forest floor, as well as the overall aboveground biomass of the forest itself, is highlighted as a cache of nutrient Mg and Ca that is tightly recycled over timescales of thousands of years. This plant-recycled pool of Mg was ultimately derived from atmospheric and soil mineral weathering sources of Mg, however, these annualized fluxes of Mg are very small in the present day with mineral weathering and atmospheric deposition contributing only ~ 1% and ~ 0.3% of Mg to that pool annually, respectively, while the litterfall Mg-flux contributes ~ 5%. However, if this interpretation

is correct, then litterfall should exhibit the same $\delta^{26}Mg$ values as the soil solutions, because litterfall is the main source of Mg to soils. Instead, litterfall was isotopically light (< –0.90‰) compared to the soil solutions (–0.65‰). There are two possibilities for this discrepancy. First, there is the evidence that light Mg isotopes are preferentially translocated from the foliage back into the tree before they drop during autumnal senescence. The leaves measured in this study, however, may not be representative of this process, as they may not be as isotopically heavy as foliage would be expected to become in the latter part of senescent season. Second, sugar maple seeds contain large concentrations of Mg and were not sampled in this study. If the seeds are isotopically heavy compared to the leaves (chlorophyll), which is the case for seeds from laboratory studies of plants (e.g., Black et al., 2008), then seeds are an important contributor of Mg in the litterfall. A bulk forest floor digest yields the same $\delta^{26}Mg$ value and Mg/Ca molar ratio as the soil and stream waters, and further supports that the long-term amalgamation of litterfall (leaves and seeds) at the study site is isotopically heavier than freshly the fallen litterfall collected early in autumnal senescence.

The results reported in Chapter 5 regarding the difference in $\Delta^{26}Mg_{plant\text{-}soln}$ in sugar maple fostered in the laboratory as compared to sugar maple growing in a natural environment prompts additional exploration. In order to better constrain the processes that induce Mg isotope fractionation during root uptake of Mg from the soil pool, the complex interplay between sugar maple and arbuscular mycorrhizal (AM) fungi requires a more in-depth study. Previous studies have shown that ectomycorrhizal fungi, nonmycorrhizal fungi, and rock-inhabiting microcolonial fungi do indeed fractionate Mg isotopes (Fahad et al., 2016, Pokharel et al., 2017), and that these symbiotic fungi also fractionate Mg isotopes differently contingent upon the type of growth substrate on which they are populated (Fahad et al., 2016) or at different pH (Pokharel et al., 2017). Unfortunately, there has yet to be a study regarding Mg isotope uptake effects in AM fungi, which is the type of fungi that forms a mutualistic symbiotic relationship with sugar maple. As such, a newly designed pot experiment attempting to grow sugar maple on artificial growth media, both inoculated with AM fungi and without AM fungi, would help to better constrain the impact AM fungi may have on both the ability sugar maple fine roots have to uptake Mg and also related isotopic fractionation effects. A complimentary field study may also be implemented to fingerprint microbial communities that exist in the soils of the HEW study location and could be useful to not only confirm the presence of AM fungi in the forest soils (and to analyze such fungi for Mg

isotopes), but to also sample and analyze a suite of microbiota that could influence the manner by which roots uptake Mg and fractionate Mg isotopes.

6.2. Manuscript citations

Chapter 2

Worsham S. R., Holmden C. and Qing H. (2013) Preliminary results of a magnesium isotope study of dolomite in Upper Ordovician strata, southeastern Saskatchewan, northern Williston Basin. In *Summary of Investigations 2013*, Sask. Geol. Survey **1**, 1–8.

Chapter 3

Kimmig S. R., Holmden C. and Qing H. (*in preparation*) Origin of dolomite and fluid migration pathways revealed using magnesium and strontium isotopes.

Chapter 4

Kimmig S. R. and Holmden C. (2017) Multi-proxy geochemical evidence for primary aragonite precipitation in tropical-shelf 'calcite sea' during the Hirnantian glaciation. *Geochim. Cosmochim. Acta* **206**, 254–272.

Chapter 5

Kimmig S. R., Holmden C. and Bélanger N. (*in review*) Biogeochemical cycling of Mg and its isotopes in a sugar maple (*Acer saccharum* Marsh.) stand. *Geochim. Cosmochim. Acta.*

LIST OF REFERENCES

Adams J. E. and Rhodes M. L. (1960) Dolomitization by seepage refluxion. *Bull. Am. Assoc. Petrol. Geol.* **44**, 1912–1920.

Al-Karaki G., McMichael B. and Zak J. (2004) Field response of wheat to arbuscular mycorrhizal fungi and drought stress. *Mycorrhiza* **14**, 263–269.

Albarède F. and Beard B. (2004) Analytical methods for non-traditional isotopes. In *Reviews in Mineralogy and Geochemistry* Mineral. Soc. Am. **55**, 113–152.

Anderson F. J. (2011) Structural relationships between surface lineaments and basement faulting in the northeastern Williston Basin. In *The Bakken–Three Forks Petroleum System in the Williston Basin* (Eds. J.W. Robinson, J. A. LeFever and Gaswirth S. B.), Rocky Mountain Assoc. Geol. 376–392.

Andrew A. S., Hamilton P. J., Mawson R., Talent J. A. and Whitford D. J. (1994) Isotopic correlation tools in the Middle Palaeozoic and their relation to extinction event. *APEA J.* **34**, 268–277.

Anna L. O. (2013) Geologic assessment of undiscovered oil and gas in the Williston Basin Province, Montana, North Dakota, and South Dakota. In *Assessment of Undiscovered Oil and Gas Resources of the Williston Basin Province of North Dakota, Montana, and South Dakota* (Ed. U.S. Geological Survey Williston Basin Province Assessment Team), U.S. Geological Survey Digital Data Series 69-W, 71p.

Avila L. A. and Cangialosi J. (2011) Tropical cyclone report hurricane Irene (AL092011) 21–28 August 2011. National Hurricane Center. 45p.

Bachu S. and Hitchon B. (1996) Regional-scale flow of formation waters in the Williston Basin. *AAPG Bull.* **80**, 248–264.

Bagard M. L., Schmitt A. D., Chabaux F., Pokrovsky O. S., Viers J., Stille P., Labolle F. and Prokushkin A. S. (2013) Biogeochemistry of stable Ca and radiogenic Sr isotopes in a larch covered permafrost-dominated watershed of Central Siberia. *Geochim. Cosmochim. Acta* **114**, 169–187.

Baker P. A., Gieskes J. M. and Elderfield H. (1982) Diagenesis of carbonates in deep-sea sediments—Evidence from Sr/Ca ratios and interstitial dissolved Sr^{2+} data. *J. Sed. Petrol.* **52**, 71–82.

Balthasar U., Cusack M., Faryma L., Chung P., Holmer L. E., Jin (2011) Relic aragonite from Ordovician-Silurian brachiopods: Implications for the evolution of calcification. *Geology* **39**, 967–970.

Balthasar U. and Cusack M. (2015) Aragonite-calcite seas – Quantifying the gray area. *Geology*

43, 99–102.

Bamburak J. D. and Klyne K. (2004) A possible new Mississippi Valley–type mineral occurrence near Pemmican Island in the north basin of Lake Winnipegosis, Manitoba (NTS 63B12 and 13, 63C9 and 16). In *Report of Activities 2004*. Manitoba Industry, Economic Development and Mines, Manitoba Geological Survey, pp. 266–278.

Barker A. V. and Pilbeam D. J. (2007) *Handbook of Plant Nutrition*. CRC Press, Taylor and Francis Group, 662p.

Bathurst R. G. C. (1975) *Carbonate sediments and their diagenesis*. 2nd Ed. Elsevier.

Bélanger N. and Holmden C. (2010) Influence of landscape on the apportionment of Ca nutrition in a Boreal Shield forest of Saskatchewan (Canada) using $^{87}Sr/^{86}Sr$ as a tracer. *Can. J. Soil Sci.* **90**, 267–288.

Bélanger N., Côté B., Courchesne F., Fyles J. W., Warfvinge P. and Hendershot W. H. (2002a) Simulation of soil chemistry and nutrient availability in a forested ecosystem of southern Quebec – I. Reconstruction of the time-series files of nutrient cycling using the MAKEDEP model. *Environ. Model. Software* **17**, 427–445.

Bélanger N., Courchesne F., Côté B., Fyles J. W., Warfvinge P., Hendershot W. H., (2002b) Simulation of soil chemistry and nutrient availability in a forested ecosystem of southern Quebec – II. Application of the SAFE model. *Environ. Model. Software* **17**, 445–467.

Bélanger N., Côté B., Fyles J. W., Courchesne F. and Hendershot W. H. (2004) Forest regrowth as the controlling factor of soil nutrient availability 75 years after fire in a deciduous forest of Southern Quebec. *Plant and Soil* **262**, 363–372.

Bélanger N., Holmden C., Courchesne F., Côté B. and Hendershot W. H. (2012) Constraining soil mineral weathering $^{87}Sr/^{86}Sr$ for calcium apportionment studies of a deciduous forest growing on soils developed from granitoid igneous rocks. *Geoderma* **185–186**, 84–96.

Berner R. A. (1997) The rise of plants and their effects on weathering and atmospheric CO_2. *Science* **276**, 544–546.

Berner E. K. and Berner R. A. (1996) *Global environment: Water, air, and geochemical cycles*. Prentice Hall, New Jersey.

Berner R. A, Lasaga A. C. and Garrels R. M. (1983) The carbonate-silicate geochemical cycle and its effect on atmospheric carbon dioxide over the past 100 million years. *Am. J. Sci.* **283**, 641–683.

Bethke C. M. (1985) A numerical model of compaction-driven groundwater flow and heat transfer and its application to the paleohydrology of intracratonic basins. *J. Geophys. Res.* **90**, 6817–6828.

Black J. R., Yin Q. Z. and Casey W. H. (2006) An experimental study of magnesium-isotope fractionation in chlorophyll-a photosynthesis. *Geochim. Cosmochim. Acta* **70**, 4072–4079.

Black J. R., Yin Q. Z., Rustad J. R. and Casey W. H. (2007) Magnesium isotopic equilibrium in chlorophylls. *J. Am. Chem. Soc*. **129**, 8690–8691.

Black J. R., Epstein E., Rains W. D., Yin Q. Z. and Casey W. H. (2008) Magnesium isotope fractionation during plant growth. *Environ. Sci. Technol*. **42**, 7831–7836.

Blättler C. L., Miller N. R. and Higgins J. A. (2015) Mg and Ca isotope signatures of authigenic dolomite in siliceous deep-sea sediments. *Earth Planet. Sci. Lett.* **419**, 32–42.

Böhm F., Gussone N., Eisenhauer A., Dullo W.-C., Reynaud S. and Paytan A. (2006) Calcium isotope fractionation in modern scleractinian corals. *Geochim. Cosmochim. Acta* **70**, 4452–4462.

Bolou-Bi E. B., Vigier N., Brenot A. and Poszwa A. (2009) Magnesium isotope compositions of natural reference materials. *Geostand. Geoanal. Res.* **33**, 95–109.

Bolou-Bi E. B., Poszwa A., Leyval C. and Vigiet N. (2010) Experimental determination of magnesium isotope fractionation during higher plant growth. *Geochim. Cosmochim. Acta* **74**, 2523–2537.

Bolou-Bi E. B., Vigier N., Poszwa A., Boudot J. –P. and Dambrine E. (2012) Effects of biogeochemical processes on magnesium isotope variations in a forested catchment in the Vosges Mountains (France). *Geochim. Cosmochim. Acta* **87**, 341–355.

Bolou-Bi E. B., Dambrine E., Angeli N., Pollier B., Nys C., Guerold F. and Legout A. (2016) Magnesium isotope variations to trace liming input to terrestrial ecosystems: a case study in the Vosges Mountains. *J. Environ. Qual.* **45**, 276–284.

Bots P., Benning L. G., Rickaby R. E. M. and Shaw S. (2011) The role of SO_4 in the switch from calcite to aragonite seas. *Geology* **39**, 331–334.

Bradley J. S and Powley D. E. (1994) Pressure compartments in sedimentary basins: a review. In *Basin Compartments and Seals.* (Ed. P. J. Ortoleva) AAPG Memoirs **61**, 3–26.

Braithwaite C. J. R. (1989) Stylolites as open fluid conduits. *Mar. Petrol. Geol.* **6**, 93–96.

Brand U. and Veizer J. (1980) Chemical diagenesis of a multicomponent carbonate system–1: Trace elements. *J. Sed. Petrol.* **50**, 1219–1236.

Brenchley P. J., Marshall J. D., Carden G. A. F., Robertson D. B. R., Long D. G. F., Meidla T., Hints L. and Anderson T. F. (1994) Bathymetric and isotopic evidence for a short-lived Late Ordovician glaciation in a greenhouse period. *Geology* **22**, 295–298.

Brenchley P. J., Carden G. A. F. and Marshall J. D. (1995) Environmental changes associated with the “first strike” of the Late Ordovician mass extinction. *Mod. Geol.* **20**, 69–82.

Brenot A., Cloquet C., Vigier N., Carignan J. and France-Lanord C. (2008) Magnesium isotope systematics of the lithologically varied Moselle river basin, France. *Geochim. Cosmochim. Acta* **72**, 5070–5089.

Broecker W. S. and Peng T. H. (1982) *Tracers in the Sea*. LDGO Press, Palisades, NY.

Bullen T. D. and Bailey S. W. (2005) Identifying calcium sources at an acid deposition-impacted spruce forest: a strontium isotope, alkaline earth element multi-tracer approach. *Biogeochemistry* **74**, 63–99.

Bullen T. and Chadwick O. (2016) Ca, Sr and Ba stable isotopes reveal the fate of soil nutrients along a tropical climosequence in Hawaii. *Chem. Geol.* **422**, 25–45.

Burton E. A. and Walter L. (1987) Relative precipitation rates of aragonite and Mg calcite from seawater: Temperature or carbonate ion control? *Geology* **15**, 111–114.

Calner M. (2008) Silurian global events – at the tipping point of climate change. In *Mass Extinction* (Ed. M. T. Ashraf) Berlin and Heidelberg, Springer-Verlag, pp. 21–58.

Capo R. C., Stewart B. W. and Chadwick O. A. (1998) Strontium isotopes as tracers of ecosystem processes: theory and methods. *Geoderma* **82**, 197–225.

Carder E. A., Galy A. and Elderfield, H. (2004) The magnesium isotopic composition of oceanic water masses. *Geochim. Cosmochim. Acta* **68**, A329.

Cary E. E., Wood R. J. and Schwartz R. (1990) Stable Mg isotopes as tracers using ICP-MS. *J. Micronutrient Anal.* **8**, 13–22.

Catanzaro E. J., Murphy T. J., Garner E. L. and Shields W. R. (1966) Absolute isotopic abundance ratios and atomic weight of magnesium. *J. Res. Nat. B. Stand*. – A. Physics and Chemistry **70A**, 453–458.

Cathles L. M. (2001) Capillary seals as a cause of pressure compartmentation in sedimentary basins. In *Petroleum Systems of Deep-Water Basins: Global and Gulf of Mexico Experienc*e Proceedings of the Gulf Coast Section Society of Economic Paleontologists and Mineralogists Foundation, 21st Annual Bob F. Perkins Research Conference, pp. 561–572.

Cathles L. M. (2007) Changes in sub-water table fluid flow at the end of the Proterozoic and its implications for gas pulsars and MVT lead-zinc deposits. *Geofluids* **7**, 209–226.

Cathles L. M. and Smith A. T. (1983) Thermal constraints on the formation of Mississippi Valley-type lead-zinc deposits and their implications for episodic basin dewatering and deposit genesis. *Econ. Geol.* **78**, 983–1002.

Chang V. T. –C., Makishima A., Belshaw N. S. and O'Nions R. K. (2003) Purification of Mg from low Mg biogenic carbonates for isotope ratio determination using multiple-collector ICP-MS. *J. Anal. At. Spectrom*. **18**, 296–301.

Chang V. T. –C., Williams R. J. P., Makishima A., Belshaw N. S and O'Nions R. K. (2004) Mg and Ca isotope fractionation during $CaCO_3$ biomineralisation. *Biochem. Biophys. Res. Commun.* **323**, 79–85.

Chatarpaul L., Burgess D. M. and Methven I. R. (1985) Equations for estimating above-ground nutrient content of six eastern Canadian hardwoods. Inf. Rep. PI-X-55, Petawawa National Forestry Institute, Canadian Forestry Service, Chalk River, Ontario.

Chen C. –C., Beauregard F., Côté B., Bélanger N., Courchesne F. and Hendershot W. H. (2013) Partitioning of the source of leaf calcium of American beech and sugar maple using leaf Ca/Sr ratios: a predominantly surficial but variable depth of Ca uptake. *Plant Soil* **373**, 229–242.

Chipley D. and Kyser T. K. (1992) Preservation of ancient basinal fluids in halite fluid inclusions. In *Proceedings of the 7th International Symposium on Water/Rock Interaction* (Eds. J. Kharaka and A. S. Maest, A. S.) International Association of Geochemistry and Cosmochemistry and Alberta Research Council, Sub-Group on Water-Rock Interaction, Edmonton, AB, Canada, pp. 1105–1108.

Churchman G. J. and Lowe D. J. (2012) Alteration, formation, and occurrence of minerals in soils. In *Handbook of Soil Sciences 2nd Edition, Vol. 1: Properties and Processes* (Eds. P. M. Huang, Y. Li, and M. E. Sumner) CRC Press, Taylor and Francis, Boca Raton, FL, USA pp. 20.1–20.72.

Cioppa M. T. (2003) Magnetic evidence for the nature and timing of fluid migration in the Watrous Formation, Williston Basin, Canada: a preliminary study. *J. Geochem. Explor.* **78–79**, 349–354.

Cleavitt N. L., Fahey T. J. and Battles J. J. (2011) Regeneration ecology of sugar maple (*Acer saccharum*): seedling survival in relation to nutrition, site factors, and damage by insects and pathogens. *Can. J. For. Res.* **41**, 235–244.

Cobert F., Schmitt A. –D., Bourgeade P., Labolle F., Badot P. –M., Chabaux F. and Stille P. (2011) Experimental identification of Ca isotopic fractionations in higher plants. *Geochim. Cosmochim. Acta* **75**, 5467–5482.

Cocks L. R. M. and Torsvik T. H. (2011) The Palaeozoic geography of Laurentia and western Laurussia: A stable craton with mobile margins. *Earth Sci. Rev.* **106**, 1–51.

Collier D. E. and Thibodeau B. A. (1995) Changes in respiration and chemical content during autumnal senescence of *Populus tremuloides* and *Quercus rubra* leaves. *Tree Physiol.* **15**, 759–764.

Cooper R. A. and Sadler P. M. (2012) The Ordovician Period. In *The Geologic Time Scale* (Gradstein et al., 2012). Elsevier Publ. Co.

Côté B. and Fyles J. W. (1994) Nutrient concentration and acid–base status of leaf litter of tree species characteristic of the hardwood forest of southern Quebec. *Can. J. For. Res.* **24**, 192–196.

Courchesne F., Roy A. G., Biron P. M., Cote B., Fyles J. and Hendershot W. H. (2001) Fluctuations of climatic and forest growth at the watershed scale. *Environ. Monitor. Assess.* **67**, 161–177.

Courchesne F., Hallé J. P. and Turmel M. C. (2002) Bilans élémentaires holocénes et alteration des minéraux dans trios sols forestiers du Québec méridional. *Géograph. Phys. Quat.* **56**, 5–17.

Courchesne F., Côté B., Fyles J. W., Hendershot W. H., Biron P. M., Roy A. G. and Turmel M. – C. (2005) Recent changes in soil chemistry in a forested ecosystem of southern Québec, Canada. *Soil Sci. Soc. Am. J.* **69**, 1298–1313.

Davies K. M. (2004) *Plant Pigments and Their Manipulation. Annual Plant Reviews.* Blackwell. 368p.

Davies G R. and Smith Jr. L. B. (2006) Structurally controlled hydrothermal dolomite reservoir facies: an overview. *AAPG Bull.* **90**, 1641–1690.

Davy H. (1840) *The Collected Works of Sir Humphry Davy*. (Ed. J. Davy) Smith, Elder and Co. Cornhill, London **5**, 109–116.

Davy H. (1812) *Elements of Chemical Philosophy* Part 1. Bradford and Inskeep **1**, 198p.

de Dolomieu (1791) D. Sur un genre de Pierres calcaires trés-peu effervescentes avec les acides, & phosphorescentes par la collision. *J. de Physique* **39**, 3–10. See also English translation of Dolomieu's paper with notes reporting his discovery of dolomite by A. V. Carozzi and D. H. Zenger (1981) *J. Geol. Ed.* **29**, 4–10.

de Villiers S., Dickson J. A. D. and Ellam R. M. (2005) The composition of the continental river weathering flux deduced from seawater Mg isotopes. *Chem. Geol.* **216**, 133–142.

Decoteau D. R. (2005) *Principles of plant science: Environmental factors and technology in growing plants.* Pearson Prentice Hall. 432 pp.

Deffeyes K. S., Lucia F. J. and Weylt P. K. (1964) Dolomitization: observations on the island of Bonaire, Netherlands Antilles. *Science* **143**, 678–679.

Deming D., Cranganu C. and Lee Y. (2002) Self-sealing in sedimentary basins. *J. Geophys. Res.* **107**, B12.

Derry L. A., Kurtz A. C., Ziegler K. and Chadwick O. A. (2005) Biological control of terrestrial silica cycling and export fluxes to watersheds. *Nature* **433**, 728–730.

Doig R. (1991) U-Pb Zircon dates of Morin anorthosite suite rocks, Grenville Province, Quebec. *J. Geol*. **99**, 729–738.

Drever J. I. (1974) The Magnesium Question. In *The Sea* (Ed. E. Goldberg) Wiley-Interscience, New York, **5**, pp. 337–358.

Drever J. I. (1994) The effect of land plants on weathering rates of silicate minerals. *Geochim. Cosmochim. Acta* **58**, 2325–2332.

Drouet Th., Herbauts J., Gruber W. and Demaiffe D. (2005) Strontium isotope composition as a tracer of calcium sources in two forest ecosystems in Belgium. *Geoderma* **126**, 203–223.

Duchesne L., Ouimet R. and Houle D. (2010) Nutrient transfer by leaf litterfall during a sugar maple decline episode at Lake Clair watershed, Québec, Canada. *Plant Ecol.* **208**, 213–221.

Dyke S. (2004) An outline of North American deglaciation with emphasis on central and northern Canada. In *Quaternary glaciations: extent and chronology*. (Eds. J. Ehlers and P. L. Gibbard) Elsevier, Amsterdam pp. 373–424.

Dyke A. S. and Prest V. K. (1987) Late Wisconsinan and Holocene history of the Laurentide ice sheet. *Géog. Phys. Quat.* **41**, 237–263.

Dunham J. B. (1977) Depositional environments and paleogeography of the Upper Ordovician, Lower Silurian carbonate platform of central Nevada. In Paleozoic Paleogeography of the Western United States - I. Pacific Section. Society of Economic Paleontologists and Mineralogists, Book 7 (eds. J. H. Stewart, C. H. Stevens and A. E. Fritsche), pp. 157–164.

Edmond J. M., Measures C., McDuff R. E., Chan L. H., Collier R., Grant B., Gordon L. I. and Corliss J. B. (1979) Ridge crest hydrothermal activity and the balances of the major and minor elements in the ocean: the Galapagos data. *Earth Planet. Sci. Lett.* **46**, 1–18.

Eglington B. M. and Harmer R. E. (1999) *GEODATE for Windows version 1: Isotope regression and modelling software*. Council for Geoscience Open-file report 1999–0206 O, 26 pp.

Elderfield H. and Schultz A. (1996) Mid-ocean ridge hydrothermal fluxes and the chemical composition of the ocean. *Ann. Rev. Earth Planet. Sci.* **24**, 191–224.

Emslie R. F. (1975) Major rock units of the Morin Complex, southwestern Quebec. *Geol. Survey Canada*, Paper 74–48, 45 pp.

Epstein E. and Bloom A. J. (2005) *Mineral Nutrition of Plants: Principles and Perspectives*. 2nd Ed. Sinauer Associates Inc., USA 380p.

Epstein A. G., Epstein J. B. and Harris L. D. (1977) Conodont color alteration—an index to organic metamorphism. *USGS. Prof. Pap.* **995**, 1–27.

Fahad Z. A., Bolou-Bi E. B., Köhler S. J., Finlay R. D. and Mahmood S. (2016) Fractionation and assimilation of Mg isotopes by fungi is species dependent. *Environ. Microbiol. Rep.* **8**, 956–965.

Fairbridge R. W. (1972) *The encyclopedia of geochemistry and environmental sciences. (Encyclopedia of earth sciences series).* New York: Van Nostrand Reinhold. 4A, 429p.

Fantle M. S. and DePaolo D. J. (2007) Ca isotopes in carbonate sediment and pore fluid from ODP Site 807A: The Ca^{2+} (aq)–calcite equilibrium fractionation factor and calcite recrystallization rates in Pleistocene sediments. *Geochim. Cosmochim. Acta* **71**, 2524–2546.

Fantle M. S. and Higgins J. (2014) The effects of diagenesis and dolomitization on Ca and Mg isotopes in marine platform carbonates: Implications for the geochemical cycles of Ca and Mg. *Geochim. Cosmochim. Acta* **142**, 458–481.

Farkaš J., Déjeant A., Novák M. and Jacobsen S. B. (2011) Calcium isotope constraints on the uptake and sources of Ca^{2+} in a base-poor forest: a new concept of combining stable ($\delta^{44/42}Ca$) and radiogenic (ε_{Ca}) signals.

Farkaš J., Frýda J. and Holmden C. (2016) Calcium isotope constraints on the marine carbon cycle and $CaCO_3$ deposition during the late Silurian (Ludfordian) positive $\delta^{13}C$ excursion. *Earth Planet. Sci. Lett.* **451**, 31–40.

Ferguson J. E., Henderson G. M., Kucera M. and Rickaby R. E. M. (2008) Systematic change of foraminiferal Mg/Ca ratios across a strong salinity gradient. *Earth Planet. Sci. Lett.* **265**, 153–166.

Feinstein S., Kohn B., Osadetz K., Everitt R., and O'Sullivan P. (2009) Variable Phanerozoic thermal history in the Southern Canadian Shield: evidence from an apatite fission track profile at the Underground Research Laboratory (URL), Manitoba. *Tectonophysics* **475**, 190–199.

Finnegan S., Bergmann K., Eiler J. M., Jones D. S., Fike D. A., Eisenman I., Hughes N. C., Tripati A. K. and Fischer W. W. (2011) The magnitude and duration of late Ordovician–early Silurian glaciation. *Science* **331**, 903–906.

Finney S. C., Cooper J. D. and Berry W. B. N. (1997) Late Ordovician mass extinction: sedimentologic, cyclostratigraphic, and biostratigraphic records from platform and basin successions, central Nevada. *BYU Geol. Stud.* **42**, 79–102.

Finney S. C., Berry W. B. N., Cooper J. D., Ripperdan R. L., Sweet W. C., Jacobson S. R., Soufiane A., Achab A. and Noble P. J. (1999) Late Ordovician mass extinction: a new perspective from stratigraphic sections in central Nevada. *Geology* **27**, 215–218.

Finney S. C., Berry W. B. N. and Cooper J. D. (2007) The influence of denitrifying seawater on graptolite extinction and diversification during the Hirnantian (latest Ordovician) mass extinction event. *Lethaia* **40**, 281–291.

Folk R. L. (1965) Some aspects of recrystallization in ancient limestones. In *Dolomitization and limestone diagenesis* (eds. L. C. Pray and R. C. Murray), Soc. Econ. Paleon. Mineral. Special Publication 13, pp. 14–48.

Foster G. L., Pogge von Strandmann P. A. E. and Rae J. W. B. (2010) Boron and magnesium isotopic composition of seawater. *Geochem. Geophys. Geosyst.* **11**, Q08015.

Fowler M. G., Stasiuk L. D., Li M., Obermajer M. and Osadetz K. G. (1998) Reexamination of the Red River petroleum system, southeastern Saskatchewan, Canada. In *Eighth International Williston Basin Symposium* (Eds. J. E. Christopher, C. F. Gilboy, D. F. Paterson and S. L. Bend) Sask. Geol. Soc., Special Publication 13, 11–13.

Friedman R. M. and Martignole J. (1995) Mesoproterozoic sedimentation, magmatism, and metamorphism in the southern part of the Grenville Province (western Quebec): U–Pb geochronological constraints. *Can. J. Earth Sci.* **32**, 2103–2114.

Galy A., Belshaw N., Halicz L. and O'Nions R. (2001) High precision measurement of magnesium-isotopes by multiple-collector inductively coupled plasma mass spectrometry. *Int. J. Mass Spectrom.* **208**, 89–98.

Galy A., Bar-Matthews M., Halicz L. and O'Nions R. K. (2002) Mg isotopic composition of carbonate: insight from speleothem formation. *Earth Planet. Sci. Lett*. **201**, 105–115.

Galy A., Yoffe O., Janney P., Williams R., Cloquet C., Alard O., Halicz L., Wadhwa M., Hutcheon I., Ramon E. and Carignan J. (2003) Magnesium-isotope heterogeneity of the isotopic standard SRM980 and new reference materials for magnesium isotope-ratio measurements. *J. Anal. At. Spectrom.* **18**, 1352–1356.

Gerhard L. C., Anderson S. B., LeFever J. A. and Carlson C. G. (1982) Geological development, origin, and energy mineral resources of the Williston Basin, North Dakota. *Am. Assoc. Petrol. Geol. Bull.* **66**, 989–1020.

Gerhard L. C., Anderson S. B. and LeFever J. A. (1987) Structural history of the Nesson Anticline, North Dakota. In *Williston Basin: anatomy of a cratonic oil province* (Ed. M. W. Longman)

Rocky Mountain Association of Geologists, pp. 337–353.

Geske A., Zorlu J., Richter D. K., Buhl D., Niedermayr A. and Immenhauser A. (2012) Impact of diagenesis and low grade metamorphosis on isotope ($\delta^{26}Mg$, $\delta^{13}C$, $\delta^{18}O$ and $^{87}Sr/^{86}Sr$) and elemental (Ca, Mg, Mn, Fe and Sr) signatures of Triassic sabkha dolomites; *Chem. Geol.* **332-333**, 45–64.

Geske A., Goldstein R. H., Mavromatis V., Richter D. K., Buhl D., Kluge T., John C. M. and Immenhauser A. (2015a) The magnesium isotope ($\delta^{26}Mg$) signature of dolomites. *Geochim. Cosmochim. Acta* **149**, 131–151.

Geske A., Lokier S., Dietzel M., Richter D.K., Buhle D. and Immenhauser A. (2015b) Magnesium isotope composition of sabkha porewater and related (Sub-) Recent stoichiometric dolomites, Abu Dhabi (UAE). *Chem. Geol.* **393**–**394**, 112–124.

Gingras M. K., Pemberton S. G., Muelenbachs K. and Machel H. (2004) Conceptual models for burrow-related, selected dolomitization with textural and isotopic evidence from the Tyndall Stone, Canada. *Geobiology* **2**, 21–30.

Gischler E., Dietrich S., Harris D., Webster J. M. and Ginsburg R. N. (2013) A comparative study of modern carbonate mud in reefs and carbonate platforms: Mostly biogenic, some precipitated. *Sed. Geol.* **292**, 36–55.

Given K. R. and Lohmann K. C. (1985) Derivation of the original isotopic composition of Permian marine cements. *J. Sed. Petrol.* **55**, 430–439.

Gussone N., Böhm F., Eisenhauer A., Dietzel M., Heuser A., Teichert B. M. A., Reitner J., Wörheide G. and Dullo W. C. (2005) Calcium isotope fractionation in calcite and aragonite. *Geochim. Cosmochim. Acta* **69**, 4485–4494.

Haidl F. M., Jensen G. K. S. and Yang C. (2013) Economic potential of Red River strata in Saskatchewan: drilling deeper for additional resources. In *At the Centre of the Continent* Geol. Assoc. Can., Min. Assoc. Can., Jt. Ann. Meet., Winnipeg, Manitoba, Abst., **36**, 106.

Hardie L. A. (1996) Secular variation in seawater chemistry: An explanation for the coupled secular variation in the mineralogies of marine limestones and potash evaporites over the past 600 m.y. *Geology* **24**, 279–283.

Harris A. G., Wardlaw B. R., Rust C. C., and Merrill K. G. (1980) Maps for assessing thermal maturity (conodont color alteration index maps) in Ordovician through Triassic rocks in Nevada and Utah and adjacent parts of Idaho and California. *USGS Misc. Invest.* Map I-1249, scale 1:2,500,000.

Heap M. J., Baud P., Reuschlé T. and Meredith P. G. (2014) Stylolites in limestones: barriers to fluid flow? *Geology* **42**, 51–54.

Hendershot W. H., Lalande H. and Duquette M. (2007) Ion exchange and exchangeable cations. In *Soil sampling and methods of analysis* (Eds. M. R. Carter and E. G. Gregorich). CRC Press, Boca Raton, FL, USA, 10 pp.

Higgins J. A. and Schrag D. P. (2010) Constraining magnesium cycling in marine sediments using magnesium isotopes. *Geochim. Cosmochim. Acta* **74**, 5039–5053.

Higgins J. A. and Schrag D. P. (2012) Records of Neogene seawater chemistry and diagenesis in deep-sea carbonate sediments and pore fluids. *Earth Planet. Sci. Lett.* **357–358**, 386–396.

Higgins J. A. and Schrag D. P. (2015) The Mg isotopic composition of Cenozoic seawater – evidence for a link between Mg-clays, seawater Mg/Ca, and climate. *Earth Planet. Sci. Lett.* **416**, 73–81.

Hindshaw R. S., Reynolds B. C., Wiederhold J. G., Kretzschmar R. and Bourdon B. (2011) Calcium isotopes in a proglacial weathering environment: Damma glacier, Switzerland. *Geochim. Cosmochim. Acta* **75**, 106–118.

Hindshaw R. S., Reynolds B. C., Wiederhold J. G., Kiczka M., Kretzschmar R. and Bourdon B. (2013) Calcium isotope fractionation in alpine plants. *Biogeochemistry* **112**, 373–388.

Hippler D., Buhl D., Witbaard R., Richter D. K. and Immenhauser A. (2009) Towards a better understanding of magnesium-isotope ratios from marine skeletal carbonates. *Geochim. Cosmochim. Acta* **73**, 6134–6146.

Hoch W. A., Zeldin E. L. and McCown B. H. (2001) Physiological significance of anthocyanins during autumnal leaf senescence. *Tree Physiol.* **21**, 1–8.

Hoch W. A., Singsaas E. L. and McCown B. H. (2003) Resorption protection. Anthocyanins facilitate nutrient recovery in autumn by shielding leaves from potentially damaging light levels. *Plant Physiol.* **133**, 1296–1305.

Holland H. D. (2005) Sea level, sediments and the composition of seawater. *Am. J. Sci.* **305**, 220–239.

Holmden C. (2009) Ca isotope study of Ordovician dolomite, limestone, and anhydrite in the Williston Basin: implications for subsurface dolomitization and local Ca cycling. *Chem. Geol.* **268**, 180–188.

Holmden C. and Bélanger N. (2010) Ca isotope cycling in a forested ecosystem. *Geochim. Cosmochim. Acta* **74**, 995–1015.

Holmden C., Creaser R. A., Muehlenbachs K., Leslie S. A. and Bergström S. M. (1998) Isotopic evidence for geochemical decoupling between ancient epeiric seas and bordering oceans: Implications for secular curves. *Geology* **26**, 567–570.

Holmden C., Panchuk K. and Finney S. C. (2012a) Tightly coupled records of Ca and C isotope changes during the Hirnantian glaciation event in an epeiric sea setting. *Geochim. Cosmochim. Acta* **98**, 94–106.

Holmden C., Papanastassiou D. A., Blanchon P. and Evans S. (2012b) $\delta^{44/40}$Ca variation in modern shallow water carbonates and its bearing on seawater Ca-cycling in the geological past. *Geochim. Cosmochim. Acta* **83**, 179–194.

Hover V. C., Walter L. M. and Peacor D. R. (2001) Early marine diagenesis of biogenic and Mg-calcite: New constraints from high-resolution STEM and AEM analyses of modem carbonate platform carbonates. *Chem. Geol.*, **175**, 221–248.

Hu Z., Hu W., Wang X., Lu Y., Wang L., Liao Z. and Li W. (2017) Resetting of Mg isotopes between calcite and dolomite during burial metamorphism: outlook of Mg isotopes as geothermometer and seawater proxy. *Geochim. Cosmochim. Acta* **208**, 24–40.

Huang K. –J., Teng F. –Z., Wei G. –J., Ma J. –L. Bao Z. –Y. (2012) Adsorption- and desorption controlled magnesium isotope fractionation during extreme weathering of basalt in Hainan Island, China. *Earth Planet. Sci. Lett.* **359–360**, 73–83.

Huang K. –J., Shen B., Lang X. –G., Tang W. –B., Peng Y., Ke S., Kaufman A. J., Ma H. –R. and Li F. –B. (2015) Magnesium isotopic compositions of the Mesoproterozoic dolostones: implications for Mg isotopic systematics of marine carbonates. *Geochim. Cosmochim. Acta* **164**, 333–351.

Hunt J. M. (1990) Generation and migration of petroleum from abnormally pressured fluid compartments. *AAPG Bull.* **74**, 1–12.

Husson J. M., Higgins J. A., Maloof A. C. and Schoene B. (2015) Ca and Mg isotope constraints on the origin of Earth's deepest δ^{13}C excursion. *Geochim. Cosmochim. Acta* **160**, 243–266.

Iampen H. T. and Rostron B. J. (2000) Hydrogeochemistry of pre-Mississippian brines, Williston Basin, Canada-USA. *J. Geochem. Explor,* **69-70**, 29–35.

Immenhauser A., Della Porta G., Kenter J. A. M. and Bahamonde J. R. (2003) An alternative model for positive shifts in shallow-marine carbonate δ^{13}C and δ^{18}O. *Sedimentology* **50**, 953–959.

Immenhauser A., Holmden C. and Patterson W. P. (2008) Interpreting the carbon-isotope record of ancient shallow epeiric seas: Lessons from the recent. In *Dynamics of Epeiric Seas* (eds. Holmden C. and Pratt B.) Geol. Assoc. Can. Special Paper 48, pp. 137–174.

Immenhauser A., Buhl D., Richter D., Niedermayr A., Riechelmann D., Dietzel M. and Schulte U. (2010) Magnesium-isotope fractionation during low-Mg calcite precipitation in a limestone cave – field study and experiments. *Geochim. Cosmochim. Acta* **74**, 4346–4364.

Iverson W. P., Martinsen R. S. and Surdam R. C. (1994) Pressure seal permeability and two-phase flow. In *Basin Compartments and Seals* (Ed. P. J. Ortoleva) AAPG Memoirs **61**, 313–319.

Jaanusson V. (1966) Fossil brachiopods with probable aragonitic shells. *GFF* **88**, 279–281.

Jacobson A. D. and Holmden C. (2008) δ^{44}Ca evolution in a carbonate aquifer and its bearing on the equilibrium isotope fractionation factor for calcite. *Earth Planet. Sci. Lett.* **270**, 349–353.

Jacobson A. D., Zhang Z., Lundstrom C. and Huang F. (2010) Behavior of Mg isotopes during dedolomitization in the Madison Aquifer, South Dakota. *Earth Planet. Sci. Lett.* **297**, 446–452.

Jensen G. K. S., Rostron B. J. Duke M. J. M. and Holmden C. (2006) Bromine and stable isotopic profiles of formation waters from potash mine-shafts, Saskatchewan, Canada. *J. Geochem. Explor.* **89**, 170–173.

Jin J., Harper D. A. T., Rasmussen J. A. and Sheehan P. M. (2012) Late Ordovician massive-bedded Thalassinoides ichnofacies along the palaeoequator of Laurentia. *Palaeogeogr. Palaeoclimatol. Palaeoecol.* **367–368**, 73–88.

Jones D. L. (1998) Organic acids in the rhizosphere – a critical review. *Plant and Soil* **205**, 25–44.

Jones D. S., Creel R. C. and Rios B. A. (2016) Carbon isotope stratigraphy and correlation of depositional sequences in the Upper Ordovician Ely Springs Dolostone, eastern Great Basin, USA. *Palaeogeogr. Palaeoclimatol. Palaeoecol.* **458**, 85–101.

Kaczmarek S. E. and Sibley D. F. (2014) Direct physical evidence of dolomite recrystallization. *Sedimentology* **61**, 1862–1882.

Katz A. (1973) The interaction of magnesium with calcite during crystal growth at 25–90°C and one atmosphere. *Geochim. Cosmochim. Acta* **37**, 1563–1586.

Kendall A. C. (1976) The Ordovician carbonate succession (Bighorn Group) of southeastern Saskatchewan. *Sask. Dep. Miner. Resour, Rep.* **180**, 1–185.

Kendall A. C. (1977) Origin of dolomite mottling in Ordovician limestones from Saskatchewan and Manitoba. *Bull. Can. Petrol. Geol.* **25**, 480–504.

Kershaw S. (2013) Palaeozoic stromatoporoids futures: A discussion of their taxonomy, mineralogy and applications in palaeoecology and palaeoenvironmental analysis. *J. Palaeogeogr.* **2**, 163–182.

Kimmig S. R. and Holmden C. (2017) Multi-proxy geochemical evidence for primary aragonite precipitation in a tropical-shelf 'calcite sea' during the Hirnantian glaciation. *Geochim. Cosmochim. Acta* **206**, 254–272.

Kinsman D. J. J. (1969) Interpretation of Sr^{2+} concentrations in carbonate minerals and rocks. *J. Sed. Petrol.* **39**, 486–508.

Kittrick J. A. and Hope E. W. (1963) A procedure for the particle-size separation of soils for X-ray Diffraction analysis. *Soil Science* **96**, 319–325.

Klironomos J. N. (1995) Arbuscular mycorrhizae of *Acer saccharum* in different soil types. *Can. J. Bot.* **73**, 1824–1830.

Knoll A. H. (2003) Biomineralization and evolutionary history. In *Reviews in Mineralogy and Geochemistry* Mineral. Soc. Am. **54,** 329–356.

Koehler G., Kyser T. K., Enkin R. and Irving E. (1997) Paleomagnetic and isotopic evidence for the diagenesis and alteration of evaporites in the Paleozoic Elk Point Basin, Saskatchewan, Canada. *Can. J. Earth Sci.* **34**, 1619–1629.

Kohm J. A. and Louden R. O. (1978) Ordovician Red River Formation, eastern Montana and western North Dakota: relationships between lithofacies and production. In *The economic geology of the Williston Basin: Williston Basin Symposium*. (Eds. D. Estelle and R. Miller) Montana Geol. Soc. 24th Ann. Field Conf. Guide., **99–117**.

Kozłowski W. and Sobién K (2012) Mid-Ludfordian coeval carbon isotope, natural gamma ray and magnetic susceptibility excursions in the Mielnik IG-1 borehole (Eastern Poland)–Dustiness as a possible link between global climate and the Silurian carbon isotope record. *Palaeogeogr. Palaeoclimatol. Palaeoecol.* **339–341**, 74–97.

Kozłowski W. (2015) Eolian dust influx and massive whitings during the kozlowski/Lau Event: carbonate hypersaturation as a possible driver of the mid-Ludfordian Carbon Isotope Excursion. *Bull. Geosci.* **90**, 807–840.

Kreis L. K. and Kent D. M. (2000) Basement controls on Red River sedimentation and hydrocarbon production in southeastern Saskatchewan. In *Summary of Investigations 2000*. Sask. Geol. Survey **1**, 21–42.

Krogh T. E. and Hurley P. M. (1968) Strontium isotope variation and whole-rock isochron studies Grenville Province of Ontario. *J. Geophys. Res.* **73**, 7107–7125.

Kump L. R., Arthur M. A., Patzkowski M. E., Gibbs M. T., Pinkus D. S. and Sheehan P. M. (1999) A weathering hypothesis for glaciation at high atmospheric pCO_2 during the Late Ordovician. *Palaeogeogr. Palaeoclimatol. Palaeoecol.* **152**, 173–187.

Lambert M. –C., Ung C. –H. and Raulier F. (2005) Canadian national tree aboveground biomass equations. *Can. J. For. Res.* **35**, 1996–2018.

Land L. S. (1967) Diagenesis of skeletal carbonates. *J. Sed. Petrol.* **37**, 914–930.

Land L. S. (1973) Contemporaneous dolomitization of Middle Pleistocene reefs by meteoric water, north Jamaica. *Bull. Mar. Sci.* **23**, 64–92.

Land L. S. (1980) The isotopic and trace element geochemistry of dolomite: the state of the art. In *Concepts and Models of Dolomitization* (Eds. D. H. Zenger et al.) SEPM Special Publication 28, pp. 87–110.

Land L. S. (1985) The origin of massive dolomite. *J. Geol. Ed.* **33**, 112–125.

Land L. S. (1998) Failure to precipitate dolomite at 25°C from dilute solution despite 1000-fold oversaturation after 32 years. *Aquat. Geochem.* **4**, 361–368.

Langmeier M., Ginsburg S. and Matile Ph. (1993) Chlorophyll breakdown in senescent leaves: demonstration of Mg-dechelatase activity. *Physiol. Plant*. **89**, 347–353.

Langmuir C. H., Vocke Jr., R. D. and Hanson G. N. (1978) A general mixing equation with applications to Icelandic basalts. *Earth. Planet Sci. Lett.* **37**, 380–392.

LaPorte D. F., Holmden C., Patterson W. P., Loxton J. D., Melchin M. J., Mitchell C. E., Finney S. C. and Sheets H. D. (2009) Local and global perspectives on carbon and nitrogen cycling during the Hirnantian glaciation. *Palaeogeogr. Palaeoclimatol. Palaeoecol.* **276**, 182–195.

Lasemi Z. and Sandberg P. A. (1984) Transformation of aragonite-dominated lime muds to microcrystalline limestones. *Geology* **12**, 420–423.

Lea D. W., Mashiotta T. A. and Spero H. J. (1999) Controls on magnesium and strontium uptake in plaktonic foraminifera determined by live culturing. *Geochim. Cosmochim. Acta* **63**, 2369–2379.

Leach D., Bradley D., Lewchuk M. T., Symons D. T. A., de Marsily G. and Brannon J. (2001) Mississippi Valley-type lead-zinc deposits through geological time: implications from recent age-dating research. *Mineral. Dep.* **36**, 711–740.

Leach D. Taylor R. D., Fey D. L., Diehl S. F. and Saltus R. W. (2010) A deposit model for Mississippi Valley-type lead-zinc ores. *USGS Sci. Invest. Rep.* 2010-5070-A, 52p.

Lee T. and Papanastassiou D. A. (1974) Mg isotopic anomalies in the Allende meteorite and correlation with O and Sr effects. *Geophys. Res. Lett.* **1**, 225–228.

Lee J. and Morse J. W. (2010) Influences of alkalinity and pCO_2 on $CaCO_3$ nucleation from estimated Cretaceous composition of seawater representative of "calcite seas." *Geology* **38**, 115–118.

Lehnert O., Eriksson M. J., Calner M., Joachimski M. and Buggisch W. (2007) Concurrent sedimentary and isotopic indications for global climatic cooling in the late Silurian. *Acta Palaeontol. Sin.* **46**, 249–255.

Leicester H. M. and Klickstein H. S (1952) *A Source Book in Chemistry*, *1400–1900*. Harvard University Press, Cambridge, MA.

Li W., Chakraborty S., Beard B. L., Romanek C. S. and Johnson C. M. (2012) Magnesium isotope fractionation during precipitation of inorganic calcite under laboratory conditions. *Earth Planet. Sci. Lett.* **333–334**, 304–316.

Li W., Beard B. L., Li C., Xu H. and Johnson C. M. (2015) Experimental calibration of Mg isotope fractionation between dolomite and aqueous solution and its geological implications. *Geochim. Cosmochim. Acta* **157**, 164–181.

Likens G. E., Driscoll C. T. and Buso D. C. (1996) Long-term effects of acid rain: response and recovery of a forest ecosystem. *Science* **272**, 244–246.

Ling M. X., Sedaghatpour F., Teng F. Z., Hays P. D., Strauss J. and Sun W. D. (2011) Homogenous magnesium isotopic composition of seawater: an excellent geostandard for Mg isotope analysis. *Rapid Commun. Mass Spectrom.* **25**, 2828–2836.

Liu G. E. and Côté B. (1993) Neutralization and buffering capacity of leaves of sugar maple, largetooth aspen, paper birch and balsam fir. *Tree Physiology* **12**, 15–21.

Longman M. W., Fertal T. G. and Glennie J. S. (1983) Origin and geometry of Red River dolomite reservoirs, western Williston Basin. *Amer. Assoc. Petrol. Geol. Bull.* **67**, 744–771.

Longman M. W. and Haidl F. M. (1996) Cyclic deposition and development of porous dolomites in the Upper Ordovician Red River Formation, Williston Basin. In *Paleozoic Systems of the Rocky Mountain Region* (Eds. M. W. Longman and M. D. Sonnenfeld). Rocky Mountain Section. SEPM. Soc. Sed. Geol., pp. 29–46.

Lovett G. M., Lindberg S. E., Richter D. D. and Johnson D. W. (1985) The effects of acidic deposition on cation leaching from three deciduous forest canopies. *Can. J. For. Res.* **15**, 1055–1060.

Loydell D. K. (2007) Early Silurian positive $\delta^{13}C$ excursions and their relationship to glaciations, sea-level changes and extinction events. *Geol. J.* **42**, 531–546.

MacDonald J. D., Bélanger N., Sauvé S., Courchesne F. and Hendershot W. H. (2007) Collection and characterization of soil solutions. In *Soil sampling and methods of analysis*. 2nd ed. (Eds. M. R. Carter and E. G. Gregorich) CRC Press, Boca Raton, FL. pp. 179–198.

Machel H. G. (2004) Concepts and models of dolomitization: a critical reappraisal. In *The Geometry and Petrogenesis of Dolomite Hydrocarbon Reservoirs* (Eds. C. J. R. Braithwaite, G. Rizzi and G. Darke). Geological Society of London, Special Publication 235, 7–63.

Machel H. G. and Anderson J. H. (1989) Pervasive subsurface dolomitization of the Nisku

Formation in central Alberta. *J. Sed. Petrol*. **59**, 891–911.

Malone M. J., Baker P. A. and Burns S. J. (1996) Recrystallization of dolomite: an experimental study from 50-200°C. *Geochim. Cosmochim. Acta* **60**, 2189–2207.

Marschner H. (1995) *Mineral nutrition of higher plants*. Academic Press, London. 889p.

Martignole J. and Schrijver K. (1970) Tectonic setting and evolution of the Morin anorthosite, Grenville Province, Québec. *Bull. Geol. Soc. Finland* **42**, 165–209.

Mason B. (1992) *Victor Moritz Goldschmidt: Father of modern geochemistry.* The Geochemical Society, Special Publication 4.

Mavromatis V., Prokushkin A. S., Pokrovsky O. S., Viers J. and Korets M. A. (2014) Magnesium isotopes in permafrost-dominated Central Siberian larch forest watersheds. *Geochim. Cosmochim. Acta* **147**, 76–89.

Mavromatis V., Rinder T., Prokushkin A. S., Pokrovsky O. S., Korets M. A., Chmeleff J. and Oelkers E. H. (2016) The effect of permafrost, vegetation, and lithology on Mg and Si isotope composition of the Yenisey River and its tributaries at the end of the spring flood. *Geochim. Cosmochim. Acta* **191**, 32–46.

Mazzullo S. J. (1980) Calcite pseudospar replacive of marine acicular aragonite, and implications for aragonite cement diagenesis. *J. Sed. Petrol.* **50**, 409–422.

McCourt G. H. (1993) Acidification and buffering mechanisms in soil ecosystems. McGill University, Dept. of Renewable Resources M. Sc. thesis, 64p.

Melchin M. J. and Holmden C. (2006) Carbon isotope chemostratigraphy in Arctic Canada: Sea-level forcing of carbonate platform weathering and implications for Hirnantian global correlation. *Palaeogeogr. Palaeoclimatol. Palaeoecol.* **234**, 186–200.

Mengel K. and Kirkby E. A. (2001) *Principles of plant nutrition* 5th Ed. Kluwer Academic Publishers. Springer Netherlands. 849p.

Miller E. K., Blum J. D. and Friedland A. J. (1993) Determination of soil exchangeable-cation loss and weathering rates using Sr isotopes. *Nature* **362**, 438–441.

Millero F. J. (1974) The physical chemistry of seawater. *Ann. Rev. Earth Planet. Sci*. **2**, 101–150.

Milliman J. D. (1993) Production and accumulation of calcium carbonate in the ocean: Budget of a nonsteady-state. *Global Biogeochem. Cycles* **7**, 927–957.

Moore C. H. (1989) *Carbonate Diagenesis and Porosity*. Developments in Sedimentology 46, Elsevier, Amsterdam, 338p.

Moore C. H., Chowdhury A. and Chan L. (1988) Upper Jurassic Smackover platform dolomitization, northwestern Gulf of Mexico: a tale of two waters. In *Sedimentology and Geochemistry of Dolostones* (Eds. P. O. Roehl and P. W. Choquette) SEPM Special Publication 43, 175–189.

Moore J., Jacobson A. D., Holmden C. and Craw D. (2013) Tracking the relationship between mountain uplift, silicate weathering, and long-term CO_2 consumption with Ca isotopes: Southern Alps, New Zealand. *Chem. Geol.* **341**, 110–127.

Morrow D. W. (1982) Diagenesis 2; Dolomite – Part 2 Dolomitization models and ancient dolostones. *Geosci. Can.* **9**, 95–107.

Morse J. W., Wang Q. and Tsio M. –Y. (1997) Influences of temperature and Mg:Ca ratio on $CaCO_3$ precipitates from seawater. *Geology* **25**, 85–87.

Nash M. C., Troitzsch U., Opdyke B. N., Trafford J. M., Russell B. D. and Kline D. I. (2011) First discovery of dolomite and magnesite in living coralline algae and its geobiological implications; *Biogeosciences* **8**, 3331–3340.

Nezat C. A., Blum J. D., Yanai R. D. and Hamburg S. P. (2007) A sequential extraction to determine the distribution of apatite in granitoid soil mineral pools with application to weathering at the Hubbard Brook Experimental Forest, NH, USA. *Appl. Geochem.* **22**, 2406–2421.

Nezat C. A., Blum J. D., Yanai R. D. and Park B. B. (2008) Mineral sources of calcium and phosphorus in soils of the northeastern United States. *Soil Sci. Soc. Am. J.* **72**, 1786–1794.

Noodén L. D., Guiamét J. J. and John I. (1997) Senescence mechanisms. *Physiol. Plant.* **101**, 746–753.

Norford B. S., Haidl F. M., Bezys R. K., Cecile M. P., McCabe F. R. and Paterson D. F. (1994) Middle Ordovician to Lower Devonian strata of the Western Canada Sedimentary Basin. In *Geological Atlas of the Western Canada Sedimentary Basin* (G. D. Mossip and I. Shetson) Can. Soc. Petrol. Geol., Alberta Research Council, pp. 109–127.

O'Brien C. and Hendershot W. H. (1993) Separating streamflow into groundwater, solum and upwelling flow and its implications for hydrochemical modelling. *J. Hydrol.* **146**, 1–12.

Oomori T., Kaneshima H., Maezato Y. and Kitano Y. (1987) Distribution coefficient of Mg^{2+} ions between calcite and solution at 10–50°C. *Mar. Chem.* **20**, 327–336.

Opfergelt S., Georg R. B., Delvaux B., Cabidoche Y. –M., Burton K. W. and Halliday A. N. (2012) Mechanisms of magnesium isotope fractionation in volcanic soil weathering sequences, Guadeloupe. *Earth Planet. Sci. Lett.* **341–344**, 176–185.

Opfergelt S., Burton K. W., Georg R. B., West A. J., Guicharnaud R. A., Sigfússon B., Siebert C.,

Gíslason S. R. and Halliday A. N. (2014) Magnesium retention on the soil exchange complex controlling Mg isotope variations in soils, soil solutions and vegetation in volcanic soils, Iceland *Geochim. Cosmochim. Acta* **125**, 110–130.

Osadetz K. G., Kohn B. P., Feinstein S. and O'Sullivan P. B. (2002) Thermal history of Canadian Williston basin from apatite fission-track thermochronology—implications for petroleum systems and geodynamic history. *Tectonophysics* **349**, 221–249.

Palombi D. D. (2008) Regional hydrogeological characterization of the northeastern margin in the Williston Basin. University of Alberta, Edmonton, M. Sc. thesis, 196p.

Panchuk K. M., Holmden C. E. and Leslie S. A. (2006) Local controls on carbon cycling in the Ordovician midcontinent region of North America, with implications for carbon isotope secular curves. *J. Sed. Res.* **76**, 200–211.

Patterson W. and Walter L. M (1994) Depletion of ^{13}C in seawater $\sum CO_2$ on modern carbonate platforms: Significance for the carbon isotopic record of carbonates. *Geology* **22**, 885–888.

Peng Y., Shen B., Lang X. –G., Huang K., –J., Chen J. –T., Yan Z., Tang W. –b., Ke S., Ma H. –R. and Li F. –B. (2016) Constraining dolomitization by Mg isotopes: a case study from partially dolomitized limestones of the middle Cambrian Xuzhuang Formation, North China. *Geochem. Geophys. Geosyst.* **17**, 1109–1129.

Pessarakli M. (2016) *Handbook of photosynthesis* 3rd Ed. CRC Press, Taylor & Francis Group, Boca Raton, FL, USA 846p.

Pogge von Strandmann P. A. E. (2008) Precise magnesium isotope measurements in core top planktic and benthic foraminifera. *Geochem. Geophys. Geosyst.* **9**, 1–13.

Pogge von Strandmann P. A. E., James R. H., van Calsteren P., Gíslason S. R. and Burton K. W. (2008a) Lithium, magnesium and uranium isotope behavior in the estuarine environment of basaltic islands. *Earth Planet. Sci. Lett.* **274**, 462–471.

Pogge von Strandmann P. A. E., Burton K. W., James R. H., van Calsteren P., Gíslason S. and Sigfússon B. (2008b) The influence of weathering processes on riverine magnesium isotopes in a basaltic terrain. *Earth Planet. Sci. Lett.* **276**, 187–197.

Pogge von Strandmann P. A. E., Opfergelt S., Lai Y. –J., Sigfússon B., Gislason S. R. and Burton K. W. (2012) Lithium, magnesium and silicon isotope behavior accompanying weathering in a basaltic soil and pore water profile in Iceland. *Earth Planet. Sci. Lett.* **339–340**, 11–23.

Pokharel R., Gerrits R., Schuessler J., Floor G., Gorbushina A. and von Blanckenburg F. (2017) Mg isotope fractionation during uptake by a rock-inhabiting, model microcolonial fungus Knufia petricola at acidic and neutral pH. *Environ. Sci. Technol.* **51**, 9691–9699.

Porter S. M. (2010) Calcite and aragonite seas and the *de novo* acquisition of carbonate skeletons. *Geobiology* **8**, 256–277.

Powley D. E. (1990) Pressures and hydrogeology in petroleum basins. *Earth Sci. Rev.* **29**, 215–226.

Pratt B. R. and Haidl F. M. (2008) Microbial patch reefs in Upper Ordovician Red River strata, Williston Basin, Saskatchewan: signal of heating in a deteriorating epeiric sea. In *Dynamics of Epeiric Seas* (Eds. B. R. Pratt and C. Holmden) Geol. Assoc. Can. Special Paper 48, 303–340.

Qing H. and Mountjoy E. W. (1992) Large-scale fluid flow in the Middle Devonian Presqu'ile barrier, Western Canada Sedimentary Basin. *Geology* **20**, 903–906.

Qing H. and Mountjoy E. W. (1994) Formation of coarsely crystalline, hydrothermal dolomite reservoirs in the Presqu'ile barrier, Western Canada Sedimentary Basin. *AAPG Bull*. **78**, 55–77.

Qing H., Kent D. and Bend S. (2001) Preliminary results of isotopic geochemistry of Ordovician Red River carbonates, subsurface of southeastern Saskatchewan: implication for process of dolomitization and diagenetic modification of dolomites. In *Summary of Investigations 2001* Sask. Geol. Survey **1**, 3–9.

Qing H., Bend S., Kent D. and Haidl F. (2004) Petrography and isotopic geochemistry of Ordovician Red River dolomites, Midale Pool and 3-8-1-11W2, southeastern Saskatchewan. In *Proceedings of Dolomites: The Spectrum: Mechanisms, Models, Reservoir Development* Can. Soc. Petrol. Geol., Seminar and Core Conference, Calgary, Alberta, Canada, pp. 1–19.

Ra K. (2010) Determination of Mg isotopes in chlorophyll *a* for marine bulk phytoplankton from the northwestern Pacific Ocean. *Geochem. Geophys. Geosyst.* **11**, Q12011.

Ra K. and Kitagawa H. (2007) Magnesium isotope analysis of different chlorophyll forms in marine phytoplankton using multi-collector ICP-MS. *J. Anal. At. Spectrom*. **22**, 817–821.

Ra K., Kitagawa H. and Shiraiwa Y. (2010) Mg isotopes and Mg/Ca values of coccoliths from cultured specimens of the species *Emiliania huxleyi* and *Gephyrocapsa oceanica*. *Mar. Micropaleontol.* **77**, 119–124.

Ragsdale H. L., Lindberg S. E., Lovett G. M. and Schaefer D. A. (1992) Atmospheric deposition and throughfall fluxes of base cations. In *Atmospheric Deposition and Nutrient Cycling.* (Eds. D. W. Johnson and S. E. Lindberg) Springer-Verlag, Berlin, pp. 235–253.

Riechelmann S., Buhl D., Schröder-Ritzrau A., Spötl C., Riechelmann D. F. C., Richter D. K., Kluge T., Marx T. and Immenhauser A. (2012) Hydrogeochemistry and fractionation pathways of Mg isotopes in a continental weathering system: lessons from field

experiments.

Riechelmann S., Mavromatis V., Buhl D., Dietzel M., Eisenhauer A. and Immenhauser A. (2016) Impact of diagenetic alteration on brachiopod shell magnesium isotope (δ^{26}Mg) signatures: Experimental versus field data. *Chem. Geol.* **440**, 191–206.

Ries J. B. (2006) Aragonitic algae in calcite seas: Effect of seawater Mg/Ca ratio on algal sediment production. *J. Sed. Res.* **76**, 515–523.

Ries J. B. (2010) Review: geological and experimental evidence for secular variation in seawater Mg/Ca (calcite-aragonite seas) and its effects on marine biological calcification. *Biogeosciences* **7**, 2795–2849.

Ross D. (1995) Recommended soil tests for determining soil cation exchange capacity. In *Recommended Soil Testing Procedures for the Northeastern United States*. Northeast Regional Bulletin 493 (Eds. J. T. Sims and A. Wolf) Agricultural Experiment Station, University of Delaware, Newark, DE, USA, pp. 62–69.

Ross R. J. (1976) Ordovician sedimentation in the western United States. In *The Ordovician System*, (Ed. M. G. Bassett), Cardiff pp. 73–105.

Rostron B. J. and Holmden C. (2000) Fingerprinting formation-waters using stable isotopes, Midale Area, Williston Basin, Canada. *J. Geochem. Explor.* **69–70**, 219–223.

Rostron B. J. and Holmden C. (2003) Regional variations in oxygen isotopic compositions in the Yeoman and Duperow aquifers, Williston basin (Canada-USA). *J. Geochem. Explor*. **78-79**, 337–341.

Rubinson M. and Clayton R. N. (1969) Carbon-13 fractionation between aragonite and calcite. *Geochim. Cosmochim. Acta* **33**, 997–1002.

Rustad J. R., Casey W. H., Yin Q. –Z. Bylaska E. J., Felmy A. R., Bogatko S. A., Jackson V. E. and Dixon D. A. (2010) Isotopic fractionation of Mg^{2+}(aq), Ca^{2+}(aq), and Fe^{2+}(aq) with carbonate minerals. *Geochim. Cosmochim. Acta* **74**, 6301–6323.

Ryu J. –S., Jacobson A. D., Holmden C., Lundstrom C. and Zhang Z. (2011) The major ion, $\delta^{44/40}$Ca, $\delta^{44/42}$Ca, and $\delta^{26/24}$Mg geochemistry of granite weathering at pH = 1 and T =25ºC: power-law processes and the relative reactivity of minerals. *Geochim. Cosmochim. Acta* **75**, 6004–6026.

Saenger C. and Wang Z. (2014) Magnesium isotope fractionation in biogenic and abiogenic carbonates: implications for paleoenvironmental proxies. *Quat. Sci. Rev.* **90**, 1–21.

Sandberg P.A. (1983) An oscillating trend in Phanerozoic non-skeletal carbonate mineralogy. *Nature.* **305**, 19–22.

Sandberg P. A. (1985) Aragonite cements and their occurrence in ancient limestone. In *Carbonate Cements Society for Sedimentary Geology* (Ed. N. Schneidermann and P. M. Harris), Soc. Econ. Paleon. Mineral. Special Publication 36, 33–57.

Schauble E. A. (2011) First-principles estimates of equilibrium magnesium isotope fractionation in silicate, oxide, carbonate and hexaaquamagnesium(2+) crystals. *Geochim. Cosmochim. Acta* **75**, 844–869.

Schmitt A. –D., Vigier N., Lemarchand D., Millot R., Stille P. and Chabaux F. (2012) Processes controlling the stable isotope compositions of Li, B, Mg and Ca in plants, soils and waters: a review. *C. R. Geosci.* **344**, 704–722.

Schmitt A. –D., Cobert F., Bourgeade P., Ertlen D., Labolle F., Gangloff S., Badot P. –M., Chabaux F. and Stille P. (2013) Calcium isotope fractionation during plant growth under a limited nutrient supply. *Geochim. Cosmochim. Acta* **110**, 70–83.

Shields M. J. and Brady P. V. (1995) Mass balance and fluid flow constraints on regional-scale dolomitization, Late Devonian, Western Canada Sedimentary Basin. *Bull. Can. Petrol. Geol.* **43**, 371–392.

Shosa J. D. and Cathles L. M. (2001) Experimental investigation of capillary blockage of two phase flow in layered porous media. In *Petroleum Systems of Deep-Water Basins* GCSSEPM Foundation, 21st Ann. Res. Conf., pp. 725–740.

Shurr G. W., Hammond R. H. and Bretz R. F. (1994) Cretaceous paleotectonism and postdepositional tectonism in south-central South Dakota: an example of epeirogenic tectonism in continental lithosphere. In *Perspectives on the eastern margin of the Cretaceous Western Interior Basin* (Eds. G. W. Shurr, G. A. Ludvigson and R. H. Hammond). Geol. Soc. Am. Special Paper 287, 237–256.

Sibson R. H. (1994) Crustal stress, faulting and fluid flow. In *Geofluids: origin, migration and evolution of fluids in sedimentary basins* (Ed. J. Parnell) Geol. Soc. Special Publication 78, 69–84.

Smith S. V. and Kroopnick P. (1981) Carbon-13 isotopic fractionation as a measure of aquatic metabolism. *Nature* **294**, 252–253.

Smith S. E. and Read D. J. (1997) *Mycorrhizal Symbiosis* 2nd Ed. San Diego, USA, Academic Press, 800p.

Speed R. C. and Sleep N. H. (1982) Antler orogeny and foreland basin: a model. *Geol. Soc. Am. Bull.* **93**, 815–828.

Soil Classification Working Group (SCWG) (1998) The Canadian System of Soil Classification. *Agric. and Agri-Food Can*. Publ. 1646 (Revised). 187p.

Spötl C. and Pitman J. K. (1998) Saddle (baroque) dolomite in carbonates and sandstones: a reappraisal of a burial-diagenetic concept. In *Carbonate Cementation in Sandstones* (Ed. S. Morad) Int. Assoc. Sedimentol. Special Publication 26, 437–460.

Stanley S. M. and Hardie L. A. (1998) Secular oscillations in the carbonate mineralogy of reef-building and sediment-producing organisms driven by tectonically forced shifts in seawater chemistry. *Palaeogeogr. Palaeoclimatol. Palaeoecol.* **144**, 3–19.

Steuber T. and Veizer J. (2002) Phanerozoic record of plate tectonic control of seawater chemistry and carbonate sedimentation. *Geology* **30**, 1123–1126.

Stewart B. W., Capo R. C. and Chadwick O. A. (1998) Quantitative strontium isotope models for weathering, pedogenesis and biogeochemical cycling. *Geoderma* **82**, 173–195.

Sverjensky D. A. (1986) Genesis of Mississippi Valley-type lead-zinc deposits. *Ann. Rev. Earth Planet. Sci.* **14**, 177–199.

Swart P. K. (2008) Global Synchronous Changes in the Carbon Isotopic Composition of Carbonate Sediments Unrelated to Changes in the Global Carbon Cycle. *PNAS* **105**, 13741–13745.

Swart P. K. (2015) The geochemistry of carbonate diagenesis: The past, present and future. *Sedimentology* **62**, 1233–1304.

Swart P. K. and Eberli G. (2005) The nature of the $\delta^{13}C$ of periplatform sediments: Implications for stratigraphy and the global carbon cycle. *Sed. Geol.* **175**, 115–129.

Swart P. K., Ruiz J. and Holmes C. W. (1987) Use of strontium isotopes to constrain the timing and mode of dolomitization of upper Cenozoic sediments in a core from San Salvador, Bahamas. *Geology* **15**, 262–265.

Swart P. K., Reijmer J. J. and Otto R. (2009) Variations in the $\delta^{13}C$, $\delta^{18}O$, and mineralogy of surface sediments on Great Bahama Bank: implications for reading the fossil record. In *Perspectives in Carbonate Geology: A Tribute to the Career of Robert Nathan Ginsburg* (eds. P. Swart, G. Eberli and J. McKenzie), IAS/Wiley-Blackwell, London. Int. Assoc. Sedimentol. Special Publication **41**, 47–60.

Szabo E. and Cioppa M. T. (2006) Multiple magnetization events in the Red River carbonates, Williston Basin, Canada: evidence for fluid-flow? *J. Geochem. Explor.* **89**, 384–388.

Tang J., Dietzel M., Böhm F., Köhler S. J. and Eisenhauer A. (2008) Sr^{2+}/Ca^{2+} and $^{44}Ca/^{40}Ca$ fractionation during inorganic calcite formation: II. Ca isotopes. *Geochim. Cosmochim. Acta* **72**, 3733–3745.

Taylor S. R. and McLennan S. M. (1985) *The Continental Crust: Its Composition and Evolution*. Blackwell, Oxford 312p.

Teng F. –Z. (2017) Magnesium isotope geochemistry. In *Reviews in Mineralogy and Geochemistry* Mineral. Soc. Am. **82**, 219–287.

Teng F. –Z. and Yang W. (2014) Comparison of factors affecting the accuracy of high-precision magnesium isotope analysis by multi-collector inductively coupled plasma mass spectrometry. *Rapid Commun. Mass Spectrom*. **28**, 19–24

Teng F. –Z., Wadhwa M. and Helz R. T. (2007) Investigation of magnesium isotope fractionation during basalt differentiation: implications for a chondritic composition of the terrestrial mantle. *Earth Planet. Sci. Lett.* **261**, 84–92.

Teng F. –Z., Li W. –Y., Rudnick R. L. and Gardner R. (2010) Contrasting lithium and magnesium isotope fractionation during continental weathering. *Earth Planet. Sci. Lett.* **300**, 63–71.

Thomas G. E. (1974) Lineament-block tectonics: Williston-Blood Creek Basin. *Am. Assoc. Petrol. Geol. Bull.* **58**, 1305–1322.

Tipper E. T., Galy A. and Bickle M. J. (2006a) Riverine evidence for a fractionated reservoir of Ca and Mg on the continents: implications for the oceanic Ca cycle. *Earth Planet. Sci. Lett.* **247**, 267–279.

Tipper E. T., Galy A., Gaillardet J., Bickle M. J., Elderfield H. and Carder E. A. (2006b) The magnesium isotope budget of the modern ocean: constraints from riverine magnesium isotope ratios. *Earth Planet. Sci. Lett*. **250**, 241–253.

Tipper E. T., Galy A. and Bickle M. J. (2008) Calcium and magnesium isotope systematics in rivers draining the Himalaya- Tibetan-Plateau region: lithological or fractionation control? *Geochim. Cosmochim. Acta* **72**, 1057–1075.

Tipper E. T., Gaillardet J., Louvat P., Capmas F. and White A. F. (2010) Mg isotope constraints on soil pore-fluid chemistry: evidence from Santa Cruz, California. *Geochim. Cosmochim. Acta* **74**, 3883–3896.

Tipper E. T., Calmels D., Gaillardet J., Louvat P., Capmas F. and Dubacq B. (2012a) Positive correlation between Li and Mg isotope ratios in the river waters of the Mackenzie Basin challenges the interpretation of apparent isotopic fractionation during weathering. *Earth Planet. Sci. Lett*. **333–334**, 35–45.

Tipper E. T., Lemarchand E., Hindshaw R. S., Reynolds B. C. and Bourdon B. (2012b) Seasonal sensitivity of weathering processes: hints from magnesium isotopes in a glacial stream. *Chem. Geol.* **312–313**, 80–92.

Trotter J. A., Williams I. S., Barnes C. R., Lécuyer C. and Nicoll R. S. (2008) Did cooling oceans trigger Ordovician biodiversification? Evidence from conodont thermometry. *Science*. **321**, 550–554.

Trotter J. A., Williams I. S., Barnes C. R., Männik P., Simpson A. (2016) New conodont $\delta^{18}O$ records of Silurian climate change: implications for environmental and biological events. *Palaeogeogr. Palaeoclimatol. Palaeoecol*. **443**, 34–48.

Vahrenkamp V. C. and Swart P. K. (1990) New distribution coefficient for the incorporation of strontium into dolomite and its implications for the formation of ancient dolomites. *Geology* **18**, 387–391.

van der Heijden G., Legout A., Midwood A., Craig C. –A., Pollier B., Ranger J, Dambrine E (2013) Mg and Ca root uptake and vertical transfer in soils assessed by an in situ ecosystem-scale multi-isotopic (^{26}Mg & ^{44}Ca) tracing experiment in a beech stand (Breuil-Chenue, France). *Plant Soil* **369**, 33–45.

van der Heijden G., Legout A., Pollier B., Ranger J. and Dambrine E. (2014a) The dynamics of calcium and magnesium inputs by throughfall in a forest ecosystem on base poor soil are very slow and conservative: evidence from an isotopic tracing experiment (^{26}Mg and ^{44}Ca). *Biogeochemistry* **118**, 413–442.

van der Heijden G., Dambrine E., Pollier B., Zeller B., Ranger J. and Legout A. (2014b) Mg and Ca uptake by roots in relation to depth and allocation to aboveground tissues: results from an isotopic labeling study in a beech forest on base-poor soil. *Biogeochemistry* **122**, 375–393.

Veizer J. (1977) Diagenesis of pre-Quaternary carbonates as indicated by tracer studies. *J. Sed. Petrol.* **47** 565–581.

Veizer J. (1983) Chemical diagenesis of carbonates: Theory and application of the trace element technique. In *Stable Isotopes in Sedimentary Geology: Sot. Econ. Paleont. Mineral. Short Course* 10, pp. 3–l to 3–100.

Vizcayno-Soto G. and Côté B. (2004) A boundary-line approach to determine standards of nutrition for mature trees from spatial variation of growth and foliar nutrient concentrations in natural environments. *Comm. Soil Sci. Plant Anal.* **35**, 2965–2985.

Waite A. J. and Swart P. K. (2015) The inversion of aragonite to calcite during the sampling of skeletal archives: Implications for proxy interpretation. *Rap. Commun. Mass Spectrom.* **29**, 955–964.

Walker C. J. and Willows R. D. (1997) Mechanism and regulation of Mg-chelatase. *Biochem. J.* **327**, 321–333.

Walker T. S., Bais H. P., Grotewold E. and Vivanco J. M. (2003) Root exudation and rhizosphere biology. *Plant Physiol.* **132**, 44–51.

Walter L. M. and Burton E. A. (1990) Dissolution of recent platform carbonate sediments in marine pore fluids. *Am. J. Sci.* **290**, 601–643.

Wang Z., Hu P., Gaetani G., Liu C., Saenger C., Cohen A. and Hart S. (2013) Experimental calibration of Mg isotope fractionation between aragonite and seawater. *Geochim. Cosmochim. Acta* **102**, 113–123.

Warren J. K. (1999) *Evaporites: Their Evolution and Economics*. Blackwell Scientific Publications, Oxford, 438p.

Warren J. K. (2000) Dolomite: occurrence, evolution and economically important associations. *Earth Sci. Rev.* **52**, 1–81.

Wedepohl K. H. (1969) *Handbook of Geochemistry*. Springer-Verlag.

Whitaker F., Smart P. L. and Jones G. D. (2004) Dolomitization: from conceptual to numerical models. In *The Geometry and Petrogenesis of Dolomite Hydrocarbon Reservoirs* (Eds. C. J. R. Braithwaite, G. Rizzi and G. Darke) Geol. Soc., London, Special Publications **235**, 99–139.

Whittaker R. H., Bormann F. H., Likens G. E. and Siccama T. G. (1974) The Hubbard Brook Ecosystem Study: forest biomass and production. *Ecol. Monogr.* **44**, 233–252.

Wiegand B. A., Chadwick O. A., Vitousek P. M. and Wooden J. L. (2005) Ca cycling and isotopic fluxes in forested ecosystems in Hawaii. *Geophys. Res. Lett.* **32**, L11404.

Wigforss-Lange J. (1999) Carbon isotope ^{13}C enrichment in Upper Silurian (Whitcliffian) marine calcareous rocks in Scania, Sweden. *GFF* **121**, 273–279.

Wilkinson B. H. and Algeo T. J. (1989) Sedimentary carbonate record of calcium-magnesium cycling. *Am. J. Sci.* **289**, 1158–1194.

Wilkinson B. H. and Given R. K. (1986) Secular variation in abiotic marine carbonates: Constraints on Phanerozoic atmospheric carbon dioxide contents and oceanic Mg/Ca ratios. *J. Geol.* **94**, 321–333.

Wilkinson, B. H., Buczynski C. and Owen R. M. (1984) Chemical control of carbonate phases: Implications from upper Pennsylvanian calcite-aragonite ooids of southeastern Kansas. *J. Sed. Petrol.* **54**, 932–947.

Wilkinson S. R., Welch R. M., Mayland H. F. and Grunes D. L. (1990) Magnesium in plants: uptake, distribution, function, and utilization by man and animals. *Met. Ions Biol. Syst.* **26**, 33–56.

Willows R. D. (2003) Biosynthesis of chlorophylls from protoporphyrin IX. *Nat. Prod. Rep.* **20**, 327–341.

Wilson E. N., Hardie L. A. and Phillips O. M. (1990) Dolomitization from geometry, flow patterns, and the origin of massive dolomite: the Triassic Latemar buildup, northern Italy. *Am. J.*

Sci. **290**, 741–796.

Wimpenny J., Gíslason S. R., James R. H., Gannoun A., Pogge Von Strandmann P. A. E. and Burton K. W. (2010) The behaviour of Li and Mg isotopes during primary phase dissolution and secondary mineral formation in basalt. *Geochim. Cosmochim. Acta* **74**, 5259–5279.

Wimpenny J., Burton K. W., James R. H., Gannoun A., Mokadem F. and Gíslason S. (2011) The behaviour of magnesium and its isotopes during glacial weathering in an ancient shield terrain in West Greenland. *Earth Planet. Sci. Lett.* **304**, 260–269.

Wimpenny J., Colla C. A., Yin Q. –Z, Rustad J. R. and Casey W. H. (2014a) Investigating the behaviour of Mg isotopes during the formation of clay minerals. *Geochim. Cosmochim. Acta* **128**, 178–194.

Wimpenny J., Yin Q. –Z., Tollstrup D., Xie L. –W. and Sun J. (2014b) Using Mg isotope ratios to trace Cenozoic weathering changes: a case study from the Chinese loess plateau. *Chem. Geol.* **376**, 31–43.

Wombacher F., Eisenhauer A., Böhm F., Gussone N., Kinkel H., Lezius J., Noé S., Regenberg M. and Rüggeberg A. (2006) Magnesium stable isotope compositions in biogenic $CaCO_3$. In *European Geosciences Union*, *Geophys. Res. Abs.* **8**, EGU06–A–06353.

Wombacher F., Eisenhauer A., Heuser A. and Weyer S. (2009) Separation of Mg, Ca and Fe from geological reference materials for stable isotope ratio analyses by MC-ICP-MS and double-spike TIMS. *J. Anal. At. Spectrom* **24**, 627–636.

Wombacher F., Eisenhauer A., Böhm F., Gussone N., Regenberg M., Dullo W. C. and Rüggeberg A. (2011) Magnesium stable isotope fractionation in marine biogenic calcite and aragonite. *Geochim. Cosmochim. Acta* **75**, 5797–5818.

Worsham S. R., Holmden C. and Qing H. (2013) Preliminary results of a magnesium isotope study of dolomite in Upper Ordovician strata, southeastern Saskatchewan, northern Williston Basin. In *Summary of Investigations 2013*, Sask. Geol. Survey, **1**, 1–8.

Yoshimura T., Tanimizu M., Inoue M., Suzuki A., Iwasaki N. and Kawahata H. (2011) Mg isotope fractionation in biogenic carbonates of deep-sea coral, benthic foraminifera, and hermatypic coral. *Anal. Bioanal. Chem.* **401**, 2755–2769.

Young E. and Galy A. (2004) The isotope geochemistry and cosmochemistry of magnesium. In *Reviews in Mineralogy and Geochemistry* Mineral. Soc. Am. **55**, 197–230.

Young E. D., Ash R. D., Galy A. and Belshaw N. S. (2002) Mg isotope heterogeneity in the Allende meteorite measured by UV laser ablation–MC–ICPMS and comparisons with O isotopes. *Geochim. Cosmochim. Acta* **66**, 683–698.

Zenger D. H, Dunham J. B. and Ethington R. L. (1980) Concepts and Models of Dolomitization– a symposium, *Soc. Econ. Paleontol. Mineral*., Special Publication 28, 320p.

Zenger D. H. and Mazzullo S. J. (1982) *Dolomitization*. Benchmark Papers in Geology**.** Hutchinson Ross Publishing, Stroudsburg, PA 65, 426p.

Zenger D. H. (1996) Dolomitization of the "C" zone, Red River Formation (Upper Ordovician) in a deep core, Williston Basin, Richland County, eastern Montana. University of Wyoming *Contrib. Geol.* **31**, 57–75.

APPENDIX A – Development of Laboratory Protocols

A1. Magnesium separation from matrix elements

To separate Mg from a complex sample matrix, an in-house laboratory standard with known concentrations of multiple elements was created (Mg-Test). Purified single element standards were diluted to values typically found in a soil leachate solution (based on Wombacher et al., 2009) in a 30 ml total volume test stock solution. Approximate solution concentrations of chosen elements are as follows: 200 µg/ml Na, 60 µg/ml of Mg, Ca, K, Al, and Fe, 20 µg/ml Sr and Ba, and 6 µg/ml of Ti, Mn, Cr, Li, B, and Be. Thirty ml stock solutions were created, from which 0.5 ml aliquots were taken, brought up in 0.5 ml of hydrochloric acid (HCl) (0.5N) or nitric acid (HNO_3) (0.5N), and loaded on cation exchange columns. The test solution was eluted from the columns in 1ml increments with the cuts dried down and brought back up in 0.5 ml of 0.3N HNO_3 for signal intensity analysis on the Thermo Scientific Neptune MC-ICP-MS. The final elution scheme for the two-stage Mg separation from matrix elements using Bio-Rad® AG® MP-50 H-form 100–200 mesh cation exchange resin is provided in Figs. A3 and A4. For samples with known high concentrations of transition metals, a third pre-treatment column was used containing 1 ml Bio-Rad® AG® 1-X8 Cl-form 100–200 mesh anion exchange resin to rid the sample of Fe and Mn prior to cation exchange chemistry.

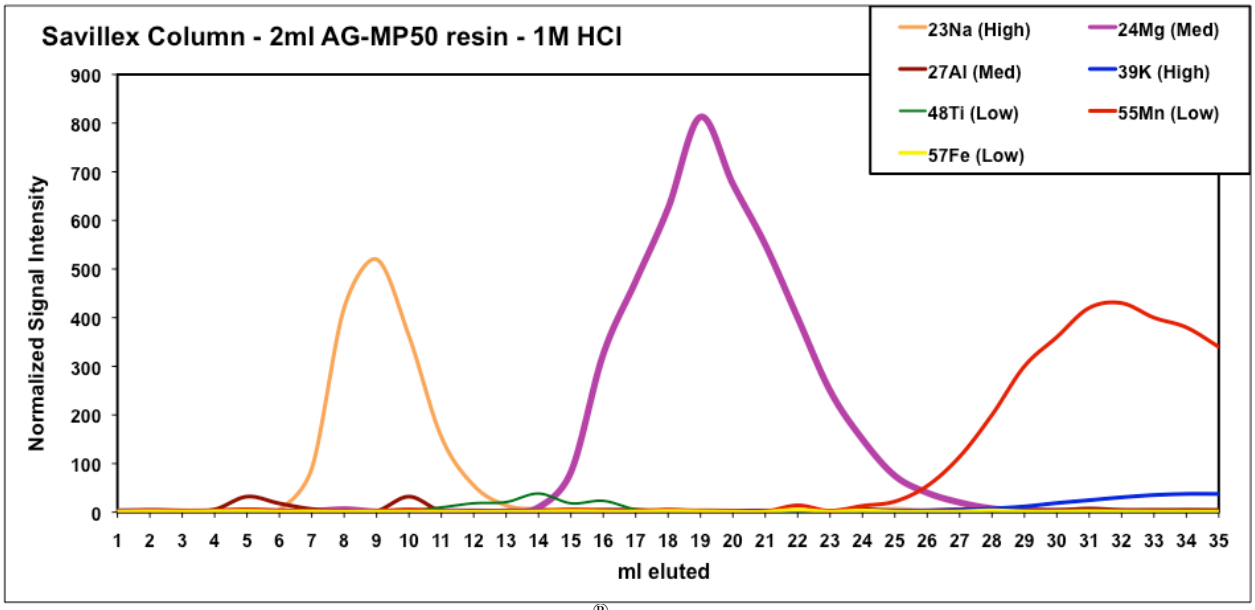

Figure A1 Column calibration for a Savillex® Teflon column with an inner diameter of 6 mm. Approximately 2 ml of Bio-Rad® AG® MP-50 resin and 1N HCl was used for separation. Only the

elements overlapping, or close to overlapping the Mg peak are shown. Signal intensities (measured in mV) were normalized to the lowest values of each isotope. Instrument resolution is shown with elements of interest as High, Medium, or Low resolution. Instrument RF power was run on 'cold plasma' (800 W) during signal intensity checks.

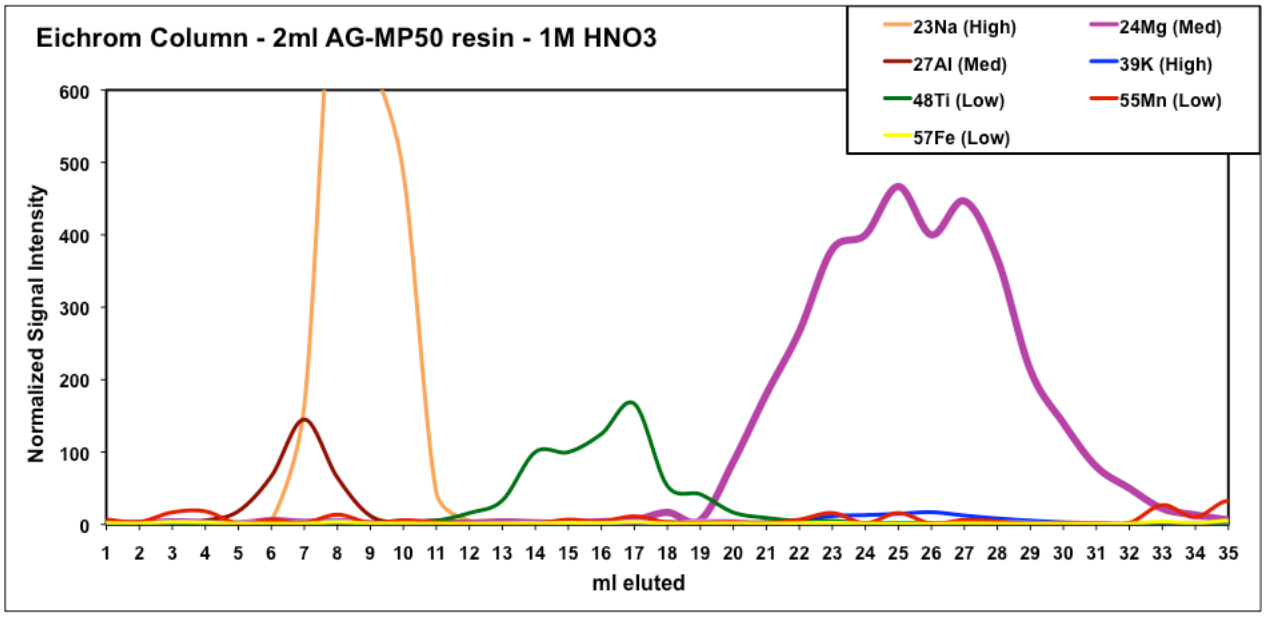

Figure A2 Column calibration of a polypropylene Eichrom® Technologies column. Approximately 2 ml of Bio-Rad® AG® MP-50 resin and 1N HNO_3 was used for separation. Only the elements overlapping, or close to overlapping the Mg peak are shown. Signal intensities (measured in mV) were normalized to the lowest values. Instrument resolution is shown with elements of interest as High, Medium, or Low resolution. Instrument RF power was run on 'cold plasma' (800 W) during signal intensity checks. All cation exchange separations in this thesis used 2 ml Bio-Rad® AG® MP-50 H-form 100–200 mesh cation exchange resin and the polypropylene Eichrom® Technologies columns.

ELUTION SCHEME Mg - EICHROM COLUMNS with 2ml AG-MP50 resin

STEP ONE - *1N HCl*

COLUMN EQUILIBRATION

1. Remove columns from storage. Clean with MQ H2O & wipe clean
2. Fill reservoir with 6N HCl, let drain completely
3. Flush column with 3ml MQ H2O - Use small increments to minimize resin disruption (0.5ml, 0.5ml, 1ml, 1ml)
4. Equilibrate column with 10ml 1N HCl - Use small increments to minimize resin disruption (0.5ml, 0.5ml, 1ml, 1ml, 7ml)

SAMPLE PREPARATION

1. Add 0.5 ml of 0.5N HCl to dried sample. Sonicate for 5 min. If sample is not dissolved continue to sonicate.
2. Transfer to a microcentrifuge tube.
3. Centrifuge for 7 minutes at 10,000 r.p.m.
4. **Remove 0.5 ml of sample MAKING SURE NOT TO PICK UP DEBRIS and load carefully. Do NOT disturb resin.**
5. Let sample enter resin completely
6. Use only acid rinsed/leached centrifuge tubes and pipette tips for the following steps

SAMPLE I.D. COLUMN #	1	2	3	4	5	6	Notes
0.5N HCl							
LOAD SAMPLE	0.5 ml	0.5 ml	0.5 ml	0.5 ml	0.5 ml	0.5 ml	
RINSE 1X	0.5 ml	0.5 ml	0.5 ml	0.5 ml	0.5 ml	0.5 ml	
RINSE 1X	1 ml	1 ml	1 ml	1 ml	1 ml	1 ml	
1N HCl							
Elute	8 ml	8 ml	8 ml	8 ml	8 ml	8 ml	
Collect ppMg1	2 ml	2 ml	2 ml	2 ml	2 ml	2 ml	Yield check
Collect Mg	*22 ml*	*22 ml*	*22 ml*	*22 ml*	*22 ml*	*22 ml*	*Dry down for Step Two - HNO3*
Collect ppMg2	2 ml	2 ml	2 ml	2 ml	2 ml	2 ml	Yield check - add to ppMg1 container
CLEANING COLUMNS							
6N HCl	Fill reservoir	Fill reservoir	Fill reservoir	Fill reservoir	Fill reservoir	Fill reservoir	
MQ H2O	10 ml	10 ml	10 ml	10 ml	10 ml	10 ml	

Add ~3 ml MQ H2O and store in appropriately labeled 15 ml centrifuge tubes

Figure A3 Step one of the Mg elution scheme using 2 ml Bio-Rad® AG-MP50 H-form 100–200 mesh resin and 1N HCl.

STEP TWO - *1N HNO3*

COLUMN EQUILIBRATION

1. Remove columns from storage. Clean with MQ H2O & wipe clean
2. Fill reservoir with 6N HCl, let drain completely
3. Flush column with 3ml MQ H2O - Use small increments to minimize resin disruption (0.5ml, 0.5ml, 1ml, 1ml)
4. Equilibrate column with 10ml 1N HNO3 - Use small increments to minimize resin disruption (0.5ml, 0.5ml, 1ml, 1ml, 7ml)

SAMPLE PREPARATION

1. Add 0.5 ml of 0.5N HNO3 to dried sample from STEP ONE. Sonicate for 5 min. If sample is not dissolved continue to sonicate.
2. Transfer to a microcentrifuge tube.
3. Centrifuge for 7 minutes at 10,000 r.p.m.
4. **Remove 0.5 ml of sample MAKING SURE NOT TO PICK UP DEBRIS and load carefully. Do NOT disturb resin.**
5. Let sample enter resin completely.
6. Use only acid rinsed/leached centrifuge tubes and pipette tips for the following steps

SAMPLE I.D. COLUMN #	1	2	3	4	5	6	Notes
0.5N HNO3							
LOAD SAMPLE	0.5 ml	0.5 ml	0.5 ml	0.5 ml	0.5 ml	0.5 ml	
RINSE 1X	0.5 ml	0.5 ml	0.5 ml	0.5 ml	0.5 ml	0.5 ml	
RINSE 1X	1 ml	1 ml	1 ml	1 ml	1 ml	1 ml	
1N HNO3							
Elute	13 ml	13 ml	13 ml	13 ml	13 ml	13 ml	
Collect ppMg1	2 ml	2 ml	2 ml	2 ml	2 ml	2 ml	Yield check - combine with HCl ppMg2
Collect Mg	*24 ml*	*24 ml*	*24 ml*	*24 ml*	*24 ml*	*24 ml*	*Final Sample - dry down, bring up in 0.3N HNO3*
Collect ppMg2	2 ml	2 ml	2 ml	2 ml	2 ml	2 ml	Yield check - add to HNO3 ppMg1 container
CLEANING COLUMNS							
MQ H2O	3 ml	3 ml	3 ml	3 ml	3 ml	3 ml	
6N HCl	Fill reservoir	Fill reservoir	Fill reservoir	Fill reservoir	Fill reservoir	Fill reservoir	
MQ H2O	10 ml	10 ml	10 ml	10 ml	10 ml	10 ml	

Add ~3 ml MQ H2O and store in appropriately labeled 15 ml centrifuge tubes

Figure A4 Step two of the Mg elution scheme using 2 ml Bio-Rad® AG-MP50 H-form 100–200 mesh cation exchange resin and 1N HNO_3. The final sample was dried down, treated with one drop of high purity H_2O_2 and 15N HNO_3, and brought up with 0.3N HNO_3 to created a stock solution of 30 ppm to await isotopic analysis. Prior to instrument introduction, an aliquot of the concentrated sample was diluted to 1 ppm using 0.3N HNO_3 for analysis.

FOR HIGH Fe SAMPLES

ELUTION SCHEME Mg - EICHROM COLUMNS with 1ml AG X8 Anion Exchange resin

COLUMN EQUILIBRATION

1. Remove columns from storage. Clean with MQ H2O & wipe clean
2. Fill reservoir with 10ml 6N HCl, let drain completely

SAMPLE PREPARATION

1. Add 1-2 ml of 6N HCl to dried sample. Sonicate for 5 min. If sample is not dissolved continue to sonicate.
2. Use only acid rinsed/leached centrifuge tubes and pipette tips

SAMPLE I.D. COLUMN #	1	2	3	4	5	6
6N HCl (COLLECT IMMEDIATELY)						
LOAD SAMPLE	1-2 ml	1-2 ml	1-2 ml	1-2 ml	1-2 ml	1-2 ml
Collect Sample	2 ml	2 ml	2 ml	2 ml	2 ml	2 ml
CLEANING COLUMNS						
0.5N HCl	10 ml	10 ml	10 ml	10 ml	10 ml	10 ml
MQ H2O	10 ml	10 ml	10 ml	10 ml	10 ml	10 ml
0.5N HNO3	10 ml	10 ml	10 ml	10 ml	10 ml	10 ml
MQ H2O	10 ml	10 ml	10 ml	10 ml	10 ml	10 ml

Add ~3 ml MQ H2O and store in appropriately labeled 15 ml centrifuge tubes

Figure A5 Pre-treatment step of the Mg elution scheme using 1 ml Bio-Rad® AG® 1-X8 H-form 100–200 mesh anion exchange resin and 6N HCl.

A2. Organic-rich sample UV treatment system

Due to the high organic content of the samples that will be analyzed in this study, additional steps must be taken to eliminate organics from samples prior to and following column separation. Typical procedures for the denaturing of organics in sample solutions include high temperature hydrogen peroxide (H_2O_2) and HNO_3 reaction over several hours. Some may also consider perchloric acid ($HClO_4$) for complete organic denaturing; however, $HClO_4$ treatment has been demonstrated to induce mass dependent effects on Mg isotopes (Chang et al., 2003). In some cases, organic matter has withstood conventional treatment. To help eliminate the time consuming step of organic breakdown, and potential introduction of contaminated reagents with repeated H_2O_2 and HNO_3 treatments, UV light was applied to high-organic samples as an alternative way to quickly and efficiently destroy dissolved organics in sample solutions. In order to accomplish UV light treatments, a custom UV box was designed and constructed using clean room appropriate materials including UV stabilized HDPE, nylon screws, easily removable polished Al sheeting, and a quartz plate on which the samples may be placed (Fig. A6a, b; Fig. A7). Original concept based on a UV box housed at the University of Michigan Biogeochemistry and Environmental Isotope Geochemistry Laboratory (BEIGL).

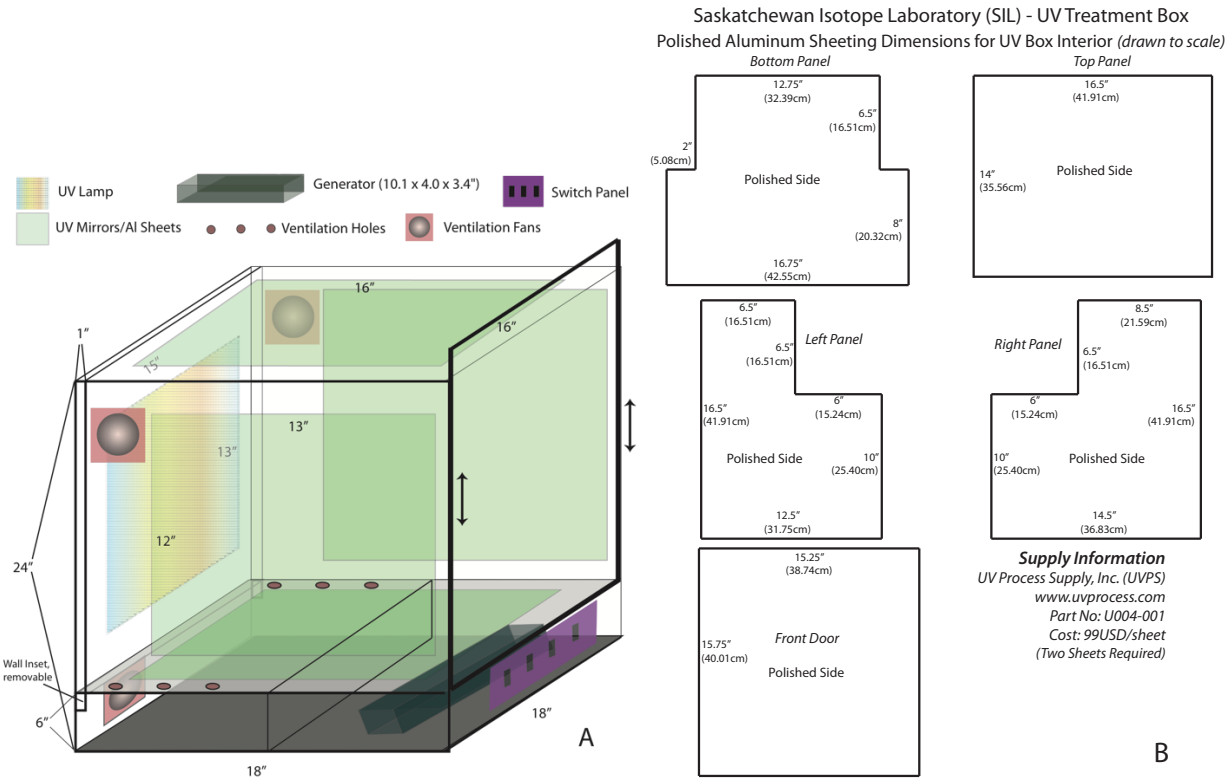

Figure A6 (A) Ultraviolet radiation organic treatment box concept design. Walls are constructed with opaque HDPE plastic sheeting (0.5 in.). (B) Interior is covered with polished Al mirrors cut to specified dimensions, in order to increase UV light reflectance and exposure to samples.

Figure A7 Final UV treatment system. The lamp and generator were specially selected for the simultaneous transmission of both 185 nm and 254 nm wavelength UV radiation. The HDPE plastic box was custom molded with the help of W. D. Plastics Ltd., Saskatoon.

APPENDIX B – Additional Data

B1. Figures

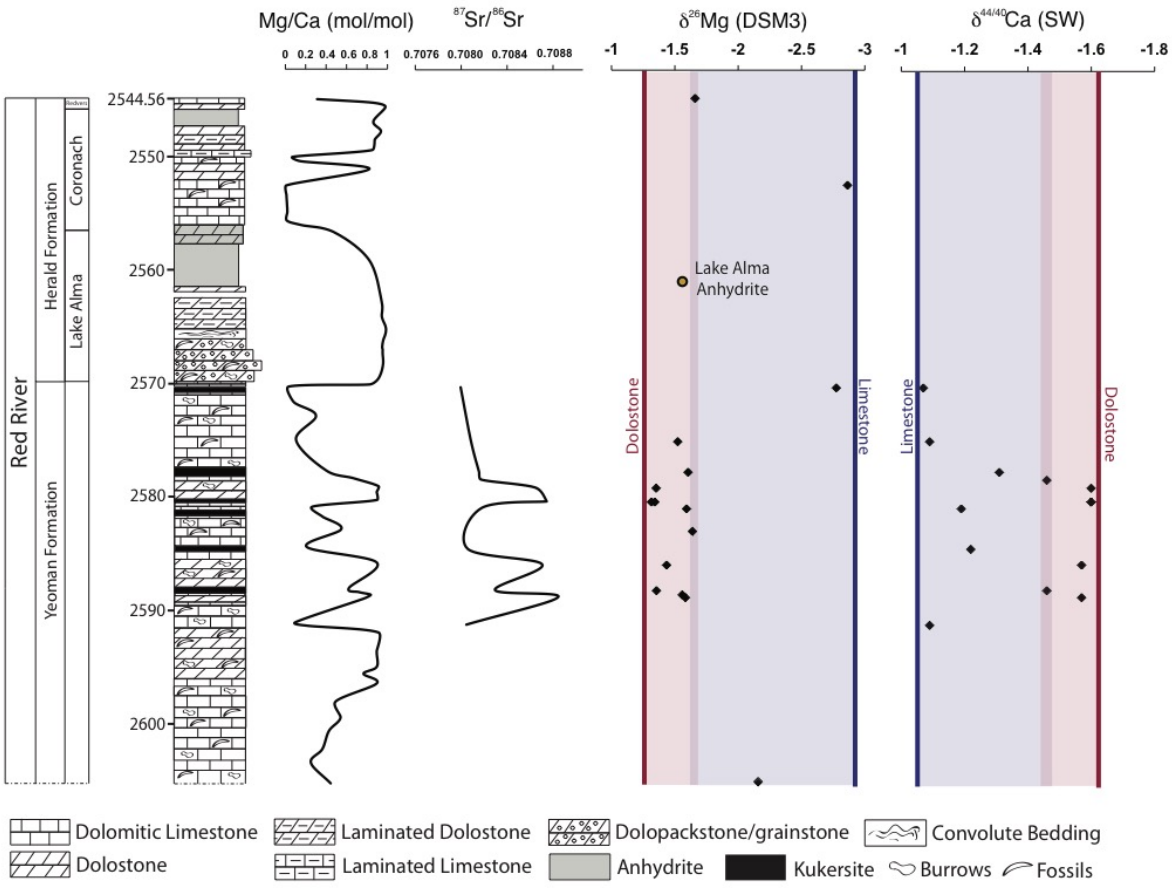

Figure B1 Profiles of Mg/Ca (mol/mol), $^{87}Sr/^{86}Sr$, $\delta^{26}Mg$ (‰DSM3), (mmol/mol), and $\delta^{44/40}Ca$ (‰SW) through the Midale, Saskatchewan, Berkeley et al. core (12-2-7-11W2), measured from whole-rock samples. All profiles are well-correlated. Lithology and stratigraphic ages are modified from Holmden (2009). Note that the scales for both the $\delta^{26}Mg$ and $\delta^{44/40}Ca$ profiles are inversed. Shifts in $^{87}Sr/^{86}Sr$ to more radiogenic values at Mg/Ca ≈ 1 indicate that Late Ordovician seawater (0.7080; Holmden (2009)) was unlikely the fluid from which the dolomite precipitated.

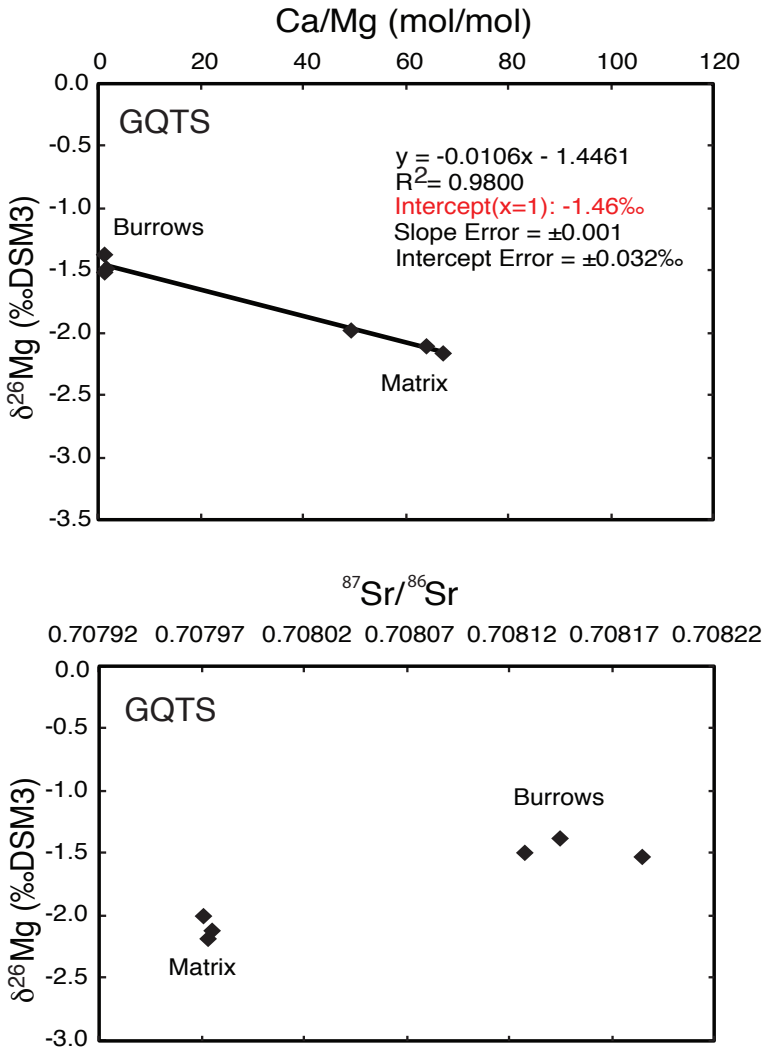

Figure B2 (A) Cross plot of δ^{26}Mg (‰DSM3) *vs*. Ca/Mg (mol/mol), as also shown in Chapter 3 Fig. 3.4. The intercept value at x = 1 may be used to predict the stoichiometric dolomite value of sampled the outcrop piece. (B) The δ^{26}Mg *vs.* $^{87}Sr/^{86}Sr$ values of carbonates collected from the Garson Quarry Tyndall Stone (GQTS). Note that the limestone matrix samples and the dolomitized burrow samples are isotopically distinct for both Mg and Sr isotopes, and demonstrate that while the limestone matrix remained undolomitized and records an $^{87}Sr/^{86}Sr$ value of Late Ordovician seawater (0.7080; Holmden (2009), the burrows could not have been precipitated from Ordovician seawater.

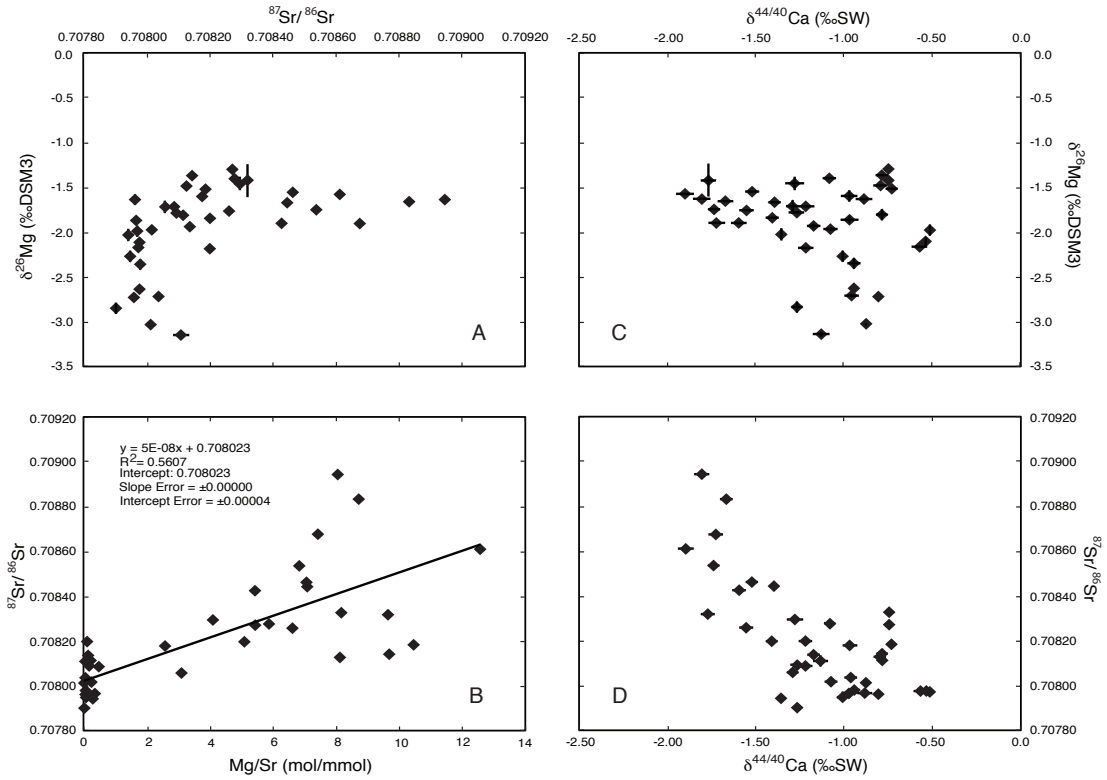

Figure B3 Cross plots of isotopic and elemental ratio data for the burrow and matrix carbonates reported in Chapter 3. (A) δ^{26}Mg (‰DSM3) values *vs*. $^{87}Sr/^{86}Sr$ values. Note the hyperbolic trend, which is indicative of two-component mixing, likely between limestone and dolomite. (B) $^{87}Sr/^{86}Sr$ values *vs*. Mg/Sr (mol/mmol). The estimated $^{87}Sr/^{86}Sr$ value of Ordovician seawater is 0.7080 (Holmden, 2009), the samples exhibit scattering around this estimated value. (C) $\delta^{44/40}$Ca (‰SW) values *vs*. δ^{26}Mg (‰DSM3) values. More negative $\delta^{44/40}$Ca values and less negative δ^{26}Mg values correspond to burrow dolomite and illustrate less scatter than do the matrix limestone samples, indicated by more positive $\delta^{44/40}$Ca values and more negative δ^{26}Mg values. (D) $\delta^{44/40}$Ca (‰SW) values *vs.* $^{87}Sr/^{86}Sr$ values showing a large shift in $\delta^{44/40}$Ca values of burrow and matrix carbonate of up to 1.5‰. More negative $\delta^{44/40}$Ca values and radiogenic $^{87}Sr/^{86}Sr$ values correspond to burrow dolomite, while more positive $\delta^{44/40}$Ca values and less radiogenic $^{87}Sr/^{86}Sr$ values correspond to matrix limestone.

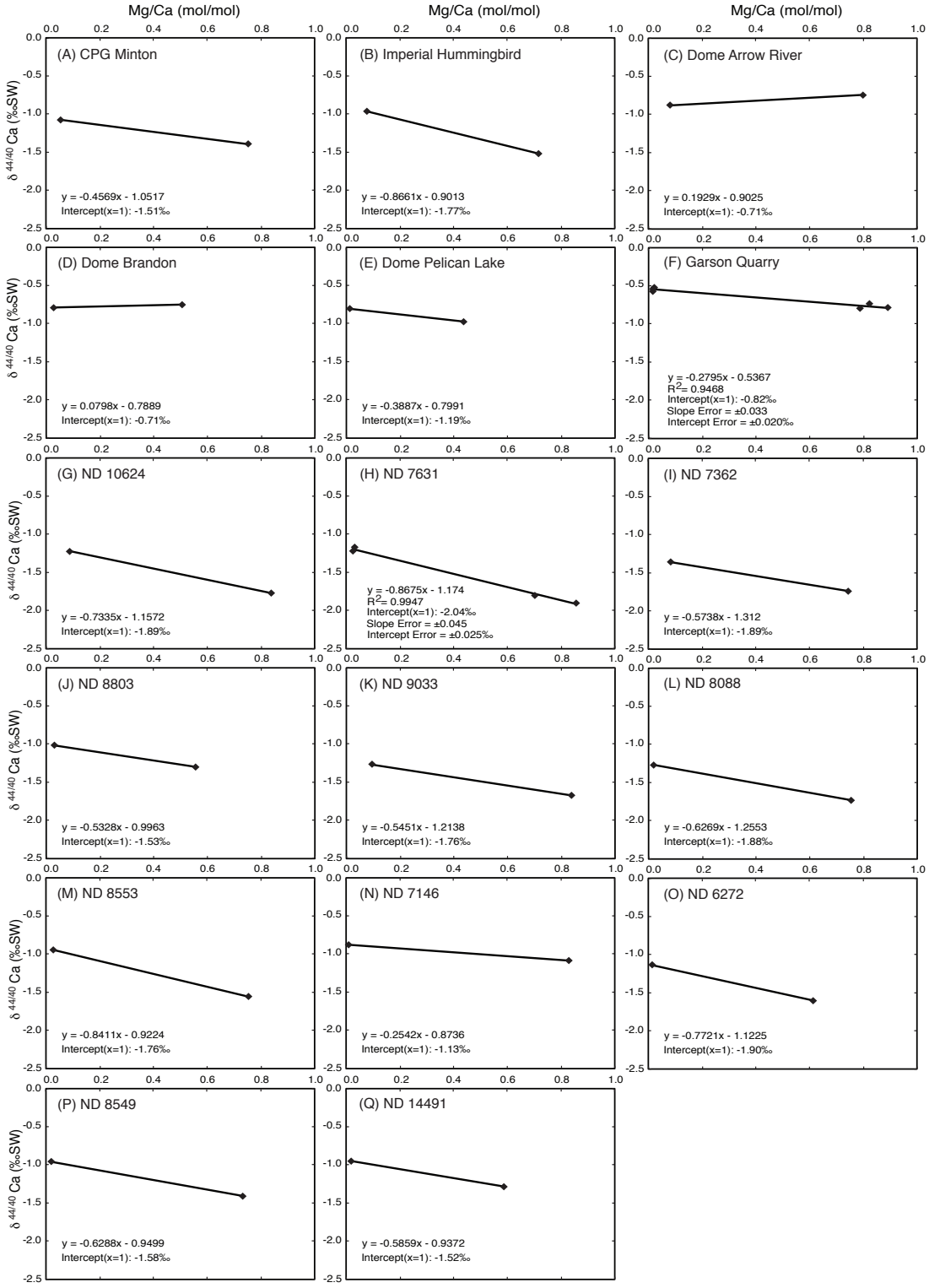

Figure B4 (A) Cross plot of $\delta^{44/40}$Ca (‰SW) values *vs*. Mg/Ca (mol/mol) for limestone matrix and dolomitized burrow samples in Red River cores collected throughout the Williston Basin.

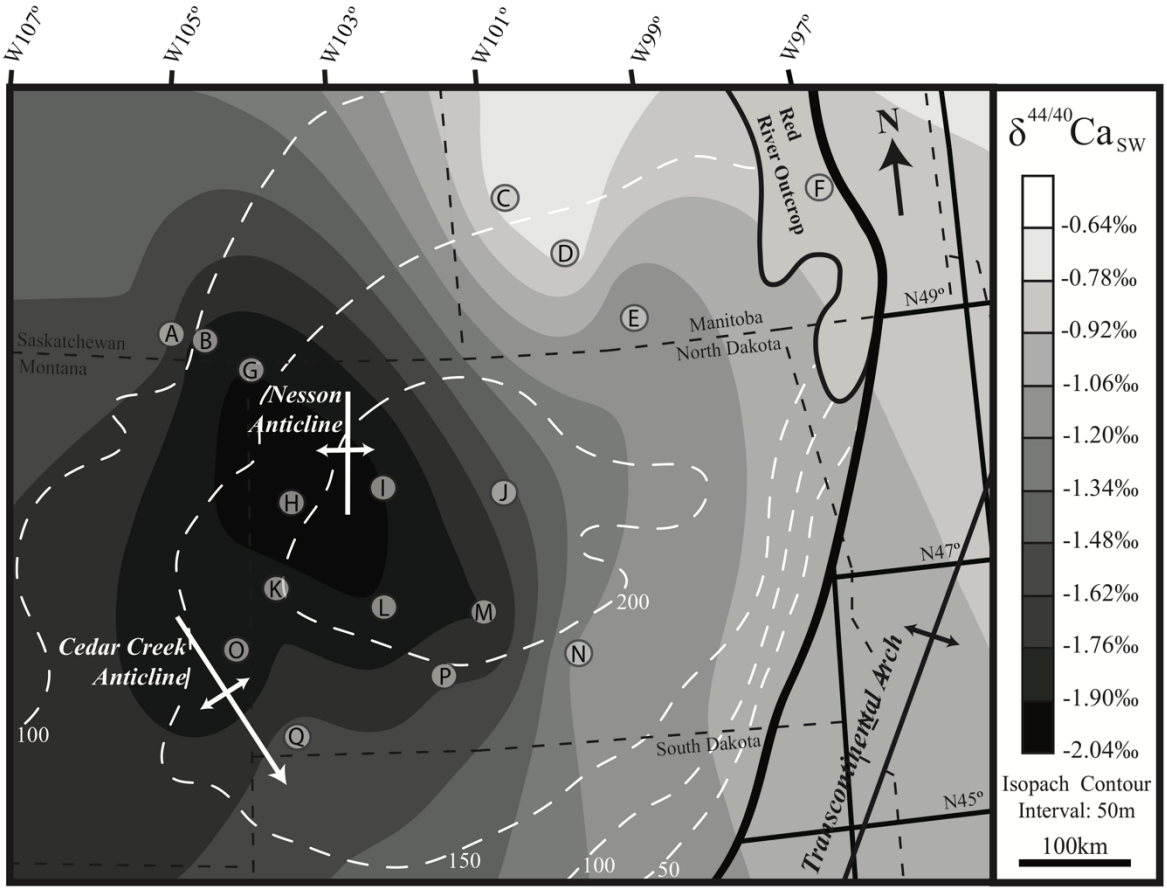

Figure B5 Contour map of the $\delta^{44/40}Ca$ (‰SW) end-member, stoichiometric dolomite values calculated from carbonates collected from well cores, shown in Fig. B4, when the Mg/Ca (mol/mol) ratio is equal to one. Well core locations are indicated by the letter designations denoting sampling locations, same as in Fig. B4 and as discussed in Chapter 3.

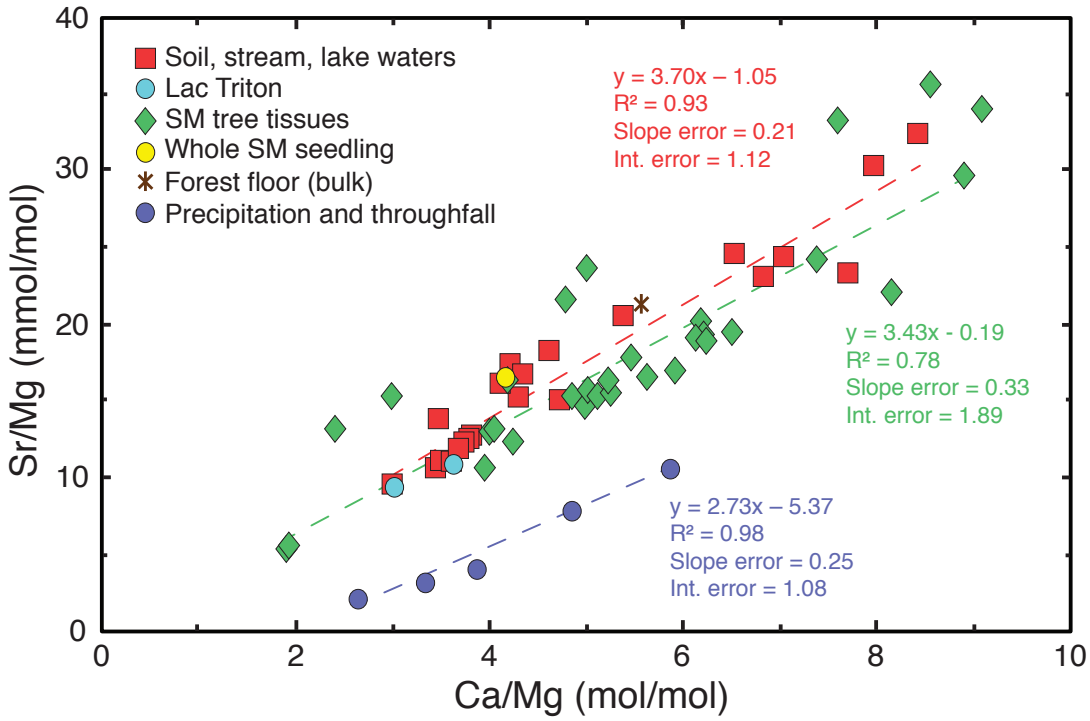

Figure B6 Cross plot of Sr/Mg (mmol/mol) *vs*. Ca/Mg (mol/mol) ratios of soil, stream and lake waters (depicted as red squares, Lac Triton indicated separately as light blue circles), sugar maple (SM) tree tissues and saps (depicted as green diamonds), a whole SM seedling grown on the forest floor (depicted as a yellow circle), a bulk digest of the forest floor (FH) horizon as a brown star, and bulk precipitation and throughfall (depicted as dark blue circles) samples discussed in Chapter 5. Trend-lines showing the lines of best fit are indicated for each of the soil, stream and lake water sample group as a dashed red line, for the SM tree tissue sample group as a green dashed line, and for the precipitation and throughfall sample group as a dark blue dashed line.

B2. Tables

Table B1

Isotopic and elemental data for carbonates and evaporites sampled from well cores spatially distributed across the Williston Basin. Includes fully dolomitized cores and outcrop samples as well as cores with burrow-only dolomitization (discussed in Chapters 2 and 3). Samples analyzed during the same analytical instrument session have errors ± 2SE (standard errors of the mean) while samples analyzed during differently tuned analytical sessions have ± 2σ. Sample solutions processed through chemistry multiple times are shown as 'rep' and the element.

Sampled from W.M. Laird Core and Sample Library, Grand Forks, ND

Sample	Type	Core	Box	Depth (m)	Sample Mass (g)	Total Sol'n (ml)	N (Mg)	δ^{26}Mg (‰ DSM3)	2SE	2σ	δ^{25}Mg (‰ DSM3)	2SE	2σ
Core 6272													
Location: Golden Valley County - LT2 22-137-106													
Coordinates: 46.670066N, 104.041191W													
1	Matrix + Burrow		21	3245.1	0.048	30.6	4	-2.06	0.03		-1.08	0.02	
2	Matrix		21	3245.1	0.042	31.2	4	-3.14	0.03		-1.62	0.03	
3	Matrix		21	3245.1	0.036	30.2	4	-2.77	0.02		-1.46	0.02	
4	Burrow		21	3245.1	0.044	31.1	4	-1.82	0.04		-0.94	0.02	
5	Burrow		21	3245.1	0.050	30.1	4	-1.90	0.02		-0.98	0.01	
Core 7146													
Location: Emmons County - NWNE 15-136-75													
Coordinates: 46.602055N, 100.091856W													
1	Matrix	7		1421.3	0.056	30.2	2	-2.86		0.06	-1.49		0.03
2	Matrix	7		1421.3	0.047	30.1	4	-3.03	0.02		-1.58	0.02	
3	Matrix	7		1421.3	0.053	30.3	4	-1.53	0.06		-0.79	0.04	
4	Burrow	7		1421.3	0.048	30.2	2	-1.46		0.14	-0.76		0.08
5	Burrow	7		1421.3	0.043	30.2	2	-1.49		0.12	-0.78		0.08
6	Burrow	7		1421.3	0.049	30.2	3	-1.40	0.06		-0.74	0.03	
Core 7362													
Location: Mountrail County - NESW 13-155-91													
Coordinates: 48.245928N, 102.323022W													
1	Matrix			3947.7	0.050	30.2	2	-1.93		0.06	-1.01		0.04
2	Matrix			3947.7	0.056	30.2	3	-1.83	0.04		-0.95	0.01	
3	Matrix			3947.7	0.042	30.2	3	-2.02	0.07		-1.03	0.05	
4	Burrow			3947.7	0.055	30.4	2	-1.83		0.08	-0.95		0.05
5	Burrow			3947.7	0.057	30.4	3	-1.75	0.04		-0.90	0.02	
6	Burrow			3947.7	0.052	30.3	3	-1.90	0.05		-0.97	0.03	
Core 7612													
Location: Ward County - SESW 15-155-87													
Coordinates: 48.241659N, 101.848567W													
1	Matrix			3395.1	0.058	30.3	2	-1.81		0.01	-0.95		0.01
2	Matrix			3395.1	0.048	30.4	2	-1.80		0.04	-0.92		0.03
3	Matrix			3395.1	0.053	30.2	3	-1.79	0.06		-0.94	0.04	
4	Burrow			3395.1	0.044	30.4	2	-1.79		0.04	-0.91		0.02
5	Burrow			3395.1	0.055	30.3	3	-1.85	0.07		-0.96	0.04	
6	Burrow			3395.1	0.052	30.3	4	-1.82	0.04		-0.95	0.03	
Core 7631													
Location: McKenzie County - NENE 33-151-99													
Coordinates: 47.861113N, 103.349790W													
1	Burrow		2	4288.9	0.032	31.0	4	-1.63	0.03		-0.83	0.03	
2	Matrix		2	4288.9	0.036	31.1	4	-2.18	0.03		-1.14	0.03	
3	Matrix		2	4289.0	0.044	30.1	3	-1.94	0.03		-1.02	0.02	
4	Burrow		2	4289.0	0.032	29.9	3	-1.58	0.01		-0.82	0.04	
5	Saddle Dolomite		2	4287.2	0.009	30.3	4	-1.87	0.03		-0.97	0.01	
6	Anhydrite		2	4287.2	0.052	30.1	4	-1.90	0.04		-0.97	0.01	
Core 8088													
Location: Stark County - NWNE 28-141-93													
Coordinates: 47.008456N, 102.469626W													
1	Matrix			3586.9	0.054	30.3	3	-2.12	0.01		-1.11	0.00	
2	Matrix			3586.9	0.044	30.3	3	-2.76	0.06		-1.45	0.05	
3	Matrix			3586.9	0.045	30.3	4	-2.84	0.06		-1.47	0.05	
4	Burrow			3586.9	0.049	30.3	2	-1.92		0.06	-1.00		0.05
5	Burrow			3586.9	0.059	30.3	4	-1.88	0.04		-0.98	0.01	
6	Burrow			3586.9	0.052	30.3	4	-1.90	0.05		-0.99	0.04	

Core 8549
Location: Grant County - SESE 16-134N-87W
Coordinates: 46.417301N, 101.614W

1	Matrix		2530.2	0.044	30.3	4	-1.85	0.06		-0.94	0.02	
2	Matrix		2530.2	0.043	30.3	4	-2.00	0.02		-1.05	0.02	
3	Matrix		2530.2	0.057	30.4	4	-2.71	0.02		-1.42	0.03	
4	Burrow		2530.2	0.051	30.4	3	-1.81	0.05		-0.94	0.05	
5	Burrow		2530.2	0.050	30.4	2	-1.79		0.02	-0.92		0.03
6	Burrow		2530.2	0.048	30.3	4	-1.84	0.04		-0.95	0.03	

Core 8553
Location: Morton County - SENW 17-140-82
Coordinates: 46.944383N, 101.063286W

1	Matrix		2420.6	0.057	30.3	3	-1.86	0.06		-0.96	0.01	
2	Matrix		2420.6	0.054	30.3	3	-2.06	0.07		-1.09	0.03	
3	Matrix		2420.6	0.052	30.3	4	-2.35	0.06		-1.22	0.04	
4	Burrow		2420.6	0.045	30.3	4	-1.86	0.05		-0.96	0.03	
5	Burrow		2420.6	0.050	30.3	4	-1.81	0.04		-0.92	0.02	
6	Burrow		2420.6	0.048	30.3	4	-1.75	0.04		-0.89	0.02	

Core 8803
Location: McHenry County - NENE 22-151-80
Coordinates: 47.889943N, 100.888204W

1	Matrix		2399.4	0.045	30.3	4	-1.85	0.01		-0.95	0.02	
2	Matrix		2399.4	0.055	30.3	4	-2.27	0.06		-1.19	0.03	
3	Matrix		2399.4	0.041	30.3	3	-1.98	0.04		-1.03	0.02	
4	Burrow		2399.4	0.049	30.2	3	-1.71	0.07		-0.89	0.04	
5	Burrow		2399.4	0.048	30.2	4	-1.74	0.03		-0.92	0.02	
6	Burrow		2399.4	0.052	30.2	2	-1.68		0.02	-0.88		0.02

Core 9033
Location: Billings County - NESW 4-142-102
Coordinates: 47.142311N, 103.618585W

1	Matrix	22	3831.7	0.046	29.7	4	-1.78	0.01		-0.92	0.01	
2	Matrix	22	3831.7	0.044	29.9	4	-2.01	0.04		-1.04	0.02	
3	Burrow	22	3831.7	0.038	31.1	4	-1.66	0.02		-0.89	0.01	
4	Burrow	22	3831.7	0.035	30.1	4	-1.65	0.04		-0.88	0.02	

Core 10624
Location: Divide County - NESE 9-163-102
Coordinates: 48.958008N, 103.927548W

1	Anhydrite	1	3212.1	0.146	30.1	4	-1.46	0.05		-0.77	0.02	
2	Laminated Dolomite	1	3212.4	0.043	30.1	4	-1.51	0.04		-0.78	0.01	
3	Matrix	4	3223.1	0.039	30.1	4	-1.44	0.05		-0.76	0.03	
4	Matrix	4	3223.1	0.045	29.9	4	-1.71	0.06		-0.90	0.04	
5	Burrow	4	3223.1	0.042	30.1	4	-1.45	0.03		-0.75	0.02	
6	Burrow	4	3223.1	0.045	29.8	2	-1.42		0.19	-0.72	0.04	0.08

Core 14491
Location: Bowman County - NWNE 27-130-102
Coordinates: 46.060560N, 103.419366W

2	Matrix + Burrow		2901.7	0.039	31.0	4	-2.90	0.05		-1.51	0.01	
3	Matrix		2901.7	0.046	30.2	3	-2.63	0.00		-1.36	0.02	
4	Matrix		2901.7	0.036	30.1	3	-2.04	0.03		-1.06	0.01	
5	Burrow		2901.7	0.045	30.9	4	-1.48	0.03		-0.76	0.01	
6	Burrow		2901.7	0.050	29.8	4	-1.46		0.07	-0.76		0.01

Sampled from the Manitoba Energy and Mines Core Library

Sample	Type	Core	Box	Depth (m)	Sample Mass (g)	Total Sol'n (ml)	N (Mg)	δ^{26}Mg (‰ DSM3)	2SE	2σ	δ^{25}Mg (‰ DSM3)	2SE	2σ
Dome Brandon													
Location 03-05-09-19WPM													
Coordinates: 49.7114N, 100.003W													
1	Matrix	4	5	1020.4	0.047	30.1	4	-1.71	0.04		-0.89	0.02	
1_repMg	Matrix	4	5	1020.4			3	-1.74	0.06		-0.91	0.03	
2	Matrix	4	5	1020.4	0.055	30.2	3	-1.40	0.03		-0.74	0.02	
3	Matrix	4	5	1020.4	0.056	30.2	3	-1.80	0.06		-0.94	0.05	

4	Burrow	4	5	1020.4	0.048	30.2	4	-1.30	0.05		-0.68	0.02	
5	Burrow	4	5	1020.4	0.044	30.2	3	-1.34	0.04		-0.66	0.01	
6	Burrow	4	5	1020.4	0.047	30.2	4	-1.35	0.03		-0.71	0.02	
Dome Pelican Lake													
Location 07-34-04-15WPM													
Coordinates: 49.3455N, 99.3962W													
1	Matrix	5	7	1002.4	0.053	30.2	3	-2.20	0.06		-1.17	0.05	
2	Matrix	5	7	1002.4	0.046	30.2	2	-2.72		0.01	-1.42		0.01
3	Matrix	5	7	1002.4	0.045	30.2	2	-1.93		0.02	-1.00		0.02
4	Burrow	5	7	1002.4	0.049	30.3	3	-1.59	0.06		-0.85	0.05	
4_repSr	Burrow												
5	Burrow	5	7	1002.4	0.042	30.2	4	-1.65	0.03		-0.88	0.02	
6	Burrow	5	7	1002.4	0.055	30.2	4	-1.71	0.04		-0.89	0.03	
Dome Arrow River													
Location 12-10-14-25WPM													
Coordinates: 50.1747N, 100.801W													
1	Matrix	4	9	1222.7	0.044	30.2	4	-1.64	0.06		-0.86	0.04	
2	Matrix	4	9	1222.7	0.060	30.2	2	-1.54		0.00	-0.79		0.01
3	Burrow	4	9	1222.7	0.044	30.2	4	-1.42	0.04		-0.74	0.04	
4	Burrow	4	9	1222.7	0.053	30.2	3	-1.47	0.04		-0.78	0.03	

Sampled from Saskatchewan Industry and Resources - Petroleum Geology Subsurface Geological Laboratory

Sample	Sample Type	Core	Box	Depth (m)	Sample Mass (g)	Total Sol'n (ml)	N (Mg)	δ^{26}Mg (‰ DSM3)	2SE	2σ	δ^{25}Mg (‰ DSM3)	2SE	2σ
UofR Regina													
Location: 03-08-17-19W2													
Coordinates: 50.413389N and 104.587575W													
1	Burrow	1	7	1994.4-1994.9	0.036	29.7	3	-1.67	0.02		-0.87	0.01	
2	Burrow	1	7	1994.4-1994.9	0.034	28.5	4	-1.66	0.01		-0.87	0.01	
3	Matrix	1	7	1994.4-1994.9	0.031	30.6	3	-1.61	0.03		-0.83	0.04	
4	Matrix + Burrow	1	7	1994.4-1994.9	0.037	29.5	4	-1.60	0.03		-0.82	0.04	
5	Matrix	1	7	1994.4-1994.9	0.032	29.3	4	-1.63	0.03		-0.85	0.03	
6	Laminated Dolomite	1	10	1999.6	0.041	29.7	4	-1.56	0.03		-0.79	0.03	
CPG Minton													
Location: 03-17-03-21W-2M													
Coordinates: 49.204611N and 104.800658W													
1	Matrix	3	5	2811.2	0.038	30.1	3	-1.97	0.02		-1.02	0.01	
2	Matrix	3	5	2811.2	0.037	29.6	3	-1.74	0.03		-0.89	0.01	
3	Burrow	3	5	2811.2	0.032	28.9	3	-1.67	0.02		-0.88	0.01	
4	Burrow	3	5	2811.2	0.030	30.3	3	-1.64	0.02		-0.87	0.01	
Imperial Hummingbird													
Location: 06-13-02-19W2													
Coordinates: 49.121552N and 104.423971W													
1	Burrow	14	1	3031.2	0.035	27.9	3	-1.55	0.02		-0.79	0.01	
2	Burrow	14	1	3031.2	0.039	28.9	4	-1.56	0.03		-0.81	0.02	
3	Matrix	14	1	3031.2	0.038	28.7	4	-1.86	0.04		-0.97	0.02	
4	Matrix	14	1	3031.2	0.036	29.2	4	-1.66	0.02		-0.86	0.01	
Home Dome (CNRL) Torquay													
Location 03-08-01-11W2													
Coordinates: 49.016017N and 103.443013W													
1	Saddle Dolomite	3	16	3195.6	0.005	49.8	2	-1.37		0.14	-0.72		0.08
2	Kukersite	3	9	3187.3	0.017	49.7	4	-1.71	0.03		-0.89	0.02	
3	Laminated Dolomite	3	6	3183.2	0.009	49.7	2	-1.43		0.03	-0.74		0.03
4	Matrix	4	11	3209.1	0.006	49.7	2	-1.43		0.08	-0.75		0.06
5	Burrow 1	4	11	3209.1	0.008	49.8	2	-1.30		0.04	-0.68		0.00
6	Burrow 2	4	11	3209.1	0.008	49.4	2	-1.35		0.08	-0.70		0.03
7	Matrix	4	2	3198.7	0.008	49.5	2	-1.30		0.11	-0.67		0.05
8	Burrow	4	2	3198.7	0.013	49.3	2	-1.27		0.00	-0.67		0.01
9	Burrow	3	14	3193.3	0.009	49.4	2	-1.58		0.25	-0.82		0.11
10	Matrix 1	3	14	3193.3	0.012	49.7	2	-1.48		0.12	-0.78		0.07
11	Matrix 2	3	14	3193.3	0.006	49.6	4	-1.53	0.03		-0.79	0.02	
12	Matrix 3	3	14	3193.3	0.009	49.6	4	-1.52	0.03		-0.79	0.01	

13	Matrix 4	3	14	3193.3	0.009	49.8	2	-1.62		0.13	-0.85		0.08
14	Saddle Dolomite 1	4	13	3211.0	0.041	30.1	4	-1.45	0.05		-0.75	0.02	
15	Saddle Dolomite 2	4	13	3211.0	0.039	29.0	4	-1.45	0.04		-0.77	0.04	
17	Burrow	4	5	3201.8	0.032	28.9	4	-1.50	0.03		-0.78	0.02	
18	Matrix	4	5	3201.8	0.041	29.4	4	-1.54	0.02		-0.79	0.02	
19	Burrow	4	5	3201.8	0.033	29.1	4	-1.60	0.02		-0.83	0.02	
20	Matrix	4	5	3201.8	0.038	28.7	4	-1.63	0.00		-0.85	0.01	
21	Burrow	4	5	3201.8	0.036	29.5	4	-1.59	0.03		-0.82	0.03	
22	Matrix	4	5	3201.8	0.036	28.3	4	-1.54	0.01		-0.80	0.02	
23	Matrix + Burrow	4	5	3201.8	0.038	29.2	4	-1.56	0.00		-0.80	0.01	
24	Matrix + Burrow	4	5	3201.8	0.038	28.0	4	-1.56	0.02		-0.81	0.01	
Imperial Constance													
Location 08-36-03-29W2													
Coordinates: 49.2516N and 105.775W													
1	Matrix	9	8	2640.4	0.054	35.2	4	-1.52	0.02		-0.79	0.01	
2	Matrix	9	8	2640.4	0.062	35.3	4	-1.55	0.01		-0.81	0.01	
3	Burrow	9	8	2640.4	0.061	35.3	3	-1.55	0.02		-0.81	0.01	
4	Burrow	9	8	2640.4	0.055	35.3	4	-1.59	0.04		-0.81	0.02	
Husky Glen Ewen													
Location 16-23-02-01W2													
Coordinates: 49.016017N and 103.443013W													
1	Matrix	2	11	2551.0	0.046	30.3	4	-1.40	0.04		-0.72	0.03	
2	Matrix	2	11	2551.0	0.050	30.3	4	-1.40	0.05		-0.73	0.03	
3	Burrow	2	11	2551.0	0.049	30.4	4	-1.36	0.03		-0.71	0.02	
4	Burrow	2	11	2551.0	0.049	30.4	4	-1.29	0.04		-0.68	0.03	
Berkley et al. Midale Core (Longview et al Midale V1U)													
Location 12-2-7-11W2													
Coordinates: 49.531198N and 103.404064W													
3	Limestone (Redvers)	1	1	2544.6	0.013	49.7	4	-1.66	0.05		-0.87	0.04	
4	Limestone (Yeoman)	4	11	2602.3	0.005	48.1	4	-1.64	0.02		-0.84	0.02	
5	Limestone (Yeoman)	4	14	2605.3	0.013	49.5	4	-2.16	0.04		-1.12	0.02	
6	Anhydrite (Lk Alma)	1		2560.7	0.014	48.9	4	-1.56	0.03		-0.81	0.02	
8	Whole Rock	4	2	2589.4	0.053	36.9	3	-1.60	0.08		-0.81	0.03	
7	Whole Rock	4	2	2589.4	0.057	35.9	3	-1.67	0.07		-0.87	0.04	
6	Whole Rock	4	2	2589.9	0.053	35.4	4	-1.58	0.02		-0.83	0.02	
5	Whole Rock	4	3	2590.4	0.060	36.7	3	-1.68	0.07		-0.88	0.03	
9	Whole Rock	4	3	2591.0	0.057	36.3	4	-1.69	0.03		-0.86	0.03	
4	Whole Rock	4	3	2591.3	0.057	36.3	3	-1.60	0.05		-0.84	0.02	
3	Whole Rock	4	4	2591.4	0.054	35.4	3	-1.61	0.02		-0.84	0.01	
1	Whole Rock	4	4	2591.6	0.045	36.4	4	-1.54	0.04		-0.81	0.02	
2	Whole Rock	4	4	2591.7	0.057	35.6	4	-1.56	0.05		-0.81	0.02	
10	Whole Rock	4	4	2592.2	0.055	36.3	4	-1.32	0.05		-0.69	0.01	
Garson Quarry Tyndall Stone													
Location Garson Quarry, MB													
Coordinates: 50.102916N, 96.608620'W													
GQTS 1	Burrow			Outcrop	0.014	30.1	4	-1.52	0.03		-0.81	0.02	
GQTS 2	Matrix			Outcrop	0.017	30.2	4	-2.16	0.03		-1.13	0.01	
GQTS 3	Burrow			Outcrop	0.021	30.0	4	-1.48	0.04		-0.76	0.04	
GQTS 4	Matrix			Outcrop	0.023	30.3	4	-2.10	0.05		-1.09	0.03	
GQTS 5	Burrow			Outcrop	0.013	30.4	4	-1.37	0.03		-0.74	0.02	
GQTS 6	Matrix			Outcrop	0.025	30.1	4	-1.98	0.06		-1.05	0.04	

Sampled from University of Saskatchewan Teaching Collections

Sample	Sample Type	Core	Box	Depth (m)	Sample Mass (g)	Total Sol'n (ml)	N (Mg)	δ^{26}Mg (‰ DSM3)	2SE	2σ	δ^{25}Mg (‰ DSM3)	2SE	2σ
Zortman Dolomite													
Location Alder's Gulch, near Zortman, Little Rocky Mountains, Montana													
Coordinates: 47.9178N, 108.5263W													
Collected 1964 - Dr. WGE Caldwell													
Zort_dol	Whole Rock			Outcrop	0.049	30.1	4	-1.71	0.04		-0.89	0.02	

Table B1 (cont'd)

Sample	Type	$\delta^{44/40}$Ca (‰ SW)	2SE	$^{87}Sr/^{86}Sr$	2SE	Ca/Mg (mol/mol)	Mg/Ca (mol/mol)	Sr/Ca (mmol/mol)	Ca/Sr (mol/mmol)	Sr/Mg (mmol/mol)	Mg/Sr (mol/mmol)
Sampled from W.M. Laird Core and Sample Library, Grand Forks, ND											
Core 6272											
Location: Golden Valley County - LT2 22-137-106											
Coordinates: 46.670066N, 104.041191W											
1	Matrix + Burrow					18.0	0.055	0.279	3.58	5.04	0.20
2	Matrix	-1.13	0.04	0.708109	0.000026	81.1	0.012	0.263	3.81	21.3	0.05
3	Matrix					64.1	0.016	0.284	3.52	18.2	0.05
4	Burrow					1.74	0.574	0.102	9.76	0.179	5.60
5	Burrow	-1.60	0.04	0.708426	0.000014	1.63	0.615	0.113	8.85	0.184	5.44
Core 7146											
Location: Emmons County - NWNE 15-136-75											
Coordinates: 46.602055N, 100.091856W											
1	Matrix					97.0	0.010	0.186	5.38	18.0	0.06
2	Matrix	-0.88	0.03	0.708013	0.000010	113	0.009	0.244	4.10	27.6	0.04
3	Matrix					7.19	0.139	0.166	6.04	1.19	0.84
4	Burrow					1.49	0.671	0.132	7.59	0.196	5.09
5	Burrow					3.35	0.298	0.151	6.62	0.507	1.97
6	Burrow	-1.08	0.03	0.708278	0.000015	1.21	0.827	0.141	7.11	0.170	5.88
Core 7362											
Location: Mountrail County - NESW 13-155-91											
Coordinates: 48.245928N, 102.323022W											
1	Matrix					7.01	0.143	0.249	4.02	1.74	0.57
2	Matrix					2.77	0.361	0.201	4.97	0.557	1.79
3	Matrix	-1.36	0.02	0.707942	0.000004	12.1	0.083	0.303	3.30	3.67	0.27
4	Burrow					1.77	0.566	0.159	6.29	0.281	3.56
5	Burrow	-1.74	0.03	0.708535	0.000005	1.35	0.743	0.109	9.22	0.146	6.85
6	Burrow					3.08	0.324	0.219	4.57	0.675	1.48
Core 7612											
Location: Ward County - SESW 15-155-87											
Coordinates: 48.241659N, 101.848567W											
1	Matrix	-1.61	0.04	0.708238	0.000007	2.08	0.481	0.315	3.17	0.656	1.52
2	Matrix					1.25	0.800	0.168	5.94	0.211	4.75
3	Matrix	-1.94	0.03	0.708570	0.000007	1.11	0.899	0.086	11.7	0.096	10.5
4	Burrow					1.12	0.896	0.083	12.0	0.093	10.8
5	Burrow					1.13	0.886	0.080	12.6	0.090	11.1
6	Burrow					1.16	0.863	0.069	14.6	0.080	12.6
Core 7631											
Location: McKenzie County - NENE 33-151-99											
Coordinates: 47.861113N, 103.349790W											
1	Burrow	-1.80	0.04	0.708945	0.000004	1.42	0.703	0.087	11.5	0.124	8.07
2	Matrix	-1.22	0.04	0.708198	0.000008	41.0	0.024	0.209	4.79	8.57	0.117
3	Matrix	-1.17	0.04	0.708137	0.000016	31.8	0.031	0.215	4.65	6.85	0.146
4	Burrow	-1.90	0.05	0.708612	0.000008	1.17	0.857	0.068	14.7	0.080	12.6
5	Saddle Dolomite	-1.63	0.04	0.711258	0.000014	1.05	0.955	0.086	11.6	0.090	11.1
6	Anhydrite					63.6	0.016	0.937	1.07	59.6	0.017
Core 8088											
Location: Stark County - NWNE 28-141-93											
Coordinates: 47.008456N, 102.469626W											
1	Matrix					12.8	0.078	0.371	2.70	4.73	0.212
2	Matrix					47.9	0.021	0.464	2.16	22.2	0.045
3	Matrix	-1.27	0.03	0.707902	0.000005	54.5	0.018	0.495	2.02	27.0	0.037
4	Burrow					1.47	0.682	0.111	9.04	0.162	6.17
5	Burrow					2.99	0.335	0.242	4.13	0.724	1.38
6	Burrow	-1.73	0.04	0.708675	0.000005	1.33	0.752	0.101	9.87	0.135	7.42
Core 8549											
Location: Grant County - SESE 16-134N-87W											

Coordinates: 46.417301N, 101.614W											
1	Matrix					6.94	0.144	0.220	4.54	1.53	0.654
2	Matrix					12.2	0.082	0.260	3.84	3.17	0.316
3	Matrix	-0.96	0.04	0.708035	0.000007	56.5	0.018	0.252	3.97	14.2	0.070
4	Burrow					2.14	0.467	0.185	5.40	0.396	2.52
5	Burrow					1.63	0.613	0.148	6.77	0.241	4.14
6	Burrow	-1.41	0.03	0.708200	0.000006	1.37	0.732	0.144	6.94	0.197	5.08
Core 8553											
Location: Morton County - SENW 17-140-82											
Coordinates: 46.944383N, 101.063286W											
1	Matrix					16.6	0.060	0.221	4.52	3.67	0.272
2	Matrix					22.8	0.044	0.270	3.71	6.14	0.163
3	Matrix	-0.94	0.03	0.707979	0.000005	40.4	0.025	0.251	3.99	10.1	0.099
4	Burrow					1.47	0.680	0.141	7.12	0.207	4.84
5	Burrow					2.67	0.375	0.200	5.00	0.533	1.88
6	Burrow	-1.56	0.04	0.708260	0.000007	1.33	0.753	0.114	8.81	0.151	6.63
Core 8803											
Location: McHenry County - NENE 22-151-80											
Coordinates: 47.889943N, 100.888204W											
1	Matrix					11.3	0.088	0.276	3.62	3.13	0.32
2	Matrix	-1.01	0.03	0.707947	0.000006	36.1	0.028	0.328	3.05	11.8	0.08
3	Matrix					19.4	0.051	0.356	2.81	6.91	0.14
4	Burrow	-1.29	0.03	0.708057	0.000003	1.80	0.556	0.180	5.56	0.324	3.09
5	Burrow					2.12	0.472	0.210	4.77	0.445	2.25
6	Burrow					2.16	0.462	0.179	5.57	0.388	2.58
Core 9033											
Location: Billings County - NESW 4-142-102											
Coordinates: 47.142311N, 103.618585W											
1	Matrix	-1.27	0.04	0.708093	0.000015	10.4	0.096	0.527	1.90	5.48	0.18
2	Matrix					26.1	0.038	0.402	2.49	10.5	0.10
3	Burrow	-1.67	0.04	0.708832	0.000010	1.19	0.839	0.096	10.4	0.115	8.71
4	Burrow					1.21	0.824	0.100	10.0	0.121	8.27
Core 10624											
Location: Divide County - NESE 9-163-102											
Coordinates: 48.958008N, 103.927548W											
1	Anhydrite	-1.67	0.03	0.707924	0.000009	19.6	0.051	1.77	0.565	34.7	0.03
2	Laminated Dolomite					1.05	0.948	0.121	8.26	0.128	7.83
3	Matrix					2.93	0.342	0.148	6.76	0.433	2.31
4	Matrix	-1.22	0.04	0.708087	0.000005	11.6	0.086	0.184	5.43	2.14	0.47
5	Burrow					1.36	0.737	0.093	10.7	0.127	7.89
6	Burrow	-1.77	0.04	0.708319	0.000010	1.20	0.837	0.087	11.5	0.104	9.65
Core 14491											
Location: Bowman County - NWNE 27-130-102											
Coordinates: 46.060560N, 103.419366W											
2	Matrix + Burrow					76.1	0.013	0.286	3.50	21.8	0.05
3	Matrix	-0.95	0.03	0.707977	0.000006	65.7	0.015	0.226	4.43	14.8	0.07
4	Matrix					33.9	0.029	0.229	4.36	7.77	0.13
5	Burrow					1.74	0.575	0.131	7.61	0.229	4.37
6	Burrow	-1.28	0.05	0.708295	0.000007	1.71	0.585	0.143	7.01	0.244	4.10

Sampled from the Manitoba Energy and Mines Core Library

Sample	**Type**	**$\delta^{44/40}$Ca (‰ SW)**	**2SE**	**$^{87}Sr/^{86}Sr$**	2SE	**Ca/Mg (mol/mol)**	**Mg/Ca (mol/mol)**	**Sr/Ca (mmol/mol)**	**Ca/Sr (mol/mmol)**	**Sr/Mg (mmol/mol)**	**Mg/Sr (mol/mmol)**
Dome Brandon											
Location 03-05-09-19WPM											
Coordinates: 49.7114N, 100.003W											
1	Matrix					32.4	0.031	0.122	8.21	3.95	0.25
1_repMg	Matrix										
2	Matrix					8.56	0.117	0.106	9.46	0.904	1.11
3	Matrix	-0.79	0.03	0.708116	0.000012	38.9	0.026	0.114	8.80	4.42	0.23
4	Burrow	-0.75	0.03	0.708270	0.000009	1.98	0.504	0.093	10.7	0.185	5.41
5	Burrow					1.98	0.506	0.083	12.1	0.164	6.12
6	Burrow					2.40	0.417	0.095	10.5	0.228	4.39
Dome Pelican Lake											

Location 07-34-04-15WPM											
Coordinates: 49.3455N, 99.3962W											
1	Matrix					42.2	0.024	0.334	2.99	14.1	0.07
2	Matrix	-0.80	0.03	0.707959	0.000009	74.7	0.013	0.266	3.76	19.9	0.05
3	Matrix					16.6	0.060	0.294	3.40	4.87	0.21
4	Burrow	-0.97	0.04	0.708176	0.000007	2.30	0.435	0.170	5.88	0.390	2.56
4_repSr	Burrow			0.708178	0.000009						
5	Burrow					2.16	0.463	0.161	6.20	0.349	2.87
6	Burrow					2.24	0.446	0.166	6.03	0.372	2.69
Dome Arrow River											
Location 12-10-14-25WPM											
Coordinates: 50.1747N, 100.801W											
1	Matrix	-0.89	0.04	0.707963	0.000003	12.4	0.081	0.291	3.43	3.61	0.28
2	Matrix					5.30	0.189	0.205	4.87	1.09	0.92
3	Burrow	-0.75	0.03	0.708326	0.000005	1.25	0.798	0.098	10.2	0.122	8.18
4	Burrow					1.36	0.733	0.162	6.19	0.220	4.54

Sampled from Saskatchewan Industry and Resources - Petroleum Geology Subsurface Geological Laboratory

Sample	**Sample Type**	**$\delta^{44/40}$Ca (‰ SW)**	**2SE**	**$^{87}Sr/^{86}Sr$**	2SE	**Ca/Mg (mol/mol)**	**Mg/Ca (mol/mol)**	**Sr/Ca (mmol/mol)**	**Ca/Sr (mol/mmol)**	**Sr/Mg (mmol/mol)**	**Mg/Sr (mol/mmol)**
UofR Regina											
Location: 03-08-17-19W2											
Coordinates: 50.413389N and 104.587575W											
1	Burrow	-1.48	0.05	0.708369	0.000054	1.23	0.815	0.092	10.9	0.112	8896
2	Burrow					1.22	0.817	0.093	10.8	0.113	8824
3	Matrix					2.06	0.486	0.155	6.47	0.318	3143
4	Matrix + Burrow					2.11	0.474	0.135	7.39	0.285	3505
5	Matrix	-1.22	0.03	0.707900	0.000032	3.79	0.264	0.209	4.78	0.793	1261
6	Laminated Dolomite					1.25	0.800	0.095	10.5	0.119	8422
CPG Minton											
Location: 03-17-03-21W-2M											
Coordinates: 49.204611N and 104.800658W											
1	Matrix	-1.08	0.04	0.708017	0.000003	18.4	0.054	0.225	4.44	4.14	0.054
2	Matrix					5.92	0.169	0.186	5.38	1.10	0.169
3	Burrow	-1.40	0.03	0.708445	0.000015	1.33	0.752	0.106	9.44	0.141	0.752
4	Burrow					1.32	0.758	0.104	9.63	0.137	0.758
Imperial Hummingbird											
Location: 06-13-02-19W2											
Coordinates: 49.121552N and 104.423971W											
1	Burrow	-1.52	0.04	0.708463	0.000007	1.40	0.717	0.102	9.83	0.142	7046
2	Burrow					2.12	0.471	0.154	6.49	0.327	3060
3	Matrix	-0.97	0.05	0.707967	0.000004	12.8	0.078	0.224	4.47	2.85	350
4	Matrix					3.87	0.258	0.161	6.20	0.624	1602
Home Dome (CNRL) Torquay											
Location 03-08-01-11W2											
Coordinates: 49.016017N and 103.443013W											
1	Saddle Dolomite	-1.26	0.04	0.708240	0.000020	1.31	0.764	0.156	6.40	0.204	4.89
2	Kukersite			0.708460	0.000020	1.62	0.619	0.236	4.24	0.381	2.63
3	Laminated Dolomite			0.709055	0.000017	1.05	0.949	0.126	7.94	0.133	7.53
4	Matrix	-1.45	0.04	0.709089	0.000013	1.07	0.933	0.088	11.3	0.095	10.6
5	Burrow 1	-1.62	0.03	0.709022	0.000023	1.07	0.935	0.075	13.4	0.080	12.5
6	Burrow 2	-1.51	0.04	0.709066	0.000062	1.19	0.840	0.081	12.3	0.097	10.3
7	Matrix			0.708834	0.000017	1.17	0.852	0.087	11.5	0.102	9.8
8	Burrow			0.708856	0.000032	1.15	0.869	0.069	14.5	0.080	12.6
9	Burrow					1.08	0.923	0.060	16.6	0.065	15.3
10	Matrix 1					1.19	0.843	0.078	12.8	0.093	10.8
11	Matrix 2			0.708467	0.000012	1.13	0.885	0.070	14.3	0.079	12.6
12	Matrix 3			0.708552	0.000018	1.15	0.867	0.080	12.4	0.093	10.8
13	Matrix 4			0.708482	0.000021	1.22	0.822	0.165	6.05	0.201	4.97
14	Saddle Dolomite 1			0.709326	0.000004	3.86	0.259	1.36	0.735	8.67	115
15	Saddle Dolomite 2			0.709693	0.000004	1.14	0.878	0.120	8.36	0.225	4453
17	Burrow					1.26	0.794	0.110	9.06	0.229	4361
18	Matrix					2.02	0.495	0.127	7.88	0.422	2367
19	Burrow					1.19	0.841	0.097	10.3	0.191	5245

20	Matrix					1.68	0.595	0.121	8.29	0.334	2994
21	Burrow	-1.45	0.05	0.708776	0.000052	1.22	0.817	0.114	8.74	0.231	4330
22	Matrix	-1.09	0.03	0.708118	0.000003	3.93	0.254	0.183	5.46	1.19	842
23	Matrix + Burrow					2.04	0.491	0.148	6.75	0.498	2010
24	Matrix + Burrow					3.50	0.286	0.184	5.45	1.06	945
Imperial Constance											
Location 08-36-03-29W2											
Coordinates: 49.2516N and 105.775W											
1	Matrix	-1.35	0.03	0.708892	0.000007	1.08	0.926	0.049	20.4	0.087	11472
2	Matrix					1.17	0.855	0.278	3.60	0.536	1866
3	Burrow					1.08	0.930	0.059	16.9	0.105	9517
4	Burrow	-1.42	0.04	0.708480	0.000006	1.06	0.947	0.067	14.9	0.117	8557
Husky Glen Ewen											
Location 16-23-02-01W2											
Coordinates: 49.016017N and 103.443013W											
1	Matrix	-1.87	0.05	0.709042	0.000008	1.16	0.863	0.118	8.46	0.226	4427
2	Matrix					1.13	0.881	0.121	8.26	0.226	4416
3	Burrow					1.12	0.893	0.102	9.78	0.189	5294
4	Burrow	-1.79	0.04	0.708901	0.000006	1.11	0.905	0.090	11.1	0.164	6115
Berkley et al. Midale Core (Longview et al Midale V1U)											
Location 12-2-7-11W2											
Coordinates: 49.531198N and 103.404064W											
3	Limestone (Redvers)			0.708053	0.000018	8.98	0.111	0.187	5.35	1.68	1
4	Limestone (Yeoman)			0.708300	0.000020	1.92	0.520	0.168	5.96	0.323	3
5	Limestone (Yeoman)			0.709171	0.000029	22.6	0.044	0.451	2.22	10.2	0
6	Anhydrite (Lk Alma)					79.6	0.013	1.68	0.596	134	0
8	Whole Rock					5.55	0.180	0.185	5.40	1.69	1
7	Whole Rock					5.81	0.172	0.194	5.15	1.86	1
6	Whole Rock					3.57	0.280	0.172	5.81	1.01	1
5	Whole Rock					6.04	0.166	0.193	5.17	1.92	1
9	Whole Rock					6.13	0.163	0.178	5.63	1.80	1
4	Whole Rock					5.01	0.200	0.189	5.30	1.56	1
3	Whole Rock					5.28	0.189	0.201	4.97	1.75	1
1	Whole Rock					3.80	0.263	0.200	4.99	1.26	1
2	Whole Rock					2.27	0.440	0.118	8.49	0.441	2
10	Whole Rock					1.14	0.877	0.070	14.4	0.131	8
Garson Quarry Tyndall Stone											
Location Garson Quarry, MB											
Coordinates: 50.102916N, 96.608620'W											
GQTS 1	Burrow	-0.73	0.03	0.708184	0.000010	1.21	0.824	0.079	12.7	0.096	
GQTS 2	Matrix	-0.57	0.04	0.707974	0.000007	67.3	0.015	0.133	7.54	8.92	
GQTS 3	Burrow	-0.80	0.04	0.708127	0.000008	1.27	0.789	0.097	10.3	0.123	
GQTS 4	Matrix	-0.54	0.03	0.707975	0.000010	63.9	0.016	0.147	6.79	9.41	
GQTS 5	Burrow	-0.79	0.03	0.708144	0.000010	1.12	0.892	0.092	10.8	0.103	
GQTS 6	Matrix	-0.52	0.03	0.707971	0.000006	49.3	0.020	0.138	7.26	6.79	

Sampled from University of Saskatchewan Teaching Collections

Sample	Sample Type	$\delta^{44/40}$Ca (‰ SW)	2SE	$^{87}Sr/^{86}Sr$	2SE	Ca/Mg (mol/mol)	Mg/Ca (mol/mol)	Sr/Ca (mmol/mol)	Ca/Sr (mol/mmol)	Sr/Mg (mmol/mol)	Mg/Sr (mol/mmol)
Zortman Dolomite											
Location Alder's Gulch, near Zortman, Little Rocky Mountains, Montana											
Coordinates: 47.9178N, 108.5263W											
Collected 1964 - Dr. WGE Caldwell											
Zort_dol	Whole Rock	-1.03	0.04	0.708424	0.000007	1.45	0.689	0.080	12.4	0.117	8.56

Table B1 (cont'd)

Sampled from W.M. Laird Core and Sample Library, Grand Forks, ND										
Sample	**Type**	**Na (μg/g)**	**Mg (μg/g)**	**Al (μg/g)**	**K (μg/g)**	**Ca (μg/g)**	**Mn (μg/g)**	**Fe (μg/g)**	**Sr (μg/g)**	**Ba (μg/g)**
Core 6272										
Location: Golden Valley County - LT2 22-137-106										
Coordinates: 46.670066N, 104.041191W										
1	Matrix + Burrow	262	10357	25.4	41.3	308181	90.9	194	188	3.11
2	Matrix	164	2463	24.4	47.5	329340	84.6	99.4	189	4.82
3	Matrix	172	3088	25.9	27.4	326284	83.0	115	203	7.39
4	Burrow	194	72280	78.6	36.5	207718	291	1186	46.5	2.11
5	Burrow	173	72466	40.6	46.5	194449	277	1117	48.0	3.80
Core 7146										
Location: Emmons County - NWNE 15-136-75										
Coordinates: 46.602055N, 100.091856W										
1	Matrix	411	2204	15.4	43.1	352354	32.4	76.0	143	1.13
2	Matrix	599	1794	34.5	63.0	335351	32.6	148	179	1.15
3	Matrix	556	27589	48.7	67.8	327049	74.1	521	118	1.78
4	Burrow	612	90460	131	134	222380	177	1476	64.1	13.1
5	Burrow	871	56239	123	104	310946	120	942	103	3.26
6	Burrow	1049	97544	167	178	194475	191	1601	59.8	38.3
Core 7362										
Location: Mountrail County - NESW 13-155-91										
Coordinates: 48.245928N, 102.323022W										
1	Matrix	341	26067	69.6	134	301192	66.5	215	164	2.84
2	Matrix	458	60042	122	119	273940	71.3	343	121	2.57
3	Matrix	472	16553	105	113	330341	48.0	188	219	3.07
4	Burrow	464	83797	203	143	244177	86.0	560	84.9	3.44
5	Burrow	414	92154	242	236	204550	88.4	618	48.5	3.25
6	Burrow	341	57526	180	159	292335	70.0	398	140	3.29
Core 7612										
Location: Ward County - SESW 15-155-87										
Coordinates: 48.241659N, 101.848567W										
1	Matrix	4079	70923	222	341	243312	108	1087	168	7.09
2	Matrix	1053	102134	223	271	210573	124	1192	77.5	3.66
3	Matrix	761	110984	129	153	203661	125	1161	38.2	2.17
4	Burrow	1056	111793	108	85.6	205644	119	1063	37.5	1.86
5	Burrow	766	107397	116	148	199923	123	947	34.8	4.02
6	Burrow	765	112334	115	128	214669	118	988	32.2	2.29
Core 7631										
Location: McKenzie County - NENE 33-151-99										
Coordinates: 47.861113N, 103.349790W										
1	Burrow	273	84465	129	124	198233	161	986	37.7	4.31
2	Matrix	138	4761	62.3	125	322265	70.9	125	147	8.72
3	Matrix	159	5679	48.5	62.3	298160	60.9	113	140	6.03
4	Burrow	124	89242	156	127	171799	154	879	25.6	4.27
5	Saddle Dolomite	116	105426	54.1		181944	290	37.4	34.3	9.18
6	Anhydrite	25.0	2490	22.7	89.6	261200	29.7	22.1	535	BDL
Core 8088										
Location: Stark County - NWNE 28-141-93										
Coordinates: 47.008456N, 102.469626W										
1	Matrix	192	16280	49.6	39.7	342379	67.7	180	277	2.41
2	Matrix	186	4407	41.7	55.0	347880	58.6	124	353	2.82
3	Matrix	266	3947	56.8	61.9	355019	57.4	92.8	384	3.03
4	Burrow	205	92227	136	123	222831	143	712	53.9	3.28
5	Burrow	179	56289	66.5	64.0	277353	105	522	147	2.66
6	Burrow	196	99955	134	114	219200	137	748	48.6	2.28

Core 8549										
Location: Grant County - SESE 16-134N-87W										
Coordinates: 46.417301N, 101.614W										
1	Matrix	855	27909	47.1	86.9	319454	588	344	154	1.37
2	Matrix	1589	16458	30.0	33.1	329854	49.6	221	188	1.90
3	Matrix	569	3649	17.9	220	339723	57.4	75.1	187	6.92
4	Burrow	694	70610	102	109	249213	99.1	736	101	3.68
5	Burrow	641	88280	131	82.8	237631	124	1070	76.8	2.18
6	Burrow	530	96857	129	75.6	218084	109	950	68.7	1.87
Core 8553										
Location: Morton County - SENW 17-140-82										
Coordinates: 46.944383N, 101.063286W										
1	Matrix	565	11889	50.5	132	325498	56.0	164	157	3.70
2	Matrix	955	9099	55.0	98.8	341621	38.3	148	202	2.01
3	Matrix	564	5237	84.9	76.2	348560	36.0	125	191	1.70
4	Burrow	591	92181	209	174	223387	96.2	644	68.6	2.09
5	Burrow	500	58390	158	176	256599	73.7	502	112	1.83
6	Burrow	467	98975	132	114	216862	107	788	53.8	1.58
Core 8803										
Location: McHenry County - NENE 22-151-80										
Coordinates: 47.889943N, 100.888204W										
1	Matrix	570	17911	30.6	171	334571	52.0	243	202	3.85
2	Matrix	556	5887	37.9	94.6	350480	33.1	135	251	2.92
3	Matrix	720	9955	32.6	76.1	319153	34.3	181	248	1.98
4	Burrow	307	77072	71.0	89.3	228769	74.6	722	89.9	1.65
5	Burrow	696	69592	69.0	92.2	243258	65.8	625	112	1.50
6	Burrow	326	72051	47.6	60.5	257080	76.1	870	101	1.50
Core 9033										
Location: Billings County - NESW 4-142-102										
Coordinates: 47.142311N, 103.618585W										
1	Matrix	272	16286	63.6	98.7	279561	181	458	322	17.83
2	Matrix	587	6450	84.3	134	277285	136	252	244	9.65
3	Burrow	287	95634	128	140	187999	523	2142	39.6	5.15
4	Burrow	349	91483	127	130	182965	495	2037	39.9	7.85
Core 10624										
Location: Divide County - NESE 9-163-102										
Coordinates: 48.958008N, 103.927548W										
1	Anhydrite	161	7455	41.4	113	240950	15.5	84.6	933	2.10
2	Laminated Dolomite	1192	99578	168	189	173210	90.5	1108	45.9	3.09
3	Matrix	573	49263	53.0	78.5	237850	100	712	77.0	3.46
4	Matrix	888	15725	45.7	167	300681	80.9	341	121	3.68
5	Burrow	547	85446	69.1	93.4	191168	133	883	39.0	3.33
6	Burrow	599	89369	80.8	108	176109	138	821	33.4	3.81
Core 14491										
Location: Bowman County - NWNE 27-130-102										
Coordinates: 46.060560N, 103.419366W										
2	Matrix + Burrow	440	2799	30.4	66.6	351257	31.4	97.5	220	1.82
3	Matrix	370	3331	47.7	83.1	360807	33.5	90.4	178	1.78
4	Matrix	461	6103	46.5	70.4	341190	35.0	112	171	4.02
5	Burrow	256	78722	45.4	67.7	225809	115	1250	64.9	1.66
6	Burrow	328	79984	90.8	155	225519	108	962	70.4	2.95

Sampled from the Manitoba Energy and Mines Core Library

Sample	Type	Na (µg/g)	Mg (µg/g)	Al (µg/g)	K (µg/g)	Ca (µg/g)	Mn (µg/g)	Fe (µg/g)	Sr (µg/g)	Ba (µg/g)
Dome Brandon										
Location 03-05-09-19WPM										
Coordinates: 49.7114N, 100.003W										
1	Matrix	1064	6705	12.7	28.4	358477	53.0	204	95.4	BDL
1_repMg	Matrix									
2	Matrix	1187	22699	22.4	47.5	320331	71.8	423	74.0	BDL
3	Matrix	1642	5725	23.2	352	367277	67.5	231	91.3	5.08

4	Burrow	773	80446	55.2	98.5	263164	133	1179	53.6	2.56
5	Burrow	1355	85716	70.5	56.0	279269	140	1327	50.5	1.52
6	Burrow	687	66134	64.7	51.9	261295	119	1102	54.3	1.69
Dome Pelican Lake										
Location 07-34-04-15WPM										
Coordinates: 49.3455N, 99.3962W										
1	Matrix	697	4871	54.6	121	339185	55.0	176	248	2.74
2	Matrix	513	2980	34.0	49.4	367173	37.9	116	214	1.05
3	Matrix	788	12196	51.1	76.1	333531	42.5	230	214	1.15
4	Burrow	2035	66599	163	190	252212	78.3	715	93.7	1.91
4_repSr	Burrow									
5	Burrow	1440	69239	149	165	246722	87.0	777	87.0	1.71
6	Burrow	1713	70366	137	137	260189	87.3	785	94.4	2.13
Dome Arrow River										
Location 12-10-14-25WPM										
Coordinates: 50.1747N, 100.801W										
1	Matrix	1146	16770	119	160	342300	103	529	218	1.79
2	Matrix	221	34397	96.8	86.2	300348	101	817	135	1.65
3	Burrow	411	103025	145	113	212964	168	1438	45.4	2.35
4	Burrow	459	94767	135	110	213083	140	1252	75.2	1.72

Sampled from Saskatchewan Industry and Resources - Petroleum Geology Subsurface Geological Laboratory

Sample	Sample Type	Na (µg/g)	Mg (µg/g)	Al (µg/g)	K (µg/g)	Ca (µg/g)	Mn (µg/g)	Fe (µg/g)	Sr (µg/g)	Ba (µg/g)
UofR Regina										
Location: 03-08-17-19W2										
Coordinates: 50.413389N and 104.587575W										
1	Burrow	2605	112316	138	604	227241	114	678	45.5	2.94
2	Burrow	1229	107390	112	376	216786	159	575	43.9	7.19
3	Matrix	11415	71696	105	306	243293	123	768	82.2	BDL
4	Matrix + Burrow	4062	75012	110	237	260723	122	842	77.1	1.74
5	Matrix	7282	49348	47.2	535	308336	102	601	141	BDL
6	Laminated Dolomite	2704	102311	65.2	300	210775	152	930	43.8	1.68
CPG Minton										
Location: 03-17-03-21W-2M										
Coordinates: 49.204611N and 104.800658W										
1	Matrix	355	11357	33.4	79.4	344615	40.5	126	170	1.83
2	Matrix	634	33876	45.9	87.1	330764	55.4	242	134	1.50
3	Burrow	514	101363	115	135	222385	78.5	373	51.5	8.21
4	Burrow	501	104570	124	133	227402	81.6	376	51.6	2.96
Imperial Hummingbird										
Location: 06-13-02-19W2										
Coordinates: 49.121552N and 104.423971W										
1	Burrow	328	103086	236	215	237129	169	1324	52.7	3.11
2	Burrow	346	77306	198	187	270533	141	1066	91.1	2.17
3	Matrix	300	16473	70.7	82.7	346841	68.5	323	170	1.50
4	Matrix	440	51349	97.8	106	327577	117	866	116	1.87
Home Dome (CNRL) Torquay										
Location 03-08-01-11W2										
Coordinates: 49.016017N and 103.443013W										
1	Saddle Dolomite	3709	127223	423	1909	274442		5805	93.7	BDL
2	Kukersite	742	87428	1270	664	232990		2308	120	4.60
3	Laminated Dolomite	1558	126620	423	1079	220126		3077	60.6	BDL
4	Matrix	1632	132649	370	415	234419		4196	45.2	BDL
5	Burrow 1	1261	127223	370	498	224414		2238	36.6	BDL
6	Burrow 2	4822	122399	582	5230	240137		3427	42.7	6.10
7	Matrix	9273	113355	1958	6060	219411		1609	41.7	3.10
8	Burrow	1780	111546	318	498	211549		2448	32.0	BDL
9	Burrow	890	130841	106	249	233705		1399	30.8	BDL
10	Matrix 1	2300	116973	212	498	228702		2168	39.1	BDL
11	Matrix 2	1335	133855	318	1245	249428		1259	38.2	BDL
12	Matrix 3	1780	124811	212	996	237278		1958	41.7	11.3

13	Matrix 4	5786	109737	370	1992	220126		2238	79.6	0.60
14	Saddle Dolomite 1	810	37142	55.8	51.4	236506	73.4	1462	704	1.54
15	Saddle Dolomite 2	910	117433	50.0	44.1	220528	232	4480	57.7	1.69
17	Burrow	261	101706	146	143	211256	97.2	851	51.0	2.85
18	Matrix	221	76670	91.4	92.8	255352	79.2	771	70.8	3.00
19	Burrow	319	110015	226	178	215588	104	982	45.9	3.55
20	Matrix	263	90698	94.7	152	251182	99.3	837	66.2	5.61
21	Burrow	539	109672	179	156	221480	104	835	55.4	4.68
22	Matrix	399	47636	97.1	132	308740	65.3	584	124	3.26
23	Matrix + Burrow	287	78393	91.7	107	263219	80.2	745	85.3	4.74
24	Matrix + Burrow	365	51907	123	168	299215	68.1	612	120	4.54
Imperial Constance										
Location 08-36-03-29W2										
Coordinates: 49.2516N and 105.775W										
1	Matrix	224	103177	441	474	183642	130	831	19.7	2.01
2	Matrix	225	96997	804	849	187106	123	792	114	1.55
3	Burrow	296	106912	189	168	189553	116	786	24.6	1.79
4	Burrow	239	100046	157	225	174274	122	716	25.6	2.58
Husky Glen Ewen										
Location 16-23-02-01W2										
Coordinates: 49.016017N and 103.443013W										
1	Matrix	987	96765	180	417	184973	326	2784	47.8	1.45
2	Matrix	5260	97979	159	370	183335	328	2759	48.5	1.38
3	Burrow	808	109191	111	175	201726	344	2431	45.1	1.42
4	Burrow	636	114883	119	148	209384	367	2761	41.1	1.91
Berkley et al. Midale Core (Longview et al Midale V1U)										
Location 12-2-7-11W2										
Coordinates: 49.531198N and 103.404064W										
3	Limestone (Redvers)	445	24480	212		362350		1469	148	
4	Limestone (Yeoman)	3932	91046	529	1411	288736		1329	106	10.4
5	Limestone (Yeoman)	445	10250			381646		1958	376	4.90
6	Anhydrite (Lk Alma)	148	2472			324471		909	1190	
8	Whole Rock	374	33463	154	152	306087	97.7	696	124	2.29
7	Whole Rock	372	33445	151	208	320157	103	578	136	2.52
6	Whole Rock	313	49360	162	273	290554	135	863	109	7.54
5	Whole Rock	286	30120	138	142	299902	79.6	534	127	1.73
9	Whole Rock	255	30490	178	192	308414	77.3	557	120	2.30
4	Whole Rock	256	36010	191	199	297246	80.1	577	123	2.18
3	Whole Rock	243	34819	413	359	303132	80.9	694	133	3.06
1	Whole Rock	402	46437	484	339	291056	100	987	128	3.88
2	Whole Rock	332	67632	241	233	253273	137	1176	65.2	3.09
10	Whole Rock	1729	102721	279	291	193065	270	1939	29.4	2.38
Garson Quarry Tyndall Stone										
Location Garson Quarry, MB										
Coordinates: 50.102916N, 96.608620'W										
GQTS 1	Burrow	190	124124	22.6	195	248527		3107	42.7	
GQTS 2	Matrix	172	3892	66.2	104	431901		1807	125	
GQTS 3	Burrow	169	128541	30.1	260	268568		4313	56.9	
GQTS 4	Matrix	144	3822	68.6	86.1	402670		1551	130	
GQTS 5	Burrow	161	129415	25.5	220	239189		2943	48.2	
GQTS 6	Matrix	89.3	4912	63.7	20.0	399582		1758	120	

Sampled from University of Saskatchewan Teaching Collections

Sample	Sample Type	Na (µg/g)	Mg (µg/g)	Al (µg/g)	K (µg/g)	Ca (µg/g)	Mn (µg/g)	Fe (µg/g)	Sr (µg/g)	Ba (µg/g)
Zortman Dolomite										
Location Alder's Gulch, near Zortman, Little Rocky Mountains, Montana										
Coordinates: 47.9178N, 108.5263W										
Collected 1964 - Dr. WGE Caldwell										
Zort_dol	Whole Rock	165	89372	211	188	214006	137	1198	37.6	3.65

APPENDIX C – Presentation Abstracts

C1. Invited talks

Using a novel Mg isotope tracer to investigate the dolomitization of the Red River Formation in the Williston Basin

The University of Idaho/Washington State University Fall 2015 Seminar Series.

October 2015 | Pullman, WA, USA

Worsham, S. R.

Dolomite $CaMg(CO_3)_2$ is a highly studied mineral due to its economic importance in creating petroleum reservoir-quality porosity and permeability. It is difficult to create in the laboratory, so we must look at examples in nature for clues as to how dolomitization occurs. Mg isotopes have not previously been investigated as a tracer of dolomitizing fluids or as a tool for advancing knowledge of the process of large-scale dolomitization. Accordingly, the Mg isotope study of dolomitization in rocks of the Red River Formation of the Williston Basin represents a pioneering first step. Join us for an overview of how Mg isotopes may be used to better understand large-scale dolomitization events.

Magnesium isotope fractionation in a hardwood forest of Southern Québec, Canada

Goldschmidt Conference

August 2011 | Prague, Czech Republic

Worsham S.[1]*, Holmden C.[1], and Bélanger N.[2]

[1]Saskatchewan Isotope Laboratory, University of Saskatchewan, Saskatoon, Canada

[2]Université du Québec à Montréal, Montréal, Canada

*Presenting author

Magnesium (Mg) is an essential macronutrient for plants, acting as the coordinating cation for chlorophyll as well as serving other important metabolic functions. Recent laboratory studies have demonstrated mass dependent fractionation of Mg within plants (Black et al., 2008; Bolou-Bi et al., 2010), while there is only one confirmation of plant fractionation in the field to date (Tipper et al., 2010). Our study builds on previous work through an investigation of Mg isotope fractionation in a forested ecosystem. Broader questions motivating this work include the potential impact of forest Mg cycling on the signature of the continental weathering flux of Mg delivered to the oceans by river flow.

Mg isotope fractionation is being examined in a forested first order catchment in southern Québec, Canada, dominated by sugar maple (*Acer saccharum)* and characterized by soils developed from granite, mangerite and anorthosite. Thus far, we observe fractionation coupled with the uptake of Mg into maple trees from the soil pool as well as significant internal plant fractionation. Preliminary $\delta^{26}Mg$ ($^{26}Mg/^{24}Mg$) values for the study plot exhibit an overall fractionation range of 1.15‰ (23% of reported terrestrial variation). Most interesting is considerable fractionation associated with the degradation of chlorophyll during leaf senescence. We believe translocation of light chlorophyll-bound Mg back into the tree accounts for this finding, driving whole leaf $\delta^{26}Mg$ to higher values prior to litter fall. Measured $\delta^{26}Mg$ values of senescent leaves and litter range from –0.88 ± 0.10‰ to –1.32 ± 0.09‰. Analyses of soil water and stream water samples during low and high flow indicate that Mg isotope values in the stream may be influenced by fractionation during plant uptake; however, a lithology driven (particularly silicate weathering (Tipper et al., 2006b) control is still under investigation. With this presentation, we will review the progress made to date on factors influencing Mg isotope fractionation in a forested catchment.

C2. Conference presentations

Aragonite precipitation in the Late Ordovician 'calcite sea' – Evidence from a multi-proxy geochemical approach

Geological Society of America (GSA) Annual Meeting

October 2017 | Seattle, WA, USA

Kimmig S. R.* and Holmden C.

Saskatchewan Isotope Laboratory, Department of Geological Sciences, University of Saskatchewan, Saskatoon, SK S7N 5E2

*Presenting author

A positive excursion in $\delta^{26}Mg$ values (2–3‰) is observed, recorded in a carbonate succession in the Monitor Range, Nevada, spanning the Late Ordovician (Hirnantian) glaciation event. The increase in $\delta^{26}Mg$ values is synchronous with previously detailed $\delta^{44/40}Ca$ and $\delta^{13}C$ excursions in the same section, an observation at odds with the large difference in residence times between Mg, Ca, and C, suggesting that the isotopic shifts are not the result of global-ocean cycling. A mixing analysis reveals that the positive shift in $\delta^{26}Mg$ values in the whole-rock carbonate is due to a small increase in dolomite abundance. The analysis is also used to determine original limestone $\delta^{26}Mg$ values in marine carbonates, revealing stratigraphic changes in the $\delta^{26}Mg$ values of the carbonate deposited during the glacial sea-level lowstand, and the pre-glacial and post-glacial sea-level highstands. The limestone end-member exhibits a higher $\delta^{26}Mg$ value for carbonate deposited in the sea-level lowstand, consistent with precipitation of primary aragonite during the Hirnantian glaciation in this tropical-shelf setting, and lower $\delta^{26}Mg$ values before and after the glaciation, which is consistent with the precipitation of calcite during the sea-level highstands. However, the effects of diagenesis on $\delta^{26}Mg$ values in carbonate sediment are difficult to predict, therefore Mg isotopes alone do not permit a conclusive determination of primary carbonate polymorph mineralogy. A synchronous negative shift in $\delta^{44/40}Ca$ values, positive shift in $\delta^{13}C$ values, and intermittently high Sr/Ca ratios recorded in the carbonates deposited during the sea-level lowstand interval add support to the interpretation of aragonite deposition during the glaciation. Previous laboratory experiments have also demonstrated that aragonite can precipitate in seawater with the chemistry of a 'calcite sea' at temperatures above 20–23°C, which was likely common at low latitudes in the early Paleozoic. This study demonstrates the utility of applying a

multi-proxy geochemical approach using Mg, Ca, and C isotopes, and elemental Sr/Ca ratios to reveal aragonite that has inverted to calcite over geologic time. It also cautions against misinterpreting facies-dependent changes in carbonate mineralogy as genuine records of secular variation in seawater chemistry.

Mg isotope tracing of fluid migration during dolomitization

Geological Association of Canada/Mineralogical Association of Canada (GAC/MAC) 2017

May 2017 | Kingston, ON, Canada

Holmden C.* and Kimmig S. R.

Saskatchewan Isotope Laboratory, Department of Geological Sciences, University of Saskatchewan, Saskatoon, SK S7N 5E2

*Presenting author

Dolomite is abundant below the Devonian Prairie Evaporite Formation in the Williston Basin (Canada-USA), but relatively uncommon above this formation. For this and other reasons, brine-reflux factors prominently in models of dolomitization in the Williston Basin. However, radiogenic signatures of Sr isotopes in dolomite, first reported in the partially dolomitized Ordovician carbonates of the Red River Formation (which is interlayered with bedded anhydrite), and later in the Winnipegosis Formation directly underlying the Prairie Evaporite, are incompatible with dolomite formed from evaporatively concentrated seawater sinking into underlying carbonate units from above. Here we explore the possibility that Mg isotopes may also trace the direction of fluid-flow during dolomitization. Dolomite takes up light Mg isotopes, thus enriching dolomitizing fluids in heavy isotopes. Dolomite δ^{26}Mg values should therefore increase in the direction of paleo-fluid flow. We tested this hypothesis on dolomitized (*Thalassinoides*) burrows in the lower 'C member' carbonate of the Red River using core samples collected from wells spatially distributed across the Williston Basin. In all the cores examined, the burrows are pervasively dolomitized and the matrix is limestone. If evaporatively concentrated seawater descended through burrows and dolomitized them, then burrow dolomite δ^{26}Mg values should increase toward the center of the basin in the direction of the paleo-dip of the 'C member' carbonate beds. What we find instead is burrow dolomite δ^{26}Mg values increasing away from the center of the basin in all directions (–1.9‰$_{DSM3}$ to –1.3‰$_{DSM3}$), indicating that the dolomitizing fluids ascended rather than descended through the burrows. This is evidence that the dolomitizing fluids were connate waters that originated in the deepest part of the Williston basin. Burrow dolomite $^{87}Sr/^{86}Sr$ ratios decrease away from the basin-center supporting this interpretation. Acquired through water-rock interaction with Precambrian basement rocks, the radiogenic signature of the dolomitizing fluid will become progressively less radiogenic due to mixing with Sr released from carbonate rocks along the flow path during the process of dolomitization. We conclude that dolomitization of the Red River

burrows is unrelated to downward migrating brines associated with evaporite deposition in the Williston Basin, but possibly linked to the thermal history of the basin. We speculate that a late Paleozoic heating event triggered Mg-bearing connate waters to ascend through burrows of the ‘C member’ carbonate, and possibly other permeable units in the Williston Basin as well, dolomitizing them at higher than burial temperatures.

Mg isotope tracing of fluid migration during dolomitization

Dolomieu (200+25 Years of Dolomite) Conference on Carbonate Platforms and Dolomite
October 2016 | Selva di Val Gardena, Italy

Kimmig S. R.* and Holmden C.
University of Saskatchewan, Department of Geological Sciences
*Presenting author

Most of the carbonate rock of the Williston Basin (Canada-USA) is dolomitized below the middle Devonian Prairie Evaporite Formation, whereas dolomite is rare in carbonates above. This observation, along with numerous examples of older and smaller evaporite deposits, has guided the interpretation that dolomitization in the Williston Basin was driven by downward migrating, high Mg/Ca brines from evaporating salt pans. This view contrasts, however, with radiogenic Sr isotope signatures preserved in one of the deeper dolomitized units in the basin, the Late Ordovician Red River Formation. These high $^{87}Sr/^{86}Sr$ ratios are incompatible with dolomitization by downward percolating seawater-derived brines, suggesting instead contact with Precambrian basement rocks during upward migration of fluids during dolomitization. Here we show that the magnesium (Mg) isotope compositions in Red River dolomite can be used to determine the direction of fluid-flow during dolomitization, which has direct bearing on the model of dolomitization. The basis of the technique lies in the fractionation of Mg isotopes ($\delta^{26}Mg$) that occurs during carbonate formation, with lighter isotopes of Mg incorporated into the dolomite. Accordingly, $\delta^{26}Mg$ values of Red River dolomite should increase in the direction of fluid flow and with progressive dolomitization, reflecting the loss of light isotopes of Mg from the dolomitizing fluid into the dolomite, which enriches the dolomitizing fluid in heavy Mg isotopes.

We tested this hypothesis on dolomitized (*Thalassinoides*) burrows in the lower C unit of the Red River, which extends through the entire Williston Basin. The burrow network represents the first phase of dolomitization, and the one with the most obvious links to seawater, and/or evaporated seawater, as the source of the dolomitizing fluid. It has been suggested that seawater used the porous and permeable burrow network to filter downward into the succession. If this were true, $\delta^{26}Mg$ values should increase downward through the burrow network. What we find instead is a regional pattern of increasing $\delta^{26}Mg$ values from basin center to the basin edge ($-1.9‰_{DSM3}$ to $-1.3‰_{DSM3}$), indicating that fluids migrated upward through the burrow network for hundreds of kilometers following the regional dip of the strata. A gradient in Sr isotopes mimics that of Mg

isotopes with less radiogenic signatures in carbonates further from the basin center. We therefore conclude that dolomitization of the Red River carbonate is not tied to the spatial and temporal history of evaporite deposition in the Williston Basin, but rather to the thermal history of the basin with dolomitization likely occurring during a late Paleozoic heating event that drove Mg-rich connate waters in the center of the basin upward and outward into the overlying strata

Using a novel Mg isotope tracer to investigate the dolomitization of the Red River Formation in the Williston Basin

American Geophysical Union (AGU) Fall Meeting

December 2015 | San Francisco, CA, USA

Honors: Outstanding Student Poster Award (OSPA) – Volcanology, Geochemistry, and Petrology Section

Worsham, S. R.* and Holmden, C.

Saskatchewan Isotope Laboratory, University of Saskatchewan, Saskatoon, Saskatchewan, Canada

*Presenting author

The Williston Basin is a sub-circular intracratonic basin spanning central North America with its center in NW North Dakota. The Late Ordovician Red River Formation is an economically viable unit in the Williston Basin containing large hydrocarbon reserves in Saskatchewan, North Dakota, Manitoba and Montana. Red River dolomitization contributed to the reservoir-quality porosity and permeability observed today with three types of dolomite (burrow, matrix and saddle) possibly representing three events. Dolomitization is widely believed to have resulted from downward percolating brines, due to the stratigraphically close association between dolomite deposits and overlying basin-scale evaporites. However, in contrast, Sr isotope evidence suggests an upward fluid migration in the basin. Spatial variation of Mg isotopes (δ^{26}Mg) may serve as a direct tracer of dolomitizing fluid flow. Dolomite sequesters light isotopes of Mg from dolomitizing fluids, therefore, the fluid will evolve with time and distance to heavier δ^{26}Mg values. Accordingly, the δ^{26}Mg values of the Red River dolomite should increase in the direction of fluid flow. We test this hypothesis on Red River burrow dolomite from the Williston Basin; the first event most often attributed to downward infiltration of brines. Burrow δ^{26}Mg values range between –1.89‰ and –1.31‰. Using contouring software, the data are shown to form a pattern of increasing δ^{26}Mg values out from the center of the Williston Basin, indicating an up-dip migration of dolomitizing fluids through the burrow network, not down-dip as suggested by the brine reflux model. We conclude that dolomitization of the Red River carbonate is not tied to the spatial and temporal history of evaporite deposition in the Williston Basin, but rather to the thermal history of the basin, suggesting dolomitization likely occurred during a late Paleozoic heating event that drove Mg-rich connate waters in the center of the basin upwards into overlying strata.

Magnesium isotope cycling within *Acer saccharum* (sugar maple)

EnvironMetal Isotopes Conference (EMI)

August 2013 | Ascona, Switzerland

Worsham, S. R.[a]*, Holmden, C.[a], and Bélanger, N.[b]

[a] Department of Geological Sciences, University of Saskatchewan, Canada

[b] Université du Québec à Montréal, Montréal, Canada

*Presenting author

Magnesium (Mg) is a vital macronutrient for plants. Not only is Mg involved with metabolic functions and respiration, but it also serves as the coordinating cation of the chlorophyll molecule thus making it an essential component of photosynthesis. Previous studies have demonstrated mass dependent fractionation of Mg within laboratory grown vegetation while there has been only a handful of confirmed cases of plant fractionation in the field to date. This study builds on previous work by coupling laboratory and field based investigations of Mg isotope fractionation within *Acer saccharum* (sugar maple). Our main objective is to provide a better understanding of a forest Mg-cycle by determining to what extent δ^{26}Mg may serve as a useful tracer. A broader question motivating this work is the potential impact of forest Mg-cycling on the continental weathering flux signature of Mg delivered to the oceans by river flow.

The field site consists of a sugar maple dominated plot within a forested watershed located in southern Québec, Canada. Soils in the watershed are developed from granite, mangerite, and anorthosite. Mg isotope fractionation is observed between different plant tissues including roots, stemwood, and leaves, as well as the xylem exudates (sap). Fractionation is also associated with the breakdown of the chlorophyll molecule during leaf senescence, reflected in the light isotope enrichment of Mg in tree sap where the re-translocated Mg is stored in the xylem during the winter months. Additional reservoirs within the watershed have also been investigated and include soil waters, bulk precipitation, throughfall, and stream water. The total range of δ^{26}Mg values within the study plot is 1.37‰$_{DSM3}$ (approximately 30% of reported terrestrial variation).

Earlier laboratory based plant growth experiments have demonstrated a light isotope enrichment of Mg in soil pools, complementing heavy isotope uptake and assimilation into plants with fractionation purportedly occurring at the root-soil interface. We do not see this light isotope enrichment within the soil pool in our study site when whole seedlings (serving as analogues of adult trees) are analyzed. Sequential soil leach experiments as well as in-house potted plant

experiments are currently in progress in order to determine the extent to which fine roots of sugar maple trees fractionate Mg during plant uptake.

Magnesium isotope tracing of dolomitization in the Williston Basin

21st Annual Williston Basin Petroleum Conference (WBPC)

May 2013 | Regina, SK, Canada

Honors: Honourable Mention Student Geology Poster

Worsham, S. R.[1]*, Holmden, C.[1], and Qing, H.[2]

[1]University of Saskatchewan Department of Geological Sciences, Saskatoon, Saskatchewan, Canada

[2]University of Regina Department of Geology, Regina, Saskatchewan, Canada

*Presenting author

The isotopes of Mg in dolomite have received little attention as a potential tracer of the process of dolomitization. In this study, we report Mg isotope data for the Upper Yeoman and Lower Herald Formations within the Williston Basin. Three stages of dolomitization have been recognized on the basis of petrography and geochemistry: (1) burrows, (2) matrix, and (3) saddle dolomite.

The data acquired, thus far, reveal a small but significant range in dolomite δ^{26}Mg values, ranging from –1.31 to –1.67‰ relative to the DSM3 standard reference material. Yeoman limestone ranges from –2.16‰ to –2.86‰. For comparison, modern seawater has a δ^{26}Mg value of –0.82‰ and many igneous silicate rocks lie near –0.20‰. Nearly identical δ^{26}Mg values characterize burrow dolomite (–1.67‰) and matrix dolomite (–1.66‰) from a single core. Saddle dolomite from the same core yields a significantly higher value (–1.42‰), as do mixed samples of burrow and matrix dolomite (–1.36 ± 0.09‰, $2\sigma_{mean}$, n = 5) from a second core located ~ 25 km up-dip from the first. Three hypotheses regarding the source of the spatial and temporal range in δ^{26}Mg values in the Yeoman Formation dolomite merit further investigation: (1) multiple sources of isotopically distinct Mg-rich fluids, (2) a single-source Mg-rich fluid evolving with increasing time and distance along the fluid flow path due to preferential loss of ^{24}Mg from solution during the process of dolomitization, and (3) different local-scale conditions of dolomitization that may affect the dolomite fractionation factor, such as temperature and precipitation rate.

Magnesium isotope variability in whole-rock limestone through the Hirnantian glaciation event in an epeiric sea environment

American Geophysical Union (AGU) Fall Meeting

December 2012 | San Francisco, CA, USA

Worsham, S. R.[1]*, Holmden, C.[1], and Finney, S. C.[2]

[1]Saskatchewan Isotope Laboratory, University of Saskatchewan, Saskatoon, Saskatchewan, Canada

[2]Department of Geological Sciences, California State University at Long Beach, Long Beach, California, USA

*Presenting author

The results of a magnesium (Mg) isotope study are reported in carbonate rocks from the Monitor Range section in Nevada through the Hirnantian glaciation event. Located in the (epeiric) Martin Ridge Basin, the Monitor Range section has previously been the subject of calcium (Ca) and carbon (C) isotope studies revealing a large negative $\delta^{44/40}$Ca excursion and a large positive δ^{13}C excursion. The excursions in Ca and C isotopes are strongly negatively correlated, which is not expected on the basis of the large difference in their oceanic Ca and C residence times. The synchronousness of the excursions is evidence that the Monitor Range section records changes affecting smaller, localized Ca and C reservoirs of the Martin Ridge Basin. The ocean residence time for Mg is even longer than that of Ca. We therefore undertook this study to find out whether the potential Mg isotope changes through the Monitor Range section would record local-scale or global-scale changes in Mg-cycling during the Hirnantian glaciation. Large stratigraphic changes in δ^{26}Mg values ranging between –4.07‰ and –1.70‰ have been measured thus far. In addition, a large positive shift in δ^{26}Mg occurs at the onset of glaciation, coincident with the $\delta^{44/40}$Ca and δ^{13}C excursions as well as the glacio-eustatically controlled sea-level fall. Two explanations for the observed stratigraphic variability in δ^{26}Mg values merit consideration: (1) Changes in carbonate precipitation rate affecting both the Mg concentration and isotopic composition of the primary produced calcite, and (2) Changes in dolomite mineral abundance in the limestones. More work is in progress to decipher which of these explanations is the most likely.

Magnesium isotope cycling within *Acer saccharum* (sugar maple)

Goldschmidt Conference

June 2012 | Montréal, QC, Canada

Worsham, S.[1]*, Holmden, C.[1], and Bélanger, N.[2]

[1]Saskatchewan Isotope Laboratory, University of Saskatchewan, Saskatoon, Canada

[2]Université du Québec à Montréal, Montréal, Canada

*Presenting author

Magnesium (Mg) serves as an important macronutrient for plants being involved with metabolic functions, respiration and most importantly, photosynthesis. Previous studies have demonstrated mass dependent fractionation of Mg within laboratory grown vegetation (Black et al., 2008; Bolou-Bi et al., 2010) while there has been only one confirmed case of plant fractionation in the field (Tipper et al., 2010). This study builds on previous work by coupling laboratory and field based investigations of Mg isotope fractionation within *Acer saccharum* (sugar maple) plants. Our main objective is to determine whether Mg isotopes might serve as useful tracer of a forest Mg-cycle.

The study site consists of a sugar maple stand within a first-order catchment located in southern Québec, Canada. Significant Mg isotope fractionation has been established between different tree tissues such as roots, stemwood, and leaves (both senescent and photosynthesizing) as well as other reservoirs including soil waters, precipitation, throughfall, and stream water. The total range of $\delta^{26}Mg$ ($^{26}Mg/^{24}Mg$) values within the study plot is $1.37‰_{DSM3}$ (approximately 30% of reported terrestrial variation).

Earlier laboratory based studies of potted plants have demonstrated a light isotope enrichment of Mg in the soil pool, complementing heavy isotope uptake and incorporation into plant material (Black et al., 2008; Bolou-Bi et al., 2010). In contrast to these reported data trends, we do not see light isotope enrichment within the soil pool in nature when whole seedlings are analyzed as analogues of adult trees. We are conducting our own pot experiment with sugar maple to investigate this effect, which will guide our interpretations of this field study. Full results will be presented and discussed in detail regarding factors influencing Mg isotope cycling within a sugar maple dominated catchment.

Magnesium isotope fractionation in a hardwood forest of Southern Québec, Canada

6e Colloque annuel du Centre d'étude de la forêt (CEF)

May 2012 | Rouyn-Noranda, QC, Canada

Worsham, S.[1], Holmden C.[1], and Bélanger N.[2]*

[1]Saskatchewan Isotope Laboratory, University of Saskatchewan, Saskatoon, Canada

[2]Université du Québec à Montréal, Montréal, Canada

*Presenting author

Magnesium (Mg) is an essential macronutrient for plants, acting as the coordinating cation for chlorophyll as well as serving other important metabolic functions. Laboratory studies have demonstrated mass dependent fractionation of Mg within plants, while there is only one confirmation of plant fractionation in the field to date. Our study builds on previous work through an investigation of Mg isotope fractionation in a forested ecosystem. Our main objective is to determine whether Mg isotopes might serve as useful tracer of the forest Mg cycle. The study takes place in a forested first order catchment of southern Québec dominated by sugar maple (*Acer saccharum*) and characterized by soils developed from granite, mangerite and anorthosite. Thus far, we have found significant Mg isotope fractionation between different tree tissues such as roots, stemwood, and leaves (both senescent and photosynthesizing) as well as other reservoirs including soil waters, precipitation, throughfall, and stream water. The total range of $\delta^{26}Mg$ ($^{26}Mg/^{24}Mg$) values within the study plot is 1.37‰ (approximately 30% of reported terrestrial variation). In contrast to results previously reported in pot studies, we do not see a light isotope enrichment of Mg in the soil pool as a consequence of vegetation uptake. One of the most interesting findings is the considerable fractionation associated with the degradation of chlorophyll during leaf senescence. Full results will be presented and discussed in detail.

Magnesium and calcium isotope study of limestone and dolomite in Middle and Upper Ordovician strata of the Williston Basin

American Geophysical Union (AGU) Fall Meeting

December 2011 | San Francisco, CA, USA

Worsham, S. R.* and Holmden, C.

Saskatchewan Isotope Laboratory, University of Saskatchewan, Saskatoon, Saskatchewan, Canada

*Presenting author

Using Magnesium (Mg) and Calcium (Ca) isotopes, we investigate a complex, discontinuous, pattern of subsurface dolomitization including intervening beds of limestone through the Upper Yeoman and Lower Herald Formations within the Williston Basin, cored near the town of Midale in southeastern Saskatchewan. The character of the stratigraphic sequence suggests paleo-aquifers as an explanation of the partially dolomitized units.

Previous work has demonstrated a large range of fractionation with $\delta^{44/40}$Ca between the precursor limestone value (inferred from mixing calculations) and the dolomite value within the Yeoman Formation, suggesting that Ca isotope values could be used to identify sources of dolomitizing fluids. δ^{26}Mg in conjunction with $\delta^{44/40}$Ca may be used to better constrain the source of these Mg-rich fluids. Preliminary data reveal a range in limestone δ^{26}Mg values from –2.77 ± 0.05‰ to –2.86 ± 0.07‰ with a mean value of –2.8‰. Dolomite δ^{26}Mg values range from –1.31 ± 0.07‰ to –1.64 ± 0.06‰ with a mean value of –1.48‰.

Measured dolomite Mg isotope values are consistent with reported dolomite values from a Mississippian aged carbonate aquifer (Jacobson et al., 2010). Measured limestone Mg isotope values are analogous to modern day values reported in the literature (Wombacher et al., 2011), although modern limestones exhibit a much wider array of fractionation than dolomites. Further analyses of dolomite samples from younger stratigraphic levels within the Williston Basin sequence are being conducted in order to determine the extent of Mg isotope variability.